Twisted Magnetic Fluxtubes in the Sun

A thesis

submitted for the degree of

Doctor of Philosophy

in

The Department of Physics,

Pondicherry University,

Puducherry - 605 014, India

by

Samrat Sen

Indian Institute of Astrophysics,

Bangalore - 560 034, India

January 2020

Twisted Magnetic Fluxtubes in the Sun

Samrat Sen
Indian Institute of Astrophysics

Indian Institute of Astrophysics
Bangalore - 560 034, India

Title of the thesis	:	**Twisted Magnetic Fluxtubes in the Sun**
Name of the author	:	**Samrat Sen**
Address	:	Indian Institute of Astrophysics II Block, Koramangala Bangalore - 560 034, India
Email	:	samrat@iiap.res.in
Name of the supervisor	:	**Prof. Arun Mangalam**
Address	:	Indian Institute of Astrophysics II Block, Koramangala Bangalore - 560 034, India
Email	:	mangalam@iiap.res.in

Declaration of Authorship

I hereby declare that the matter contained in this thesis is the result of the investigations carried out by me at the Indian Institute of Astrophysics, Bangalore, under the supervision of Prof. Arun Mangalam. This work has not been submitted for the award of any other degree, diploma, associateship, fellowship, etc. of any other university or institute.

Signed: _____

Date: _____

Certificate

This is to certify that the thesis entitled **'Twisted Magnetic Fluxtubes in the Sun'** submitted to the Pondicherry University by Mr. Samrat Sen for the award of the degree of Doctor of Philosophy, is based on the results of the investigations carried out by him under my supervision and guidance, at the Indian Institute of Astrophysics. This thesis has not been submitted for the award of any other degree, diploma, associateship, fellowship, etc. of any other university or institute.

Signed: _____

Date: _____

List of Publications:

In Refereed Journals:

1. *Model of a fluxtube with a twisted magnetic field in the stratified solar atmosphere.*
   Sen, S. & Mangalam, A., 2018a, Advances in Space Research, 61, 617-627.
   Chapter 4

2. *Open and Closed Magnetic Configurations of Twisted Flux Tubes.*
   Sen, S. & Mangalam, A., 2019, Astrophysical Journal, 877(2), 127.
   Chapter 5

3. *Self-similar closed field twisted magnetic configuration of fluxtubes in the solar atmosphere.*
   Sen, S., & Mangalam, A., in preparation.
   Chapter 5

In Conference Proceedings:

1. *Fluxtube model in the solar atmosphere.*
   Sen, S. & Mangalam, A., 2018b, IAU Symposium, 340,
   DOI: 10.1017/S1743921318001096
   Chapter 5

2. *Energy distribution of solar flare events.*
   Sen, S.; Mangalam, A.; Ramesh, R., 2018, IAU Symposium, 340,
   DOI: 10.1017/S1743921318001084
   Chapter 7

Presentations

1. International Astronomical Union Symposium 340, February 2018, Birla Institute of Scientific Research, Jaipur, India.
   Title 1 : Magnetohydrostatic equilibria of flux tubes
   Title 2 : Energy distribution of solar flare events
   Nature of participation: Poster presentation.

2. Dynamic Sun-II, Solar Magnetism from Interior to the Corona, February, 2018, Siem Reap, Angkor Wat, Cambodia
   Title : Magnetohydrostatic equilibria of flux tubes
   Nature of participation: Contributed talk.

3. Dynamic Sun-I, March 2016, Benaras Hindu University, Varanasi, India.
   Title : Model of a flux tube with twisted magnetic fields
   Nature of participation: Poster presentation.

4. Astronomical Society of India meeting, May 2016, Kashmir University, Kashmir.
   Title : Model of a flux tube with twisted magnetic fields
   Nature of participation: Poster presentation.

Acknowledgements

Undertaking this Ph.D. has been a truly life-changing experience for me and it would not have been possible to do so without the support and guidance that I received from many people.

First of all, I would like to thank my Thesis supervisor Prof. Arun Mangalam for all the support and encouragement he gave me during the entire course of my Ph.D. Without his guidance and constant feedback, this Thesis would not have been achievable for me. Many thanks to my doctoral committee members, Prof. R. Ramesh, and Dr. Ramesh Naidu for their valuable feedback during the meetings.

I am thankful to IIA for providing me an excellent academic environment and the necessary facilities for my research work during my tenure. I thank the staff of the Vainu Bappu Observatory, Kavalur (Indian Institute of Astrophysics), where some of the work was done, for the hospitality provided during my visits.

I also thank all my friends and fellow students at the IIA for their constant support and encouragement.

Last but not least I would like to convey my gratitude to my parents, and my extended family for supporting me in every phase of my life to pursue my dream.

Dedicated to

Baba & Maa

Abstract

The study of magnetic fluxtubes is a very important aspect as it plays an important role in several astrophysical phenomena in the solar atmosphere. Thus, it is very important to understand the properties and structures of the magnetic configuration and thermodynamic quantities of the fluxtubes. In this Thesis, we construct two different classes of fluxtube models with twisted magnetic fields by solving the Grad-Shafranov equation (GSE) semi-analytically. We also calculate the energy distribution of a braided system of magnetic field lines using the Self-Organized Criticality (SOC) model.

The fluxtube models we build are in magnetohydrostatic (MHS) equilibria for an axisymmetric geometry, spanning from the photosphere to the lower part of the transition region within a realistic stratified solar atmosphere subject to solar gravity. We assume a general quadratic expression of the magnetic flux function for the gas pressure and poloidal current and solve the GSE analytically. One solution is a combination of a homogeneous and a particular part where the former is separable by a Coulomb function in r and exponential in z, while the particular part is an open configuration that has no z dependence. The other fluxtube model can be branched out into open and closed field solutions by using a self-similar formulation with different profile functions and incorporating stratified solar gravity to maintain the magnetohydrostatic equilibria, which is a modification of earlier self-similar models by a twist. We study the admitted parameter space that is consistent with the conditions in the solar atmosphere and derive magnetic and the thermodynamic structures inside the fluxtubes that are reasonably consistent with the photospheric magnetic bright points (MBPs) for both open and closed field Coulomb function and self-similar models as estimated from observations and simulations. The obtained open fluxtube solutions can be used as the background conditions for the numerical simulations for the study of the wave

propagation through the fluxtubes. The closed field solutions can be used to construct realistic magnetic canopies in the solar atmosphere.

We estimate winding number distributions of braided topologies. We also calculate the power-law index of the energy distribution for the solar radio flare events on 14 February 2011, and 11 March 2011, captured by Gauribidanur Radio Telescope, and compare the theoretical prediction of the power-law index with the observational estimate.

Contents

List of Figures

List of Tables

Abbreviations

AIA	**A**tmospheric **I**maging **A**ssembly
AR	**A**ctive **R**egion
BC	**B**oundary **C**ondition
FFF	**F**orce **F**ree **F**ield
GBRT	**G**auribidanur **R**adio **T**elescope
GSE	**G**rad-**S**hafranov **E**quation
HMI	**H**elioseismic and **M**agnetic **I**mager
MBP	**M**agnetic **B**right **P**oint
MHD	**M**agneto**H**ydro**D**ynamics
MHS	**M**agneto**H**ydro**S**tatics
NLFFF	**N**on-**L**inear **F**orce **F**ree **F**ield
SOC	**S**elf-**O**rganized **C**riticality
SDO	**S**olar **D**ynamics **O**bservatory
SNIP	**S**tatistic Sensitive **N**on-linear **I**terative **P**eak clipping
SS	**S**elf-**S**imilar
SST	**S**wedish **S**olar **T**elescope

Glossary of symbols

$\mathbf{g}$	Acceleration due to gravity at solar photosphere
t	Arbitrary time
$\bar{\mu}$	Average molar mass
j_ϕ	Azimuthal component of current density
B_ϕ	Azimuthal component of magnetic field intensity
ϕ	Azimuthal coordinate in cylindrical geometry
$\mathbf{j}$	Current density
μ_e	Effective molar mass
$\mathbf{E}$	Electric field intensity
σ	Electrical conductivity
p	Gas pressure
p_t	Gas pressure at the transition region
W	Global winding number
ν	Kinematic viscosity
S_0	Lundquist number
η_m	Magnetic diffusivity
W_m	Magnetic energy
$\mathbf{B}$	Magnetic field intensity
Ψ	Magnetic flux function
μ_0	Magnetic permeability in vacuum medium
R_m	Magnetic Reynold's number
ρ	Mass density
$\mathbf{v}$	Particle velocity
p_0	Photospheric gas pressure
$\mathbf{U}$	Plasma velocity
I_p	Poloidal current
j_r	Radial component of current density
r	Radial coordinate in cylindrical geometry

B_r	Radial component of magnetic field intensity
R	Radius of the fluxtube
h	Scale height
ξ	Self-similar parameter
D	Magnetic shape function
$M_\odot$	Solar mass
$R_\odot$	Solar radius
T	Temperature
p_T	Total gas pressure
χ	Twist in the magnetic field line
R_g	Universal gas constant
j_z	Vertical component of current density
z	Vertical coordinate in cylindrical geometry
B_z	Vertical component of magnetic field intensity
w	Winding number

Chapter 1

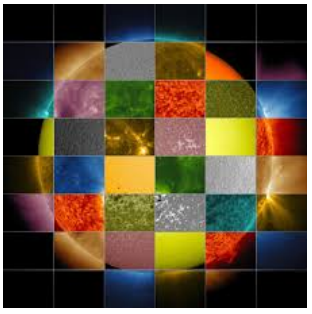

Image source: `www.thesuntoday.org`

Introduction

The light that we see by our naked eyes from the Sun is due to the optical radiation coming from its surface. The optical emission is produced by the Thomson scattering in the upper atmosphere of the Sun, which is many orders of magnitude less intense and therefore can only be seen when it is obstructed at the time of the solar eclipse. The surface of the Sun, the photosphere, is the best region to obtain information about the solar magnetic features. Several advanced ground and space observations have revealed many details of solar magnetism which play an important role in various phenomena in the solar atmosphere.

1.1 Solar interior and its atmosphere

Sun is the nearest star in our galaxy, having a radius of $R_\odot \sim 700$ Mm and a mass of $M_\odot \sim 10^{33}$ g. The importance of study about the Sun is not only as an object of fascination but also is the ultimate source of energy in our entire solar system. Another advantage of the study of the Sun is that it is the closest laboratory to study various astrophysical phenomena in great detail. The basic structure of the solar interior and its outer atmosphere is shown by the cartoon in Figure 1.1.

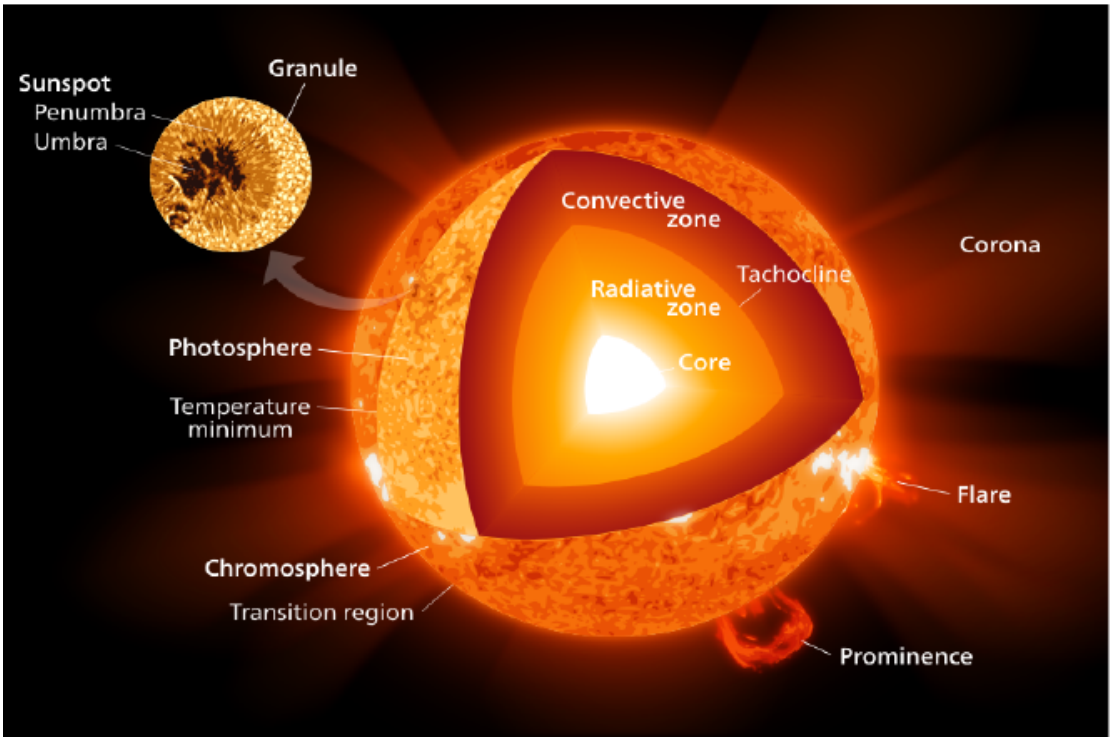

FIGURE 1.1: Structure of the solar interior and its atmosphere. Figure courtesy: `https://en.wikipedia.org/wiki/Sun`.

The formation of the Sun was due to the contraction of a rotating interstellar cloud. Due to the gravitational collapse, the central part of the interstellar cloud started contracting, and the core became hot enough to initiate the thermonuclear reactions which made the Sun a hot ball of plasma. The size of the solar core is ~ 0.2 solar radius which is made of highly dense gas of density ~ 160 g cm^{-3}, and the temperature is ~ 15 million K. The radiative zone is the next layer of the solar

interior which extends from the core to ~ 0.7 solar radii. The energy transport in this layer is mainly due to the radiative diffusion process, where the H and He ions emit X-ray photons, which get scattered, absorbed and then re-emitted by other ions. During this process of random walk, the photons take around 10^6 years to reach the end of the radiative zone. From the end of the radiative zone to the solar surface, the temperature drops down and therefore the radiation process becomes less effective. In this layer, the thermal convection becomes the dominant mode of energy transportation. This layer is called the convective zone. The gas which is in the interior part of the convective zone heats up and expands, and rises to the solar surface, where it releases energy in the surface, cools off, becomes dense and again sinks back to the base of the convective zone. This cool gas again heats up due to the top layer of the radiative zone, continuing a convective cycle, like the roiling of the water bubbles in a pan of boiling water. These convective motions of the hot plasma make the imprint of solar granulations and super granulations on the solar surface. The next layer of the solar interior is the solar surface, photosphere, where the temperature drops down to $\sim$ 6000 K. Most photons that leave the photosphere are in the optical wavelength, which is observed in the white light. The atmosphere of the Sun starts above the photosphere with the chromosphere which is an irregular layer above the photosphere that has a thickness of around 3000 km, the temperature in this region rises from 6000 K to 20000 K. The Hydrogen starts to emit light in this high temperature, which gives a reddish color (Hα line). The next part of the solar atmosphere starts at 2000 km height above the photosphere, called the transition region. This is a very thin and irregular layer where the temperature rises very rapidly from 20000 to 10^6 K. The emission lines from this layer are the C IV, O IV, and Si IV in the ultraviolet region of the solar spectrum which can be observed from space telescopes. The outer atmosphere of the Sun is called the corona, which starts above the transition region and extends up to the interplanetary region. The brightness of the solar corona is small compared to the photospheric brightness so that the corona can only be seen at the time of the total solar eclipse. The temperature of the corona

is of the order of a few million K. Due to the high temperature, the corona shines brightly in the X-rays.

1.1.1 The magnetic surface of Sun

With the recent advancement of the ground and space observations, many details on the solar surface have been revealed. The surface of the Sun, the photosphere is the best source for understanding the evolution of the magnetic field and the related phenomena. The photosphere is covered with large numbers of uneven magnetic ensembles of various spatial sizes, strength, shapes and lifetimes. The different magnetic regions in the photosphere are shown in Figure 1.2. The spatial distribution of the magnetic surface can be described by the filling factor, which is defined as $f_m = S_m/S$, where S_m and S are the surface area occupied by the magnetic field and the total area of interest respectively. The different regions in the solar surface can be categorized in terms of different filling factor values as follows.

1.1.2 The quiet Sun

This is the largest region in the solar surface with the filling factor, $f_m \ll 1$. Almost 90% of this region is covered with the small scale magnetic elements or magnetic fluxtubes. These fluxtubes trace the convective cell boundaries. The smallest part of the convective cell is the granulation network, whose size ranges from a few hundred km to a few thousand km. The image of the quiet sun region is shown in Figure 1.3, where the bright and the dark patches represent the positive and negative polarities of fluxtubes respectively. The lifetime of these individual fluxtubes of this region ranges from a few minutes to a couple of hours.

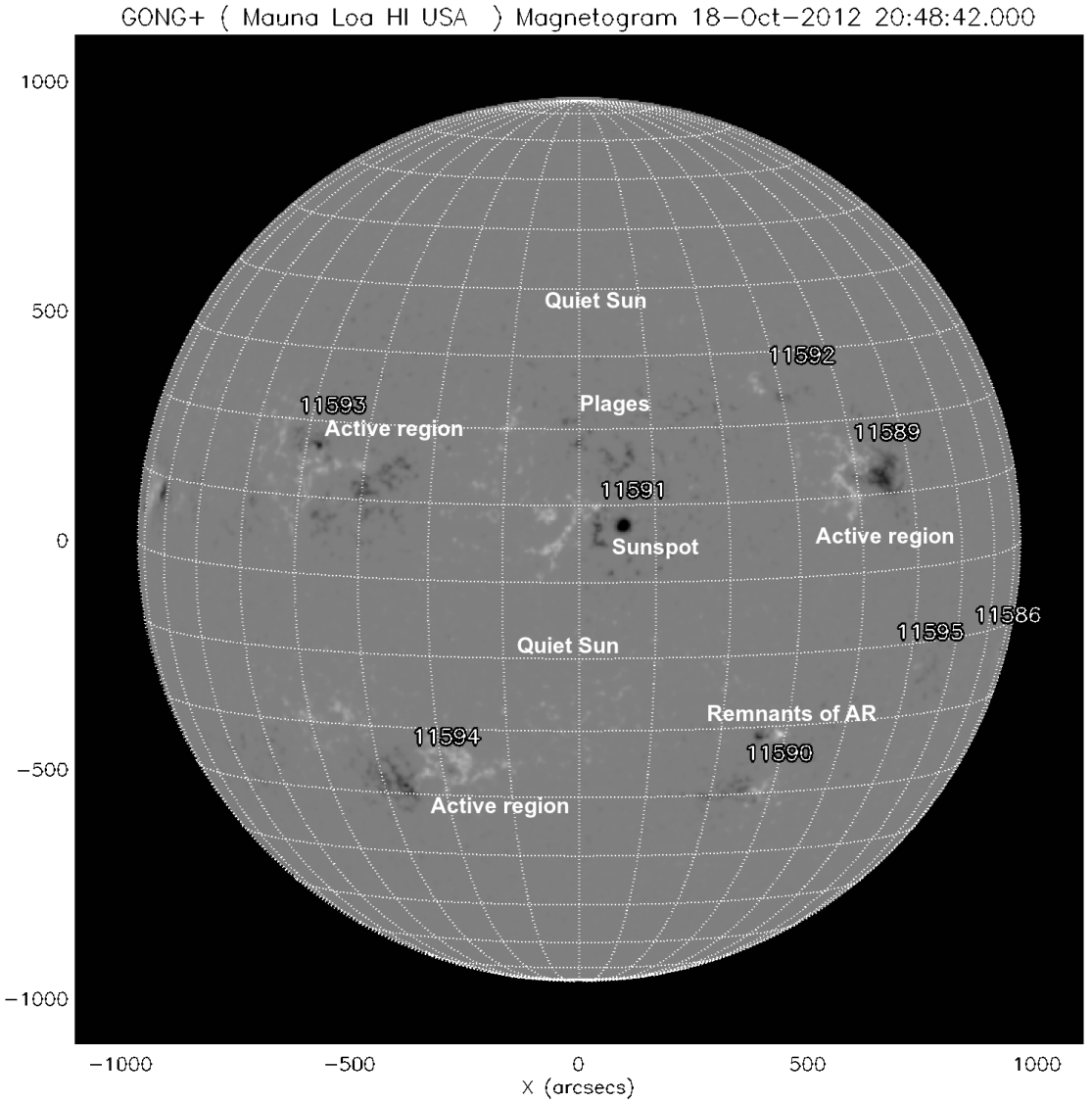

FIGURE 1.2: Full disk magnetogram image taken by AIA/HMI of SDO on 18 October 2012. The white and black patches show the different magnetic regions in the solar photosphere with positive and negative polarities respectively (Figure courtesy: `https://www.solarmonitor.org`).

1.1.3 Sunspots and active regions

Sunspots are the regions of huge magnetic flux concentrations in the photosphere, seen as dark spots of sizes $\sim 5 - 25$ Mm, whose filling factor, $f_m \simeq 1$. The temperature within the sunspots is $\simeq 4000$ K, which is lower than the average temperature of the solar surface, $\simeq 6000$ K. An image of a sunspot in the AR

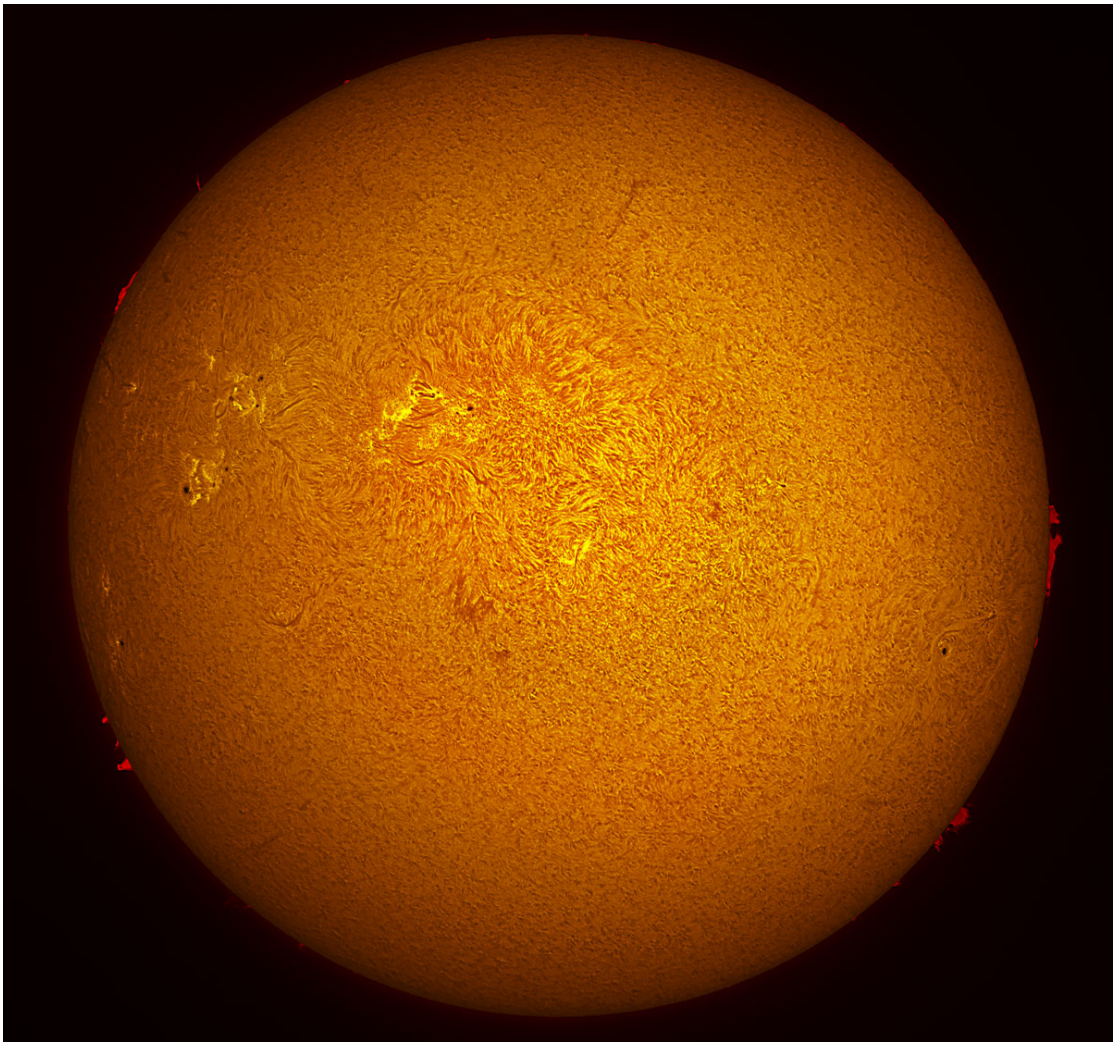

FIGURE 1.3: Full disk image of quiet sun taken taken by Coronado Solarmax 90 Hα telescope. The bright and the dark patches represent the positive and negative polarities of magnetic fields respectively. Figure source: `http://cs.astronomy.com/asy/m/sunandmoon/490622.aspx`

10030 is shown in Figure 1.4. The detailed structure of the sunspots is extremely complex. The center of a sunspot contains a strong and almost vertical magnetic field which is called the umbra. Umbra is surrounded by the penumbra. The magnetic field gradually becomes horizontal along the periphery of the penumbra forming thin magnetic filaments. The field intensity across the penumbra is very inhomogeneous, and the inclination of the magnetic field changes from 45° to 90° with the line of sight direction from inner to the outer part of the penumbra (Title *et al.* 1993). Unsteady plasma flow is observed from the inner to the outer part

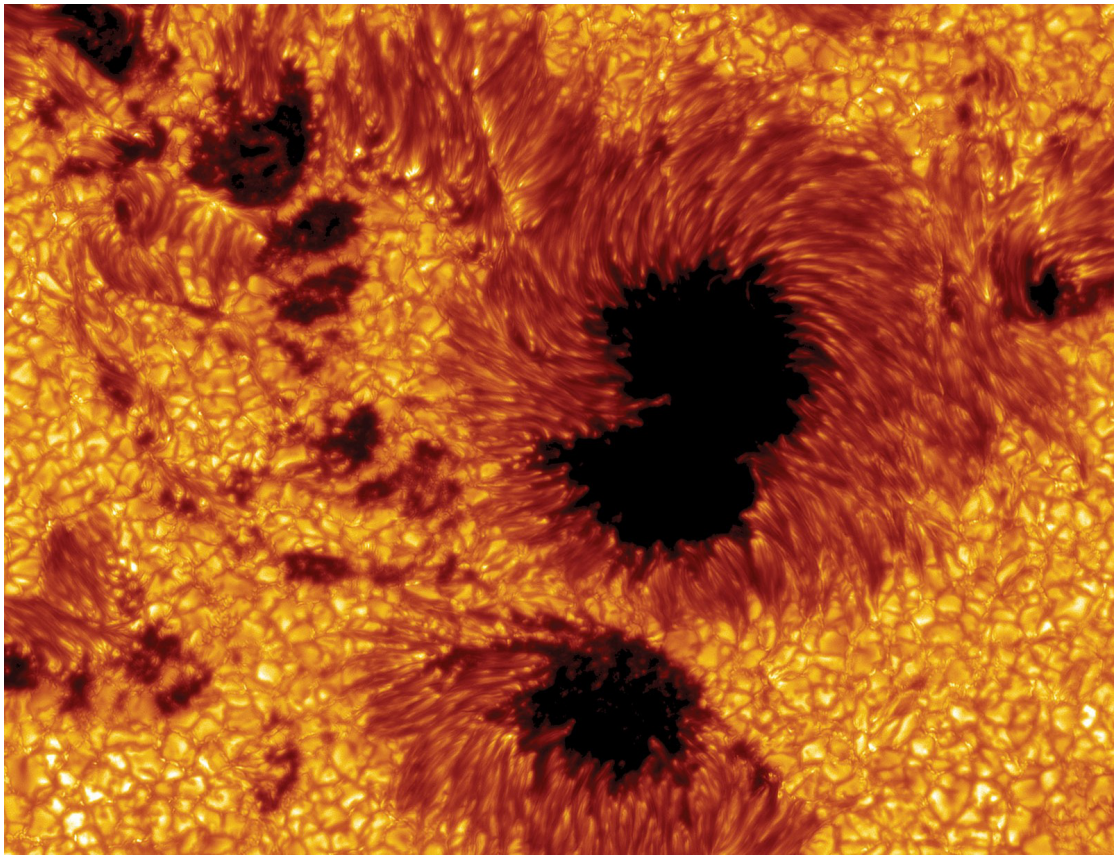

FIGURE 1.4: Image of AR 10030, observed by the Swedish Solar Telescope (SST). Image courtesy: `https://www.britannica.com/science/sunspot`.

of the sunspot penumbra with a velocity of $\sim$ 1 Km s^{-1}, in the photospheric level, which is called the "Evershed effect" (Evershed 1909). The alignments of the bright filaments in the penumbra and the plasma flow due to the Evershed effect makes an angle. A detailed study by Livingston (1991) reveals that the umbra region also consists of filamentary structures that exhibit the presence of horizontal, vertical, and diverging filaments. Newly formed or young sunspots that do not develop penumbra are called pores. The typical sizes of the pores are $\sim 3-6$ Mm, and the lifetimes are $\sim$ few hours. The gradual process and the formation of a sunspot and its appearance in the visible surface require $\sim$ a few days. Due to the presence of the opposite polarity sunspots in a close neighborhood in the active region, several electro-magnetic phenomena occur which shape the overlying atmospheres: chromosphere, transition region, and corona.

1.1.4 Plages

Plages are the magnetic flux concentrated regions present in the photosphere with filling factor, $f_m \sim 0.2 - 0.3$. Figure 1.5 shows the plage region observed by HMI/SDO instrument, where the white and the black patches represent the positive and negative magnetic polarities respectively.

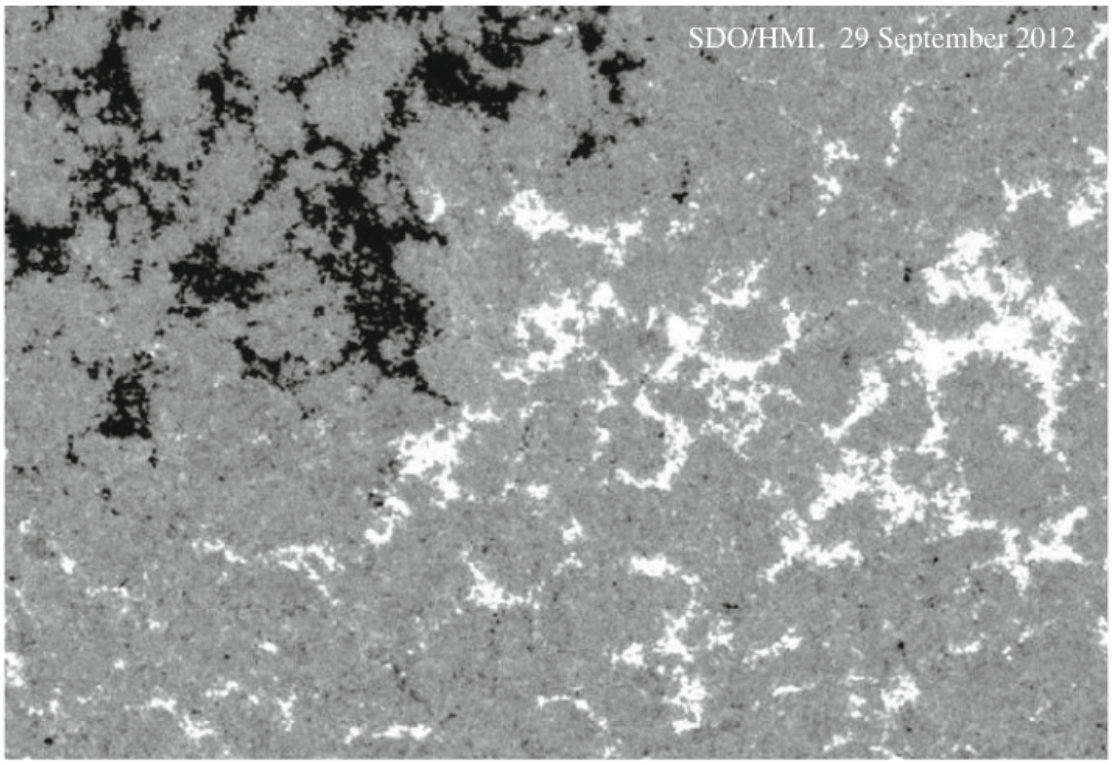

FIGURE 1.5: Image of a plage region taken by HMI/SDO instrument. The white and black patches represent the positive and negative polarities respectively. Image courtesy: Ryutova (2015).

The plage regions are mainly distinguished into two categories: mixed polarity plages, and the plages which are dominated by one magnetic polarity. The plages are originated mainly due to decay of the active regions, or they may form due to magnetic subsurface activities which elevate the emergence of the small scale magnetic fluxtubes. The typical field strength of these regions is about 100 G. The plages that are formed from the remnant active regions are bipolar, and those

which are formed from the decaying sunspots are unipolar. However, these unipolar plages may form a mixed polarity region by overlapping with the neighboring plages of opposite polarities. The dynamics and the activities of the plages are very complex. Some common effects that are shown by both the unipolar and mixed polarity plages, although the study of the properties of both types of plages are equally important as they have unique features of their own.

1.1.5 High latitudes and polar regions

At the end of each 11 years solar cycle, the sunspots and the sunspot groups migrate towards the equator region, whereas the remnants of the older cycle migrate towards polar regions. At the start of a new solar cycle, the sunspot with opposite polarities start emerging at the latitude of about $\pm 40^{\circ}$, and the newly emerged sunspots or the sunspot groups migrate towards the polar region. That is why the merging of the magnetic network elements of opposite polarities of the previous cycle and those of the new cycle can be observed in the first half of a solar cycle. Figure 1.6 shows the polar region of the North pole. The white and black spots represent the positive and negative polarity network elements respectively. The negative polarity elements appear due to the previous cycle, whereas the positive polarity network elements are from the new solar cycle. The white dashed line shown in this picture is the line that demarcates between these two polarity network regions. The filling factor near the demarcation line is important to the study of the formation and evolution of polar plumes and quiescent prominences.

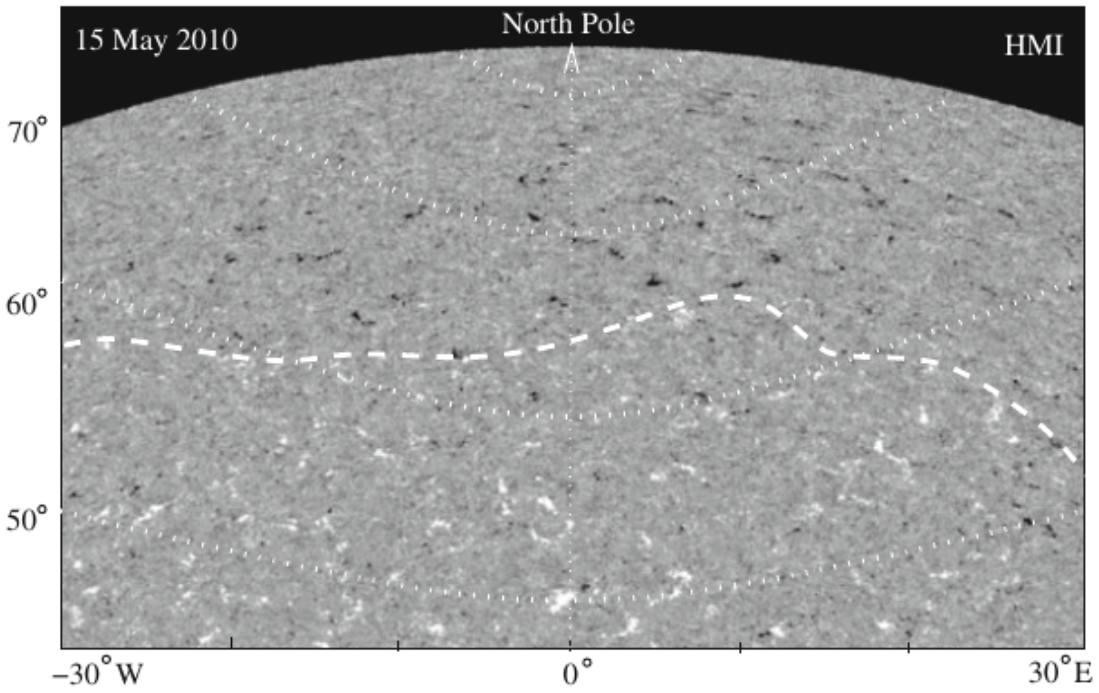

FIGURE 1.6: Magnetogram image of the high altitude solar region near the Norh pole taken by HMI on 15 May 2010. The white and black spots represent the positive and negative polarity network elements respectively. Image courtesy: Ryutova (2015).

1.2 Solar fluxtubes

Magnetic concentrations are observed in the solar surface in the form of fluxtubes, whose spatial scale varies from a few hundred km to few tens of Mm. A magnetic fluxtube is a cylindrical magnetic region with concentrated magnetic flux. The magnetic field lines are parallel to the surface of the cylindrical fluxtubes. This is an aid for visualizing the magnetic fields in the vicinity of the magnetic flux concentrated area. Figure 1.7 shows a cartoon diagram of magnetic fluxtube, where the same number of field lines are passing through two different cross-sectional areas, S_1 and S_2. Magnetic flux cannot either enter or leave the surface of a magnetic fluxtube, and the flux at each cross-sectional area of a fluxtube is equal. Hence, the field strength inside a fluxtube may vary along its length which depends on the cross-sectional area of that fluxtube, although the total flux inside

a fluxtube always remains constant with time.

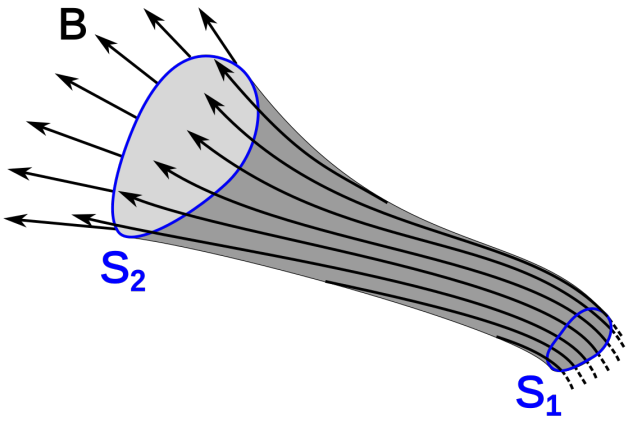

FIGURE 1.7: A cartoon diagram of a magnetic fluxtube. The number of field lines entering the surface S_1 and crossing S_2 are same (Figure courtesy: `https://en.wikipedia.org/wiki/Flux_tube`).

1.2.1 Importance of the study of solar fluxtubes

After the discovery of the million-kelvin temperature of the solar corona, which is at $\approx 10R_{\odot}$ (see Figure 1.8), there was a need to explore the heating mechanisms of the corona. There are two schools of thought for explaining the coronal heating mechanism: one is due to the dissipation of magnetically driven waves in the solar atmosphere, and the other one is due to the reconnection events. The magnetic footpoints in the solar surface are in random motion. If the photospheric motion changes on a time scale faster than what the coronal loop can adjust to, then the waves generated from the photosphere propagate through the magnetic fluxtubes and dissipate in the higher atmosphere in the form of kinetic or thermal energy. On the other hand, if the random displacements of the magnetic footpoints in the photosphere are much slower than the Alfvén transit time along a coronal loop, then the magnetic field lines, and its larger counterparts, the fluxtubes get twisted and wrapped to each other. This twisting and wrapping generate magnetic stress at the surface boundary of the fluxtubes. When the stress reaches a threshold

value, then the field lines explosively snap releasing kinetic and thermal energy. So we see that for both the wave dissipation and braiding mechanisms, the magnetic fluxtubes play a very crucial role. Hence the study of the fluxtubes is an important aspect of solar physics. The size and the magnetic field strength of the fluxtubes seen in various forms in the solar atmosphere are listed in Table 1.1.

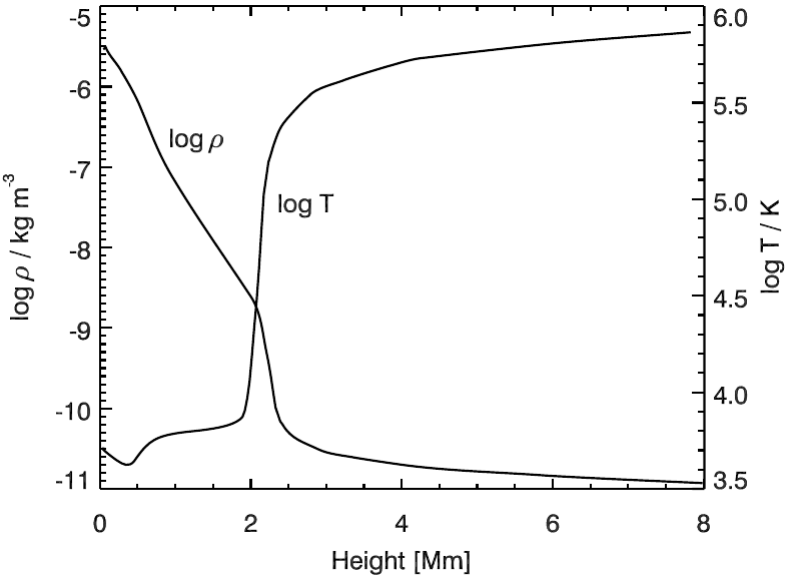

FIGURE 1.8: Variation of temperature, T and density, ρ with vertical height, z from solar surface to corona obtained by Vernazza *et al.* (1981) model. Figure courtesy: Fedun *et al.* (2009).

Fluxtubes in various forms in the solar atmosphere	Size	Magnetic field strength
Sunspots	~ 10 Mm	$3-5$ kG
Faculae	~ 400 km	$1-2$ kG
Photospheric magnetic bright points	$100-1000$ km	$0.1-1$ kG
Coronal loops	$10-10000$ km	~ 1 kG
Coronal bright points	~ 10 Mm	~ 100 G
Spicules	~ 500 km	$30-80$ G

TABLE 1.1: Magnetic field strength and size of the fluxtubes in various forms observed in the solar atmosphere.

1.2.2 Brief historical overview of various fluxtube models

Several attempts have been made earlier to construct the model of fluxtubes for both twisted and untwisted magnetic fields. Schlüter and Temesváry (1958)

studied a two dimensional (2D) axisymmetric fluxtube model without twist for sunspots using a self–similar structure, where a self-similar parameter was defined as a separable combination of r and z, and the relative vertical magnetic field strength at the axis is scaled with a Gaussian profile function of the self-similar parameter. This model is valid for open field lines where the magnetic lines of force rise from a horizontal plane and do not return in the model domain. Yun (1971) implemented a twist in the self–similar structure to model the sunspots. In this model, an empirical form of the azimuthal magnetic field strength $B_\phi(r, z)$ was taken from the data obtained from observations (Stepanov 1965). By solving for the variation of the pitch angle and gradient of the pitch angle, the thermodynamic quantities with the depth were calculated. Motivated by the model and the self–similar structure proposed by Schlüter and Temesváry (1958), Osherovitch (1982) assumed a quadratic form of gas pressure in terms of the flux function to model a closed field fluxtube where the magnetic lines of force rise and return to the same horizontal plane. The linear force free field (FFF) solution for the magnetic configuration is obtained by Chandrasekhar (1956) and carried forward by Low and Lou (1990) for the non-linear case. Prasad *et al.* (2014) obtained the complete analytic solutions for both linear and non-linear force free fields with the twisted magnetic configuration which was applied to the active region for estimating coronal magnetic structures. Steiner *et al.* (1986) have numerically studied a 2D model of open single fluxtube with a twist using the standard boundary conditions including a sheet current to study the magnetic field line structure within and outside the fluxtube. The magnetic and thermodynamic structure for both single and multiple fluxtubes which span from the photosphere to corona have been studied for the case of untwisted magnetic field (Gent *et al.* 2013, 2014), where an empirical form of the magnetic field components is motivated by a self-similar construction. A numerical model of fluxtubes has been studied by Murawski *et al.* (2015b), where an empirical form of magnetic flux function has been assumed; this was followed by a model to study the propagation of the MHD waves through the fluxtubes with an azimuthal velocity perturbation. The steady structure of the 2D

fluxtube was used as a background initial condition to study the propagation of the MHD waves. For example, Vigeesh *et al.* (2009) assumed an empirical form of gas pressure for investigating the wave propagation and energy transport through the fluxtube. Other interesting results of wave behavior in the solar atmosphere have been presented by several authors. Fedun *et al.* (2009) have studied the propagation of the acoustic wave through the solar atmosphere due to the periodic drivers at the photosphere, and Shelyag *et al.* (2010) have modeled the wave propagation through the photospheric magnetic bright points (MBPs). A flowchart of a brief historical overview of various fluxtube solutions is shown in Figure 1.9.

1.3 Aims of this Thesis

The main aims of this Thesis are listed below:

- To construct two different fluxtube models, one of which is of the separable form, and another is in a self-similar form, by solving the Grad-Shfranov equation semi-analytically and incorporating the twist in the magnetic field configuration.
- To obtain an open and closed magnetic structure of fluxtubes that span from the photosphere to the transition region, incorporating the twist, and solving GSE semi-analytically.
- To estimate the magnetic and thermodynamic structures inside the fluxtubes using realistic inputs of the solar atmosphere, and to compare our models with other pre-existing observations and simulations of magnetic bright points (MBPs).

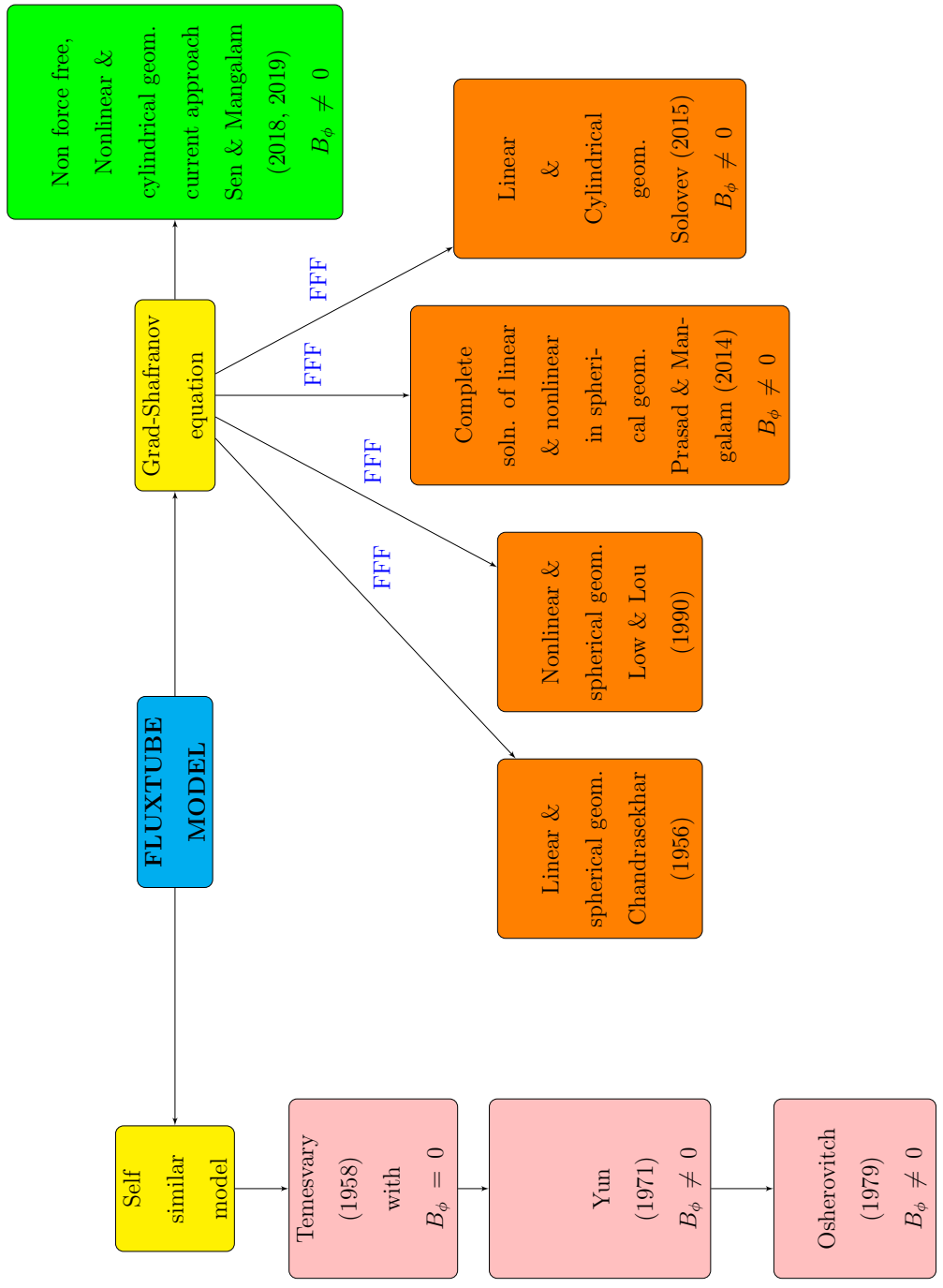

FIGURE 1.9: Flowchart of a brief historical overview of various fluxtube solutions.

- To estimate the winding number distribution of braided magnetic fields using Self-Organized Criticality (SOC) model, and to calculate the energy distribution, and power-law indices of solar flare events.
- To compare the theoretical predictions of power-law indices of energy distribution for the solar flares with the observations of radio flare events.

This thesis aims at finding new and distinct twisted magnetic fluxtube solutions solving GSE semi-analytically. We have constructed open and closed field magnetic configurations for two different models: Coulomb function, and self-similar models. The solution of the Coulomb function model is the combination of a homogeneous part and a particular part. The homogeneous part with closed geometry is separable with a Coulomb function in r whereas the z part decreases exponentially with height, and the particular part with open geometry is a power series of r which is independent of z. On the other hand, we have improved the self-similar model by incorporating twist and modifying the pressure profile, which maintains the hydrostatic pressure balance under the influence of stratified solar gravity. We compare the estimated value of the power-law indices for the solar flare events obtained by the SOC model with the observations of the radio flare events taken by Gauribidanur Radio Telescope (GBRT).

1.4 Thesis constituents

The structure of this Thesis is arranged into eight chapters in total. In Chapter 1, we present a brief overview of the magnetic surface of the Sun, and the motivation to study the magnetic elements with a brief historical overview of various magnetic fluxtube models. Chapter 2 outlines the basic concepts of MHD and applications in the astrophysical domain. We also derive the Grad-Shafranov equation (GSE) which is key to our fluxtube models. Chapter 3 presents a historical overview

of the discovery and observations of fluxtubes in the Sun. We also discuss the physical properties of the fluxtubes, the governing equations to solve fluxtube models, and a brief historical overview for various fluxtube models. In Chapter 4, we present a new and distinct fluxtube model with a twisted magnetic field by solving GSE analytically. The magnetic structure obtained in this model is closed, which means the field lines rise and fall back in the same horizontal plane. This is called the Coulomb function closed field model. In Chapter 5, we extend the Coulomb function model described in Chapter 4 for constructing open field magnetic configuration, where the field lines rise from a horizontal plane but do not come back to the same plane [or come back outside the domain of computation]. We discuss another class of fluxtube models, called the self-similar model, for obtaining the open and closed field fluxtube structures. Incorporating boundary conditions in those fluxtube solutions, and taking realistic inputs of the solar atmosphere we estimate the magnetic and thermodynamic structure inside the fluxtube and compare with observations and other simulation results of MBPs. Chapter 6 describes the mechanism of magnetic reconnections and various flare models. In Chapter 7, we discuss the winding number distribution of braided magnetic fields to estimate the power-law index of energy distribution for the solar flares. We compare this theoretical prediction with the observations of solar flare events taken by the GBRT. Chapter 8 then presents a summary of the results from all chapters, highlight the novel aspects of this Thesis with its impact. Then, we discuss future work which includes papers under preparation. The chapter-wise concept flowchart of the Thesis is shown in Fig. 1.10.

1.5 Resource summary

In this chapter, we have discussed a brief overview of the solar interior and its atmosphere, and the importance of the study of the twisted fluxtubes in the solar

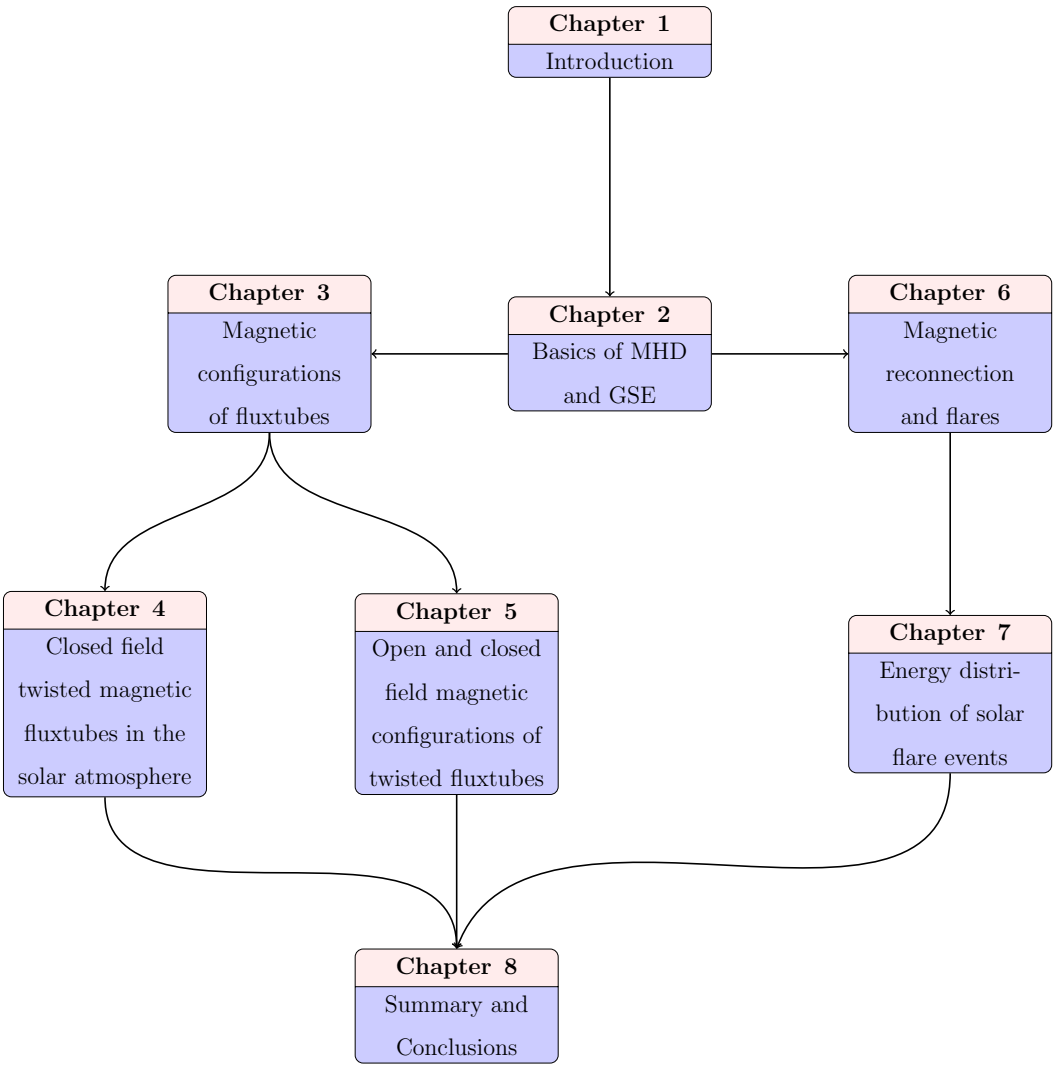

FIGURE 1.10: Flowchart of the connections between the chapters of the Thesis.

atmosphere. We have also presented a brief historical overview of various important fluxtube models. The main references and the text for this chapter are [Ryutova (2015); Fedun *et al.* (2009); Gent *et al.* (2013)].

Chapter 2

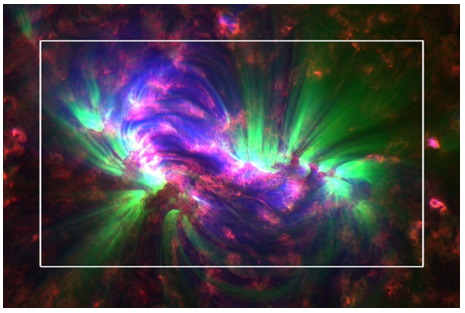

Image source: www.astronomy.com

Basics of MHD and GSE

2.1 Introduction

In this chapter, we have discussed the general properties of MHD plasmas and the corresponding equations. Before going into the details of the MHD properties, it is important to note that the validation of the MHD equations is satisfied only if there is a sufficient number of collisions between the plasma particles. To estimate the collision rate, let us consider a unit cube of energy and momentum. We consider the spatial scale of such a cube is L, which is comparable (or smaller) with the length scale of the variation of the plasma quantities, pressure, p, density, ρ, and plasma velocity, $\mathbf{U}$. If the particles inside the cube escape out in a shorter time than the time of the variation of the plasma quantities, τ, then the cube cannot be regarded as a unit cube, and the MHD equations fail (Kulsrud 2010).

Let the mean free path, thermal velocity, collision rate, and collision time for the particles within the cube are, λ_m, v_T, ν_c and τ_c respectively. Then in a time τ, the particles will go through a random walk of distance l, which is given by

$$l^2 = \frac{\tau}{\tau_c}\lambda_m^2 \approx \tau v_T \lambda_m, \tag{2.1}$$

where we use the facts that, $\tau_c = 1/\nu_c$, $\lambda_m = v_T\tau_c$, and the the collisional steps are uncorrelated.

Thus, the treatment of the plasma will be justified if $l^2 << L^2$, which can be written from eqn (2.1) as,

$$v_T\lambda_m << \frac{L^2}{\tau}. \tag{2.2}$$

Condition (2.2) satisfies if

$$\lambda_m << L \quad \text{and} \quad \tau_c >> \tau, \tag{2.3}$$

which implies, that the MHD equations are valid if the mean free path of the collisions is much smaller than the spatial variation of the plasma quantities, and the collision time of the plasma particles is much larger than the time scale of the temporal variation of the plasma quantities.

In addition, the MHD equations are valid if the resistivity of the plasma is negligible so that the entropy is conserved, and the viscosity of the medium is very small, such that the pressure is isotropic throughout the medium.

2.2 General principles

A sufficiently collisional plasma can be described macroscopically by the basic state of magnetohydrodynamics, specifying the local mass density ρ, momentum density $\rho\mathbf{U}$, gas pressure p, electric field $\mathbf{E}$ and the magnetic field strength $\mathbf{B}$ as the functions of position $\mathbf{r}$ and time t. For a strong collisional plasma, the heat flow is small and the pressure due to ions and electrons is isotropic. If η_m is the magnetic diffusivity and $\mathbf{U}$ is the plasma velocity then the magnetic Reynold's number is defined as $R_M = \dfrac{UL}{\eta_m}$. For a strong collisional plasma system, R_M is large, which is true for a large length scale L, such as astrophysical systems, the resistivity can be neglected (Cowling 1972). In this scenario, the system can be described by "ideal MHD equations".

In ideal MHD, each of the quantities ρ, $\mathbf{U}$, p, and $\mathbf{B}$ require time dependent equations. These are usually the hydrodynamic and electromagnetic equations, modified by taking into account the magnetic field and the interaction between the motions. If $\mathbf{j}$ is the current density, then from Maxwell's equations (in SI units), we have,

$$\nabla \times \mathbf{B} = \mu_0 \mathbf{j} \tag{2.4a}$$

$$\nabla \cdot \mathbf{j} = 0 \tag{2.4b}$$

$$\nabla \times \mathbf{E} = -\frac{\partial \mathbf{B}}{\partial t} \tag{2.4c}$$

$$\nabla \cdot \mathbf{B} = 0, \tag{2.4d}$$

where μ_0 is the magnetic permeability. If the plasma moves with a velocity $\mathbf{U}$, it experiences the total electric field of $\mathbf{E} + \mathbf{U} \times \mathbf{B}$ due to Lorentz force. Thus if σ

is the electrical conductivity,

$$\mathbf{j} = \sigma(\mathbf{E} + \mathbf{U} \times \mathbf{B}). \tag{2.5}$$

The eqn (2.5) is the differential form of the Ohm's law. For mass balance, the continuity equation is

$$\frac{\partial \rho}{\partial t} + \nabla \cdot (\rho \mathbf{U}) = \mathbf{0}. \tag{2.6}$$

For momentum, the Euler equation in the presence of the acceleration due to gravity $\mathbf{g}$ is,

$$\rho\left(\frac{\partial \mathbf{U}}{\partial t} + \mathbf{U} \cdot \nabla \mathbf{U}\right) = -\nabla p + \mathbf{j} \times \mathbf{B} + \rho \mathbf{g} + \mathbf{F}_{vis}, \tag{2.7}$$

where the relation between the Lagrangian derivative $\frac{\mathrm{d}}{\mathrm{dt}}$, and Eulerian derivative $\frac{\partial}{\partial t}$ is given by

$$\frac{\mathrm{d}}{\mathrm{dt}} = \frac{\partial}{\partial t} + \mathbf{U} \cdot \nabla, \tag{2.8}$$

and $\mathbf{F}_{vis}$ is the viscous force per unit volume is given by

$$\mathbf{F}_{vis} = \rho \nu \nabla^2 \mathbf{U}, \tag{2.9}$$

where ν is the kinematic viscosity. The equation for constant entropy is given by,

$$\frac{\partial}{\partial t}\left(\frac{p}{\rho^\gamma}\right) + \mathbf{U} \cdot \nabla\left(\frac{p}{\rho^\gamma}\right) = 0, \tag{2.10}$$

where γ is the adiabatic index of the plasma medium.

Now rearranging the eqn (2.5), we obtain the following form for the electric field,

$$\mathbf{E} = \frac{\mathbf{j}}{\sigma} - \mathbf{U} \times \mathbf{B}. \tag{2.11}$$

Taking the curl of equation (2.11) and using eqn (2.4a) we obtain the following equation,

$$\nabla \times \mathbf{E} = -\nabla \times (\mathbf{U} \times \mathbf{B}) + \frac{1}{\mu_0 \sigma} \nabla \times (\nabla \times \mathbf{B}). \tag{2.12}$$

Combining the equations (2.12, 2.4c, 2.4d), we find

$$\frac{\partial \mathbf{B}}{\partial t} = \nabla \times (\mathbf{U} \times \mathbf{B}) + \eta_m \nabla^2 \mathbf{B}, \tag{2.13}$$

where, $\eta_m = (\mu_0 \sigma)^{-1}$ is the magnetic diffusivity. Equation (2.13) is called the induction equation. For a material at rest ($\mathbf{U} = 0$), the induction equation reduces to the diffusion equation:

$$\frac{\partial \mathbf{B}}{\partial t} = \eta_m \nabla^2 \mathbf{B}. \tag{2.14}$$

The diffusion eqn (2.14) indicates that the field leaks with time from point to point. From the dimensional analysis of eqn (2.14), we notice that the diffusion time scale τ_d, for a length scale L is, $\tau_d \sim \frac{L^2}{\eta_m}$, which means the diffusion time is faster for a small length scale. For example, a copper sphere of radius 1 m, $\tau_d \sim 1$ s, whereas for the Sun, $\tau_d \sim 10^9$ years. For astrophysical systems, the length scale is large, therefore the magnetic Reynold's number, which is given by

$$R_m = \frac{vB/L}{\eta_m B/L^2} = \frac{Lv}{\eta_m}, \tag{2.15}$$

is very high. This implies that the transport effects are weak i.e. $\eta_m << vL$. Therefore, the induction eqn (2.13) reduces to

$$\frac{\partial \mathbf{B}}{\partial t} = \nabla \times (\mathbf{U} \times \mathbf{B}). \tag{2.16}$$

In the §2.3 we will see that the eqn (2.16) leads to the flux freezing condition. We now summarize the ideal MHD equations below (Priest 2014).

$$\text{Continuty equation:} \quad \frac{\partial \rho}{\partial t} + \nabla \cdot (\rho \mathbf{U}) = \mathbf{0}, \tag{2.17}$$

$$\text{Euler equation of motion:} \quad \rho\left(\frac{\partial \mathbf{U}}{\partial t} + \mathbf{U} \cdot \nabla \mathbf{U}\right) = -\nabla p + \mathbf{j} \times \mathbf{B} + \rho \mathbf{g} + \mathbf{F}_{vis}, \tag{2.18}$$

$$\text{Entropy equation:} \quad \frac{\partial}{\partial t}\left(\frac{p}{\rho^{\gamma}}\right) + \mathbf{U} \cdot \nabla\left(\frac{p}{\rho^{\gamma}}\right) = 0, \tag{2.19}$$

$$\text{Induction equation:} \quad \frac{\partial \mathbf{B}}{\partial t} = \nabla \times (\mathbf{U} \times \mathbf{B}) + \eta_m \nabla^2 \mathbf{B}. \tag{2.20}$$

2.3 Freezing of magnetic fields

For the astrophysical domain the conductivity of a medium, $\sigma = \infty$, hence the eqn (2.11) reduces to

$$\mathbf{E} + \mathbf{U} \times \mathbf{B} = 0. \tag{2.21}$$

The evolution of the magnetic field along the magnetic lines of force is given by

$$\frac{\mathrm{d}\mathbf{B}}{\mathrm{d}t} = \frac{\partial \mathbf{B}}{\partial t} + (\mathbf{U} \cdot \nabla)\mathbf{B}. \tag{2.22}$$

If we consider a simple closed loop C which encloses an area S, then the rate of change of the magnetic flux associated with the loop is

$$\begin{aligned}
\frac{\mathrm{d}}{\mathrm{d}t}\iint_S \mathbf{B}\cdot\mathrm{d}\mathbf{S} &= \iint_S \mathbf{B}\cdot\frac{\partial \mathbf{S}}{\partial t} + \iint_S \frac{\partial \mathbf{B}}{\partial t}\cdot\mathrm{d}\mathbf{S} \\
&= \iint_S \mathbf{B}\cdot\frac{\partial}{\partial t}(\mathbf{U}\mathrm{d}t\times\mathrm{d}\mathbf{l}) + \iint \frac{\partial \mathbf{B}}{\partial t}\mathrm{d}\mathbf{S} \\
&= -\oint_C (\mathbf{U}\times\mathbf{B})\cdot\mathrm{d}\mathbf{l} + \iint_S \frac{\partial \mathbf{B}}{\partial t}\cdot\mathrm{d}\mathbf{S} \\
&= -\iint_S \nabla\times(\mathbf{U}\times\mathbf{B})\cdot\mathrm{d}\mathbf{S} + \iint_S \frac{\partial \mathbf{B}}{\partial t}\cdot\mathrm{d}\mathbf{S} \\
&= \iint_S \left(\frac{\partial \mathbf{B}}{\partial t} - \nabla\times(\mathbf{U}\times\mathbf{B})\right)\cdot\mathrm{d}\mathbf{S}. \qquad (2.23)
\end{aligned}$$

Plugging eqn (2.16) into eqn (2.23) we obtain $\dfrac{\mathrm{d}}{\mathrm{d}t}\iint_S \mathbf{B}\cdot\mathrm{d}\mathbf{S} = 0$, which implies that the the magnetic flux through the loop C is constant with time as it moves with the plasma. In other words, the flux is frozen in the medium. Conservation of the magnetic lines of force in a plasma medium [Lundquist (1951), Roberts (1967)] can also be proved from eqn (2.22), which gives

$$\begin{aligned}
\frac{\mathrm{d}}{\mathrm{d}t}\left(\frac{\mathbf{B}}{\rho}\right) &= \frac{\partial}{\partial t}\left(\frac{\mathbf{B}}{\rho}\right) + (\mathbf{U}\cdot\nabla)\frac{\mathbf{B}}{\rho} \\
&= -\frac{\mathbf{B}}{\rho^2}\frac{\partial \rho}{\partial t} + \frac{1}{\rho}\nabla\times(\mathbf{U}\times\mathbf{B}) + \frac{1}{\rho}(\mathbf{U}\cdot\nabla)\mathbf{B} + \mathbf{B}(\mathbf{U}\cdot\nabla)\frac{1}{\rho} \\
&= \frac{\mathbf{B}}{\rho^2}\nabla\cdot(\rho\mathbf{U}) + \frac{1}{\rho}(\mathbf{B}\cdot\nabla)\mathbf{U} - \frac{1}{\rho}(\mathbf{U}\cdot\nabla)\mathbf{B} + \frac{\mathbf{U}}{\rho}(\nabla\cdot\mathbf{B}) \\
&\quad - \frac{\mathbf{B}}{\rho}(\nabla\cdot\mathbf{U}) + \frac{1}{\rho}(\mathbf{U}\cdot\nabla)\mathbf{B} + \mathbf{B}(\mathbf{U}\cdot\nabla)\frac{1}{\rho} \\
&= \frac{\mathbf{B}}{\rho^2}\mathbf{U}\cdot\nabla\rho + \mathbf{B}(\mathbf{U}\cdot\nabla)\frac{1}{\rho} + \frac{1}{\rho}(\mathbf{B}\cdot\nabla)\mathbf{U} \\
\Rightarrow \frac{\mathrm{d}}{\mathrm{d}t}\left(\frac{\mathbf{B}}{\rho}\right) &= \frac{1}{\rho}(\mathbf{B}\cdot\nabla)\mathbf{U}. \qquad (2.24)
\end{aligned}$$

To see the physical implication of the eqn (2.24), we consider a line element $\delta\mathbf{l}$ moving in a plasma medium. If $\mathbf{U}$ and $\mathbf{U}+\delta\mathbf{U}$ are the velocities of two end points

lying in the field line, then the difference in the velocity of these two points is $\delta\mathbf{U} = (\delta\mathbf{l}\cdot\nabla)\mathbf{U}$. The rate of change of length of the line segment $\mathrm{d}\mathbf{l}$ during the time interval $\mathrm{d}t$ is,

$$\frac{\mathrm{d}(\delta\mathbf{l})}{\mathrm{d}t} = \delta\mathbf{U} = (\delta\mathbf{l}\cdot\nabla)\mathbf{U}. \tag{2.25}$$

Since eqn (2.25) has the exact form like eqn (2.24), this implies that, if $\mathrm{d}\mathbf{l}$ and $\mathbf{B}/\rho$ are initially parallel to each other, they will remain parallel for all time. Therefore, if there are two points lying in a magnetic field line, they will remain on that line forever. In other words, the field lines are frozen in the plasma medium. This implies that the plasma can move freely along the field lines, but, if the motion is perpendicular to the field lines, then the field lines are either dragged or pushed by the plasma.

2.4 Magnetic field lines

In this section, we will focus on the mathematical representation of the magnetic field lines (Goosens 2003). In the previous section, we see that the magnetic field lines are glued to the plasma and dragged along in its motion. So, from the magnetic configuration in a plasma medium, we can guess the associated thermodynamic structure.

The parametric form of a 3D curve is given by,

$$x_1 = f_1(u), \quad x_2 = f_2(u), \quad x_3 = f_3(u), \tag{2.26}$$

in terms of the parameter u, and the three arbitrary functions, $f_1(u)$, $f_2(u)$, and $f_3(u)$. The tangent vector, $\mathbf{t}$, of the curve of eqn (2.26) can be written as,

$$\mathbf{t} = \frac{\mathrm{d}\mathbf{x}(u)}{\mathrm{d}u} \equiv \left[\frac{\mathrm{d}x_1(u)}{\mathrm{d}u}, \frac{\mathrm{d}x_2(u)}{\mathrm{d}u}, \frac{\mathrm{d}x_3(u)}{\mathrm{d}u}\right]^\top, \tag{2.27}$$

where the superscript $\top$ represents the transpose of the row matrix. Magnetic field lines are the 3D curve which are parallel to the tangent vector $\mathbf{t}$, hence the magnectic field components for

$$\mathbf{B} = [B_1, B_2, B_3]^\top, \tag{2.28}$$

can be written as,

$$\frac{\mathrm{d}x_1(u)}{\mathrm{d}u} = \lambda B_1, \quad \frac{\mathrm{d}x_2(u)}{\mathrm{d}u} = \lambda B_2, \quad \frac{\mathrm{d}x_3(u)}{\mathrm{d}u} = \lambda B_3, \tag{2.29}$$

where, λ is a proprtionality constant, which varies for different field lines of the same family. It is straight forward to show that,

$$\lambda = \frac{1}{|\mathbf{B}|}\frac{\mathrm{d}s}{\mathrm{d}u}, \tag{2.30}$$

where, s is the arc length of an arbitrary curve, with the following two conditions,

$$\left(\frac{\mathrm{d}s}{\mathrm{d}u}\right)^2 = \sum_{i=1}^{3}\left(\frac{\mathrm{d}x_i(u)}{\mathrm{d}u}\right)^2, \tag{2.31a}$$

$$B = \left(\sum_{i=1}^{3} B_i^2\right)^{1/2}. \tag{2.31b}$$

Hence, the differential equations for the magnetic field lines are,

$$\frac{\mathrm{d}x_1(s)}{\mathrm{d}s} = \frac{B_1}{|\mathbf{B}|}, \quad \frac{\mathrm{d}x_2(s)}{\mathrm{d}s} = \frac{B_2}{|\mathbf{B}|}, \quad \frac{\mathrm{d}x_3(s)}{\mathrm{d}s} = \frac{B_3}{|\mathbf{B}|}, \tag{2.32}$$

or,

$$\frac{\mathrm{d}x_i(s)}{\mathrm{d}s} = \frac{B_i}{|\mathbf{B}|}; \qquad (i = 1, 2, 3). \tag{2.33}$$

For the cylindrical geometry (r, ϕ, z) with axisymmetric condition, i.e. $\dfrac{\partial}{\partial \phi} \equiv 0$, the poloidal component of the magnetic field is

$$\mathbf{B}_p = B_r(r, z)\hat{r} + B_z(r, z)\hat{z}. \tag{2.34}$$

For the invariance of the toroidal component $\mathbf{B}_\phi$, and due to the solenoidal condition of the magnetic field, i.e., $\nabla \cdot \mathbf{B} = 0$, we can take the form,

$$\mathbf{B}_p = \nabla \times \left(\frac{\Psi(r, z)}{r}\ \hat{\phi} \right) \tag{2.35}$$

$$= -\frac{1}{r}\frac{\partial \Psi}{\partial z}\hat{r} + \frac{1}{r}\frac{\partial \Psi}{\partial r}\hat{z}, \tag{2.36}$$

without the loss of any generality, where Ψ is called the magnetic flux function. Hence, it is straight forward that, $(\mathbf{B}_p \cdot \nabla)\Psi = 0$, which implies that, Ψ is constant along the poloidal field. That is why Ψ is called the magnetic stream function of the poloidal magnetic field. The equation of the poloidal field line is

$$\Psi(r, z) = \text{constant}. \tag{2.37}$$

Due to the axisymmetric condition, eqn (2.37) represents the equation of a magnetic surface.

2.5 Lorentz force

For a magnetic medium of field strength **B** and current **j**, the Ampere's law is given by

$$\mathbf{j} = \frac{1}{4\pi}(\nabla \times \mathbf{B}). \tag{2.38}$$

The Lorentz force is defined as the vector product

$$\mathbf{j} \times \mathbf{B} = \frac{1}{4\pi}(\nabla \times \mathbf{B}) \times \mathbf{B}. \tag{2.39}$$

Using the vector identity, eqn (2.39) can be written as

$$\mathbf{j} \times \mathbf{B} = \frac{1}{4\pi}(\mathbf{B} \cdot \nabla)\mathbf{B} - \nabla\left(\frac{B^2}{8\pi}\right). \tag{2.40}$$

We denote the unit vector along the tangent of the field line as, $\mathbf{b} = \dfrac{\mathbf{B}}{|\mathbf{B}|}$. The first term on the RHS of the eqn (2.40) represents the directional derivative along the magnetic field line, and we represent the term $(\mathbf{B} \cdot \nabla) = B\dfrac{\mathrm{d}}{\mathrm{d}s}$, where s is the arc length along the field line (Goosens 2003). Therefore from eqn (2.40), we obtain

$$\mathbf{j} \times \mathbf{B} = \frac{\mathrm{d}}{\mathrm{d}s}\left(\frac{B^2}{8\pi}\right)\mathbf{b} + \frac{B^2}{4\pi}\frac{\mathrm{d}\mathbf{b}}{\mathrm{d}s} - \nabla\left(\frac{B^2}{8\pi}\right). \tag{2.41}$$

For a curve of arc length s and local radius of curvature R_c, the variation of the direction of the tangent along the arc is given by

$$\frac{\mathrm{d}\mathbf{b}}{\mathrm{d}s} = \frac{\mathbf{b}_n}{R_c}, \tag{2.42}$$

where, $\mathbf{b}_n$ is the unit normal vector along the local radius of curvature directed towards the center of the curvature. The third term on the RHS of eqn (2.41) can

be decomposed as

$$-\nabla\left(\frac{B^2}{8\pi}\right) = -\frac{\mathrm{d}}{\mathrm{d}s}\left(\frac{B^2}{8\pi}\right)\mathbf{b} - \nabla_\perp\left(\frac{B^2}{8\pi}\right), \tag{2.43}$$

where $\nabla_\perp$ is the gradient along the normal to the magnetic field line. Using eqns (2.41), (2.42) and (2.43), we obtain

$$\mathbf{j}\times\mathbf{B} = -\nabla_\perp\left(\frac{B^2}{8\pi}\right) + \frac{B^2}{4\pi R_c}\mathbf{b}_n. \tag{2.44}$$

The first term on the RHS of eqn (2.44) is called the the magnetic pressure force which acts isotropically along the plane perpendicular to the field line and in the direction towards the lower strength analogous to the gas pressure. This term arises due to the inhomogenity of the field strength in the medium.

The second term on the RHS of the eqn (2.44) is called the magnetic tension force, which acts along the direction towards the center of the curvature. This term arises due to the curvature of the field line and is inversely proportional to R_c, which implies that the tension force is higher for a curvature. Magnetic tension force is analogous to the mechanical tension force which arises due to the bending of a rubber band.

2.6 Magnetic energy and stress

In a medium of field strength $\mathbf{B}$, the magnetic energy density is given by $B^2/8\pi$, and the total magnetic energy, W_m, enclosed within the volume V is

$$W_m = \int_V \frac{B^2}{8\pi}\mathrm{d}V', \tag{2.45}$$

where the integration is carried over the enclosed volume V.

The rate of change of the magnetic energy is,

$$\frac{\mathrm{d}W_m}{\mathrm{d}t} = \frac{1}{8\pi}\int_V \frac{\partial}{\partial t}(B^2)\mathrm{d}V' = \frac{1}{4\pi}\int_V \mathbf{B}\cdot\frac{\partial \mathbf{B}}{\partial t}\mathrm{d}V'. \tag{2.46}$$

Following the induction eqn (2.13), we obtain from eqn (2.46)

$$\frac{\mathrm{d}W_m}{\mathrm{d}t} = \frac{1}{4\pi}\int_V \mathbf{B}\cdot[\nabla\times(\mathbf{U}\times\mathbf{B}) + \eta_m\nabla^2\mathbf{B}]\mathrm{d}V'. \tag{2.47}$$

Using the Ampere's law, eqn (2.38), and the solenoidal condition of magnetic field, $\nabla\cdot\mathbf{B} = 0$, the second term on the RHS of the eqn (2.47) reduces to,

$$\begin{aligned}\frac{1}{4\pi}\int_V \eta_m\mathbf{B}\cdot\nabla^2\mathbf{B}\mathrm{d}V' &= -\int_V \eta_m\mathbf{B}\cdot(\nabla\times\mathbf{j})\mathrm{d}V' \\ &= -\int_V \eta_m[\nabla\cdot(\mathbf{j}\times\mathbf{B}) + \mathbf{j}\cdot(\nabla\times\mathbf{B})]\mathrm{d}V' \\ &= -\eta_m\oint_S(\mathbf{j}\times\mathbf{B})\cdot\mathrm{d}\mathbf{S}' - \eta_m\int_V \mathbf{j}\cdot(\nabla\times\mathbf{B})\mathrm{d}V',\end{aligned} \tag{2.48}$$

where, S is the closed surface which encloses the volume V. If the volume V is taken to be infinite where $\mathbf{j}$ vanishes at the surface of the boundary then we see that the first term on the RHS of the eqn (2.51) vanishes, and hence the eqn (2.51) reduces to

$$\frac{1}{4\pi}\int_V \eta_m\mathbf{B}\cdot\nabla^2\mathbf{B}\mathrm{d}V' = -4\pi\int_V \frac{j^2}{\sigma}\mathrm{d}V'. \tag{2.49}$$

The negative sign on the RHS of eqn (2.49) represents the loss of energy due to the Joule heating at a rate $4\pi j^2/\sigma$, which is a consequence of energy conservation.

The first term on the RHS of the eqn (2.47) is given by

$$\begin{aligned}
&\frac{1}{4\pi}\int_V \mathbf{B}\cdot[\nabla\times(\mathbf{U}\times\mathbf{B})]\mathrm{d}V' \\
&=\frac{1}{4\pi}\int_V [\nabla\cdot[(\mathbf{U}\times\mathbf{B})\times\mathbf{B})]+(\mathbf{U}\times\mathbf{B})\times(\nabla\times\mathbf{B})]\mathrm{d}V' \\
&=\frac{1}{4\pi}\oint_S [(\mathbf{U}\times\mathbf{B})\times\mathbf{B}]\cdot\mathrm{d}\mathbf{S}'+\frac{1}{4\pi}\int_V(\mathbf{U}\times\mathbf{B})\cdot(\nabla\times\mathbf{B})\mathrm{d}V' \\
&=-\int_V \mathbf{U}\cdot(\mathbf{j}\times\mathbf{B})\mathrm{d}V'. \qquad (2.50)
\end{aligned}$$

This term represents the loss of magnetic energy due to the work done by the Lorentz force, and it is called the magnetic stress. As the work can be done on a hydrostatic system only if there is a density change in the system, similarly the work can be done on a magnetic system only if there is any extension or contraction in the magnetic field lines. Collectively, we can write eqn (2.47) as

$$\frac{\mathrm{d}W_m}{\mathrm{d}t}=-\int \mathbf{U}\cdot(\mathbf{j}\times\mathbf{B})\mathrm{d}V-4\pi\int\frac{j^2}{\sigma}\mathrm{d}V. \qquad (2.51)$$

2.7 Grad-Shafranov equation

The fundamental condition for equilibrium at all points in a magnetized plasma is given by

$$\mathbf{j}\times\mathbf{B}=\nabla p, \qquad (2.52)$$

subjected to the toroidal symmetry (Priest 2014). Taking the dot products of $\mathbf{B}$ with eqn (2.52), we obtain

$$\mathbf{B}\cdot\nabla p=0, \qquad (2.53)$$

which states that the surfaces of the constant pressure are the magnetic surfaces. Taking the dot products of $\mathbf{j}$ with eqn (2.52), we obtain

$$\mathbf{j} \cdot \nabla p = 0, \tag{2.54}$$

which represents that the current lies on the magnetic surfaces. Similarly, if we introduce a function, ψ which specifies a magnetic surface (constant on that surface), we see that

$$\mathbf{B} \cdot \nabla \psi = 0. \tag{2.55}$$

For the validity of the solenoidal condition of magnetic field i.e. $\nabla \cdot \mathbf{B} = 0$, we can express the field components in cylindrical geometry as,

$$B_r = -\frac{1}{r}\frac{\partial \psi}{\partial z}; \qquad B_z = \frac{1}{r}\frac{\partial \psi}{\partial r}. \tag{2.56}$$

Due to axisymmetric condition, we can introduce a function I_p which obeys the relations

$$j_r = -\frac{1}{r}\frac{\partial I_p}{\partial z}, \qquad j_z = \frac{1}{r}\frac{\partial I_p}{\partial r}. \tag{2.57}$$

Comparing the forms in eqn (2.57) with the Ampere's eqn,

$$j_r = -\frac{\partial B_\phi}{\partial z}, \qquad j_z = \frac{1}{r}\frac{\partial (r B_\phi)}{\partial r}, \tag{2.58}$$

we obtain the function,

$$I_p = r B_\phi, \tag{2.59}$$

which is called the poloidal current. From eqns (2.54, 2.58) we obtain

$$\nabla I_p \times \nabla p = 0, \tag{2.60}$$

which implies that $I_p = I_p(p)$, and as $p = p(\psi)$, it follows that, $I_p = I_p(\psi)$. In equilibrium, eqn (2.52) can be written in the axisymmetric cylindrical geometric form as

$$\mathbf{j_p} \times \hat{\phi}\ B_\phi + j_\phi \hat{\phi} \times \mathbf{B_p} = \nabla p, \tag{2.61}$$

where $\mathbf{j}_p$, and $\mathbf{B}_p$ are the poloidal current density and magnetic field strength respectively. Using eqns (2.56, 2.58) associated with eqn (2.61), we obtain

$$\mathbf{B_p} = \frac{1}{r}(\nabla\psi \times \hat{\phi}), \tag{2.62}$$

and

$$\mathbf{j_p} = \frac{1}{r}(\nabla I_p \times \hat{\phi}). \tag{2.63}$$

Using eqns (2.62, 2.63) into eqn (2.61), and noting the conditions $\hat{\phi} \cdot \nabla\psi = \hat{\phi} \cdot \nabla I_p = 0$, we obtain

$$-\frac{B_\phi}{r}\nabla I_p + \frac{j_\phi}{r}\nabla\psi = \nabla p. \tag{2.64}$$

Using the relations $\nabla I_p(\psi) = I_p'(\psi)\nabla\psi$, $\nabla p(\psi) = p'(\psi)\nabla\psi$, and $I_p = B_\phi r$ in eqn (2.64), we obtain

$$j_\phi = r\frac{\partial p}{\partial \psi} + B_\phi \frac{\partial I_p}{\partial \psi}. \tag{2.65}$$

To write j_ϕ in terms of ψ we take the azimuthal component of the equation $\mathbf{j} = \nabla \times \mathbf{B}$, which gives

$$r j_\phi = r\frac{\mathrm{d}}{\mathrm{d}r}\left(\frac{1}{r}\right)\frac{\mathrm{d}\psi}{\mathrm{d}r} + \frac{\mathrm{d}^2\psi}{\mathrm{d}z^2}. \tag{2.66}$$

Substituting the form of j_ϕ given by eqn (2.66) into eqn (2.65) we finally obtain

$$r\frac{\partial}{\partial r}\left(\frac{1}{r}\frac{\partial \psi}{\partial r}\right)+\frac{\partial^2 \psi}{\partial z^2}=-r^2 p'(\psi)-I_p(\psi)I_p'(\psi), \tag{2.67}$$

which is a non-linear, inhomogeneous, and second order differential equation, called the Grad-Shafranov equation (Grad and Rubin 1958; Shafranov 1958). This is a useful and important equation for fluxtube models that we have developed in our work which is discussed in the Chapters 4 and 5. For a given set of the functions $p(\psi)$, and $I_p(\psi)$, the eqn (2.67) represents an equilibrium condition of a torus. In principle, given the functions $p(\psi)$ and $I_p(\psi)$, along with the boundary conditions, eqn (2.67) can be solved in the form of $\psi(r,z)$, and it gives an equilibrium flux distribution. On the other hand, depending on the non-linear forms of $p(\psi)$ and $I_p(\psi)$, the solutions can be a non existent, unique, or many that satisfies both the GSE and the BCs.

2.8 Resource summary

This chapter is a primer for Chapter 3, where we have discussed the magnetic properties of the fluxtubes, and Chapter 6, where magnetic reconnections and some of the important solar flare models are described. The main references and texts for this chapter are [Kulsrud (2010); Priest (2014); Goosens (2003)]. This chapter is mainly devoted to the basics of MHD. We also present the derivation of the Grad-Shafranov equation, which is the key to our fluxtube models (Sen and Mangalam 2018a,b, 2019), that is presented in Chapters 4 and 5.

Chapter 3

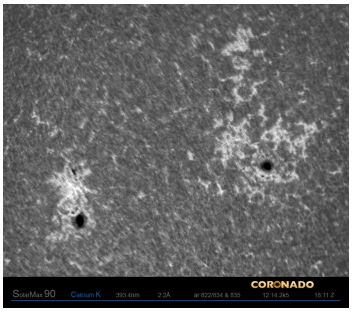

Image source: `www.spaceweather.com`

Magnetic configurations of fluxtubes

3.1 Introduction

In this chapter, we present various fluxtube models and the status of the related observations of the magnetic and thermodynamic structures. The existence of the small scale magnetic fluxtubes has been known since the late 1950s. Soon after its discovery, the study of the fluxtube enormously increased within a decade due to its interesting aspects of this key magnetic structure in the Sun. it is now accepted that the entire magnetic structure in the Sun starting from the photosphere to the corona including sunspots and coronal loops have a filamentary structure. Hence, the study of the small scale magnetic fluxtubes is a very important step to understanding the magnetic configuration of the solar atmosphere.

3.2 Observational implications of fluxtubes

From early studies of solar physics, it was known that the magnetic fields are associated with sunspots. Later on, in the late phase of 1950, Howard (1959) observed that there are small scale magnetic features, of a field strength ~ 100 Gauss exist in the quiet sun region. Exploring the correspondence between the photospheric magnetic fields, and Ca bright points, which are seen in the chromospheric temperatures studied by Babcock and Babcock (1955), Howard concluded that there is a close correspondence between the Ca plages and the photospheric magnetic fields, and the structure of the small scale magnetic fields in the photosphere and chromosphere are more or less like vertical columns. At the same time, Leighton (1959) reported that the magnetic concentrations of $100 - 200$ G are found in the plage regions, and the field patterns are in good agreement with the pattern of the Ca II emission. This was followed by Severnyi (1959) who reported observational evidence for the fine structures of the sunspots. The study of the small scale fluxtubes is important due to the following two phenomena: One is the direct correlation with the chromospheric heating, and the other is the formation of the magnetic shear due to the interaction of the two small scale magnetic columns of opposite polarities.

A few years before the direct observations of fluxtubes, Pikel'Ner (1963) gave an intuitive idea about the existence of the fluxtubes. He proposed that, due to the convective motions, the magnetic lines of forces get squeezed and assemble towards the granule periphery, and the field lines get concentrated into a network on the solar surface in the form of magnetic fluxtubes. He also predicted that with the enhancement of the convection, the chromospheric emission increases, and the network becomes observable through the Ca II and Hα lines. Moreover, he proposed that the motion of the plasma associated with the field lines are responsible for the observed mottling of the granular elements that stream towards

the periphery from the center. Still, the direct observations of these suggestions are yet to be confirmed through observations.

3.2.1 Observational evidence of small scale fluxtubes

Using the high spatial resolution measurements of magnetic fields in the photosphere, Sheeley (1966, 1967) studied the time evolution of the magnetic flux over the larger area and the development of the magnetic bipolar region. The study also finds that there is no smooth fall of the flux density over time, rather it fragments into smaller sizes gradually. Sheeley found the field strength in this magnetic structure to be 200 to 700 G and concluded that magnetic fields of a few hundred gauss occur in the tiny areas easily as 500 km in regions of the solar surface, sometimes removed from the sunspot activity. This remarkable observation became the turning point, which is a fact of the discovery of the small scale fluxtube. Almost at the same time, Steshenko (1967) estimated that the field strength of the pores of size $\sim 1''$ is about 1400 G, whereas, in the larger pores, the field strength is found to be 5350 G, which is much higher than the average field strength of the sunspot itself. On the other hand, he observed the field strength in the isolated places outside the sunspots, of up to 1000 G. Beckers and Schröter (1968) made a detailed study of the small scale magnetic configuration both inside and around the sunspot, and concluded that all the photospheric magnetic features around the unipolar sunspots are concentrated over a small region, which is around 1000 km, and the field strength is strong, which is up to 1400 G. With this further progress, it was soon understood that most of the solar surface outside the sunspots are covered with the small scale magnetic features. Later on, using the data of $17'' \times 17''$ aperture of Mount Wilson magnetogram during 26 days, Howard and Stenflo (1972) reported that around 90% of the total flux is present in the small scale fluxtubes in plages and at the supergranular cell boundaries. Frazier and Stenflo (1972) described the structure of the field lines for the small

scale magnetic elements as "mushroom effect" as it spreads out vertically with decreasing magnetic field strength.

3.2.2 The sunspot dilemma

Well before the high-resolution observations of the filamentary structure of the solar magnetic field outside the sunspot, Papathanasoglou (1971) along with the earlier findings by Severnyi (1959) reported fine structures in the sunspot umbra. The study showed that the size of umbral filaments is $< 1''$, and the spaces between the dark patches are about $0.6''$. After two decades of this amazing result, Livingston (1991) also reported direct observational evidence of the filamentary structures in the sunspot umbral region.

However, for many years after the discovery of the filamentary structure of the solar umbral region, the study of the sunspot as a whole became more fascinating and thus overshadowed the study of the filament structures. The stability analysis of the sunspots became very challenging as it requires so many complex processes to be considered, and the exploration of the search of the process became an uphill battle. Though this problem is still not yet solved entirely, the most revealing solution of this problem was proposed by Piddington (1978), where he developed a model that differed with most of the popular diffuse-field models of that time. Figure 3.1 shows the Piddington's sunspot model that consists of individual twisted fluxtubes, which are separated by magnetic free regions of plasma. The width and the separation between the fluxtubes increase with the distance from the sunspot axis that accounts for the penumbral filaments. The direction inside and outside Evershed flow, u_e, of the fluxtubes are different. Meyer *et al.* (1977) based on the Piddington's model proposed that the stability of sunspot is related to the potential energy associated with the Wilson depth. However, from the plasma theory, supported by laboratory plasma experiments, it was understood that the

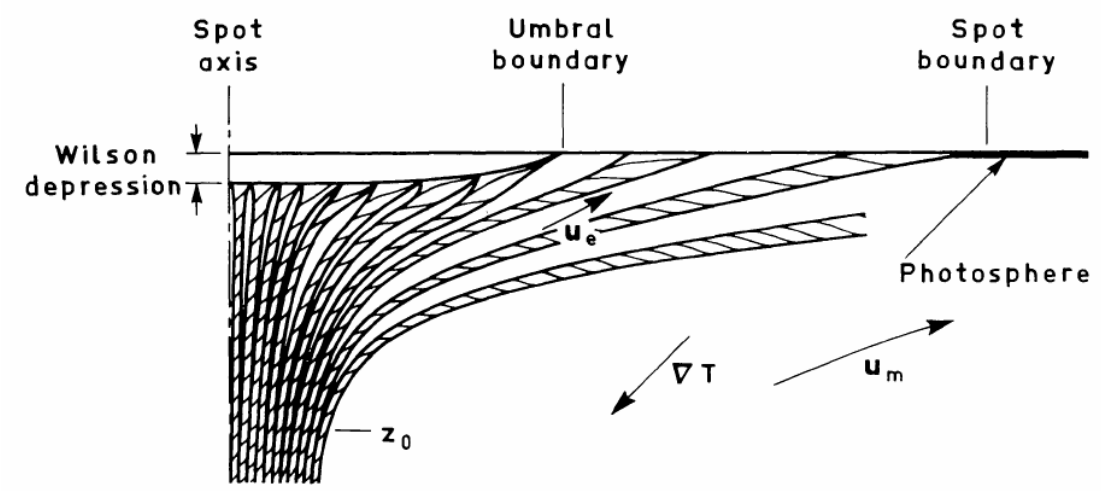

FIGURE 3.1: A cartoon diagram of a sunspot magnetic structure with the helical flux ropes given by Piddington (1978).

long plasma magnetic columns are unstable due to screw-pitch instability (Kruskal and Kulsrud 1958; Kadomtsev 1966). The condition of the inevitable twist in the fluxtube, called Kruskul-Shafranov condition, is given by

$$q = \frac{2\pi R B_z}{L B_\phi} < 1, \tag{3.1}$$

where, q is called the safety factor, and the magnetic field inside the fluxtube is $\mathbf{B}(0, B_\phi, B_z)$, radius and length of the fluxtube are R and L respectively. This implies that R has to be sufficiently smaller than L for the fluxtube to be twisted. High-resolution observations show that there is a presence of an intrinsic twist in the sunspots, flux ropes, and loops. It is to be noted that, the screw-pitch instability plays a very important role in the dynamics in the various region of the solar atmosphere. Figure 3.2 shows a detailed picture of the magnetic structure of the sunspot given by Piddington (1978). Here, the flux rope looks like a tree-like structure, where the main branches are the flux strands, which are frayed into flux fibers. These elements are driven along the supergranular boundaries, A, and are observed from the cell interior, B. The loop in section C is due to the kink instability, and, section D is called the flux threads, which are formed due to the fraying of the flux fibers. Almost all the features of Figure 3.2 are confirmed by

Ryutova *et al.* (2008), Su *et al.* (2010), and Stenflo (2013).

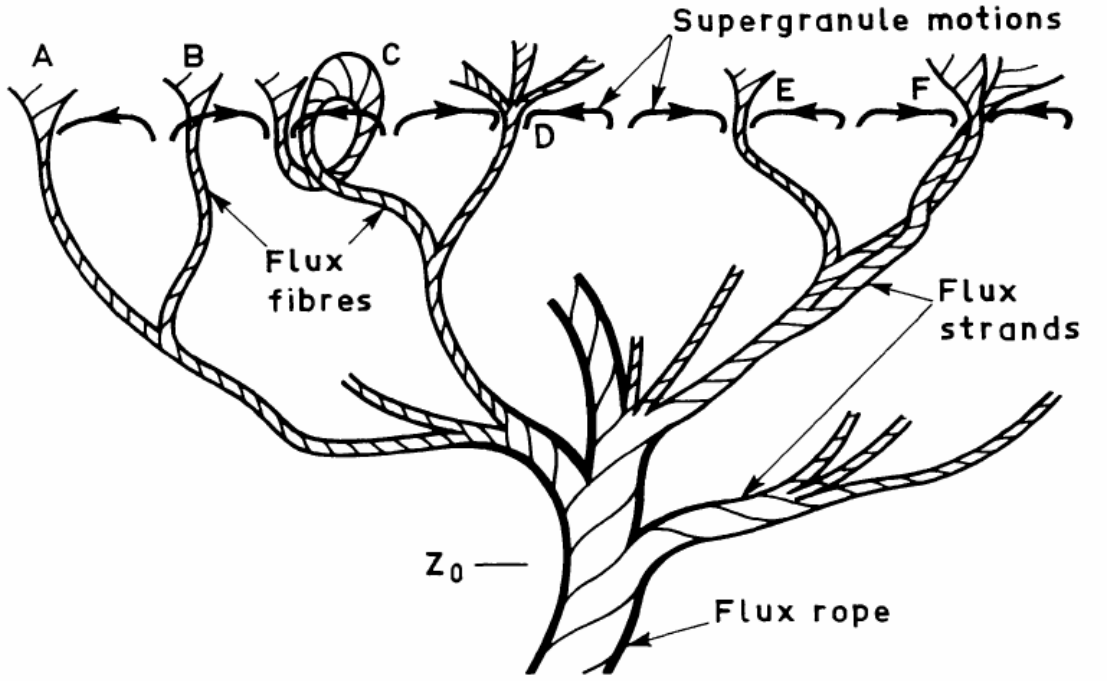

FIGURE 3.2: A schematic diagram of the different elements of the flux rope present in the filamentary structure of the sunspot (Piddington 1978).

3.3 Elements of the theory for the fluxtubes

A magnetic fluxtube is considered to be an assembly of magnetic field lines in a volume, which is enclosed by a simple closed curve. Figure 3.3 shows a cartoon diagram of a magnetic fluxtube, which is bounded by the S_1 and S_2 surfaces with fluxes F_1 and F_2 respectively. In a given magnetic configuration, one has complete freedom of choosing a particular closed curve as a fluxtube among the infinite number of possible curves in that magnetic configuration. The strength, F_M of a fluxtube is defined as,

$$F_M = \int_S \mathbf{B} \cdot \mathrm{d}\mathbf{S}, \tag{3.2}$$

where, the direction of d$\mathbf{S}$ is taken as same as $\mathbf{B}$, such that F_M is always a positive quantity. A fluxtube having the twisted field is called the magnetic flux rope. An isolated magnetic fluxtube is one, which has a magnetic free medium outside it. However, fluxtubes are the building blocks of a magnetic configuration, and they must not be thought of as an isolated structure.

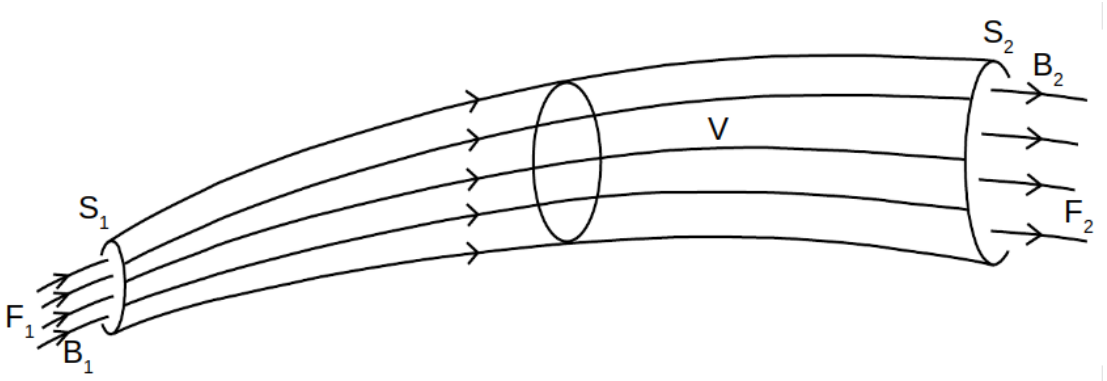

FIGURE 3.3: A cartoon diagram of a magnetic fluxtube, which is enclosed by the surface S. The arrows represent the direction of the magnetic field lines [Figure courtesy: Priest (2014)].

3.3.1 Some basic properties of magnetic fluxtubes

1. *Strength of a magnetic fluxtube remains same along its length.*

   The direction of the magnetic field lines are normal to the surface vector on the curved surface of the fluxtube (see Figure 3.3), so the contribution of the strength due to the curved surface vanishes. Hence,

   $$\int_S \mathbf{B}\cdot \mathrm{d}\mathbf{S} = \int_{S_1} \mathbf{B_1}\cdot \mathrm{d}\mathbf{S} + \int_{S_2} \mathbf{B_2}\cdot \mathrm{d}\mathbf{S}. \tag{3.3}$$

   From the divergence theorem, $\int_S \mathbf{B}\cdot \mathrm{d}\mathbf{S} = \int_V (\nabla\cdot\mathbf{B})\ \mathrm{d}V$, which vanishes due to the solenoidal condition of $\mathbf{B}$. Hence, from equation (3.3), we obtain, $F_1 \equiv \int_{S_1} \mathbf{B_1}\cdot \mathrm{d}\mathbf{S} = -\int_{S_2} \mathbf{B_2}\cdot \mathrm{d}\mathbf{S} \equiv F_2$. In other words, the strength of the fluxtube remains same along the length of the fluxtube.

2. *The average field strength of a fluxtube increases when it gets thinner, and the field strength decreases when it gets thicker.*

   From eqn (3.2), we can write that, $F_M = \bar{B}A$, where $\bar{B}$, and A are the average field strength and cross-section area of the fluxtube. As the strength, F_M, of the fluxtube remains same along the length of it, so $\bar{B}$ is inversely proportional to A, which implies that the field lines are closed for a thinner region of the fluxtube, and the field lines stay apart in a wider region.

3. *In the ideal MHD, the compression of fluxtubes, without changing its length, lead to a change of B and ρ in the same proportion.*

   Let us consider two fluxtubes of having same length L, but the radius changes from R_0 to λR_0, where λ is a proportionality constant. If the initial density and field strength of the tube is ρ_0 and B_0, and final density and field strength are ρ and B respectively, then according to the mass conservation of the plasma inside the fluxtube we have, $\rho_0 \pi R_0^2 L = \rho \pi \lambda^2 R_0^2 L$. So the final density is,

$$\rho = \frac{\rho_0}{\lambda^2}. \tag{3.4}$$

   Again, from the flux conservation theorem, we have, $B_0 \pi R_0^2 L = B \pi \lambda^2 R_0^2 L$. So the final field strength is,

$$B = \frac{B_0}{\lambda^2}. \tag{3.5}$$

   Thus, using eqns (3.4, 3.5) we obtain,

$$\frac{B}{\rho} = \frac{B_0}{\rho_0}. \tag{3.6}$$

A more general result can be been obtained by the Lundquist's identity (Lundquist 1951; Roberts 1967), given by

$$\frac{B}{\rho} = \frac{B_0}{\rho_0} \frac{\partial \mathbf{r}(\mathbf{r_0}, t)}{\partial \mathbf{r_0}}, \tag{3.7}$$

where $\mathbf{r}_0$, and $\mathbf{r}$ are the position of the fluid element at initial and arbitrary time respectively. In this case we have $\dfrac{\partial \mathbf{r}(\mathbf{r_0}, t)}{\partial \mathbf{r_0}} = 1$, hence we obtain eqn (3.6). In other words, change of B and ρ is in the same proportion inside the fluxtube. However, this relation does not hold for the coronal loops, as the plasma can flow in or out from the loop, which violates the mass conservation relation.

4. *Increasing the length of a fluxtube by keeping the width to be the same increases the field strength.*

   If the width of the fluxtube remains the same, i.e. there is no compression of the fluxtube, then the density, ρ remains constant. If we consider that, there is an increment of the length of the fluxtube by a factor λ', then by applying the mass and magnetic flux conservation law, we obtain, $B = B_0\ \lambda'$. For the elongation of the fluxtube, $\lambda' > 1$, which means $B > B_0$.

5. *Magnetic field strength,* $\mathbf{B}$ *and plasma pressure,* p *play a role for the magnetohydrostatic equilibrium of a fluxtube.*

   For a magnetic field strength $\mathbf{B}$, the magnetohydrostatic equilibrium equation of a fluxtube is given by

$$-\nabla p + \mathbf{j} \times \mathbf{B} - \rho g \mathbf{z} = 0. \tag{3.8}$$

For a magnetic field strength $\mathbf{B}(0, B_\phi, B_z)$, the current densities are

$$j_r = 0 \tag{3.9}$$

$$j_\phi = -\frac{1}{\mu}\frac{\partial B_z}{\partial r} \tag{3.10}$$

$$j_z = \frac{1}{\mu r}\frac{\partial}{\partial r}(rB_\phi). \tag{3.11}$$

The radial component of $\mathbf{j} \times \mathbf{B}$ is given by,

$$(\mathbf{j} \times \mathbf{B})_r = -\frac{1}{2\mu}\frac{\partial}{\partial r}(B_\phi^2 + B_z^2) - \frac{B_\phi^2}{\mu r} \tag{3.12}$$

Taking the radial component of eqn (3.8), and using cylindrical symmetry without gravity, we obtain

$$\frac{\mathrm{d}p}{\mathrm{d}r} + \frac{\mathrm{d}}{\mathrm{d}r}\left(\frac{B_\phi^2 + B_z^2}{2\mu}\right) + \frac{B_\phi^2}{\mu r} = 0, \tag{3.13}$$

where, r is the radial coordinate of the fluxtube geometry. Here, the second term represents the magnetic pressure, which acts along the outward direction, if $B^2/2\mu$ decreases with r. The third term represents the magnetic tension force, which acts along the inward direction of the fluxtube. The twist in the field line is defined by,

$$\chi(r) = \frac{LB_\phi(r)}{rB_z(r)}, \tag{3.14}$$

whereas, the average twist of a field line for a fluxtube of radius R is given by,

$$\bar{\chi} = \frac{1}{R}\int_0^R \chi(r)\mathrm{d}r. \tag{3.15}$$

Another related measurement of twist is called the pitch,

$$l_p = \frac{L}{n}, \tag{3.16}$$

where n is the number of turns per unit length. Hence,

$$l_p = \frac{2\pi L}{\chi}, \tag{3.17}$$

which is measured as the travelled length of the field line for a complete rotation about the axis.

3.3.2 Governing equations for fluxtube solution

The theoretical study of the MHD of the small scale fluxtubes had started in the mid 1970s. Parker (1974a) proposed that, due to the turbulent pumping of the plasma at the supergranular boundary, the region inside the fluxtube becomes vacuous. The maximum field strength of this mechanism is restricted by the energy equipartition law, $B^2/(8\pi) \approx \rho v^2/2$, which gives a maximum value of B to be small $\approx$ 500 G. Due to this small B value, obtained from the model, Parker (1974b) included the Bernoulli effect, but it increased the value of the magnetic field only by a small fraction. The structures of the fluxtube due to the turbulent pumping mechanism are shown in Figure 3.4. However, the origin and the properties of the small scale fluxtubes that appear at the solar surface is still an open question.

Later on, the study was carried forward by several authors [e.g. Cram and Wilson (1975); Defouw (1976); Roberts and Webb (1978)]. The basic governing equations for the study of the dynamics of the fluxtubes are the Maxwell's equations with

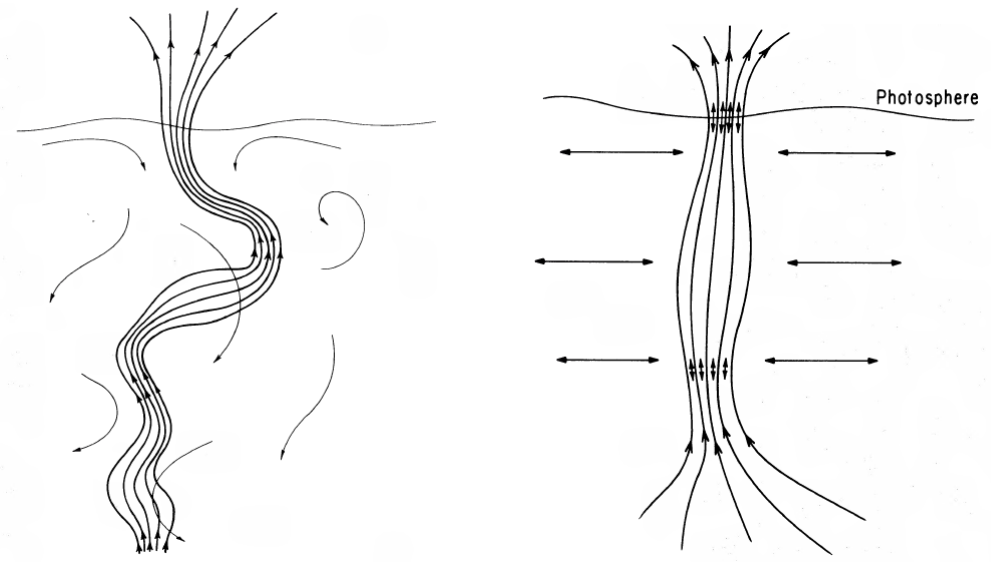

(a) (b)

FIGURE 3.4: Cartoon of the fluxtubes rising up through the solar photosphere, which shows the fluxtube structures due to the turbulent pumping mechanism (a) without and (b) with taking the Bernoulli's effect into account respectively (Parker 1974a,b).

the MHD approximation, which are summarized below:

$$\nabla \cdot \mathbf{B} = 0, \tag{3.18}$$

$$\frac{\partial \mathbf{B}}{\partial t} = \nabla \times (\mathbf{v} \times \mathbf{B}) + \eta_d \nabla^2 \mathbf{B}, \tag{3.19}$$

$$\rho \frac{\mathrm{d}\mathbf{v}}{\mathrm{d}t} = -\nabla p + \frac{1}{4\pi}(\nabla \times \mathbf{B}) \times \mathbf{B} + \rho \mathbf{g}, \tag{3.20}$$

$$\frac{\mathrm{d}\rho}{\mathrm{d}t} + \rho \nabla \cdot \mathbf{v} = 0, \tag{3.21}$$

$$\frac{\partial (\rho^{-\gamma} p)}{\partial t} + \mathbf{v} \nabla (\rho^{-\gamma} p) = 0, \tag{3.22}$$

where, η_d is the magnetic diffusivity. The magnetohydrostatic equilibrium of the fluxtube can be represented by eqn (3.20), for $\mathbf{v} = 0$, to be

$$-\nabla p + \frac{1}{4\pi}(\nabla \times \mathbf{B}) \times \mathbf{B} + \rho \mathbf{g} = 0. \tag{3.23}$$

In the presence of the magnetic field $\mathbf{B}(0, 0, B_z(r))$, taking the radial component of eqn (3.23), the equilibrium condition of the fluxtube is given by

$$p_i(r) + \frac{B_{zi}^2}{8\pi} = p_e(r) + \frac{B_{ze}^2}{8\pi}, \tag{3.24}$$

where the suffices 'i' and 'e' represent quantities internal and external to the fluxtube, respectively. However, for an isolated fluxtube, which is embedded in a magnetic free medium, $B_{ze} = 0$.

As $\mathbf{g}$ acts vertically downward, the z component of eqn (3.23), gives the density relation,

$$\frac{\mathrm{d}p}{\mathrm{d}z} + \rho g(z) = 0, \tag{3.25}$$

which upon using the ideal gas law condition, $\rho = mp/kT$, we obtain

$$p = p_0 \exp\left(- \int_0^z \frac{1}{\Lambda(z)} \mathrm{d}z \right), \tag{3.26}$$

where, $\Lambda(z) = \dfrac{kT(z)}{mg}$, is the pressure scale height and k is the Boltzman constant. Hence,

$$\rho = \rho_0 \frac{T_0}{T(z)} \exp\left(- \int_0^z \frac{1}{\Lambda(z)} \mathrm{d}z \right). \tag{3.27}$$

Thus, knowing the temperature profile, $T(z)$, inside the fluxtube, we can obtain the pressure, and density distribution (Vernazza *et al.* 1981; Avrett and Loeser 2008).

3.4 Historical overview of various fluxtube models

The fluxtube models can be broadly divided into two classes of models, which are the self-similar and the non-self-similar models. The main difference between these two models is the magnetic structure of the fluxtubes. In the self-similar model, the fluxtubes are considered to be present in a continuous magnetic medium, where the field strength of the fluxtube is maximum at the center of the fluxtube and decreases asymptotically along the radial direction. In principle, the radius of a self-similar fluxtube extends up to infinity, but in practice, the effective radius of the fluxtube is the radial distance from the axis, which encloses a significant fraction of the total flux (which is usually taken to be 90%). On the other hand, the non-self-similar fluxtube is embedded in a magnetic free medium and has a sharp boundary. As a result, there is a sharp drop in the magnetic field strength at the boundary of the fluxtube, where a current sheet exists, unlike the case for the self-similar fluxtubes. These magnetic fluxtubes are called magnetic fibrils. We will now discuss the models in some detail.

3.4.1 Self-similar fluxtube models

The basic formulation of the self-similar (SS hereafter) model was pioneered by Schlüter and Temesváry (1958) for an untwisted stationary single sunspot. This model is based on some assumptions listed below:

- The structure of the sunspot has cylindrical symmetry. The $z-$axis is perpendicular to the sunspot surface and the positive z direction is pointed towards the center of the Sun. On the axis, i.e. at $r = 0$, there is no current,

which means the radial component of the field, $B_r = 0$, and the vertical component of the field strength, B_z is maximum.

- The sunspot is assumed to be in a quasi-static equilibrium, which implies that the time derivative of all the quantities are zero. This approximation is valid for a sunspot with a long lifetime.
- The magnetic field strength and its derivative vanish at infinity.
- The motions of the plasma are neglected.
- The magnetic field has no twist, i.e. the azimuthal component of the magnetic field, $B_\phi = 0$.
- The relative magnetic flux distribution in a horizontal cross-section of the sunspot is geometrically similar.

Here, all the assumptions above make for a simple picture of a sunspot, where the last three assumptions are necessarily not true.

The SS model states that, the ratio of the vertical component, $B_z(r, z)$ and the central intensity, $B_z(0, z)$, at the same depth, depends only on a scale factor $\zeta(z)$, i.e.

$$B_z(r, z) = B_z(0, z)\frac{D(\xi)}{D_0}, \tag{3.28}$$

where, $D(\xi)$ is called the shape function, $D_0 \equiv D(\xi = 0)$, and ξ is the self-similar parameter defined by

$$\xi = \zeta(z)\ r. \tag{3.29}$$

Due to the continuity of the lines of force, the strength of $B_z(0, z)$ increases where the fluxtube is more squeezed. So, the appropriate normalization for $B_z(0, z)$ is

given by

$$B_z(0,z) = \zeta^2(z) D_0. \tag{3.30}$$

From eqns (3.28, 3.30), we obtain the general form

$$B_z(r,z) = \zeta^2(z) D(\xi). \tag{3.31}$$

Using the solenoidal condition of the magnetic field i.e. $\nabla \cdot \mathbf{B} = 0$, we obtain

$$B_r(r,z) = -\frac{\mathrm{d}\zeta(z)}{\mathrm{d}z}\, \xi D(\xi). \tag{3.32}$$

Taking the $r-$component of the eqn (3.23) in the cylindrical geometry we find

$$B_z\left(\frac{\partial B_r}{\partial z} - \frac{\partial B_z}{\partial r}\right) = 4\pi \frac{\partial p}{\partial r}. \tag{3.33}$$

Using the prime notation ($'$) to denote the derivative with respect to the depth z, we obtain the following form eqn (3.33)

$$\xi D^2(\xi)\zeta\zeta'' + \frac{1}{2}\frac{\mathrm{d}}{\mathrm{d}\xi}(\xi D(\xi))^2 \zeta'^2 + \frac{1}{2}\frac{\mathrm{d}}{\mathrm{d}\xi}(D^2(\xi))\zeta^4 = -4\pi \frac{\mathrm{d}p}{\mathrm{d}\xi}. \tag{3.34}$$

Integrating eqn (3.34) over ξ from 0 to ∞ at a fixed z and using the condition $D(\xi = \infty) = 0$, we have

$$\zeta\zeta'' \int_0^\infty \xi D^2(\xi)\mathrm{d}\xi - \frac{1}{2}\zeta^4 D_0^2 = -4\pi\Delta p, \tag{3.35}$$

where,

$$\Delta p = p(\infty, z) - p(0, z). \tag{3.36}$$

Using the forms

$$y(z) = B_z(0,z)^{1/2} = (2f)^{1/2}\zeta(z) \tag{3.37a}$$

$$f = \frac{2}{D_0}\int_0^\infty \xi D(\xi)\mathrm{d}\xi, \tag{3.37b}$$

we obtain

$$fyy'' - y^4 + 8\pi\Delta p = 0. \tag{3.38}$$

After specifying the forms of Δp and $D(\xi)$, eqn (3.38) can be solved. The magnetic and thermodynamic structure of the fluxtube can then be obtained after solving this equation. The $z-$component of eqn (3.23), gives the density relation,

$$\Delta\rho = \frac{1}{g}\frac{\mathrm{d}}{\mathrm{d}z}(\Delta p), \tag{3.39}$$

where $\Delta\rho = \rho(\infty,0) - \rho(0,z)$ represents the density difference between the fluxtube axis and infinity. Yun (1971) extended the SS model by incorporating twist, i.e. $B_\phi \neq 0$. In this case, the $r-$component of eqn (3.23) becomes

$$B_z\left(\frac{\partial B_r}{\partial z} - \frac{\partial B_z}{\partial r}\right) - \frac{B_\phi}{r}\frac{\partial}{\partial r}(rB_\phi) = 4\pi\frac{\partial p}{\partial r}. \tag{3.40}$$

Following the observations of Stepanov (1965), of the radial variation B_ϕ from the axis of the sunspot (see Figure 3.5), Yun (1971) assumed the the form of

$$B_\phi(r,z) = \gamma(z)\frac{r}{R(z)}B_z(r,z), \tag{3.41}$$

where, $\gamma(z)$ and $R(z)$ are the proportionality factor and the sunspot radius respectively at the depth z. Assuming the ratio $\gamma(z)/R(z) = K$ to be a constant, and using the SS model, eqn (3.41) reduces into

$$B_\phi(r,z) = K\xi D(\xi)\zeta(z). \tag{3.42}$$

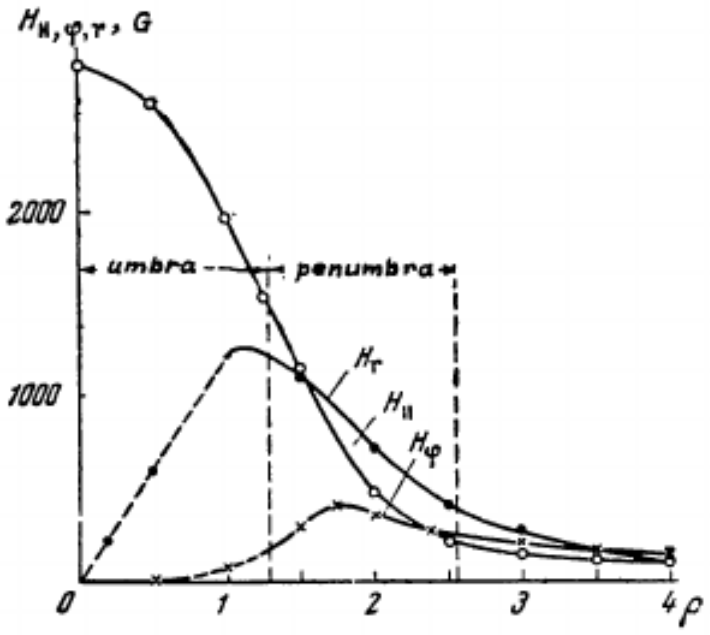

FIGURE 3.5: Radial variation of B_z, B_r and B_ϕ from the sunspot center obtained by Stepanov (1965).

Using a particular choice of the shape function, $D(\xi) = D_0 \exp(-\xi^2)$, and applying eqn (3.37b),

$$f = D_0/2 \equiv \Phi/(2\pi) \tag{3.43}$$

is obtained, where Φ is the total flux of the sunspot. From eqns (3.29, 3.37a, 3.43), the total radius $R(z)$ can be derived to be

$$R(z) = \xi_p \left(\frac{\Phi_p}{\pi B_z(0,z)} \right)^{1/2}, \tag{3.44}$$

where, Φ_p is the observed total flux value and $\xi_p = 1.63$ refers the self-similar parameter value at the sunspot penumbra obtained by Yun (1970). After finding the radius of the sunspot at a particular depth the value of K can be approximated from eqn (3.41) by the relation

$$K = \frac{B_\phi(R(z),z)}{R(z)B_z(R(z),z)}, \tag{3.45}$$

where the value of $\frac{B_\phi(R(z),z)}{B_z(R(z),z)}$ is known from the observation of Stepanov (1965).

However, Beckers and Schröter (1969) and Wittmann (1974) analyzed the inclination angle of the magnetic field lines and reported that there is a radial increment of the angle of inclination which saturates to 90° at the sunspot penumbra, which can't be explained by [Schlüter and Temesváry (1958), Yun (1971)]. Osherovitch (1982) considered p as a quadratic function of the flux function, ψ. This model gives a closed structure of the magnetic field lines, where the field lines rise and fall back into the same horizontal plane at the boundary of the fluxtube (see Figure 3.6). Figure 3.7 shows the radial variation of the field line from the axis to the fluxtube boundary, which is reasonably consistent with the observations.

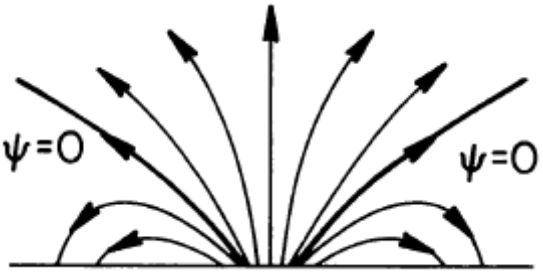

FIGURE 3.6: Geometry of the magnetic field lines inside the sunspot boundary (Osherovitch 1982).

More recently, Gent *et al.* (2013) have done a numerical study of the magnetohydrostatic equilibrium state of a single open fluxtube without a twist. Taking the surrounding of the fluxtube as a quiet Sun atmosphere into account, the magnetohydrostatic equilibrium condition for the pressure balance is derived. The simulation consists of the magnetic footpoints of 1 kG, which is the free parameter of the model and is used to obtain a realistic structure of the fluxtube. Figure 3.8 shows the geometry of the magnetic field lines inside of the fluxtube.

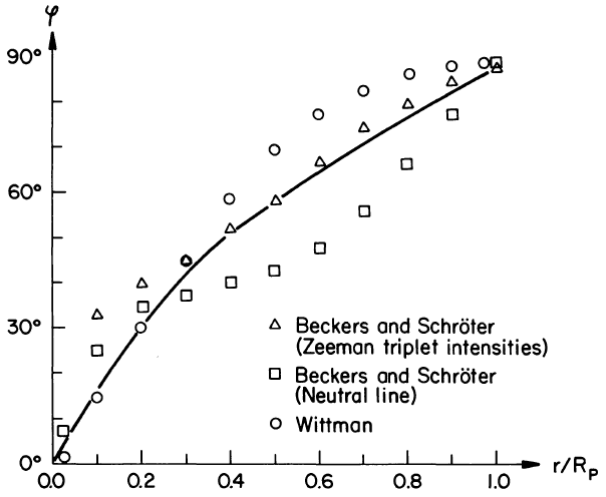

FIGURE 3.7: Comparison of the inclination angle of the field line obtained by Osherovitch (1982) with the existing observations, where R_p is the radius of the sunspot penumbra.

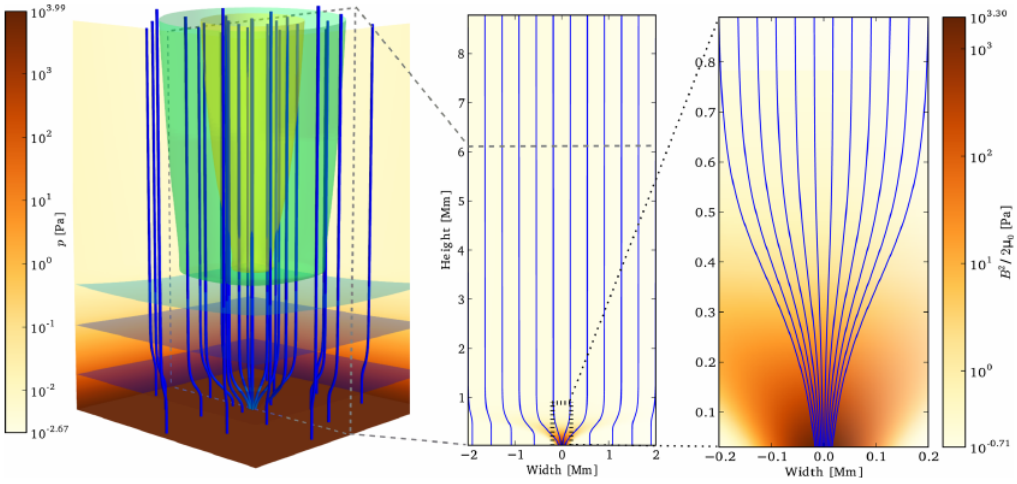

FIGURE 3.8: The figure on the left shows the 3D geometry of the magnetic field lines inside the fluxtube obtained by Gent *et al.* (2013). The color bar represents the value of the thermal pressure. A 2D vertical slice of the fluxtube is shown in the middle panel. The right image is the zoomed version of the box enclosing in the image in the middle panel.

3.4.2 Non-self-similar fluxtube models

One of the first self-consistent numerical models of a magnetohydrodynamic fluxtube was constructed by Deinzer *et al.* (1984a,b). The MHD equations for a

compressible medium and the associated energy equations are taken into account for obtaining the fluxtube structure and its dynamics. The pressure equilibrium condition of the fluxtube with the external atmosphere is also applied in the 2D fluxtube model.

Figure 3.9 shows the numerical simulations for the density, magnetic field structure, and velocity field at an evolutionary time from the stationary state. Followed

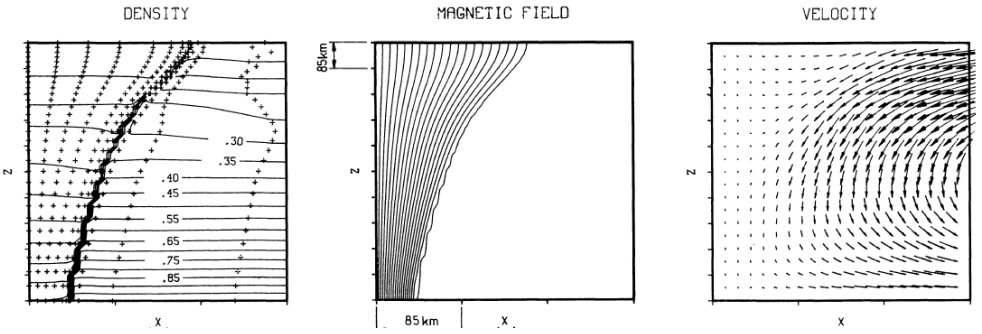

FIGURE 3.9: Results obtained from Deinzer *et al.* (1984a,b). The left figure shows the contour plot of density normalized to $\rho_0 = 1.6 \times 10^{-6}$ g cm^{-3}. The middle figure shows the magnetic lines of forces and the figure at the right shows the velocity field, where the maximum velocity is 200 m s^{-1}.

by that, Steiner *et al.* (1986) obtained a MHS numerical fluxtube model. For obtaining the magnetic structure of the fluxtube, the following set of equations

$$\mathbf{B} \cdot [\nabla p - \rho \mathbf{g}] = 0, \tag{3.46}$$

$$\mathbf{j} = \frac{1}{B^2} \mathbf{B} \times [\nabla p - \rho \mathbf{g}], \tag{3.47}$$

$$\frac{\partial^2 \psi}{\partial r^2} - \frac{1}{r} \frac{\partial \psi}{\partial r} + \frac{\partial^2 \psi}{\partial z^2} = -4\pi j, \tag{3.48}$$

need to be solved in an iterative scheme. For carrying out the iteration, the following steps are processed:

1. An initial arbitrary magnetic configuration is specified. The closer, the initial guess is to the final solution, the faster the convergence.

2. The pressure distribution is calculated by integrating the eqn (3.46) along the magnetic lines of force. The integral can be written in the form

$$p = p^* \exp\left(- \int_{z'=0}^{z} \frac{\mathrm{d}z'}{h(T(\psi, z'))} \right), \tag{3.49}$$

   where, p^* is the pressure at $z = 0$, and h is the scale height.

3. Using the eqns (3.49, 3.47), the current density j can be found in the form of

$$j = \frac{1}{B^2}\left[B_z \frac{\partial p}{\partial r} - B_r \left(\frac{\partial p}{\partial z} + \frac{p}{h} \right) \right]. \tag{3.50}$$

4. Calculating the current from eqn (3.50), eqn (3.48) can be integrated along with the appropriate boundary conditions to obtain ψ, which provides the magnetic structure. Then the procedure is returned to step 1. Then steps 2-4 are successively repeated until it convergences.

Figure 3.10 shows the magnetic lines of force inside the fluxtube. The radial variations of B_r and B_z are also shown by the dashed and solid lines respectively at different heights.

An analytical solution of a stationary magnetodydrodynamic sunspot was modeled by Solov'ev and Kirichek (2016). The magnetic structure of the sunspot model is given by three distinct flux functions, where the magnetic field lines approach to the photosphere at the edge of the sunspot boundary. The radial and vertical variations of the thermodynamic quantities like pressure, density and temperature are also calculated in the visible layers. The flux function, A_1 is represented by the potential field, which is vertically straight and expands like a diverging fan from the axis of the fluxtube. The flux function, A_1 is given by

$$A_1(r, z) = \frac{B_{0,1}}{B_0} w(z) \left[1 - \left(1 + \frac{r^2}{w(z)} \right)^{-1/2} \right], \tag{3.51}$$

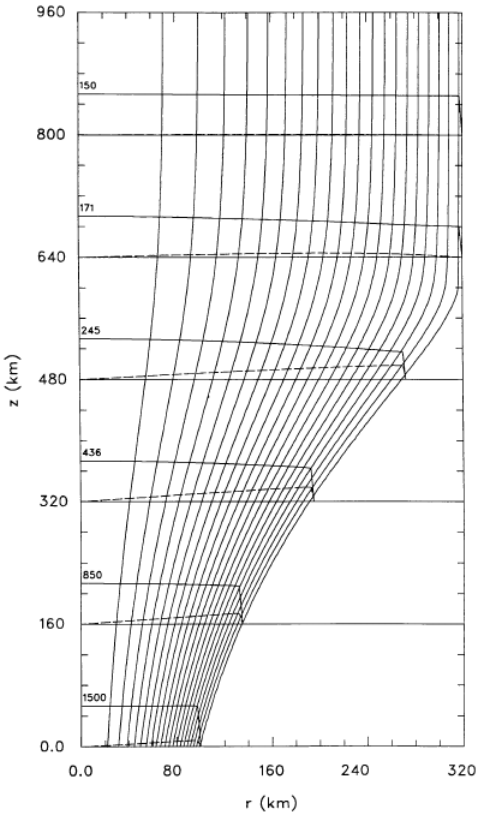

FIGURE 3.10: 2D geometry of the magnetic field lines inside the fluxtube obtained by Steiner *et al.* (1986) model.

where, $w(z)$ determines the cross-sectional shape of the fluxtube, and $\frac{B_{0,1}}{B_0}$ is the relative field strength with respect to the field strength at center, B_0. The second flux function, A_2 which is confined to a certain height describes both the umbra and penumbra of the sunspot is given by,

$$A_2(r,z) = \frac{B_{0,2}}{B_0 k} r J_1(kr)[\exp(-kz) - G(lz)], \tag{3.52}$$

where, k is the inverse scale height, $\frac{B_{0,2}}{B_0}$ is the contribution from the second flux function, $J_1(kr)$ is the Bessel's function of first kind, and

$$G(z) = -\frac{ck}{a^2 k_0} \exp[-ak_0 z(1 + bk_0 z + hk_0^3 z^3)], \tag{3.53}$$

is a non-dimensional function where, a, b, c, and h are the positive dimensionless

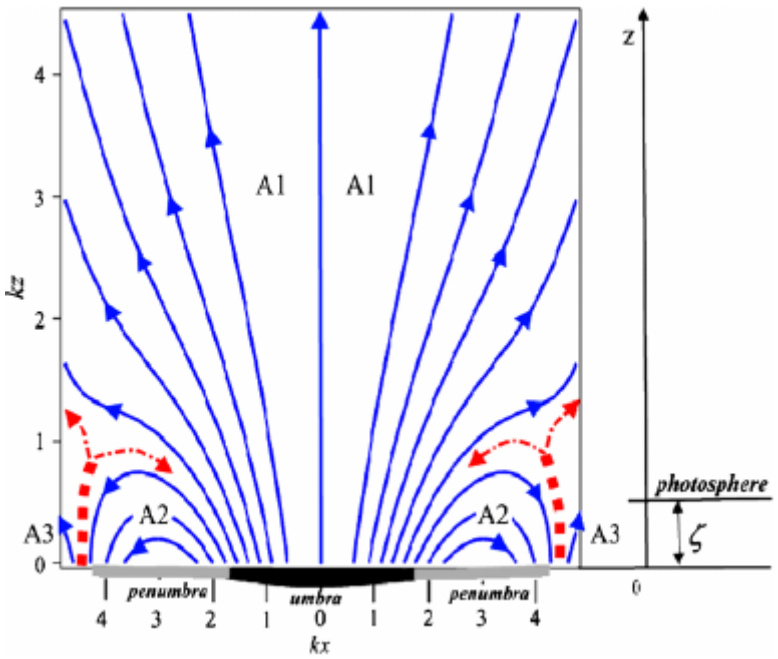

FIGURE 3.11: The magnetic structure inside a fluxtube for a typical sunspot model obtained from Solov'ev and Kirichek (2016).

factors, and $k_0 = 1$ Mm^{-1} is a constant. The A_2, which is represented by eqn (3.52) is limited up to the first root of $J_1(kr)$. Moving farther out along the radial direction, another flux function,

$$A_3(r) = B_{0,3}\frac{(r - r_1)^2}{2}, \tag{3.54}$$

is defined which has the same polarity as A_1, where $r_1 = 3.83$ is the first root of $J_1(r_1)$. Figure 3.11 shows that the structure of the magnetic field lines inside the fluxtube for a sunspot model. The flux function A_1 extends upwards into the corona, while flux function, A_2 forms a loop that rise and returns into the photosphere at the edge of the fluxtube, and A_3 is the external field of the penumbra.

3.5 Summary

This chapter is premier to understand the Chapters 4, and 5, where we have discussed the fluxtube models we have developed. In this chapter, we presented a brief historical background for the discovery of the solar fluxtubes, and their observational implications. Then we present the theoretical aspects of the physics of the fluxtubes and some important basic properties of it. We also discussed the governing equations to obtain fluxtube solutions.

The main texts and references for this chapter are Ryutova (2015), Priest (1982), Schlüter and Temesváry (1958), Steiner *et al.* (1986), Gent *et al.* (2013), and Solov'ev and Kirichek (2016). The magnetic configuration for the fluxtube models given by Schlüter and Temesváry (1958), Deinzer *et al.* (1984a,b), and Gent *et al.* (2013) are untwisted, whereas the twist is implemented in the numerical model obtained by Steiner *et al.* (1986) for an open field magnetic configuration. Solov'ev and Kirichek (2016) have obtained a fluxtube solution for sunspots for open and closed field configuration but without the twist. The fluxtube models (Sen and Mangalam 2018a, 2019) we develop has the twisted magnetic configuration, and branch out into open and closed field magnetic structures. We discuss these models in more details in the Chapters 4, and 5.

Chapter 4

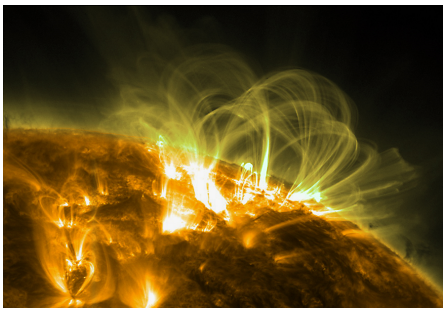

Image source: www.vofoundation.org

Closed field twisted magnetic fluxtubes in the solar atmosphere

4.1 Introduction

The study of small scale magnetic structures in the solar photosphere is important because they play a crucial role in the evolution of active regions and sunspots (Muller and Mena 1987; Centeno *et al.* 2007). Magnetic bright points (MBPs) are likely to be the fluxtubes observed in the photosphere (Berger *et al.* 1995; Centeno *et al.* 2007; Lagg *et al.* 2010). The topological rearrangement of these magnetic fluxtubes due to the motion of the photospheric footpoints or magnetic reconnections, contribute to the coronal heating (Muller *et al.* 1994; van Ballegooijen

The work presented in this chapter is partly published in:
Sen and Mangalam (2018a)

1986). A three dimensional (3D) single fluxtube model with the untwisted magnetic field has been studied by solving linear elliptic partial differential equation by numerical iterative process (Steiner *et al.* 1986). Schlüter and Temesváry (1958) and Osherovich (1984) studied a 3D fluxtube for sunspots using a self–similar model. The magnetic and thermodynamic structure inside fluxtube with an untwisted magnetic field that spans from the photosphere to the lower part of the solar corona is studied by Gent *et al.* (2013). Both 2D and 3D numerical models of fluxtubes with the energy propagation through the torsional Alfven waves have been studied by Murawski *et al.* (2015a,b), where an empirical form of magnetic flux function was assumed. Vigeesh *et al.* (2009) assumed an empirical form of gas pressure to investigate the wave propagation and energy transport through a fluxtube. Several interesting results of wave behavior in the solar photosphere and chromosphere have been presented by several authors (Bogdan *et al.* 2003; Fedun *et al.* 2009; Shelyag *et al.* 2010).

In this work, we construct a 3D single cylindrical vertical straight magnetic fluxtube semi-analytically with a twisted magnetic field by obtaining a new solution of poloidal flux function by solving Grad–Shafranov equation (GSE; Grad and Rubin (1958); Shafranov (1958)). We assume a specific form of gas pressure and poloidal current, which has been used to study the equilibrium solution of terrestrial plasma (Atanasiu *et al.* 2004). An equilibrium solution near the magnetic axis of the plasma torus has been reported previously, using a plasma pressure and poloidal current profile that varies linearly with the poloidal flux function (Solov'ev 1968). We obtain an analytic solution by assuming a form that is quadratic in the poloidal flux function and derive the magnetic field structure and thermodynamic quantities inside the fluxtube using the solution that represents an ideal MHS equilibrium. In the future, we will look to explore fully the profile functions that will improve the solution set.

The overview of the work is as follows. In §2, the GSE has been derived assuming a specific form of the profile function of gas pressure and poloidal current and the solution of the equation is presented. In §3, we discuss the boundary condition

that is physically acceptable and can be used for realistic modeling of a fluxtube. In §4, the mode wise variation of the profile functions is presented and in §5, we compare the model with the observations. Finally, we conclude with a comparison with other existing models.

4.2 Solution of Grad-Shafranov equation

We assume an axisymmetric cylindrical geometry, with gas pressure p and take the poloidal current I_p constant along a magnetic field line. We express $p(\Psi, z)$ and $I_p(\Psi)$ in terms of the poloidal flux function $\Psi(r, z)$ and z and consider a straight vertical axisymmetric fluxtube that spans the altitude from photosphere ($z = 0$) to the transition region ($z = 2.15$ Mm) that is in equilibrium with the atmosphere outside with the uniform gravity $\mathbf{g}(= -g\hat{z})$ acting vertically downward. The force balance equation in MHS equilibrium takes the form

$$-\nabla p + \frac{1}{4\pi}(\nabla \times \mathbf{B}) \times \mathbf{B} + \rho \mathbf{g} = 0, \tag{4.1}$$

where ρ denotes the mass density and $\mathbf{B}$ is the magnetic field associated with the poloidal flux function $\Psi(r, z) = \int_0^r B_z(r', z) r' \mathrm{d}r'$ (scaled by the factor $\frac{1}{2\pi}$) in the following form

$$B_r = -\frac{1}{r}\frac{\partial \Psi}{\partial z}; \quad B_z = \frac{1}{r}\frac{\partial \Psi}{\partial r}; \quad B_\phi = \frac{I_p}{r}. \tag{4.2}$$

This form of B_r, B_ϕ and B_z ensures the solenoidal condition of magnetic field. Now splitting the MHS force balance equation (4.1) into r and z directions, we

find two different scalar partial differential equations

$$-\frac{\partial p}{\partial r}+\frac{1}{4\pi}\left(B_r\frac{\partial B_r}{\partial r}+B_z\frac{\partial B_r}{\partial z}-\frac{1}{2}\frac{\partial B^2}{\partial r}\right)=0 \tag{4.3a}$$

$$-\frac{\partial p}{\partial z}+\frac{1}{4\pi}\left[\frac{1}{r}\frac{\partial \Psi}{\partial z}\left(\frac{1}{r^2}\frac{\partial \Psi}{\partial r}-\frac{1}{r}\frac{\partial^2 \Psi}{\partial r^2}\right)-\frac{1}{r^2}\frac{\partial \Psi}{\partial z}\frac{\partial^2 \Psi}{\partial z^2}-\frac{1}{2r^2}\frac{\partial}{\partial z}(I_p^2)\right]-\rho g=0. \tag{4.3b}$$

If the gas pressure and poloidal current are functions of Ψ alone i.e., $p_1(\Psi)$ and $I_p(\Psi)$ respectively, then from the eqns (4.3a, 4.2) it follows that

$$\frac{\partial^2 \Psi}{\partial r^2}-\frac{1}{r}\frac{\partial \Psi}{\partial r}+\frac{\partial^2 \Psi}{\partial z^2}=-\frac{1}{2}\frac{\partial I_p^2(\Psi)}{\partial \Psi}-4\pi r^2\frac{\partial p_1(\Psi)}{\partial \Psi}. \tag{4.4}$$

Plugging in p_1 and I_p^2 in eqn (4.3b), we find

$$-\frac{\partial p_1(\Psi)}{\partial z}+\frac{1}{4\pi}\left[\frac{1}{r^2}\frac{\partial \Psi}{\partial z}\left(\frac{1}{r}\frac{\partial \Psi}{\partial r}-\frac{\partial^2 \Psi}{\partial r^2}\right)-\frac{1}{r^2}\frac{\partial \Psi}{\partial z}\frac{\partial^2 \Psi}{\partial z^2}-\frac{1}{2r^2}\frac{\partial I_p^2(\Psi)}{\partial z}\right]-\rho g=0. \tag{4.5}$$

By multiplying both sides of eqn (4.5) by $4\pi r^2\dfrac{\partial z}{\partial \Psi}$ and using eqn (4.4), we obtain $g\rho\dfrac{\partial z}{\partial \Psi}=0$ which implies that ρ is zero, which means that the vertical hydrostatic pressure balance will not be maintained. Therefore, to balance the vertical hydrostatic pressure inside the fluxtube, we introduce a new function, $p_2(z)$ such that,

$$p(r,z)=p_1(\Psi)+p_2(z).$$

We assume $p_1(\Psi)$ and $I_p^2(\Psi)$ to be second order polynomials of Ψ

$$p(r,z)=p_1(\Psi)+p_2(z) \tag{4.6a}$$

$$I_p^2(r,z)=\tilde{\alpha}\Psi^2+\tilde{\beta}\Psi+I_0^2 \tag{4.6b}$$

where

$$p_1(\Psi)=\tilde{a}\Psi^2+\tilde{b}\Psi,$$

and the parameters $\tilde{a}, \tilde{b}, \tilde{\alpha}, \tilde{\beta}$ and I_0^2 are to be determined by appropriate boundary conditions. The function $p_2(z)$ is to be evaluated later. The substitution of p given by eqn (4.6a) in eqn (4.3a) gives eqn (4.4) and we obtain the following second order scalar partial linear inhomogeneous differential equation

$$\frac{\partial^2\Psi}{\partial r^2} - \frac{1}{r}\frac{\partial\Psi}{\partial r} + \frac{\partial^2\Psi}{\partial z^2} = -(ar^2+\alpha)\Psi - (br^2+\beta), \tag{4.7}$$

with the rescaled parameters, $a = 8\pi\tilde{a}; \alpha = \tilde{\alpha}; b = 4\pi\tilde{b}; \beta = \tilde{\beta}/2$. To solve eqn (4.7), we split Ψ in two parts: a homogeneous part, $\Psi_h(r,z)$ and an inhomogeneous part $\Psi_p(r)$, i.e. $\Psi(r,z) = \Psi_h(r,z) + \Psi_p(r)$. Using this form in eqn (4.7), we separate the homogeneous and the inhomogeneous parts to obtain the following expressions:

$$\frac{\partial^2\Psi_h}{\partial r^2} - \frac{1}{r}\frac{\partial\Psi_h}{\partial r} + \frac{\partial^2\Psi_h}{\partial z^2} = -(ar^2+\alpha)\Psi_h \tag{4.8a}$$

$$\frac{\partial^2\Psi_p}{\partial r^2} - \frac{1}{r}\frac{\partial\Psi_p}{\partial r} = -(ar^2+\alpha)\Psi_p - (br^2+\beta). \tag{4.8b}$$

To solve the homogeneous part, we seek a solution of the form $\Psi_h(r,z) = S(r)Z(z)$. Then we separate out the r and z part in eqn (4.8a) as follows

$$\frac{S''}{S} - \frac{1}{r}\frac{S'}{S} + ar^2 + \alpha = -\frac{Z''}{Z} = -k^2, \tag{4.9}$$

where k is an arbitrary real constant. Motivated by the fact that the poloidal flux function $\Psi(r,z)$ decreases with z, we assume that the solution of the z-part of eqn (4.9) takes the form

$$Z(z) = Ce^{-kz}, \tag{4.10}$$

where C is an arbitrary constant. To solve the r–part of eqn (4.9), we substitute $x = \frac{\sqrt{a}r^2}{2}$ (where $a > 0$) and insert it in eqn (4.9) to find

$$\frac{\mathrm{d}^2S}{\mathrm{d}x^2} + \left(1 + \frac{2\eta}{x}\right)S = 0, \tag{4.11}$$

whose solutions are given by Coulomb wave functions $F_L(-\eta, x)$ and $G_L(-\eta, x)$ (Abramowitz and Stegun 1972) (page $537-544$) with $L=0$ and $\eta = \dfrac{\alpha+k^2}{4\sqrt{a}}$. The solution of eqn (4.11) takes the following form

$$S(r) = C_1 F_0\big(-\eta, \frac{\sqrt{a}r^2}{2}\big) + C_2 G_0\big(-\eta, \frac{\sqrt{a}r^2}{2}\big). \tag{4.12}$$

Here $F_0\big(-\eta, \frac{\sqrt{a}r^2}{2}\big)$ and $G_0\big(-\eta, \frac{\sqrt{a}r^2}{2}\big)$ are called the regular and irregular Coulomb wave functions respectively which are complex quantities with real arguments (Boersma 1968), given by

$$F_0(-\eta, \frac{\sqrt{a}r^2}{2}) = C_0(\eta) M_{-i\eta,1/2}(i\sqrt{a}r^2), \tag{4.13}$$

$$G_0(-\eta, \frac{\sqrt{a}r^2}{2}) = iC_0(\eta) M_{-i\eta,1/2}(i\sqrt{a}r^2) + D_0(\eta) W_{-i\eta,1/2}(i\sqrt{a}r^2), \tag{4.14}$$

where $M_{-i\eta,1/2}(i\sqrt{a}r^2)$ and $W_{-i\eta,1/2}(i\sqrt{a}r^2)$ are called the Whittaker-M and Whittaker-W function (see Figure 4.3) and the constants $C_0(\eta)$ and $D_0(\eta)$ are defined by

$$C_0(\eta) = \frac{1}{2}|\Gamma(1-i\eta)|e^{-\frac{\pi}{2}(i-\eta)} \tag{4.15}$$

and

$$D_0(\eta) = \frac{\Gamma(1-i\eta)}{|\Gamma(1-i\eta)|}e^{-\frac{\pi\eta}{2}}. \tag{4.16}$$

The Whittaker function has been used by several authors in their models of the solar atmosphere albeit in different physical problems (eg. Tsinganos (1979) in the context of inviscid flows, and also in the context of MHD waves by Hindman and Jain (2008) and Erdélyi and Fedun (2010)). Now $B_z(r,z)$ has to be a finite quantity that varies linearly with the term $\dfrac{1}{r}\dfrac{\mathrm{d}S}{\mathrm{d}r}$ but $\dfrac{1}{r}\dfrac{\mathrm{d}}{\mathrm{d}r}[G_0(-\eta, \dfrac{\sqrt{a}r^2}{2})]$ blows up at $r=0$; therefore for B_z to be finite on the axis of the fluxtube C_2 in eqn (4.12) must vanish. As a result $S(r)$ takes the form

$$S(r) = C_1 F_0\big(-\eta, \frac{\sqrt{a}r^2}{2}\big), \tag{4.17}$$

and the homogeneous part of the solution is given by

$$\Psi_h(r,z) = Ce^{-kz}F_0\big(-\eta, \frac{\sqrt{a}r^2}{2}\big). \tag{4.18}$$

A similar but a different solution, which is oscillatory in z is used for laboratory plasma for both a D-shaped plasma and toroidally diverted plasma (Atanasiu *et al.* 2004). The general solution of eqn (4.7) is given by the sum of the homogeneous part $\Psi_h(r,z)$ given above and an inhomogeneous part $\Psi_p(r)$ which is presented in Sen and Mangalam (2019). We have found that the presence of $\Psi_p(r)$ term in the poloidal flux function $\Psi(r,z)$, implies that p and I_p^2 cannot be simultaneously positive for any combination of b and β in the physical parameter domain space for all r and z. For avoiding these unphysical effects we present the case of $\Psi = \Psi_h$ and an exploration of the general solution $\Psi = \Psi_h + \Psi_p$ will be studied later. Since $\Psi(r,z)$ and its complex conjugate function, $\Psi^*(r,z)$ are the valid solutions of eqn (4.7), we construct a solution of eqn (4.7) by redefining $\dfrac{\Psi(r,z) + \Psi^*(r,z)}{2} \rightarrow \Psi(r,z) \equiv \varsigma(r)Z(z)$.

4.3 Boundary conditions and the reduced form of p and I_p

The ideal magnetic fluxtube is embedded in a magnetic field free region with no current outside the fluxtube boundary. We make the following standard assumptions $B_r(r = R, z) = 0$ and $B_\phi(r = R, z) = 0$ to ensure that there is no net current I_p at the fluxtube boundary. The pressure at the photosphere ($z = 0$) outside the fluxtube is $p_0 = 1.228 \times 10^5$ dyne cm^{-2} and at the transition region ($z_{tr} = 2.15$ Mm) is $p_{tr} = 0.1058$ dyne cm^{-2} and is taken from Avrett-Loeser model (Avrett

and Loeser 2008). We summarize the boundary conditions below

$$B_r(R, z) = 0 \tag{4.19a}$$

$$B_\phi(R, z) = 0 \tag{4.19b}$$

$$p(R, 0) = p_0 \tag{4.19c}$$

$$p_t(R, z_{tr}) = p_{tr} \tag{4.19d}$$

Assuming that pressure decreases exponentially from photosphere to transition region, we use the following expression for the external pressure

$$p_{ex}(z) = p_0 \exp(-2kz), \tag{4.20}$$

where $k = \dfrac{1}{2 \times 2.15} \ln\left(\dfrac{p_0}{p_{tr}}\right)$ $\text{Mm}^{-1} = 3.248$ Mm^{-1}. Matching the pressure scale heights, we see that $p_2(z)$ eqn (4.6a) also decreases exponentially with z as

$$p_2(z) = p_{20} \exp(-2kz), \tag{4.21}$$

where p_{20} will need to be calculated. Taking $\Psi(r, z) = \Psi_h(r, z)$, the reduced forms of p and I_p^2 are given by

$$p(\Psi, z) = \frac{a}{8\pi}\Psi^2 + p_2(z) \quad (a > 0) \tag{4.22}$$

and

$$I_p^2(\Psi) = \alpha\Psi^2 \quad (\alpha > 0). \tag{4.23}$$

Taking the radial component of the MHS force balance equation (4.1) and adding the contribution of the radial force due to the presence of sheet current j_ϕ at the

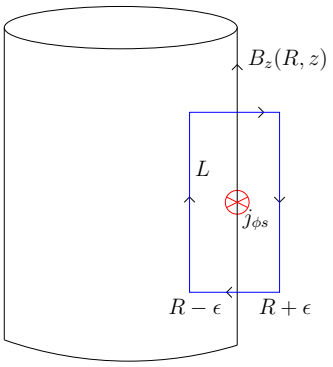

FIGURE 4.1: Fluxtube geometry at the boundary showing the sheet current.

boundary we write the force balance equation

$$-\frac{\partial p}{\partial r}\bigg|_{r=R}+\frac{1}{4\pi}\left(B_r\frac{\partial B_r}{\partial r}+B_z\frac{\partial B_r}{\partial z}\right)\bigg|_{r=R}-\frac{\partial}{\partial r}\left(\frac{B^2}{8\pi}\right)\bigg|_{r=R}+j_\phi(r)B_z(r)\bigg|_{r=R}=0. \tag{4.24}$$

Now the sheet current j_ϕ can be expressed as a delta function $j_\phi(r)=j_{\phi s}\delta(r-R)$ which is non zero only at the boundary. Integrating eqn (4.24) w.r.t. r from $r=R-\epsilon$ to $r=R+\epsilon$ where ϵ is an infinitesimal positive quantity we obtain

$$\begin{aligned}-\int_{R-\epsilon}^{R+\epsilon}\frac{\partial p}{\partial r}dr+\frac{1}{4\pi}\left(\int_{R-\epsilon}^{R+\epsilon}B_r\frac{\partial B_r}{\partial r}dr+\int_{R-\epsilon}^{R+\epsilon}B_z\frac{\partial B_r}{\partial z}dr\right)\\-\int_{R-\epsilon}^{R+\epsilon}\frac{\partial}{\partial r}\left(\frac{B^2}{8\pi}\right)dr+\int_{R-\epsilon}^{R+\epsilon}j_\phi(r)B_z(r)\mathrm{d}r=0,\end{aligned} \tag{4.25}$$

which leads to the MHS force balance at the boundary to be given by

$$p_{in}-p_{ex}+j_{\phi s}B_z(R)+\frac{1}{4\pi}\left[B_r\frac{\partial B_r}{\partial r}+B_z\frac{\partial B_r}{\partial z}\right]_R+\frac{B_i^2-B_e^2}{8\pi}=0, \tag{4.26}$$

where $[...]_R$ denotes the jump condition at the boundary and B_i and B_e are the magnetic fields inside and outside the fluxtube boundary. This is an improved boundary pressure condition for a magnetic fluxtube, as previous studies have ignored the sheet current. Now to calculate $j_{\phi s}$, we assume an infinitesimal current

loop at the boundary which has a vertical height of length L and radial extent from $R-\epsilon$ to $R+\epsilon$. Using Stokes line integral theorem along the closed loop (see Fig.4.1), we see that

$$B_z L = 4\pi L \int_{R-\epsilon}^{R+\epsilon} j_{\phi s}\delta(r-R)\mathrm{d}r, \tag{4.27}$$

which implies $j_{\phi s} = \dfrac{B_z}{4\pi}$. Since $B_r(R) = B_\phi(R) = B_e(R) = 0$ for any height z and $p_{in}(R,z) = p_2(z)$, from eqn (4.26), the total pressure at the boundary inside the fluxtube is $p_2(z) + \dfrac{3B_z^2(R)}{8\pi}$ and matching the pressures gives

$$p_2(z) = p_{ex}(z) - \frac{3B_z^2(R,z)}{8\pi}. \tag{4.28}$$

The mass density inside the fluxtube obtained from eqn (4.3b) is

$$\rho(z) = -\frac{1}{g}\frac{\mathrm{d}p_2(z)}{\mathrm{d}z}, \tag{4.29}$$

and the density inside the fluxtube varies only with z and at the transition region ($z_{tr} = 2.15$ Mm), which should match with the external density which is typically $\rho_{tr} = 2.77 \times 10^{-14}$ g cm^{-3} (Avrett and Loeser 2008). From eqn (4.28) and eqn (4.20) we see that

$$p_{20} = \frac{g}{2k} e^{2kz_{tr}} \rho_{tr}. \tag{4.30}$$

In our model g is assumed not to vary much from photosphere to the transition region and its value is taken to be $g = 274$ m s^{-2}, the value at the solar surface and that determines $p_{20} = 1.36 \times 10^4$ dyne cm^{-2}. Using the forms of $B_z(r,z)$ from eqn (4.2, 4.18) we obtain $B_z(0,0) = 4\sqrt{a}C \equiv B_{z0}$, and the relation between C, B_{z0} and a is derived in the following.

The real component of Ψ is given by,

$$\mathrm{Re}(\Psi) = \frac{\Psi + \Psi*}{2}$$

and by using eqn (4.13) and eqn (4.18) we can express the flux function in the form of Whittaker–M functions as

$$\Psi(r,z) = Ce^{-kz}\Big[M_{-i\eta,1/2}(i\sqrt{a}r^2) + M_{i\eta,1/2}(-i\sqrt{a}r^2)\Big]. \tag{4.31}$$

Whittaker–M function can be expressed in terms of hypergeometric function by the standard relation (Dixit and Moll 2015)

$$M_{t,m}(z) = e^{-z/2}z^{m+1/2}F_1^1(1/2+m-t, 1+2m, z). \tag{4.32}$$

Here F_1^1 represents the hypergeometric functions with the parameters t, m and argument z. Therefore eqn (4.31) takes the form

$$\Psi(r,z) = Ce^{-kz}\sqrt{a}r^2\Big[e^{-i\sqrt{a}r^2/2}F_1^1(1+i\eta, 2, i\sqrt{a}r^2) + e^{i\sqrt{a}r^2/2}F_1^1(1-i\eta, 2, -i\sqrt{a}r^2)\Big]. \tag{4.33}$$

It follows from eqn (4.2) that B_z takes the form

$$B_z(r,z) = \frac{\sqrt{a}C}{2}e^{-kz}e^{-i\sqrt{a}r^2/2}\Big[(8+4i\sqrt{a}r^2)F_1^1\left(\frac{4\sqrt{a}+i(k^2+\alpha)}{4\sqrt{a}}, 2, i\sqrt{a}r^2\right) - \tag{4.34}$$
$$r^2(4i\sqrt{a}+k^2+\alpha)F_1^1\left(\frac{4\sqrt{a}+i(k^2+\alpha)}{4\sqrt{a}}, 3, i\sqrt{a}r^2\right)\Big].$$

So, $B_z(r,z)$ at $r = z = 0$ is by definition B_{z0} takes the form from eqn (4.34) as,

$$B_{z0} = 4\sqrt{a}CF_1^1\left(\frac{4\sqrt{a}+i(k^2+\alpha)}{4\sqrt{a}}, 2, 0\right). \tag{4.35}$$

But $F_1^1\left(\frac{4\sqrt{a}+i(k^2+\alpha)}{4\sqrt{a}}, 2, 0\right) = 1$ is an identity and therefore we finally have

$$C = \frac{B_{z0}}{4\sqrt{a}}. \tag{4.36}$$

We define a physical observable B_0 which is the average magnetic field strength at the base within the fluxtube as

$$B_0 = \frac{1}{R}\int_0^R \sqrt{B_r^2(r,0) + B_z^2(r,0) + B_\phi^2(r,0)}\mathrm{d}r \tag{4.37}$$

where R is the radius of the fluxtube. Therefore we have two free parameters R and B_0 that we can tune to fit our model with the observations. At $z = 0$, from eqn (4.28), we get

$$\frac{3B_z^2(R,0)}{8\pi} = p_0 - p_{20}. \tag{4.38}$$

Therefore, from eqns (4.19a, 4.19b, 4.19c) we determine a, α and C in terms of the free parameters R and B_0 and hence the thermodynamic quantities within fluxtube. The temperature within the fluxtube is calculated by the ideal gas law according to the following form

$$T(r,z) = \frac{\bar{\mu}p(r,z)}{\rho(z)R_g}, \tag{4.39}$$

where $R_g = 8.314$ J mol^{-1} K^{-1} is the universal gas constant and

$$\bar{\mu} = \frac{1}{z_{max}}\int_0^{z_{max}} \mu_{eff}(z)\mathrm{d}z = 1.116,$$

is the average value of the mean effective molar mass from photosphere to transition region given by an empirical formula $\mu_{eff}(z) = 1.288\big[1 - 0.535\big(\frac{z}{2.152}\big)^3\big]$ (Solov'ev and Kirichek 2015) in the domain of $0 < z < 2.152$ Mm. A formulary of the different quantities are listed in Table 4.1.

Functions	r–part	z–part
$\Psi(r,z)$	$\varsigma(r)$	$Z(z)$
$B_r(r,z)$	$\frac{3.248\times10^{-8}}{r}\varsigma(r)$	$Z(z)$
$B_\phi(r,z)$	$\sqrt{\alpha}\frac{\varsigma(r)}{r}$	$Z(z)$
$B_z(r,z)$	$\frac{\varsigma'(r)}{r}$	$Z(z)$
$p(r,z)$	$\frac{a}{8\pi}\varsigma^2(r)+p_{20}$	$Z^2(z)$
$\rho(r,z)$	1	$(3.22\times10^{-8})Z^2(z)$
$T(r,z)$	$0.0416\big(\frac{a}{8\pi}\varsigma^2(r)+p_{20}\big)$	1

TABLE 4.1: A formulary of the derived functions obtained from the solution of GSE. Here, $\varsigma(r) = C\big[F_0\big(-\eta,\frac{\sqrt{a}r^2}{2}\big)+F_0^*\big(-\eta,\frac{\sqrt{a}r^2}{2}\big)\big]$ and $Z(z)=e^{-kz}$. The value of the constants are $\bar{\mu}=1.116$, $g=2.74\times10^4$ cm s^{-2}, $k=3.248\times10^{-8}$ cm^{-1}, $p_{20}=1.36\times10^4$ dyne cm^{-2}. All the quantities in the table are in cgs units.

4.4 Mode analysis of different profile functions

The quantities a,α and C are functions of the free parameters R, B_0 and the mode number n whose values are given in Table 4.2 for a sample set of the free parameters. The solutions to Ψ, B, p and T are shown for different mode numbers,

R (km)	B_0 (kG)	mode no.	C (10^{17} Mx)	α (10^{-14} cm^{-2})	a (10^{-28} cm^{-4})
100	1	1	0.335061	7.50448	20.0417
100	1	2	0.144828	15.6546	107.27
100	1	3	0.0915463	24.0161	268.473

TABLE 4.2: Values of the quantities a,α and C for $R=100$ km and $B_0=1$ kG for three different modes.

in Figs. 4.2–4.5 respectively.

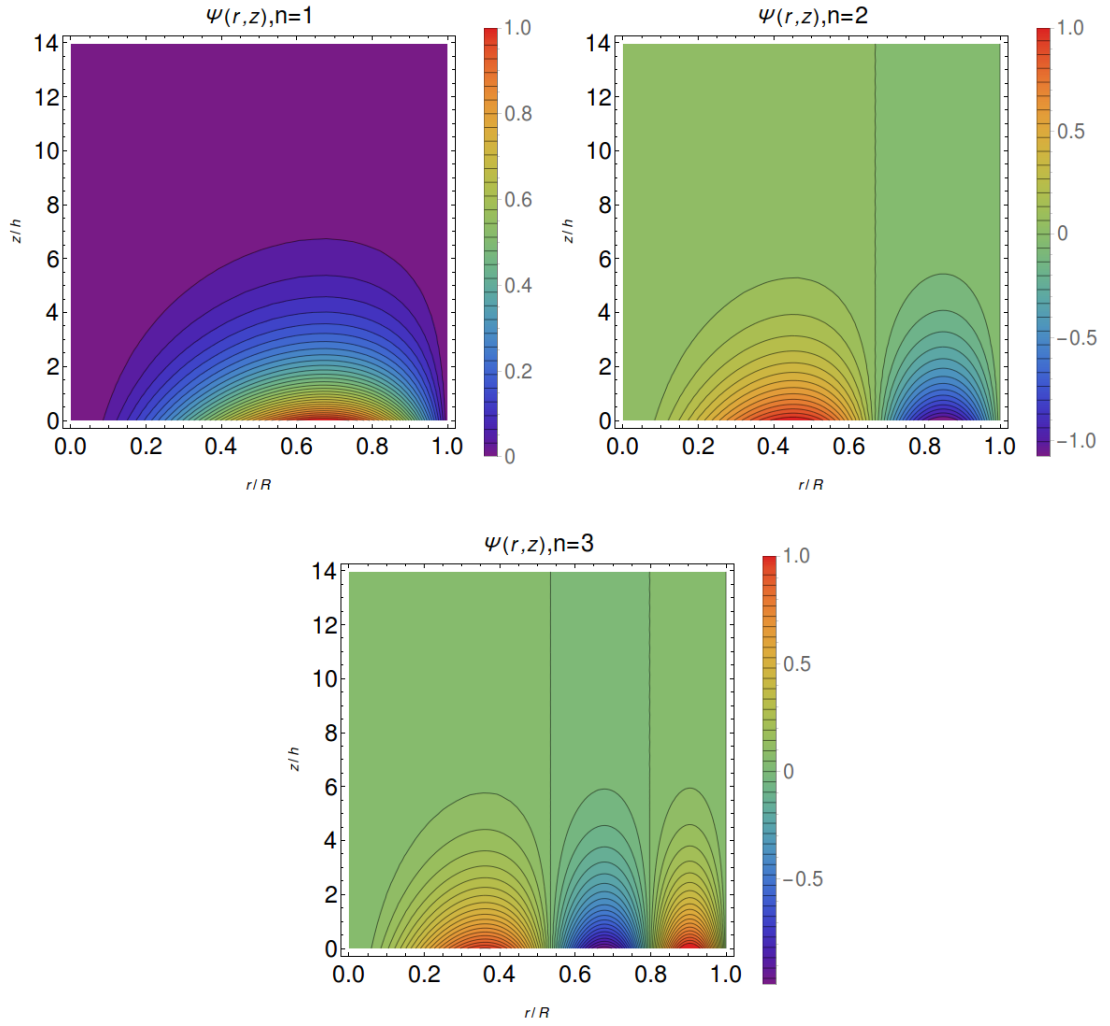

FIGURE 4.2: The vertical cross–sections of normalized poloidal flux function for three different modes n for $R = 100$ km and $B_0 = 1$ kG are shown. The contours represent the magnetic lines of force in the $r - z$ plane. The amplitude of the flux function, normalized to the peak value, is represented by a colour bar. The horizontal axis is scaled to the radius of the fluxtube R and the vertical axis is scaled with the pressure scale height, $h = 162$ km.

All the profile functions are normalized to their peak values and the radial distance to the total radius of the fluxtube R. As per the boundary conditions, the flux function, Ψ vanishes both at the axis and at the boundary of the fluxtube, where the total gas pressure is $p_2(z)$. The solutions of higher modes have, the profile functions with higher frequency along the radial direction and realistically we may not have such reversible fields, as they are unstable. Therefore, we use the fundamental mode ($n = 1$) for further analysis. The 3D topology of the magnetic

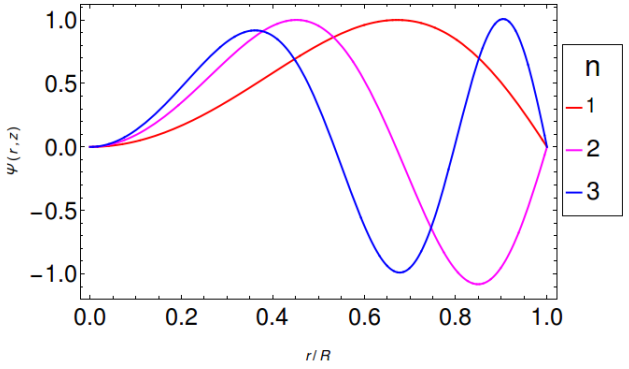

FIGURE 4.3: The radial variations of the normalized poloidal flux function for three different modes for $R = 100$ km and $B_0 = 1$ kG are shown.

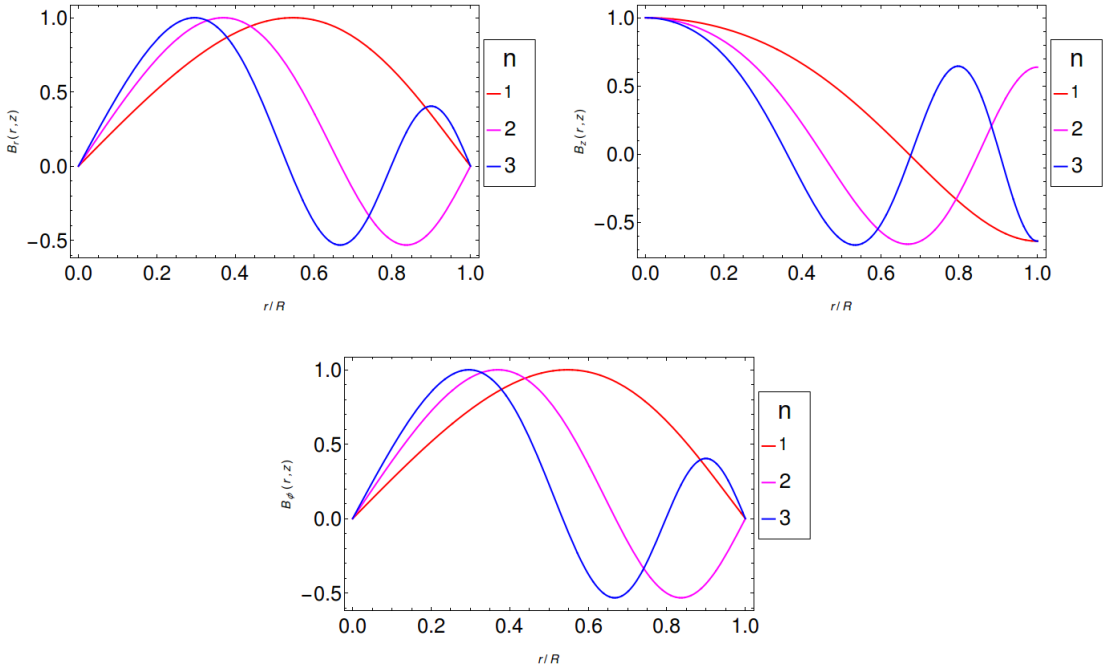

FIGURE 4.4: The radial variations of the normalized B_r, B_ϕ and B_z fields for different modes for $R = 100$ km and $B_0 = 1$ kG are shown.

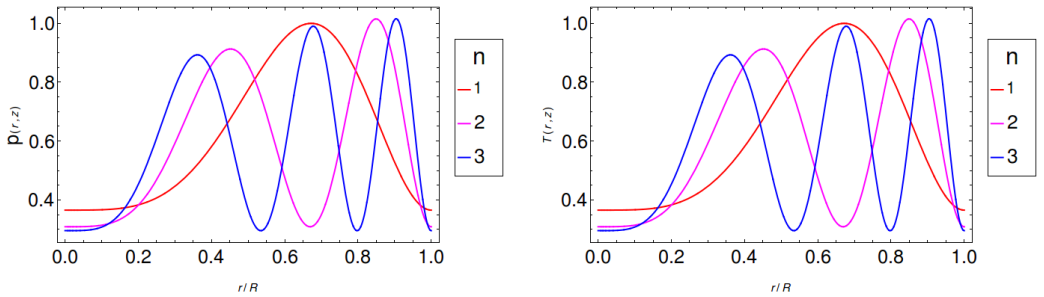

FIGURE 4.5: *Left:* The radial variations of normalized gas pressure within the fluxtube are shown for three different modes n, *Right:* The radial variations of normalized temperature profile inside the fluxtube are shown for three different modes n. Both the plots are for $R = 100$ km and $B_0 = 1$ kG.

field lines inside the fluxtube for the fundamental mode is shown in Fig. 4.9.

4.5 Comparing the model with observations

Now we compare our model with the observations reported from high resolution and high cadence instruments. Small scale magnetic structures, *i.e.*, MBPs, are the best candidates for comparison because such structures can be assumed to consist of fluxtubes. MBPs are seen in G-band filtergrams or are identified by making spectro-polarimetric measurements (Utz *et al.* 2009, 2013; Yang *et al.* 2016). The radial variation of the profile functions p, ρ and T and the magnetic components B_r, B_ϕ and B_z are independent of z, but the amplitude decreases exponentially with z except for T. In the following, we validate the model by comparing the observed magnetic field strengths and radius of MBPs with those calculated in our model and estimate the magnetic field strength and thermodynamic quantities at the transition region which may be verified by future observations.

The MBPs number distribution, magnetic field strength, and size distribution have been reported by Utz *et al.* (2009, 2013) at the photosphere. The size distribution of MBPs peaks around 200 km and 160 km for low and high spatial sampling rates,

respectively (Utz *et al.* 2009). The magnetic field strength distribution is bimodal with two peaks at $\sim$ 1400 G and $\sim$ 200 G (Utz *et al.* 2013). Since MBPs are observed as the region of unipolar flux concentrations, we construct a cylindrical boundary inside the simulation domain where the vertical magnetic field B_z is positive. We call this cut–off radius as r_0, where the line of sight magnetic field B_z vanishes. The value of B_z after this grid line becomes negative. In Fig. 4.6, the vertical grid line denotes the boundary radius r_0. We study two different cases for $r_0 = 80$ and 100 km which corresponds to the peak values for the MBP size distribution, for which R is found to be 127 and 159 km respectively. For both cases, we calculate B_0 and the mean value of B_z, $\bar{B_z}$ in the radial direction up to r_0 and find that for realistic values of the thermodynamic quantities inside the fluxtube, the upper limit of the vertical magnetic field strength B_{z0} is 2.37 kG. Beyond this value of B_{z0}, the viable solutions will shift to the higher modes. The temperature inside the fluxtube increases as the value of B_{z0} decreases and temperature inside the fluxtube becomes greater than the typical photospheric temperature when $B_{z0} < 2.31$ kG. Thus it can be considered as the lower cut off limit of the magnetic field strength. The $\bar{B_z}$ value is only sensitive to B_{z0} but not on r_0, and the thermodynamic quantities inside the fluxtube remain the same for both $r_0 = 80$ and 100 km. We found $\bar{B_z} = 1.42$ and 1.4 kG for $B_{z0} = 2.37$ and 2.31 kG respectively. The radial and vertical variations of the vertical magnetic field strength, gas pressure, density and temperature inside the fluxtube are shown in Figs. 4.7 and 4.8. We see that the vertical magnetic field strength decreases from 2.37 kG (on the axis at $z = 0$) to zero at the MBP boundary (r_0, see Fig. 4.6). The variation of gas pressure and temperature from axis to the MBP boundary is very small; at the photosphere, the gas pressure changes 1.358×10^4 (on the axis at $z = 0$) to 1.373×10^4 dyne cm^{-2} (at MBP boundary) and it decreases with z to 3.12×10^{-2} dyne cm^{-2} (at MBP boundary) at the transition region ($z = 2$ Mm). The temperature changes from 5656 K (on the axis) to 5718 K (at MBP boundary) which is small compared to the outside photosphere temperature (6583 K) (Avrett and Loeser 2008). The average temperature inside fluxtube has been

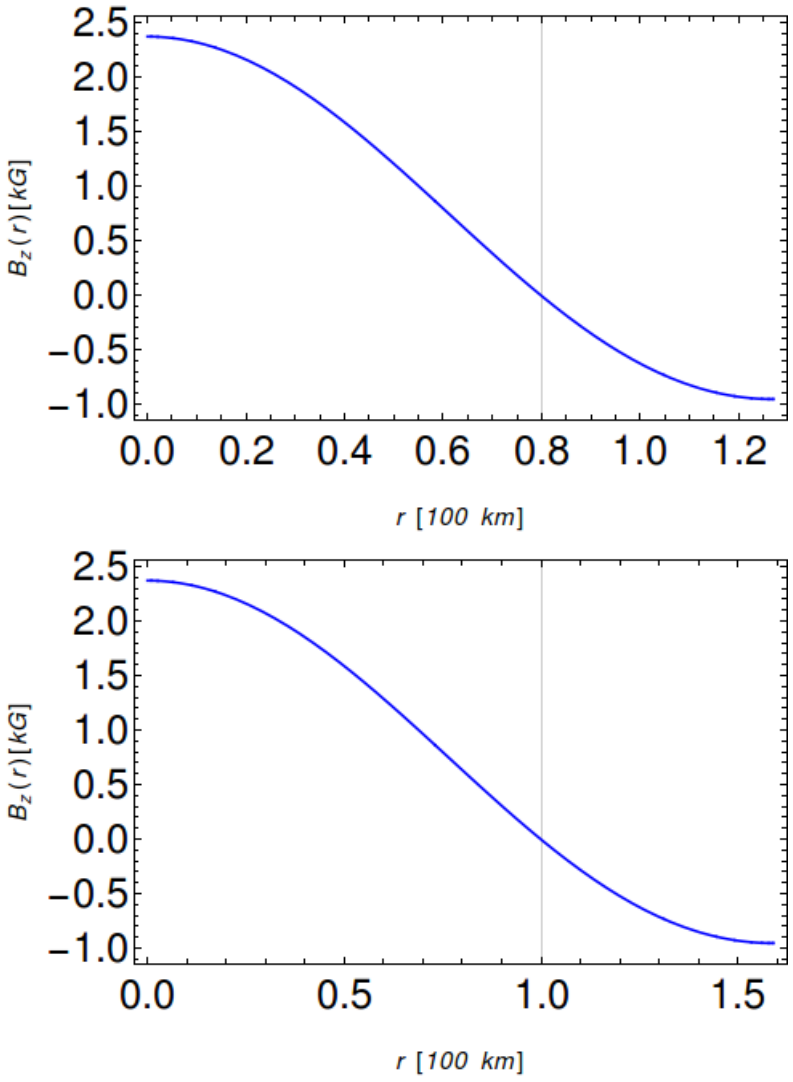

FIGURE 4.6: The radial variations of the magnetic field strength at the photosphere ($z = 0$) within the fluxtube for $R = 127$ km (top) and 159 km (bottom) are shown. The vertical grid line denotes the radius (r_0) beyond which B_z becomes negative. The values of r_0 are 80 km and 100 km for the top and bottom panels respectively. The horizontal axes are scaled in units of 100 km and the vertical axes are scaled in units of kG for both top and bottom panels. The mean value of B_z up to r_0 is 1.42 kG in both panels.

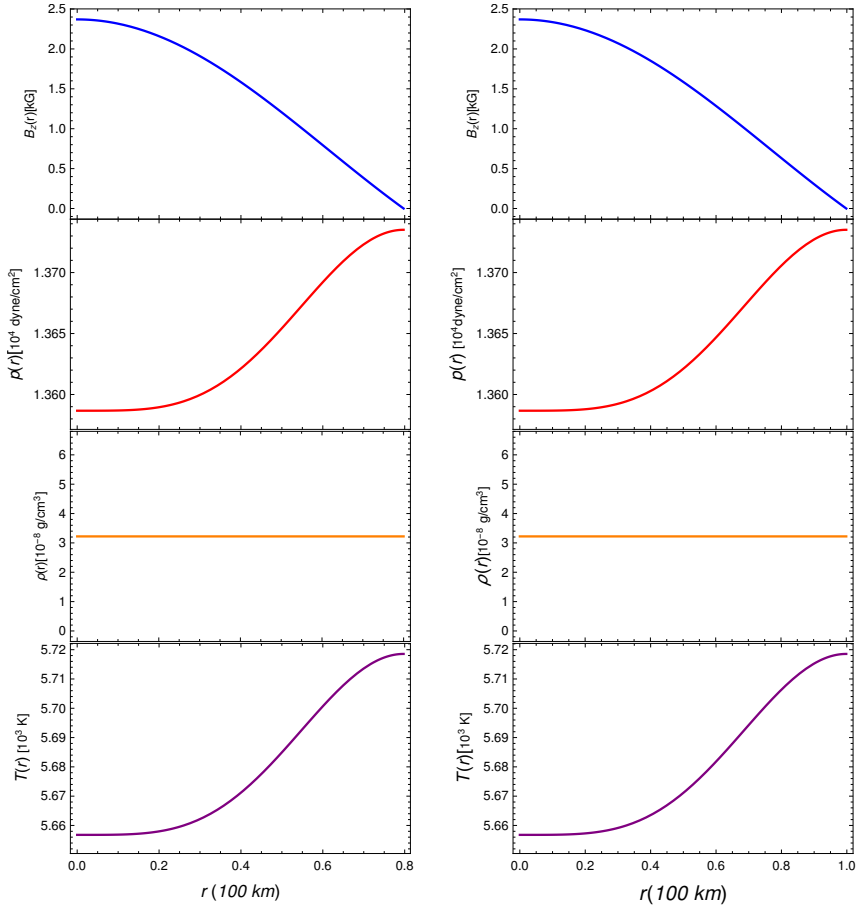

FIGURE 4.7: From top to bottom: Predicted radial variation of vertical magnetic field strength, gas pressure, density and temperature from the axis to the boundary of the fluxtube for two different sizes of MBPs (80 km radius in the left panel and 100 km radius in the right panel). The horizontal axis is scaled in units of 100 km and the vertical axes of B_z, p, ρ, T are scaled in units of kG, 10^4 dyne cm^{-2}, 10^{-8} g cm^{-3} and 10^3 K respectively.

calculated by integrating the temperature from axis to the MBP boundary and is found to be 5679 K. The density distribution is constant along the radius of the fluxtube at a given height which decreases with height from 3.22×10^{-8} g cm^{-3} at the photosphere to 7.33×10^{-14} g cm^{-3} at the transition region. The values of the quantities estimated from our model are summarized in Table 4.3.

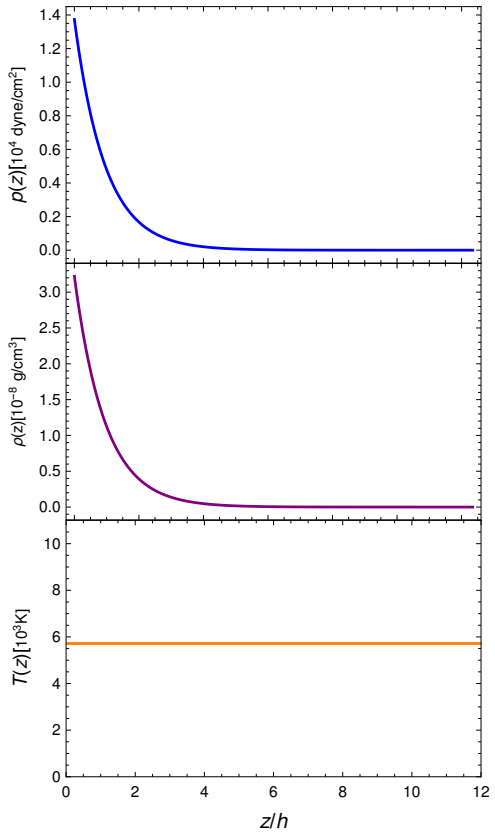

FIGURE 4.8: The figure shows the variation of gas pressure, density and temperature at the BP boundary along z. The horizontal axis represents the height from the photosphere scaled with the pressure scale height $h = 162$ km, and the vertical axes represents pressure, density and temperature from top to bottom respectively.

4.6 Conclusions and discussion

In this work, we constructed a single fluxtube with the twisted magnetic field by solving GSE analytically. We summarize our results below:

1. We have an improved boundary condition by incorporating the sheet current as compared to the previous studies e.g. Solov'ev and Kirichek (2016).

2. Our model depends on the form of the external pressure distribution which is assumed as an exponentially decreasing function with z. Future observations

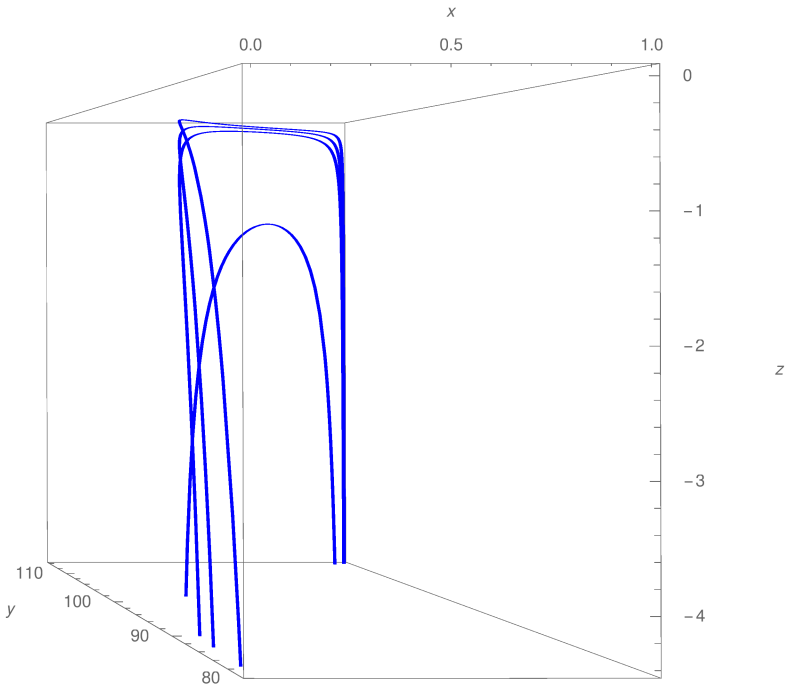

FIGURE 4.9: The figure shows the 3D topology of the magnetic field lines inside the fluxtube. The scales are in arbitrary units.

r	z (Mm)	B_z (G)	p (dyne cm^{-2})	ρ (g cm^{-3})	T (K)
0	0	2370	1.358×10^{4}	3.22×10^{-8}	5656
0	2	2.19	3.09×10^{-2}	7.33×10^{-14}	5656
r_0	0	0	1.373×10^{4}	3.22×10^{-8}	5718
r_0	2	0	3.12×10^{-2}	7.33×10^{-14}	5718

TABLE 4.3: Table of the results obtained from our model for $r_0 = 80$ and 100 km

leading to a more accurate form of pressure distribution from the photosphere to the transition region can be used to improve our model. The plasma β parameter inside the fluxtube remains constant with z but it varies along r; $\beta < 1$ is obeyed from the chromosphere to the transition region but not in the photosphere and lower atmosphere. Therefore the magnetic effects will dominate the gas dynamics throughout the simulation domain.

3. In our model, the temperature varies along the radial direction, but it is constant along the vertical direction z. In other models e.g. Gent *et al.* (2013) the temperature rises with the height from the photosphere to the transition region and in Vigeesh *et al.* (2011) the temperature decreases from 6300 K at the surface to 4000 K (at $z = 600$ km) and then it remains the same up to 1200 km.

4. The effects of shock wave dissipation and magnetic reconnection start to dominate in the corona which causes the coronal heating. We have not considered these mechanisms in our model and therefore, we have not modeled the region in the corona or higher and have restricted our simulation domain to end at the transition region.

5. Recently Hewitt *et al.* (2014); Uitenbroek and Criscuoli (2013); Riethmüller and Solanki (2016), have simulated bright points using MuRAM and Copenhagen-Stagger code. We find that the magnitude of magnetic field strengths, pressure, and densities reported in these studies are in fair agreement with our predictions but the temperature distribution along z is in variance with the results of the numerical simulations.

Chapter 5

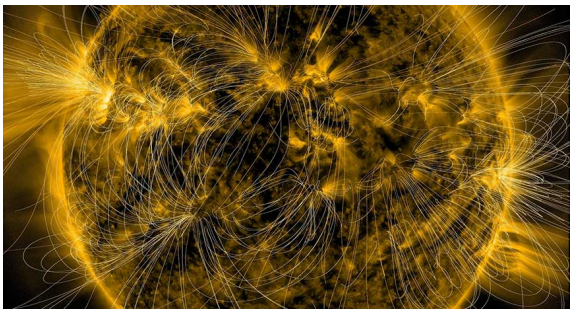

Image source: www.greatlakesledger.com

Open and closed magnetic configurations of twisted fluxtubes

5.1 Introduction

The small scale magnetic structure in the solar photosphere plays an important role in several phenomena like the evolution of active regions (Muller and Mena 1987; Aschwanden *et al.* 2000; Centeno *et al.* 2007), heating of corona through the

The work presented in this chapter is the part of the following papers:
(i) Sen and Mangalam (2018b)
(ii) Sen and Mangalam (2019)
(iii) Sen and Mangalam (in preparation)

dissipation of waves (Ruzmaikin and Berger 1998; Srivastava *et al.* 2017) and reconnection between fluxtubes (van Ballegooijen 1986; Muller *et al.* 1994). Magnetic fluxtubes span from the photosphere to the higher atmosphere and are observed in the form of small scale magnetic structures. The topological rearrangement of these fluxtubes due to the motion of the photospheric footpoints gives rise to the magnetic reconnection leading to the energy release in the solar corona (Parker 1988; Peter *et al.* 2005; Thalmann *et al.* 2013). Therefore, the modeling of the proverbial fluxtube is one of the key aspects to understand various phenomena on the solar surface and its outer atmosphere.

Several attempts have been made earlier to construct the model of fluxtubes for both twisted and untwisted magnetic fields. Schlüter and Temesváry (1958) studied a two dimensional (2D) axisymmetric fluxtube model without twist for sunspots using self–similar structure, where a self-similar parameter was defined as a combination of r and z, and the relative vertical magnetic field strength at any arbitrary point with respect to the magnetic field strength at the axis is scaled with a Gaussian profile function of the self-similar parameter. This model is valid for open field lines where the magnetic lines of force rise from a horizontal plane and do not return in the model domain. Yun (1971) implemented a twist in the self–similar structure to model the sunspots. In this model, an empirical form of the azimuthal magnetic field strength $B_\phi(r, z)$ was taken from the data obtained from observations (Stepanov 1965). By solving for the variation of the pitch angle and gradient of the pitch angle, the thermodynamic quantities with the depth were calculated. Motivated by the model and the self–similar structure proposed by Schlüter and Temesváry (1958), Osherovitch (1982) assumed a quadratic form of the flux function for the gas pressure to model a closed field fluxtube, where the magnetic lines of force rise and return to the same horizontal plane.
Steiner *et al.* (1986) have numerically studied a 2D model of open single fluxtube with a twist using the standard boundary conditions including sheet current to

study the magnetic field line structure within and outside the fluxtube. The magnetic and thermodynamic structure for both single and multiple fluxtubes which span from the photosphere to corona have been studied for the case of untwisted magnetic field (Gent *et al.* 2013, 2014), where an empirical form of the magnetic field components is motivated by a self-similar construction. A numerical model of fluxtubes has been studied by Murawski *et al.* (2015b), where an empirical form of magnetic flux function has been assumed; this was followed by a model to study the propagation of the MHD waves through the fluxtubes with an azimuthal velocity perturbation. The steady structure of the 2D fluxtube was used as a background initial condition to study the propagation of the MHD waves. For example, Vigeesh *et al.* (2009) assumed an empirical form of gas pressure for investigating the wave propagation and energy transport through the fluxtube. Other interesting results of wave behavior in the solar atmosphere have been presented by several authors. Fedun *et al.* (2009) have studied the propagation of the acoustic wave through the solar atmosphere due to the periodic drivers at the photosphere, and Shelyag *et al.* (2010) have modeled the wave propagation through the photospheric magnetic bright points (MBPs).

In this work, we have constructed two different models of fluxtubes with twisted magnetic field for open and closed field lines by solving Grad–Shafranov equation (GSE) (Grad and Rubin 1958; Shafranov 1958). Here, we have assumed a quadratic form of the flux function for the gas pressure and poloidal current which has been used to study the equilibrium solution of terrestrial plasma (Atanasiu *et al.* 2004), and we extend it to solar fluxtubes. As the MHD waves follow the magnetic field lines, it is important to model fluxtubes with open field lines, so that MHD waves propagate through the fluxtube and dissipate in the upper atmosphere, which is a key aspect of the coronal heating. A key aspect of this work is to show that the closed field model, reported in Sen and Mangalam (2018a) (SM18 hereafter), is a special case of the open field model with a twisted field line. The fluxtube we build is axisymmetric in structure and spans vertically upward from the photosphere to the transition region. In the case of a linear form of the flux

function for the gas pressure and poloidal current, an equilibrium solution near the magnetic axis of a plasma torus has been reported by Solov'ev (1968). SM18 have studied the homogeneous solution of GSE which is a special case of the general solution of the quadratic case to model a fluxtube with closed field lines with a twist. Here, we present the full solution of the GSE including both homogeneous and the particular parts to model a twisted open field fluxtube. The other model we have built is a self–similar magnetic structure with a twist, with a generalized Gaussian (or power law) incorporated into the magnetic shape functions; the gas pressure and poloidal current are taken to be quadratic functions of the flux function. The self–similar fluxtube model expands with height which spans from the photosphere to transition region. After building the solutions semi–analytically and applying appropriate boundary conditions (BCs), we calculate the magnetic field structure and thermodynamic quantities inside the fluxtube. As magnetic bright points (MBPs) observed in the photosphere (Muller and Mena 1987; Centeno *et al.* 2007; Lagg *et al.* 2010; Shelyag *et al.* 2010) are likely to be fluxtubes, we compare our model with the existing observations and simulations of MBPs.

The work is organized as follows. In §5.2, we apply the GSE to the cylindrical fluxtube case and describe the common BCs which are physically realistic and used in modeling of our fluxtubes. In §5.3, we present the Coulomb function model for open and closed fields, the appropriate BCs, and show how the open field Coulomb model generalizes the Coulomb field closed model. The solution of the self-similar model and the appropriate BCs are presented in §5.4. In §5.5, the results of our simulations and the variation of the magnetic and thermodynamic profile functions are presented for Coulomb function and self-similar models, and in §5.6, the results obtained from the models are applied to the existing observations of MBPs and the simulations for other solar fluxtubes. In §5.7, we have compared between the Coulomb function and self-similar models and find the regime of the validity; we have also discussed the advancement made and how the models for open and closed field fluxtubes are useful for building realistic structures. Finally, in §5.8,

we summarize and highlight the major points of the work and conclude how the work may be useful for future numerical studies.

5.2 Grad–Shafranov equation for the cylindrical fluxtube

In a magnetic medium of field strength $\mathbf{B}$, with gas (or plasma) pressure p and mass density ρ, the magnetohydrostatic (MHS) pressure balance equation is given by

$$-\nabla p + \frac{1}{4\pi}(\nabla \times \mathbf{B}) \times \mathbf{B} + \rho \mathbf{g} = 0, \tag{5.1}$$

where $\mathbf{g}$ denotes the acceleration due to gravity at the solar surface. The individual components of $\mathbf{B}$ can be expressed in terms of the poloidal flux function, $\Psi(r,z) = \int_0^r r' B_z(r',z)\mathrm{d}r'$, in the following way

$$B_r = -\frac{1}{r}\frac{\partial \Psi}{\partial z}; \quad B_z = \frac{1}{r}\frac{\partial \Psi}{\partial r}; \quad B_\phi = \frac{I_p}{r}, \tag{5.2}$$

where I_p represents the poloidal current. These forms of B_r, B_ϕ and B_z automatically ensure the solenoidal condition for $\mathbf{B}$. Using the axisymmetric condition we split the MHS equilibrium eqn (5.1) into r and z direction and plug in the forms of magnetic field components from eqn (5.2), to find two scalar partial differential equations

$$\frac{\partial \Psi}{\partial r}\frac{\partial^2 \Psi}{\partial z^2} + \frac{\partial \Psi}{\partial r}\frac{\partial^2 \Psi}{\partial r^2} - \frac{1}{r}\left(\frac{\partial \Psi}{\partial r}\right)^2 + \frac{1}{2}\frac{\partial I_p^2}{\partial r} = -4\pi r^2 \frac{\partial p}{\partial r} \tag{5.3a}$$

$$-\frac{\partial p}{\partial z} + \frac{1}{4\pi}\left[\frac{1}{r}\frac{\partial \Psi}{\partial z}\left(\frac{1}{r^2}\frac{\partial \Psi}{\partial r} - \frac{1}{r}\frac{\partial^2 \Psi}{\partial r^2}\right) - \frac{1}{r^2}\frac{\partial \Psi}{\partial z}\frac{\partial^2 \Psi}{\partial z^2} - \frac{1}{2r^2}\frac{\partial I_p^2}{\partial z}\right] - \rho g = 0, \tag{5.3b}$$

where we assume the form of the gas pressure to be

$$p(r,z) = p_1(\Psi) + p_2(z); \tag{5.4}$$

this form is required in order to have a non-zero density (see SM18). The ϕ part of eqn (5.1) gives $\nabla\Psi \times \nabla I_p = 0$, which implies $I_p = I_p(\Psi)$. We have the following form from eqns (5.3a, 5.4) for the GSE to be given by

$$\frac{\partial^2\Psi}{\partial r^2} - \frac{1}{r}\frac{\partial\Psi}{\partial r} + \frac{\partial^2\Psi}{\partial z^2} = -\frac{1}{2}\frac{\partial I_p^2(\Psi)}{\partial\Psi} - 4\pi r^2\frac{\partial p_1(\Psi)}{\partial\Psi}. \tag{5.5}$$

From eqns (5.3b, 5.4) we find

$$-\frac{\partial p_2}{\partial z} - \frac{\partial p_1(\Psi)}{\partial z} + \frac{1}{4\pi}\left[\frac{1}{r^2}\frac{\partial\Psi}{\partial z}\left(\frac{1}{r}\frac{\partial\Psi}{\partial r} - \frac{\partial^2\Psi}{\partial r^2}\right) - \frac{1}{r^2}\frac{\partial\Psi}{\partial z}\frac{\partial^2\Psi}{\partial z^2} - \frac{1}{2r^2}\frac{\partial I_p^2(\Psi)}{\partial z}\right] = \rho g. \tag{5.6}$$

Following SM18, by multiplying $4\pi r^2\dfrac{\partial z}{\partial\Psi}$ on both sides of eqn (5.6) and using eqn (5.5), we obtain

$$\rho(z) = -\frac{1}{g}\frac{\mathrm{d}p_2(z)}{\mathrm{d}z}. \tag{5.7}$$

We will see later that the prescription of $p_2(z)$ will lead ρ to be a positive quantity, and hence the density within the fluxtube is independent of the radial distance r but varies with height z. The temperature, T, inside the fluxtube is calculated by the ideal gas law according to the following form

$$T(r,z) = \frac{\bar{\mu}\ p(r,z)}{R_g\ \rho(z)}, \tag{5.8}$$

where, $R_g = 8.314$ J mol^{-1} K^{-1} represents the gas constant and

$$\bar{\mu} = \frac{1}{z_t}\int_0^{z_t}\mu_e(z)\mathrm{d}z = 1.12 \tag{5.9}$$

is the mean effective molar mass from photosphere to transition region given by the empirical relation, $\mu_e(z) = 1.288\left[1 - 0.535(\frac{z}{2.152})^3\right]$ (Solov'ev and Kirichek 2015) in the domain of $0 < z < 2.152$ Mm. The formulary of the derived functions for the Coulomb function helical fluxtube model are summarized in the Table 5.6. In §5.3 and §5.4, we reduce the GSE for different models of fluxtubes having open or closed field line structures. A flowchart of the solutions of the two different fluxtube models obtained is shown in Fig. 5.1.

Before we solve for the various cylindrical structures, we discuss the boundary conditions below that are crucial to the models, applicable to both open and closed field fluxtubes. The magnetic field lines that rise from a horizontal plane and do not return to the same plane within the domain of interest, are called open field lines (see Figs. [5.6, 5.12, 5.13]). On the other hand, the field lines that rise and return to the same horizontal plane are called the closed field lines (see Fig. 5.7). We take an idealized case in which the fluxtube is embedded in a magnetic field free region where there is no current outside the fluxtube. We apply the following standard BCs which are used by several authors [e.g. Mangalam and Krishan (2000); Solov'ev and Kirichek (2015); Sen and Mangalam (2018a)], that $[B_r(r = 0, z) = 0,\ B_\phi(r = 0, z) = 0]$ which implies that the magnetic field line is vertical at the axis of the fluxtube. At the boundary, the radial component vanishes i.e. $B_r(r = R, z) = 0$. We also use the BCs that the total pressure at the boundary of the fluxtube matches with the external pressure and the radial average of the internal gas pressure at the transition region ($z = z_t$) is equal to p_t, where the pressure at the photosphere ($z = 0$) outside the fluxtube is taken to be $p_0 = 1.228 \times 10^5$ dyne cm^{-2} and at the transition region ($z_t = 2$ Mm), it is $p_t = 0.1488$ dyne cm^{-2}; these are taken from Avrett-Loeser model (Avrett and Loeser 2008). We specify the appropriate BCs to model both open and closed field fluxtubes below:

$$\text{BC 1:} \quad B_r(r=0,z)=0 \tag{5.10a}$$

$$\text{BC 2:} \quad B_\phi(r=0,z)=0 \tag{5.10b}$$

$$\text{BC 3:} \quad B_r(R,z)=0 \tag{5.10c}$$

$$\text{BC 4:} \quad p_T(R,z)=p_e(z) \tag{5.10d}$$

$$\text{BC 5:} \quad \frac{1}{R}\int_0^R p(r,z_t)\mathrm{d}r = p_t. \tag{5.10e}$$

The BCs that distinguishes between the closed and open field fluxtubes is the following

$$B_\phi(R,z)\begin{cases} = 0; & \text{closed field} \\ \neq 0; & \text{open field,} \end{cases} \tag{5.11}$$

which reduces to the condition,

$$\Psi(R,z)=\Psi_b\begin{cases} = 0; & \text{closed field} \\ \neq 0; & \text{open field,} \end{cases} \tag{5.12}$$

which is derived in §5.3. The open (general) solution is obtained in §5.3 and it is reduced to the special case of the closed solution by taking $\Psi_b = 0$ is presented in §5.3.

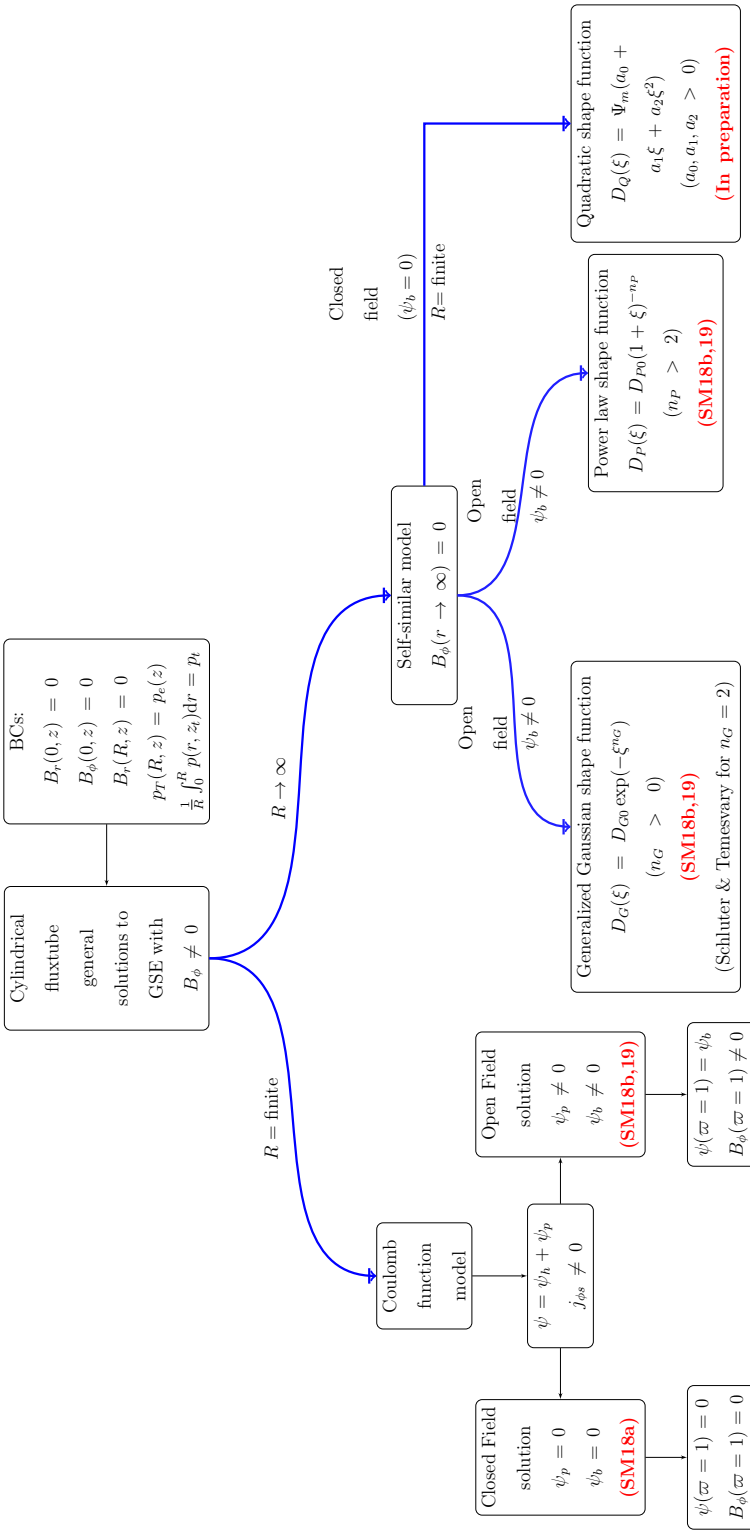

FIGURE 5.1: Flowchart of the Coulomb function and self-similar fluxtube models along with the applicable boundary conditions, that are presented in this chapter.

5.3 Coulomb function solution of helical fluxtube model

For the magnetohydrostatic equilibria with uniform solar gravity and axisymmetric condition, we have split $p(r,z) = p_1(\Psi(r,z)) + p_2(z)$ in order to have a non-zero density (SM18a). If we take the form of $p_1(\Psi)$ as a linear function of Ψ, we found that the BCs 1–5 [eqn (5.10a)–(5.10e)], which are crucial for our model, will not be satisfied for arbitrary R values. On the other hand, the quadratic function of Ψ, which is more general than the linear form, is the simplest allowed form for p_1 and I_p, satisfies all the BCs [eqns (5.10a)–(5.10e)], where R becomes a free parameter, and can be chosen any value within the domain of our interest. Therefore, we assume $p_1(\Psi)$ and $I_p^2(\Psi)$ to be polynomials of Ψ upto second order (Atanasiu *et al.* 2004),

$$p_1(\Psi) = \frac{1}{4\pi}\left(\frac{a'}{2}\Psi^2 + b'\Psi\right), \tag{5.13a}$$

$$I_p^2(\Psi) = \alpha'\Psi^2 + 2\beta'\Psi + I_0^2, \tag{5.13b}$$

where the parameters $a', b', \alpha', \beta', I_0$ are to be determined by appropriate boundary conditions (BCs) and the function $p_2(z)$ will be evaluated later. Plugging eqns (5.13a, 5.13b) into eqn (5.5) we obtain a second order scalar linear partial differential equation

$$\frac{\partial^2\Psi}{\partial r^2} - \frac{1}{r}\frac{\partial\Psi}{\partial r} + \frac{\partial^2\Psi}{\partial z^2} = -(a'r^2 + \alpha')\Psi - (b'r^2 + \beta'). \tag{5.14}$$

We define the dimensionless parameters (in the LHS) by introducing the scaling relations,

$$\begin{aligned} &\varpi = r/R, \quad \tau = R/z_0, \quad \psi_b = \frac{\Psi_b\sqrt{a'}}{B_0}, \quad a = \frac{a'R^4}{4}, \\ &\alpha = \frac{\alpha'}{4\sqrt{a'}}, \quad b = \frac{b'}{B_0\sqrt{a'}}, \quad \beta = \frac{R^2\beta'}{\Psi_b}, \end{aligned} \tag{5.15}$$

where Ψ_b, R, B_0 are the boundary flux, radius and the magnetic field strength at the center of the fluxtube respectively, and $\bar{z} = z/z_0$, where z_0 is a constant. To solve this equation, we split $\psi = \Psi/\Psi_b$ into homogeneous ψ_h and particular part ψ_p, i.e. $\psi = \psi_h + \psi_p$. We plug ψ into eqn (5.14) and separate out the homogeneous and particular parts to obtain the following dimensionless equations

$$\frac{\partial^2\psi_h}{\partial\varpi^2} - \frac{1}{\varpi}\frac{\partial\psi_h}{\partial\varpi} + \tau^2\frac{\partial^2\psi_h}{\partial\bar{z}^2} = -4\sqrt{a}(\sqrt{a}\varpi^2 + 2\alpha)\psi_h, \tag{5.16}$$

$$\frac{\partial^2\psi_p}{\partial\varpi^2} - \frac{1}{\varpi}\frac{\partial\psi_p}{\partial\varpi} = -(4a\varpi^2 + 8\sqrt{a}\alpha)\psi_p - \left(\frac{4ab}{\psi_b}\varpi^2 + \beta\right). \tag{5.17}$$

The solution of eqn (5.16) is separable and given by $\psi_h(\varpi, \bar{z}) = s(\varpi)Z(\bar{z})$ which has been shown in SM18 to be given by

$$s(\varpi) = cF_0(-\alpha - \kappa^2, \sqrt{a}\varpi^2) \qquad (\text{with } a > 0), \tag{5.18}$$

where $F_0(-\alpha - \kappa^2, \sqrt{a}\varpi^2)$ represents the Coulomb function (Abramowitz and Stegun 1972) and $\kappa = \dfrac{kR}{2\sqrt{2}a^{1/4}}$, where the value of k is evaluated later. The z–part solution of eqn (5.16) is given by

$$Z(\bar{z}) = \exp\left(-\frac{2\sqrt{2}\kappa a^{1/4}\bar{z}}{\tau}\right). \tag{5.19}$$

The homogeneous solution takes the following form

$$\psi_h(\varpi, \bar{z}) = c\exp\left(-\frac{2\sqrt{2}\kappa a^{1/4}\bar{z}}{\tau}\right)F_0(-\alpha - \kappa^2, \sqrt{a}\varpi^2). \tag{5.20}$$

The solution of the inhomogeneous eqn (5.17) is given by a power series solution

$$\psi_p(\varpi) = -\frac{\beta}{8\alpha} + \frac{i\sqrt{a}\varpi^2}{2}e^{-i\sqrt{a}\varpi^2}\left(\frac{\beta}{8\alpha} - \frac{b}{\psi_b}\right)\sum_{n=0}^{\infty}\frac{F_2^1\left(n+2, 1; n+2+i\alpha; \frac{1}{2}\right)(i\sqrt{a}\varpi^2)^n}{(n+1+i\alpha)n!}. \tag{5.21}$$

A similar but different homogeneous solution which is oscillatory along $z-$direction has been used for the cases of both $D-$shaped and toroidally diverted laboratory

plasma (Atanasiu *et al.* 2004). The general solution of the GS eqn (5.14) is given by $\psi = \psi_h + \psi_p$. Since $\psi(\varpi, \bar{z})$ and $\psi^*(\varpi, \bar{z})$, its complex conjugate, are the valid solutions of eqn (5.14), we construct a real solution of eqn (5.14) by redefining $\frac{\psi_h(\varpi,\bar{z}) + \psi_h^*(\varpi,\bar{z})}{2} \rightarrow \psi_h(\varpi, \bar{z})$ and $\frac{\psi_p(\varpi) + \psi_p^*(\varpi)}{2} \rightarrow \psi_p(\varpi)$ which leads to

$$\frac{\psi(\varpi,\bar{z}) + \psi^*(\varpi,\bar{z})}{2} \rightarrow \psi(\varpi,\bar{z}) = \psi_C^X = \begin{cases} \psi_C^C = \psi_h & \text{(closed field)} \\ \psi_C^O = \psi_h + \psi_p & \text{(open field)} \end{cases} .$$

The solution ψ_h alone gives the closed field structure of fluxtube (SM18), which we denote as ψ_C^C; the general solution is a combination of ψ_h and ψ_p and we denote the open field fluxtube structure as ψ_C^O.
The total flux function $\psi_C^X(\varpi, \bar{z})$ is given by

$$\psi_C^X(\varpi,\bar{z}) = s(\varpi)Z(\bar{z}) + \psi_p(\varpi), \tag{5.22}$$

where $s(\varpi)$ and $\psi_p(\varpi)$ are given by eqns (5.18) and (5.21) respectively. Now, $\psi_C^X(\varpi, \bar{z})$ has to be zero at the axis (i.e. $\varpi = 0$) for all $\bar{z}$, to keep the field finite at the origin. Since $s(0) = 0$, which satisfies the BC 1 [eqn (5.10a)], we obtain from eqn (5.22), $\psi_p(\varpi = 0) = 0$. From eqn (5.21), we have $\psi_p(\varpi = 0) = -\frac{\beta}{8\alpha}$. Therefore, we obtain $\beta = 0$. From eqn (5.21), $\psi_p(\varpi)$ reduces to

$$\psi_p(\varpi) = \frac{i\sqrt{a}b\varpi^2}{4\psi_b}\Bigg[e^{i\sqrt{a}\varpi^2}\sum_{n=0}^{\infty}\frac{F_2^1\big(n+2,1;n+2-i\alpha;\frac{1}{2}\big)(-i\sqrt{a}\varpi^2)^n}{(n+1-i\alpha)n!} - e^{-i\sqrt{a}\varpi^2}\sum_{n=0}^{\infty}\frac{F_2^1\big(n+2,1;n+2+i\alpha;\frac{1}{2}\big)(i\sqrt{a}\varpi^2)^n}{(n+1+i\alpha)n!}\Bigg]. \tag{5.23}$$

From eqns (5.2) and (5.22) we have

$$B_z(\varpi,\bar{z}) = \frac{B_0\psi_b}{2\sqrt{a}\varpi}\left(\frac{\partial\psi_h}{\partial\varpi} + \frac{\partial\psi_p}{\partial\varpi}\right). \tag{5.24}$$

The homogeneous solution $s(\varpi)$ which is given by the eqn (5.18), can be represented in terms of the Whittaker–M function (SM18), where the Whittaker–M

function can be expressed in terms of hypergeometric function by the standard relation (Dixit and Moll 2015)

$$M_{t,m}(\nu) = e^{-\nu/2}\nu^{m+\frac{1}{2}}F_1^1\left(\frac{1}{2}+m-t, 1+2m, \nu\right), \tag{5.25}$$

where F_1^1 represents the hypergeometric function with the arguments t, m and ν. Taking the real part of $\psi_h(\varpi, \bar{z})$ from eqn (5.20) and $\psi_p(\varpi)$ from (5.23), and using eqns [(5.24), (5.25)] we obtain

$$\begin{aligned} B_z(\varpi,\bar{z}) =& B_0\psi_b c\exp\left(-\frac{2\sqrt{2}\kappa a^{1/4}\bar{z}}{\tau}\right)\Big[8(1+i\sqrt{a}\varpi^2)F_1^1(1+i\alpha,2,2i\sqrt{a}\varpi^2)- \\ & 8\sqrt{a}\varpi^2F_1^1(1+i\alpha,3,2i\sqrt{a}\varpi^2)\Big] + \frac{B_0\psi_b}{2\sqrt{a}}\left(\frac{\psi_p'(\varpi)+\psi_p'^*(\varpi)}{2\varpi}\right) \end{aligned} \tag{5.26}$$

where, $B_0 \equiv B_z(0,0)$, and from eqn (5.26) we obtain,

$$1 = 8\psi_b c + \frac{\psi_b}{2\sqrt{a}}\left[\frac{\psi_p'(\varpi)+\psi_p'^*(\varpi)}{2\varpi}\right]_{\varpi=0}, \tag{5.27}$$

where the identity $F_1^1(1+i\alpha, 2, 0) = 1$ is applied. By expanding the last term on the RHS of eqn (5.27), we obtain

$$1 = 8\psi_b c + \frac{ib}{2}\left[\frac{F_2^1(1,-i\alpha,2-i\alpha,-1)}{1-i\alpha} - \frac{F_2^1(1,i\alpha,2+i\alpha,-1)}{1+i\alpha}\right] \tag{5.28}$$

and the expression for c is given by

$$c = \frac{1}{8\psi_b}\left[1 - \frac{ib}{2}\left(\frac{F_2^1(1,-i\alpha,2-i\alpha,-1)}{1-i\alpha} - \frac{F_2^1(1,i\alpha,2+i\alpha,-1)}{1+i\alpha}\right)\right]. \tag{5.29}$$

Hence, we obtain the explicit form for

$$B_z(\varpi,\bar{z}) = \frac{B_0}{8\varpi}\left[\left\{1-\frac{ib}{2}\left(\frac{F_2^1(1,-i\alpha,2-i\alpha,-1)}{1-i\alpha}-\frac{F_2^1(1,i\alpha,2+i\alpha,-1)}{1+i\alpha}\right)\right\}\right. \tag{5.30}$$

$$\cdot\exp\left(-\frac{2\sqrt{2}\kappa a^{1/4}\bar{z}}{\tau}\right)\frac{\mathrm{d}}{\mathrm{d}\varpi}[F_0(-\alpha-\kappa^2,\sqrt{a}\varpi^2)+F_0^*(-\alpha-\kappa^2,\sqrt{a}\varpi^2)]$$

$$+ib\frac{\mathrm{d}}{\mathrm{d}\varpi}\left\{\varpi^2 e^{i\sqrt{a}\varpi^2}\sum_{n=0}^{\infty}\frac{F_2^1(n+2,1,n+2-i\alpha,1/2)(-i\sqrt{a}\varpi^2)^n}{(n+1-i\alpha)n!}\right.$$

$$\left.\left.-\varpi^2 e^{-i\sqrt{a}\varpi^2}\sum_{n=0}^{\infty}\frac{F_2^1(n+2,1,n+2+i\alpha,1/2)(-i\sqrt{a}\varpi^2)^n}{(n+1+i\alpha)n!}\right\}\right].$$

From eqns (5.2, 5.22) we have

$$B_r(\varpi,\bar{z}) = -\frac{B_0\psi_b\tau}{2\sqrt{a}}s(\varpi)Z'(\bar{z}), \tag{5.31}$$

whose explicit form is given by

$$B_r(\varpi,\bar{z}) = \frac{B_0\kappa}{2\sqrt{2}a^{1/4}\varpi}\exp\left(\frac{-2\sqrt{2}\kappa a^{1/4}\bar{z}}{\tau}\right) \tag{5.32}$$

$$\cdot[F_0(-\alpha-\kappa^2,\sqrt{a}\varpi^2)+F_0^*(-\alpha-\kappa^2,\sqrt{a}\varpi^2)]$$

$$\cdot\left[1-\frac{ib}{2}\left(\frac{F_2^1(1,-i\alpha,2-i\alpha,-1)}{1-i\alpha}-\frac{F_2^1(1,i\alpha,2+i\alpha,-1)}{1+i\alpha}\right)\right].$$

From eqn (5.2) we obtain the toroidal component

$$B_\phi(\varpi,\bar{z}) = \frac{\sqrt{2}B_0\alpha^{1/2}\psi_b}{a^{1/4}\varpi}(\psi_h+\psi_p), \tag{5.33}$$

whose explicit form is given by

$$
\begin{aligned}
B_\phi(\varpi,\bar{z}) = \frac{B_0\alpha^{1/2}a^{-1/4}}{4\sqrt{2}}\Bigg[\frac{1}{\varpi} \\
\cdot\Bigg\{1-\frac{ib}{2}\Bigg(\frac{F_2^1(1,-i\alpha,2-i\alpha,-1)}{1-i\alpha}-\frac{F_2^1(1,i\alpha,2+i\alpha,-1)}{1+i\alpha}\Bigg)\Bigg\} \\
\cdot\exp\Bigg(-\frac{-2\sqrt{2}\kappa\bar{z}}{\tau}\Bigg)[F_0(-\alpha-\kappa^2,\sqrt{a}\varpi^2)+F_0^*(-\alpha-\kappa^2,\sqrt{a}\varpi^2)] \\
+ib\varpi\Bigg\{e^{i\sqrt{a}\varpi^2}\sum_{n=0}^{\infty}\frac{F_2^1(n+2,1,n+2-i\alpha,1/2)(-i\sqrt{a}\varpi^2)^n}{(n+1-i\alpha)n!} \\
-e^{-i\sqrt{a}\varpi^2}\sum_{n=0}^{\infty}\frac{F_2^1(n+2,1,n+2+i\alpha,1/2)(-i\sqrt{a}\varpi^2)^n}{(n+1+i\alpha)n!}\Bigg\}\Bigg].
\end{aligned}
\tag{5.34}
$$

Applying the BC 3 [eqn (5.10c)] and using eqn (5.31), we find $s(\varpi=1)=0$. From BC 2 [eqn (5.10b)] and eqn (5.13b) we find $I_0=0$. We assume that the external pressure from photosphere to transition region decreases exponentially as

$$p_e(z) = p_0\exp(-2kz), \tag{5.35}$$

where k is the pressure scale height, which is determined by the relation, $k=\dfrac{1}{2z_t}\ln\left(\dfrac{p_0}{p_t}\right)=3.405$ Mm^{-1}, where $p_0=1.22\times10^5$ dyne cm^{-2}, $p_t=0.148$ dyne cm^{-2}, and $z_t=2$ Mm. By matching the pressure scale heights inside and outside the fluxtube, we see that $p_2(z)$ follows

$$p_2(z) = p_{20}\exp(-2kz), \tag{5.36}$$

where p_{20} is evaluated later. Finally, we have the expression of $p(r,z)$ from eqns (5.4, 5.13a) to be given by

$$p(r,z) = \frac{1}{4\pi}\left(\frac{a'}{2}\Psi^2+b'\Psi\right)+p_{20}\exp(-2kz), \tag{5.37}$$

whose explicit form is given by

$$p(\varpi,\bar{z}) = B_0^2\Bigg[\left(\frac{\psi_b^2 s^2(\varpi)}{8\pi}+\bar{p}_{20}\right)Z^2(\bar{z}) + \left(\frac{\psi_b^2 s(\varpi)\psi_p(\varpi)}{4\pi}+\frac{b\psi_b s(\varpi)}{2\sqrt{2a}}\right)Z(\bar{z}) + \left(\frac{\psi_b^2\psi_p^2}{8\pi}+\frac{b\psi_b\psi_p}{2\sqrt{2a}}\right)\Bigg], \tag{5.38}$$

where $\bar{p}_{20} = p_{20}/B_0^2$, and $s(\varpi),\ Z(\bar{z}),\ \psi_p(\varpi)$ are given by eqns (5.18, 5.19, 5.23) respectively. We now calculate the total pressure at the boundary of the fluxtube that includes the contribution due to gas pressure and the magnetic forces due to the presence of the sheet currents j_ϕ (SM18) and j_z. The pressure and radial component of the MHS force balance eqn (5.1) yields

$$-\frac{\partial p}{\partial r}\bigg|_{r=R} + \frac{1}{4\pi}\left(B_r\frac{\partial B_r}{\partial r}+B_z\frac{\partial B_r}{\partial z}\right)\bigg|_{r=R} - \frac{\partial}{\partial r}\left(\frac{B^2}{8\pi}\right)\bigg|_{r=R} + j_\phi(R)B_z(R) - j_z(R)B_\phi(R) = 0. \tag{5.39}$$

The sheet currents j_ϕ and j_z take the forms

$$j_\phi(r) = j_{\phi s}\ \delta(r-R), \tag{5.40a}$$

$$j_z(r) = j_{zs}\ \delta(r-R). \tag{5.40b}$$

Integrating eqn (5.39) with respect to r from $r = R-\epsilon$ to $r = R+\epsilon$ where ϵ is an infinitesimal positive quantity we obtain

$$-\int_{R-\epsilon}^{R+\epsilon}\frac{\partial p}{\partial r}dr + \frac{1}{4\pi}\left(\int_{R-\epsilon}^{R+\epsilon}B_r\frac{\partial B_r}{\partial r}dr + \int_{R-\epsilon}^{R+\epsilon}B_z\frac{\partial B_r}{\partial z}dr\right) - \int_{R-\epsilon}^{R+\epsilon}\frac{\partial}{\partial r}\left(\frac{B^2}{8\pi}\right)dr + \int_{R-\epsilon}^{R+\epsilon}j_\phi(r)B_z(r)\mathrm{d}r - \int_{R-\epsilon}^{R+\epsilon}j_z(r)B_\phi(r)\mathrm{d}r = 0, \tag{5.41}$$

which leads to

$$p_i(R,z) - p_e(z) + j_{\phi s}\ B_z(R) - j_{zs}\ B_\phi(R) + \frac{1}{4\pi}\left[B_r\frac{\partial B_r}{\partial r}+B_z\frac{\partial B_r}{\partial z}\right]_R + \frac{B_i^2(R,z)-B_e^2(R,z)}{8\pi} = 0, \tag{5.42}$$

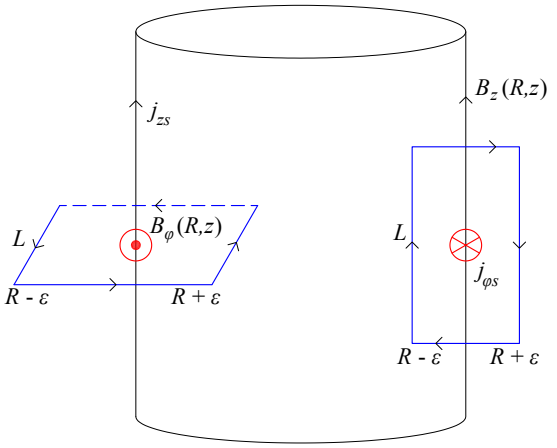

FIGURE 5.2: Geometry of the fluxtube at the boundary showing sheet currents.

where $[...]_R$ denotes the jump condition at the boundary and $\{B_i, p_i\}$ and $\{B_e, p_e\}$ are the internal and external magnetic fields and gas pressures in the fluxtube respectively. To calculate $j_{\phi s}$ and j_{zs}, we assume an infinitesimal current loop of vertical height L and radial extent $R-\epsilon$ to $R+\epsilon$ placed at the boundary of the fluxtube (see Fig. 5.2) and by applying the line integral along the loop, we obtain

$$B_z(R)L = 4\pi L \int_{R-\epsilon}^{R+\epsilon} j_{\phi s}\delta(r-R)\mathrm{d}r \tag{5.43a}$$

$$-B_\phi(R)L = 4\pi L \int_{R-\epsilon}^{R+\epsilon} j_{zs}\delta(r-R)\mathrm{d}r, \tag{5.43b}$$

which implies

$$j_{\phi s} = \frac{B_z(R)}{4\pi} \tag{5.44a}$$

$$j_{zs} = -\frac{B_\phi(R)}{4\pi}. \tag{5.44b}$$

The total internal magnetic field is given by, $B_i^2 = B_r^2 + B_\phi^2 + B_z^2$. Applying the BC 3 [eqn (5.10c)] and $B_e = 0$, we have from eqn (5.42),

$$p_i(R,z) - p_e(z) + \frac{3B_z^2(R,z)}{8\pi} + \frac{3B_\phi^2(R,z)}{8\pi} = 0. \tag{5.45}$$

By expanding eqn (5.45) we obtain

$$\frac{\psi_b^2}{3}\left(1 + \frac{6\alpha}{\sqrt{a}}\right) + \frac{2}{3}b\psi_b + \frac{\psi_b^2}{4a}\left[\frac{1}{\varpi^2}\left(s'(\varpi)\exp\left(-\frac{2\sqrt{2}\kappa a^{1/4}\bar{z}}{\tau}\right) + \psi_p'(\varpi)\right)^2\right]_{\varpi=1} \tag{5.46}$$
$$= \bar{p}\exp\left(-\frac{4\sqrt{2}\kappa a^{1/4}\bar{z}}{\tau}\right),$$

where $\psi_b = \psi_p(\varpi = 1)$ and $\bar{p} = \dfrac{8\pi(p_0 - p_{20})}{3B_0^2}$. By equating the coefficients of $\exp\left(-\dfrac{2\sqrt{2}\kappa a^{1/4}\bar{z}}{\tau}\right)$, $\exp\left(-\dfrac{4\sqrt{2}\kappa a^{1/4}\bar{z}}{\tau}\right)$ and the constant quantity between both sides of eqn (5.46), we obtain

$$\left(\frac{1}{\varpi^2}s'(\varpi)\psi_p'(\varpi)\right)_{\varpi=1} = 0, \tag{5.47a}$$
$$\frac{\psi_b^2}{4a}\left(\frac{s'^2(\varpi)}{\varpi^2}\right)_{\varpi=1} = \bar{p}, \tag{5.47b}$$
$$\frac{\psi_b^2}{3}\left(1 + \frac{6\alpha}{\sqrt{a}}\right) + \frac{2b\psi_b}{3} + \frac{\psi_b^2}{4a}\left[\frac{\psi_p'^2(\varpi)}{\varpi^2}\right]_{\varpi=1} = 0. \tag{5.47c}$$

From eqns (5.47a, 5.47b) we find that $\left(\frac{\psi_p'(\varpi)}{\varpi}\right)_{\varpi=1} = 0$, as $\bar{p} \neq 0$ and hence from eqn (5.47c)

$$b = -\frac{\psi_b}{2}\left(1 + \frac{6\alpha}{\sqrt{a}}\right). \tag{5.48}$$

We now summarize the set of equations we need to solve numerically for the open field model to be given by

$$s(\varpi = 1) = 0, \tag{5.49a}$$

$$\left(\frac{\psi_p'(\varpi)}{\varpi}\right)_{\varpi=1} = 0, \tag{5.49b}$$

$$\left(\frac{s'^2(\varpi)}{\varpi^2}\right)_{\varpi=1} = \frac{4a\bar{p}}{\psi_b^2}, \tag{5.49c}$$

$$b = -\frac{\psi_b}{2}\left(1 + \frac{6\alpha}{\sqrt{a}}\right), \tag{5.49d}$$

$$\int_0^1 p(\varpi, \bar{z}_t)\mathrm{d}\varpi = p_t. \tag{5.49e}$$

The explicit forms of the eqns (5.49a–5.49e) are

$$F_0(-\alpha - \kappa^2, \sqrt{a}) + F_0^*(-\alpha - \kappa^2, \sqrt{a}) = 0, \tag{5.50}$$

$$\left[\frac{1}{\varpi^2}\frac{\mathrm{d}}{\mathrm{d}\varpi}\left(\varpi^2 e^{i\sqrt{a}\varpi^2}\sum_{n=0}^{\infty}\frac{F_2^1(n+2,1,n+2-i\alpha,1/2)(-i\sqrt{a}\varpi^2)^n}{(n+1-i\alpha)n!}\right.\right.$$
$$\left.\left.-\varpi^2 e^{-i\sqrt{a}\varpi^2}\sum_{n=0}^{\infty}\frac{F_2^1(n+2,1,n+2+i\alpha,1/2)(i\sqrt{a}\varpi^2)^n}{(n+1+i\alpha)n!}\right)\right]_{\varpi=1} = 0, \tag{5.51}$$

$$\left[1 - \frac{ib}{2}\left(\frac{F_2^1(1,-i\alpha,2-i\alpha,-1)}{1-i\alpha} - \frac{F_2^1(1,i\alpha,2+i\alpha,-1)}{1=i\alpha}\right)\right]^2$$
$$\cdot\left(\frac{\mathrm{d}}{\mathrm{d}\varpi}\left[F_0(\alpha-\kappa^2,\sqrt{a}\varpi^2) + F_0^*(\alpha-\kappa^2,\sqrt{a}\varpi^2)\right]_{\varpi=1}\right)^2 = \bar{p}a, \tag{5.52}$$

$$b = -\frac{\psi_b}{2}\left(1 + \frac{6\alpha}{\sqrt{a}}\right), \tag{5.53}$$

$$\int_0^1 \left[e^{-2\kappa_t}\left(1 - \frac{ib}{2}\left[\frac{F_2^1(1,-i\alpha,2-i\alpha,-1)}{1-i\alpha} - \frac{F_2^1(1,i\alpha,2+i\alpha,-1)}{1+i\alpha}\right]\right)^2\right.$$
$$\cdot\left(F_0(-\alpha-\kappa^2,\sqrt{a}\varpi^2) + F_0^*(-\alpha-\kappa^2,\sqrt{a}\varpi^2)\right)^2 + 8e^{-\kappa_t}\psi_b\big(\psi_p + \psi_p^* + \frac{2b}{\psi_b}\big)$$
$$\cdot\left(1 - \frac{ib}{2}\left[\frac{F_2^1(1,-i\alpha,2-i\alpha,-1)}{1-\alpha} - \frac{F_2^1(1,i\alpha,2+i\alpha,-1)}{1+\alpha}\right]\right)^2$$
$$\cdot\left(F_0(-\alpha-\kappa^2,\sqrt{a}\varpi^2) + F_0^*(-\alpha-\kappa^2,\sqrt{a}\varpi^2)\right) \tag{5.54}$$

$$\left.+\frac{\psi_b^2}{4}\big(\psi_p+\psi_p^*\big)^2 + b\psi_b(\psi_p+\psi_p^*)\right]\mathrm{d}\varpi = \bar{p} \tag{5.55}$$

respectively, where, $\psi_p(\varpi)$ is given by eqn (5.23), $\kappa_t = kz_t$, and $\psi_p(\varpi = 1) = \psi_b$. The five eqns (5.50–5.54) consists of seven unknown variables, $\{a, \alpha, b, \psi_b, \bar{p}, R, B_0\}$; so there is a unique solution to the Coulomb function open field model for a given pair of the unknown variables. The eqns (5.50) and (5.51) contain three variables a, α and R, and we use these two equations to obtain $a(R)$ and $\alpha(R)$. From eqn (5.54), we calculate $\psi_b(R, B_0, b)$ and then find $b(R, B_0)$ from eqn (5.53), and hence $\psi_b(R, B_0)$ and then evaluate $\bar{p}(R, B_0)$ from eqn (5.52). As a result, the complete solution for the open field fluxtube depends only on R and B_0 which are the free parameters of the model. As per BC1–BC5 [eqns (5.10a–5.10e)], which are used for the open field fluxtube model, the magnetic field component at the boundary of the fluxtube is given by

$$B_\phi(\varpi = 1, \bar{z}) = \frac{\sqrt{2\alpha} B_0 \psi_b^2}{a^{1/4}}. \tag{5.56}$$

If we demand additionally, that $B_\phi(\varpi = 1, \bar{z}) = 0$, then, from eqn (5.56), $\psi_b = 0$; also eqn (5.49d) gives $b = 0$. Therefore from eqn (5.23), we obtain

$$\psi_p(\varpi) = 0. \tag{5.57}$$

This represents the solution of the homogeneous part ψ_h of GSE, which has been discussed in SM18, that is applicable for closed field fluxtube model. Therefore we need to solve eqns (5.49a, 5.49c, 5.49e), which are given by the explicit forms by eqns (5.50, 5.52, 5.54) [with $b = \psi_b = 0$], numerically to find the parameters a, α and $\bar{p}$ in terms of $\{R, B_0\}$, which are the free parameters of the closed field model. The formulary of the derived functions for the Coulomb function helical fluxtube model are summarized in the Table 5.6. We discuss the various configurations of Coulomb function open and closed field structure of fluxtubes in §5.5.1.

5.4 Self-similar models

The basic formulation of self-similar model of a fluxtube is based on Schlüter and Temesváry (1958) (ST58 hereafter). For an axially symmetric cylindrical geometry (r, ϕ, z), where ϕ is ignorable, the magnetic field components are given by eqn (5.2). The coordinates r and z are combined together into a new dimensionless variable ξ which is called the self-similar parameter and as a consequence, the flux function Ψ can be expressed only as a function of ξ i.e., $\Psi(r, z) = \Psi(\xi)$ (ST58). We define the dimensionless parameters (in the LHS) by introducing the scaling relations,

$$\begin{aligned} &\varpi = r/R, \quad \tau = R/z_0, \quad \psi = \Psi/\Psi_b, \quad \psi_b = \frac{\Psi_b}{B_0 z_0^2}, \\ &\bar{p}_1 = p_1/B_0^2, \quad \bar{I}_p = \frac{I_p}{B_0 R}, \quad \bar{\chi} = \chi z_0^2, \end{aligned} \tag{5.58}$$

where, Ψ_b, R, B_0 are the boundary flux, radius and the magnetic field strength at the center of the fluxtube respectively, and $\bar{z} = z/z_0$, where z_0 is a constant length. From ST58, the self-similar parameter ξ is defined by

$$\xi = \zeta(\bar{z})\varpi, \tag{5.59}$$

which describes the radial size distribution of the fluxtube with height from the base. Plugging in eqn (5.59), we can rewrite the GS eqn (5.5) in the following form

$$\begin{aligned} &\frac{\psi_b^2}{2\tau^2}\frac{\mathrm{d}}{\mathrm{d}\xi}\left(\frac{\mathrm{d}\psi}{\mathrm{d}\xi}\right)^2\zeta'^2(\bar{z}) + \frac{\psi_b^2}{\tau^2}\frac{1}{\xi}\left(\frac{\mathrm{d}\psi}{\mathrm{d}\xi}\right)^2\zeta'(\bar{z})\zeta''(\bar{z}) \\ &+ \frac{\psi_b^2}{2\tau^4}\frac{\mathrm{d}}{\mathrm{d}\xi}\left(\frac{1}{\xi}\frac{\mathrm{d}\psi}{\mathrm{d}\xi}\right)^2\zeta^4(\bar{z}) + \frac{1}{2\xi^2}\frac{\mathrm{d}\bar{I}_p^2}{\mathrm{d}\xi}\zeta^2 = -4\pi\frac{\partial\bar{p}_1}{\partial\xi}, \end{aligned} \tag{5.60}$$

and the $z-$part of GS eqn (5.3b), gives the expression of ρ, eqn (5.7), which is self consistent for both the Coulomb function and self-similar models. We define

a quantity which is called the magnetic shape function given by

$$D_X(\xi) = \frac{1}{\xi}\frac{\mathrm{d}\psi}{\mathrm{d}\xi}. \tag{5.61}$$

Plugging eqn (5.61) into eqn (5.60) we obtain

$$\frac{\psi_b^2}{\tau^2}\xi D_X^2(\xi)\zeta\zeta'' + \frac{\psi_b^2}{2\tau^2}\frac{\mathrm{d}}{\mathrm{d}\xi}[\xi^2 D_X^2(\xi)]\zeta'^2 + \frac{\psi_b^2}{2\tau^4}\frac{\mathrm{d}}{\mathrm{d}\xi}\big(D_X^2(\xi)\big)\zeta^4 + \frac{1}{2\xi^2}\frac{\mathrm{d}\bar{I}_p^2}{\mathrm{d}\xi}\zeta^2 = -4\pi\frac{\partial\bar{p}_1}{\partial\xi}, \tag{5.62}$$

and integrating eqn (5.62) with respect to ξ from 0 to ∞ we write

$$\begin{aligned}&\frac{\psi_b^2}{\tau^2}\zeta\zeta''\int_0^\infty \xi D_X^2(\xi)\mathrm{d}\xi + \frac{\psi_b^2\zeta'^2}{2\tau^2}\big[\xi^2 D_X^2(\xi)\big]_{\xi=0}^{\infty} + \frac{\psi_b^2\zeta^4}{2\tau^4}[D_X^2(\infty) - D_X^2(0)]\\ &+ \frac{\zeta^2}{2}\int_0^\infty \frac{1}{\xi^2}\frac{\mathrm{d}\bar{I}_p^2}{\mathrm{d}\xi}\mathrm{d}\xi = -4\pi\int_0^\infty \frac{\partial\bar{p}_1}{\partial\xi}\mathrm{d}\xi.\end{aligned} \tag{5.63}$$

Following ST58, we define

$$y^2(\bar{z}) = \frac{\psi_b D_0}{\tau}\zeta^2(\bar{z}), \tag{5.64}$$

where, $y(\bar{z}) \equiv \left(\dfrac{B_z(0,\bar{z})}{B_0}\right)^{1/2}$, $B_0 \equiv B_z(0,0)$ and $D_0 \equiv D_X(\xi = 0)$. Next, using eqns (5.63) and (5.64) we obtain

$$\begin{aligned}&\frac{\psi_b}{\tau}\frac{yy''}{D_0}\int_0^\infty \xi D_X^2(\xi)\mathrm{d}\xi + \frac{\psi_b}{\tau}\frac{y'^2}{2D_0}\big[\xi^2 D_X^2(\xi)\big]_{\xi=0}^{\infty} + \frac{y^4}{2D_0^2\tau^2}[D_X^2(\infty) - D_0^2]\\ &+ \frac{\tau}{\psi_b}\frac{y^2}{2D_0}\int_0^\infty \frac{1}{\xi^2}\frac{\mathrm{d}\bar{I}_p^2}{\mathrm{d}\xi}\mathrm{d}\xi = -4\pi\int_0^\infty \frac{\partial\bar{p}_1}{\partial\xi}\mathrm{d}\xi.\end{aligned} \tag{5.65}$$

To solve the eqn (5.65), we need to specify the functional form of p_1, I_p and $D_X(\xi)$ to study the fluxtube model with twisted magnetic field under the similarity assumption. The functional form of $p_1 = \frac{f}{2}\Psi^2$ is taken from Osherovitch (1982), where f is the shape function parameter, and the poloidal current, I_p defined by Yun (1971) and Osherovitch (1979), and motivated from the observations of Stepanov (1965). Hence the form of gas pressure p and poloidal current I_p are

taken to be

$$p = p_c \exp(-2kz) + \frac{f}{2}\Psi^2 \tag{5.66}$$

$$I_p^2 = \Psi_b^2 \chi \xi^4 D_X^2(\xi), \tag{5.67}$$

for the positivity of $\rho(z)$ at all z which is given by eqn (5.7). Here, $p_2(z) = p_c \exp(-2kz)$ denotes the gas pressure at the fluxtube axis, with p_c is the pressure at the center of the fluxtube, and $\chi = \left(\frac{B_\phi}{rB_z}\right)^2$, is a constant pitch angle parameter. We deviate from [Osherovitch (1982); Yun (1971)] by employing the extra term, $p_c \exp(-2kz)$ with p_1 in eqn (5.66), to maintain the hydrostatic vertical pressure balance condition under the influence of solar gravity.

5.4.1 Self-similar open field model

To obtain the open field structure of the fluxtubes we have employed two options for the shape function $D_X(\xi)$ specified by

$$D_X(\xi) = \begin{cases} D_G(\xi) = D_{G0} \exp(-\xi^{n_G}); & (n_G > 0): \quad \text{Generalized Gaussian} \\ D_P(\xi) = D_{P0}(1+\xi)^{-n_P}; & (n_P > 2): \quad \text{Power law} \end{cases} \tag{5.68}$$

where

$$D_{G0} = \frac{n_G}{\Gamma(2/n_G)}, \tag{5.69a}$$

$$D_{P0} = (n_P - 1)(n_P - 2), \tag{5.69b}$$

We see that both the shape functions, eqn (5.68) vanish asymptotically at $\xi \to \infty$; hence from eqn (5.65) we obtain

$$\frac{\psi_b}{\tau}\frac{yy''}{D_0}\int_0^\infty \xi D_X^2(\xi)\mathrm{d}\xi - \frac{y^4}{2\tau^2} + \frac{\tau}{\psi_b}\frac{y^2}{D_0}\int_0^\infty \frac{1}{2\xi^2}\frac{\mathrm{d}\bar{I}_p^2}{\mathrm{d}\xi}\mathrm{d}\xi = -4\pi\int_0^\infty \frac{\partial \bar{p}_1}{\partial \xi}\mathrm{d}\xi. \quad (5.70)$$

Next, we evaluate the integrals of the eqn (5.70) for both generalized Gaussian and power law shape functions. We will see later that, from eqn (5.77), that the flux function $\psi_P(\xi)$ varies as ξ^{2-n_P}, in the domain $0 < \xi < \infty$; therefore $\psi_P(\xi)$ will converge to a finite value at $\xi \to \infty$, if $n_p > 2$. The results of the integrals are provided in Table 5.1.

Functions	Shape function $D_G(\xi) \quad (n_G > 0)$	Shape function $D_P(\xi) \quad (n_P > 2)$
$\int_0^\infty \xi D_X^2(\xi)\mathrm{d}\xi$	$\frac{n_G}{\Gamma(2/n_G)2^{2/n_G}}$	$\frac{(n_P-1)(n_P-2)^2}{2(2n_P-1)}$
$\int_0^\infty \frac{1}{2\xi^2}\frac{\mathrm{d}\bar{I}_p^2}{\mathrm{d}\xi}\mathrm{d}\xi$	$\frac{\bar{\chi}\psi_b^2 n_G}{2^{2/n_G}\tau^2\Gamma(2/n_G)}$	$\frac{\bar{\chi}\psi_b^2(n_P-2)^2(n_P-1)}{2\tau^2(2n_P-1)}$
$\int_0^\infty \frac{\partial \bar{p}_1}{\partial \xi}\mathrm{d}\xi$	$\bar{f}\psi_b^2/2$	$\bar{f}\psi_b^2/2$
$\lambda_X(n)$	$2^{2/n_G-1}$	$\frac{2n_P-1}{n_P-2}$

TABLE 5.1: Expression of the integrals in eqn (5.70) and λ_X in eqn (5.71), for generalized Gaussian ($X = G$), and power law ($X = P$) shape function, eqn (5.68).

Using the values of the integrals from Table 5.1 and redefining, $y'(\bar{z} = 0) \equiv y'_0$, we reduce eqn (5.70) to the following form

$$\frac{\mathrm{d}y}{\mathrm{d}\bar{z}} = \left[\frac{\lambda_X(n)}{2\psi_b\tau}(y^4-1) - 2\bar{\chi}(y^2-1) - 8\pi\psi_b\bar{f}\lambda_X(n)\tau\ln(y) + \frac{\bar{B}'^2_{z0}}{4}\right]^{1/2}, \quad (5.71)$$

where, $\bar{B'}_{z0} = \dfrac{B'_{z0} z_0}{B_0}$, $\bar{\chi} = \chi z_0^2$ and $\bar{f} = f z_0^4$. The form of eqn (5.71) is common for both generalized Gaussian ($X = G$) and power law ($X = P$) shape functions, where the functions $\lambda_X(n)$ for both shape functions are defined in Table 5.1. Here we have used the notation $B'_{z0} = B'_z(0,0)$, which represents the vertical gradient of $B_z(0,z)$ at the center. From eqn (5.71), we have the following integral relation

$$\bar{z}(y) = \int_1^y \frac{\mathrm{d}y'}{G(y')}, \tag{5.72}$$

where the function $G(y)$ is given by

$$G(y) = \left[\frac{\lambda_X(n)}{2\psi_b\tau}(y^4-1) - 2\bar{\chi}(y^2-1) - 8\pi\psi_b\bar{f}\lambda_X(n)\tau\ln(y) + \frac{\bar{B'}_{z0}^2}{4}\right]^{1/2}. \tag{5.73}$$

We evaluate the integral (5.72) numerically which gives $\bar{z} = \bar{z}(y)$. Thereafter, inverting the function between $\bar{z}$ and y, we evaluate $y = y(\bar{z})$. From eqns (5.59, 5.64) we obtain

$$\xi = \sqrt{\frac{\tau}{\psi_b D_0}}\varpi y(\bar{z}). \tag{5.74}$$

Using the similarity assumption, $B_z(r,z) = \dfrac{B_0\psi_b}{\tau}\zeta^2(z)D_X(\xi)$ (ST58), and eqns (5.2, 5.59, 5.74) we calculate the magnetic field components, representing the most general self-similar solution, to be

$$B_z(\varpi,\bar{z}) = \frac{B_0}{D_0}y^2(\bar{z})D_X(\xi) \tag{5.75a}$$

$$B_r(\varpi,\bar{z}) = -\frac{B_0\varpi}{D_0}y(\bar{z})y'(\bar{z})D_X(\xi) \tag{5.75b}$$

$$B_\phi(\varpi,\bar{z}) = \frac{\sqrt{\bar{\chi}}B_0}{D_0}\varpi y^2(\bar{z})D_X(\xi). \tag{5.75c}$$

The flux function for the self-similar model is obtained by integrating the shape function

$$\psi_S^O(\xi) = \int_0^\xi \xi' D_X(\xi')\mathrm{d}\xi'. \tag{5.76}$$

Employing eqns (5.61, 5.68), we obtain the open flux function for generalized Gaussian, ψ_G, and power law, ψ_P, models to be given by

$$\psi_S^O(\xi) = \begin{cases} \psi_G(\xi) = 1 - \frac{\Gamma(2/n_G, \xi^{n_G})}{\Gamma(2/n_G)}; & (n_G > 0): \quad \text{Generalized Gaussian} \\ \psi_P(\xi) = 1 - (1+\xi)^{1-n_P}\big(1 + \xi(n_P - 1)\big); & (n_P > 2): \quad \text{Power law.} \end{cases} \tag{5.77}$$

From eqn (5.77), it is seen that, $\psi_G(\xi)$ and $\psi_P(\xi)$ converges to unity for $\xi \to \infty$. The structure of the self-similar model of a fluxtube is that the magnetic field decreases asymptotically in the radial direction to zero at infinity. The flux tube does not have any sharp boundary which can make a partition with the external solar atmosphere. In other words, the self-similar fluxtube is embedded in a continuous magnetic medium which has the maximum field strength at the base of the axis of the fluxtube and radius of the fluxtube is infinity. We take the effective radius of the fluxtube as the distance from the axis on the $z = 0$ plane, which makes a circular area where 90% of the total flux is enclosed. We call this radius as R_{90}. The total flux is zero at the axis and it increases asymptotically with r. The explicit forms of the magnetic field components, obtained from the eqns (5.75a, 5.75b, 5.75c) by using eqns (5.68, 5.69a, 5.69b, 5.74) are:

$$B_z(\varpi, \bar{z}) = \begin{cases} B_0 y^2(\bar{z}) \exp\left[-\left(\sqrt{\frac{\tau\Gamma(2/n_G)}{n_G \psi_b}} y(\bar{z}) \varpi \right)^{n_G} \right], & (n_G > 0): \quad \text{Generalized Gaussian} \\ B_0 y^2(\bar{z}) \left[1 + \sqrt{\frac{\tau}{(n_P - 1)(n_P - 2)\psi_b}} y(\bar{z}) \varpi \right]^{-n_P}, & (n_P > 2): \quad \text{Power law} \end{cases} \tag{5.78}$$

$$B_r(\varpi,\bar{z}) = \begin{cases} -B_0 y(\bar{z}) y'(\bar{z}) \varpi \exp\left[-\left(\sqrt{\frac{\tau\Gamma(2/n_G)}{n_G \psi_b}} y(\bar{z})\varpi \right)^{n_G} \right], & (n_G > 0): \quad \text{Generalized Gaussian} \\ -B_0 y(\bar{z}) y'(\bar{z}) \varpi \left[1 + \sqrt{\frac{\tau}{(n_P-1)(n_P-2)\psi_b}} y(\bar{z})\varpi \right]^{-n_P}, & (n_P > 2): \quad \text{Power law} \end{cases} \tag{5.79}$$

$$B_\phi(\varpi,\bar{z}) = \begin{cases} B_0 \sqrt{\bar{\chi}} y^2(\bar{z}) \varpi \exp\left[-\left(\sqrt{\frac{\tau\Gamma(2/n_G)}{n_G \psi_b}} y(\bar{z})\varpi \right)^{n_G} \right], & (n_G > 0): \quad \text{Generalized Gaussian} \\ B_0 \sqrt{\bar{\chi}} y^2(\bar{z}) \varpi \left[1 + \sqrt{\frac{\tau}{(n_P-1)(n_P-2)\psi_b}} y(\bar{z})\varpi \right]^{-n_P}, & (n_P > 2): \quad \text{Power law.} \end{cases} \tag{5.80}$$

The magnetic field components $B_r(\varpi,\bar{z})$ and $B_\phi(\varpi,\bar{z})$ for the self-similar model follow the BCs $(1,2,3)$ [eqns (5.10a, 5.10b, 5.10c)] for $R=\infty$. $B_z(\varpi,\bar{z})$ decreases monotonically with ϖ and converges to zero at infinity. The total pressure far from the fluxtube axis is only due to the gas pressure p. We use BC 4 [eqn (5.10d)] at $z=0$, for $r\to\infty$, so that

$$p(r\to\infty,0) = p_0. \tag{5.81}$$

From eqn (5.77), we see that the flux function for both generalized Gaussian and power law, converges to unity at $\varpi\to\infty$, i.e.

$$\psi_S^O(\varpi\to\infty) = 1. \tag{5.82}$$

Using eqns (5.66, 5.81), we obtain

$$\bar{f} = 2(\bar{p}_0 - \bar{p}_c), \tag{5.83}$$

and the explicit form of $p(\varpi, \bar{z})$ for both the generalized Gaussian and the power law models is given by

$$p(\varpi, \bar{z}) = B_0^2 \left(\frac{\bar{f}}{2} \psi^2 + \bar{p}_c e^{-2\bar{k}\bar{z}} \right), \tag{5.84}$$

where $\bar{p}_0 = p_0/B_0^2$ and $\bar{p}_c = p_c/B_0^2$. The formulary of the derived functions for the self-similar fluxtube model are summarized in the Table 5.6. The flowchart of the solutions to the Coulomb function and self-similar models are shown in the Fig. 5.1.

5.4.2 Self-similar closed field model

We have also obtained the closed field structure of the fluxtubes by employing the form of the shape function given by

$$D_Q(\xi) \equiv \Psi_m(a_0 + a_1\xi + a_2\xi^2), \tag{5.85}$$

where Ψ_m is the maximum flux function and a_0, a_1, a_2 are the dimensionless parameters which are to be determined by the same boundary conditions summarized below:

$$\text{BC1}: \quad B_r(r = 0, z) = 0 \tag{5.86a}$$

$$\text{BC2}: \quad B_\phi(r = 0, z) = 0 \tag{5.86b}$$

$$\text{BC3}: \quad \Psi(R, z) = 0 \tag{5.86c}$$

$$\text{BC4}: \quad B_r(R, z) = 0 \tag{5.86d}$$

$$\text{BC5}: \quad p_T(R, z) = p_e(z). \tag{5.86e}$$

The specific form of $D_Q(\xi)$ [eqn (5.85)] is chosen as a second order polynomial of ξ, to obtain a simple field configuration of the fluxtube called closed, where the

flux function, Ψ vanishes at the boundary and the magnetic field lines rise and return to the same horizontal plane [see Figure 5.21]. Plugging eqn (5.85) in eqn (5.76), we obtain

$$\Psi(\xi) = \Psi_m\left(\frac{a_0}{2}\xi^2 + \frac{a_1}{3}\xi^3 + \frac{a_2}{4}\xi^4\right), \tag{5.87}$$

and using the similarity assumption of ST58, B_z and B_r are then given by

$$B_z = \frac{\zeta^2(\bar{z})}{R^2}D(\xi) \tag{5.88a}$$

$$B_r = -\frac{\zeta'(\bar{z})}{Rz_0}\xi D(\xi). \tag{5.88b}$$

Using eqns [5.85, 5.87] with BCs 3 and 4 [eqns (5.86c), (5.86d)] we obtain

$$a_0 + a_1 + a_2 = 0 \tag{5.89a}$$

$$6a_0 + 4a_1 + 3a_2 = 0, \tag{5.89b}$$

where $0 \leq \xi \leq 1$, and $\xi = 1$ is the radius of the boundary of the fluxtube. From eqns (5.89a, 5.89b) we obtain

$$a_1 = -3a_0; \qquad a_2 = 2a_0. \tag{5.90}$$

To find the extrema of $\Psi(\xi)$, we use the relation, $\dfrac{\mathrm{d}\Psi}{\partial\xi} = 0$, and using eqns [5.87, 5.90] we obtain

$$\xi = \frac{1}{2} \quad \text{or} \quad 1, \tag{5.91}$$

and the condition for maxima is $\dfrac{\mathrm{d}^2|\Psi|}{\mathrm{d}\xi^2} < 0$. We see that, $|\Psi\big(\xi = 1/2\big)|$ is a maxima while $|\Psi\big(\xi = 1\big)| = 0$ is a minima, hence $\Psi_m \equiv |\Psi(\xi = 1/2)|$. We study the $a_0 > 0$ solution and the field reversed solution of $a_0 < 0$ can be obtained by taking $B = -B$. Now, for $a_0 > 0$, taking $\xi = \dfrac{1}{2}$ from eqn (5.91), and using eqns [5.87, 5.90], we obtain, $a_0 = 32$, so that from eqns [5.87, 5.90] the form of $\Psi(\xi)$ reduces

to

$$\Psi(\xi) = 16\Psi_m\big(\xi^2 - 2\xi^3 + \xi^4\big). \tag{5.92}$$

From BC 4 [eqn (5.86d)] and eqn (5.88b), we obtain $D(\xi = 1) = 0$; therefore integrating eqn (5.62) from $\xi = 0$ to 1 we obtain

$$\zeta\zeta'' \int_0^1 \xi D^2(\xi)\mathrm{d}\xi - \frac{\zeta^4}{2}\left(\frac{z_0}{R}\right)^2 D_0^2 + \zeta^2 z_0^2 \int_0^1 \frac{1}{2\xi^2}\frac{\partial I_p^2(\xi)}{\partial \xi}\mathrm{d}\xi = 0, \tag{5.93}$$

where $D_0 \equiv D(\xi = 0) = 32\Psi_m$, and the integrals appearing in eqn (5.93) are:

$$\int_0^1 \xi D^2(\xi)\mathrm{d}\xi = \frac{256\Psi_m^2}{15} \qquad \text{and} \qquad \int_0^1 \frac{1}{2\xi^2}\frac{\partial I_p^2}{\mathrm{d}\xi}\partial\xi = \frac{256\chi\Psi_m^2}{15}. \tag{5.94}$$

Following ST58, we define

$$\zeta(\bar{z}) = \sqrt{\frac{B_0}{D_0}}Ry(\bar{z}), \tag{5.95}$$

where $B_0 \equiv B_z(0,0)$, is the magnetic field strength at the center of the fluxtube, and $y(\bar{z})$ is a dimensionless parameter which is defined as

$$y(\bar{z}) = \sqrt{\frac{B_z(0,\bar{z})}{B_0}}. \tag{5.96}$$

Thus eqn (5.93) reduces into

$$\frac{\mathrm{d}y}{\mathrm{d}\bar{z}} = \left[\frac{15}{32\psi_m}(y^4 - 1) - \bar{\chi}(y^2 - 1) + \frac{B_{z0}'^2 z_0^2}{4B_0^2}\right]^{1/2}, \tag{5.97}$$

where $\psi_m = \dfrac{\Psi_m}{B_0 z_0^2}$, $\bar{\chi} = \chi z_0^2$, $\bar{f} = f z_0^4$ are dimensionless parameters, and B'_{z0} is the vertical gradient of the field strength at $z = 0$. Eqn (5.97) can be rewritten as

$$\frac{\mathrm{d}y}{\mathrm{d}\bar{z}} = \sqrt{\frac{15}{32\psi_m}}\big[y^4 - A_1 y^2 + A_2\big]^{1/2}, \tag{5.98}$$

where, $A_1 = \dfrac{32\psi_m\bar{\chi}}{15}$ and $A_2 = \dfrac{8\psi_m B'^2_{z0} z_0^2}{15B_0^2} + \dfrac{32\psi_m\bar{\chi}}{15} - 1$. From eqn (5.98), we obtain

$$\sqrt{\frac{15}{32\psi_m}}\int_0^{\bar{z}} \mathrm{d}z' = \int_1^{y} \frac{\mathrm{d}y'}{[(y'^2-a^2)(y'^2-b^2)]^{1/2}}, \tag{5.99}$$

where, $a = \left(\dfrac{A_1 - \sqrt{A_1^2 - 4A_2}}{2}\right)^{1/2}$ and $b = \left(\dfrac{A_1 + \sqrt{A_1^2 - 4A_2}}{2}\right)^{1/2}$. To obtain the integral on the RHS of eqn (5.99), we first find the integral without the limits is given by

$$\int \frac{\mathrm{d}y'}{\sqrt{(y'^2-a^2)(y'^2-b^2)}}. \tag{5.100}$$

Substituting $y' = a\ \sin\theta$, eqn (5.100) reduces to

$$\int \frac{\mathrm{d}y'}{\sqrt{(y'^2-a^2)(y'^2-b^2)}} = \frac{\kappa}{a}\int \frac{\mathrm{d}\theta}{\sqrt{1-\kappa^2\sin^2\theta}}, \tag{5.101}$$

where $\kappa = a/b$. The integral appeared in eqn (5.101) is called the normal Elliptic–F function of first kind (Byrd and Friedman 1971), which is defined as,

$$F(\theta,\kappa) \equiv \int \frac{\mathrm{d}\theta}{\sqrt{1-\kappa^2\sin^2\theta}}. \tag{5.102}$$

Hence, the explicit form of the integral (5.100) is given by

$$\int \frac{\mathrm{d}y'}{\sqrt{(y'^2-a^2)(y'^2-b^2)}} = \frac{1}{b}\ F\left[\arcsin\left(\frac{y'}{a}\right), \frac{a}{b}\right]. \tag{5.103}$$

From eqn (5.99), we obtain

$$\sqrt{\frac{15}{32\psi_m}}\bar{z} = \frac{1}{b}\left(F\left[\arcsin\left(\frac{w}{a}\right), \frac{a}{b}\right] - F\left[\arcsin\left(\frac{1}{a}\right), \frac{a}{b}\right]\right), \tag{5.104}$$

which can be rewritten as,

$$\arcsin(y/a) = \mathrm{am}\left[F\left[\arcsin\left(\frac{1}{a}\right), \frac{a}{b}\right] + b\bar{z}\sqrt{\frac{15}{32\psi_m}}\right), \frac{a}{b}\right], \tag{5.105}$$

where, $\mathrm{am}(u,\kappa) \equiv F^{-1}(u,\kappa)$, is the inverse of the Elliptic–F function, is called the Jacobi amplitude (Byrd and Friedman 1971). Hence from eqn (5.105), we obtain

$$y(\bar{z}) = a\ \mathrm{sn}\left[F\left[\arcsin\left(\frac{1}{a}\right), \frac{a}{b}\right] + b\bar{z}\sqrt{\frac{15}{32\psi_m}}\right), \frac{a}{b}\right], \tag{5.106}$$

where, $\mathrm{sn}(u,\kappa) \equiv \sin(\mathrm{am}(u,\kappa))$ is called the Jacobian elliptic function. From eqns [5.59, 5.95] we obtain

$$R(\bar{z}) = \frac{\sqrt{32\psi_m}}{y(\bar{z})}, \tag{5.107}$$

which expresses the variation of the radius of the fluxtube with height z. Thus we finally obtain the general form of the magnetic field components from eqns [5.2, 5.13b, 5.88a, 5.88b] to be

$$B_z(\varpi,\bar{z}) = B_0 y^2(\bar{z})\frac{D(\xi)}{D_0}, \tag{5.108a}$$

$$B_r(\varpi,\bar{z}) = -B_0\frac{R}{z_0}\varpi y(\bar{z})y'(\bar{z})\frac{D(\xi)}{D_0}, \tag{5.108b}$$

$$B_\phi(\varpi,\bar{z}) = B_0\frac{R}{z_0}\sqrt{\bar{\chi}}\varpi y^2(\bar{z})\frac{D(\xi)}{D_0}. \tag{5.108c}$$

5.5 Results obtained from the models

5.5.1 Coulomb function helical fluxtube model

This magnetohydrostatic Coulomb function helical fluxtube model consists of the free parameters R and B_0 and its functional dependence through $a(R)$, $\alpha(R)$, $\kappa(R)$, $b(R,B_0)$, $\psi_b(R,B_0)$ and $\bar{p}(R,B_0)$. We choose the parameter range, 1 kG $\leq B_0 \leq$ 1.5 kG and 100 km $\leq R \leq$ 180 km, consistent with the observations of MBP size and field strength distributions (Utz *et al.* 2009, 2013). In Table 5.2, we show the solutions for combinations of the free parameters $\{R, B_0\}$, where we notice the following trends:

- The boundary flux ψ_b decreases with R for same B_0, and with B_0 for same R within the parameter space of runs $C1 - C21$.

- Due to the pressure balance at the boundary of the fluxtube, $\bar{p}$ increases with R for same B_0, but there is no fixed trend with B_0 for same R within the parameter space of runs $C1 - C21$.

As example, we show the solution of ψ_C^O, and the magnetic and thermodynamic structure of the fluxtube for run $C4$. The radial variation of the solution of ψ_C^O, magnetic components and pressure inside the fluxtube are shown in the Figs. 5.3, 5.4 and 5.5 respectively. Examples of 3D configuration of the magnetic field lines for open and closed field are shown in the Figs. 5.6 and 5.7 for runs $C4$ and $C10$. 2D vertical projection of the magnetic field lines for ψ_C^O inside the fluxtube along $r - z$ plane is shown in the Fig. 5.8. The density inside the fluxtube is constant along the radial direction but it decreases along z whereas the temperature varies along r direction and is nearly constant along z direction at the axis. The vertical variation of B_z, p and ρ are shown in the Fig. 5.9. Conclusions from figures and tables are discussed in §5.7.

5.5.2 Self-similar open and closed field models

The self-similar model we developed consists of the dimensionless parameters $\psi_b, \bar{B'}_{z0}, \bar{f}$ and $\bar{\chi}$ which are the functions of the input parameter set $\{\Psi_b,\ B_0,\ B'_{z0},\ p_c,\ \chi\}$. The self-similar fluxtube solutions are spanned by these parameters but the structures remain similar. We use the values of these input parameters in the range, $\Psi_b = 10^{17}$–10^{18} Mx (Zhang *et al.* 1998; Hagenaar *et al.* 1999; Guglielmino *et al.* 2011), B_0 = 1–2 kG (Zhang *et al.* 1998), B'_{z0} in the range 1–2 G-km^{-1} (Wittmann 1974; Pahlke and Wiehr 1990; Balthasar and Schmidt 1993), $p_c < p_0$ [Shelyag *et al.* (2010) and SM18], which are observed for small scale magnetic

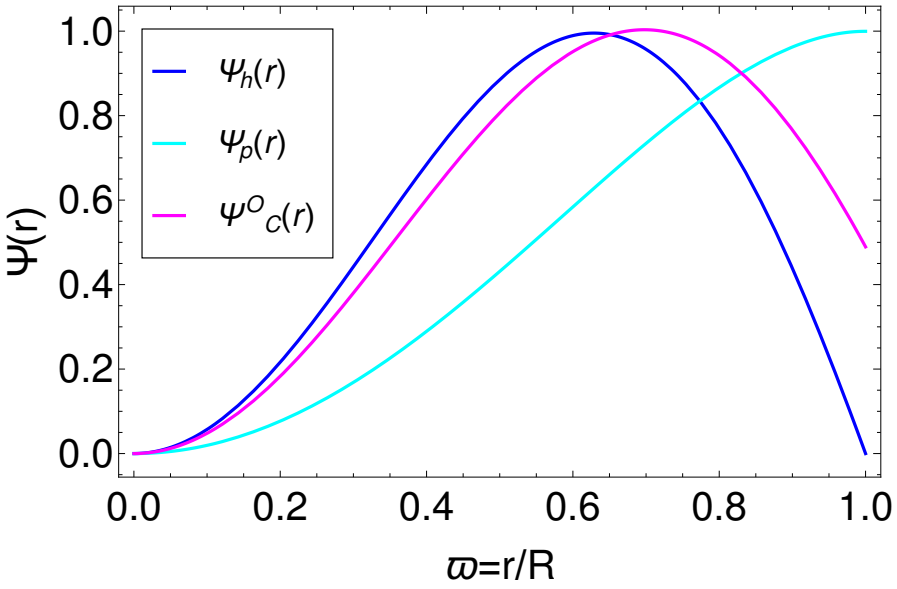

FIGURE 5.3: The radial variation of the flux function, normalized with respect to the maximum value, obtained from Coulomb function open field model for run $C4$ in Table 5.2. The horizontal axis is scaled with respect to the total radius R.

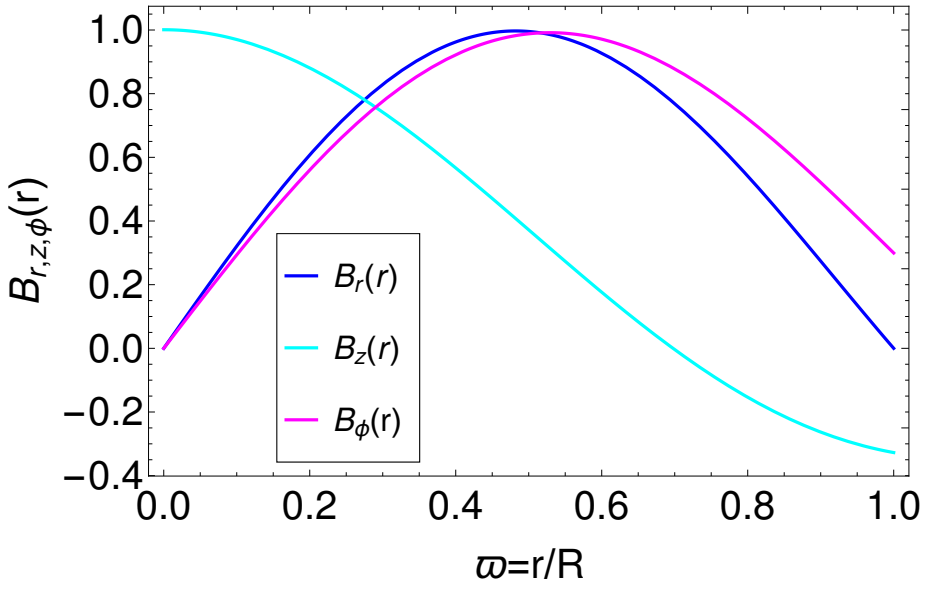

FIGURE 5.4: The radial variation of B_r, B_ϕ and B_z, normalized with respect to the maximum values of $|B_r|$, $|B_\phi|$ and $|B_z|$ respectively, obtained from the Coulomb function open field model, for run $C4$ in Table 5.2. The horizontal axis is scaled with respect to the total radius R.

Run #	B_0 [kG]	R [km]	ψ_b [10^{-3}]	a	α [10^{-2}]	κ [10^6]	b [10^{-3}]	$\bar{p}$
$C1$	1	100	2.57	9.390	2.74	4.85	−1.350	0.109
$C2$	1.2	100	2.22	9.390	2.74	4.85	−1.170	0.105
$C3$	1.5	100	1.80	9.390	2.74	4.85	−0.949	0.104
$C4$	1	120	1.92	9.388	2.54	6.99	−1.008	0.159
$C5$	1.2	120	1.62	9.388	2.54	6.99	−0.849	0.165
$C6$	1.5	120	1.31	9.388	2.54	6.99	−0.692	0.163
$C7$	1	130	1.69	9.389	2.43	8.21	−0.880	0.184
$C8$	1.2	130	1.42	9.389	2.43	8.21	−0.744	0.181
$C9$	1.5	130	1.15	9.389	2.43	8.21	−0.603	0.182
$C10$	1	140	1.50	9.383	2.31	9.52	−0.783	0.205
$C11$	1.2	140	1.25	9.383	2.31	9.52	−0.661	0.204
$C12$	1.5	140	1.00	9.383	2.31	9.52	−0.535	0.208
$C13$	1	150	1.38	9.378	2.18	10.93	−0.723	0.233
$C14$	1.2	150	1.16	9.378	2.18	10.93	−0.606	0.235
$C15$	1.5	150	0.94	9.378	2.18	10.93	−0.492	0.237
$C16$	1	160	1.31	9.388	1.98	12.43	−0.665	0.276
$C17$	1.2	160	1.11	9.388	1.98	12.43	−0.577	0.276
$C18$	1.5	160	0.89	9.388	1.98	12.43	−0.465	0.279
$C19$	1	180	1.14	9.395	1.72	15.73	−0.587	0.402
$C20$	1.2	180	0.96	9.395	1.72	15.73	−0.497	0.407
$C21$	1.5	180	0.78	9.395	1.72	15.73	−0.405	0.409

TABLE 5.2: Numerical values of the different parameters obtained from the Coulomb function open field fluxtube model for different combinations of R and B_0 are shown; the units of the various quantities are in the square brackets at the top.

structures in the photosphere. The generalized Gaussian profile reduces to the Gaussian profile for $n_G = 2$, and it has been shown in §5.4 that, for the power law profile, the flux function converges to finite value, at infinite radius, only for $n_P > 2$. We study the different cases for $n_G = 2$–3, $n_P = 3$–4 and $\bar{\chi} = 0.01$–100 for different combinations of the other parameter sets $\{\bar{\Psi}_b, \bar{B'}_{z0}, \bar{f}\}$, which are shown

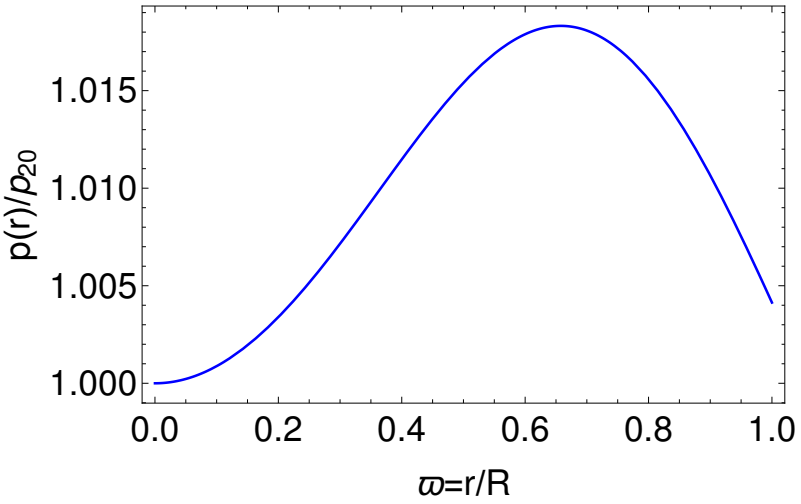

FIGURE 5.5: The radial variation of p normalized with the value at the center of the fluxtube p_{20}, obtained from Coulomb function open field model, for run $C4$ in Table 5.2. The horizontal axis is scaled with the total radius R.

in runs $S1$–$S19$ of Table 5.3. For the parameter set of runs $S1$–$S19$, we find the following results:

- For same Ψ_b and B_0, with the increase of n_G and n_P, R_G and R_P decrease respectively.
- For same n_G, n_P and Ψ_b, with the increase of B_0, R_G and R_P decrease; whereas for same n_G, n_P and B_0; R_G and R_P increase with the increasing of Ψ_b.
- For a fixed parameter set $\{\psi_b,\ \bar{B}'_{z0}\ \bar{f},\ \bar{\chi}\}$, we notice that $R_G > R_P$ for $n_G = 2$ and $n_P = 3$, but for values $n_G \geq 2.5$ and $n_P \geq 3.5$, $R_G < R_P$; this means that the radii of the fluxtubes for the power law profiles falls off more quickly than those of the generalized Gaussian profiles for higher values of n_G and n_P.

As an example, we show the solution of ψ_S^O and the magnetic and thermodynamic structures for run $S1$ of Table 5.3. The values of the magnetic and thermodynamic

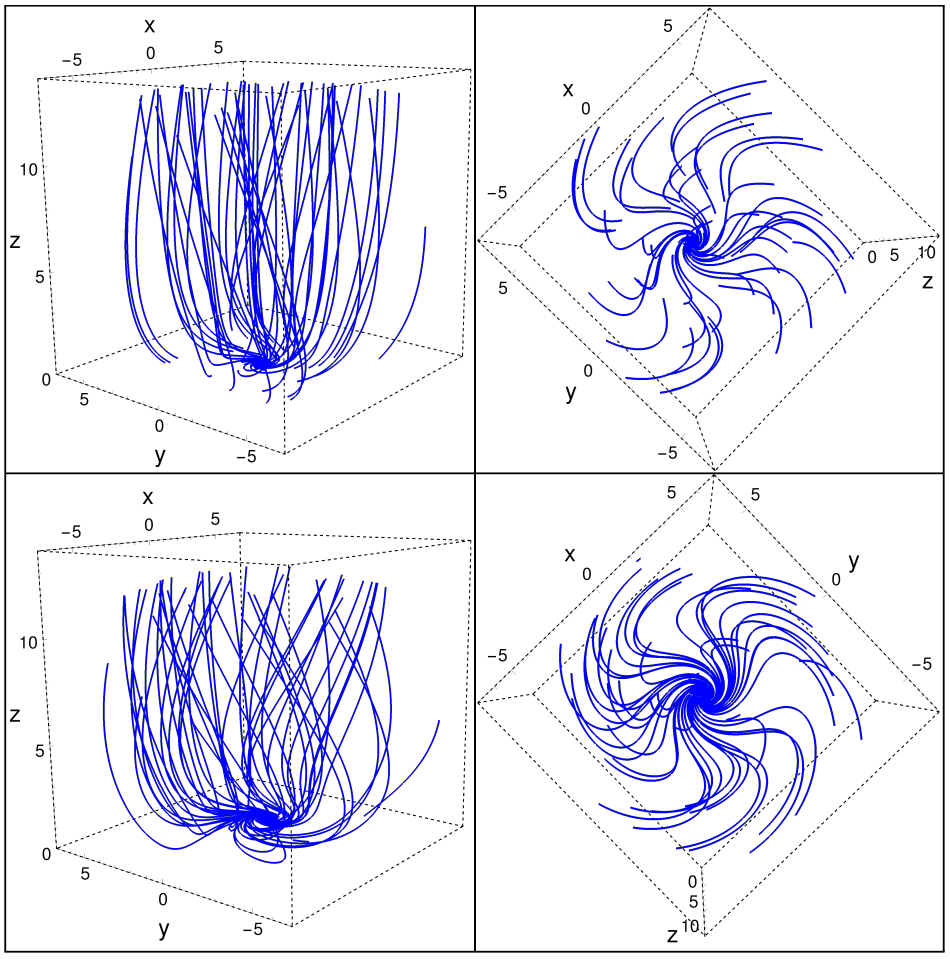

FIGURE 5.6: The 3D configuration of 50 different magnetic field lines for open field fluxtube obtained from the Coulomb function helical fluxtube model. The left and right columns show the side and top view of the configuration. The domain of the simulation box is $-7 \leq x \leq 7$, $-7 \leq y \leq 7$ where the x and y axes are scaled in units of 20 km. The vertical domain is $0 \leq z \leq 14$ where the z axis is scaled in units of 150 km. The field line configurations for the bottom and the top rows are simulated for the parameter sets of runs $C4$ and $C10$ respectively in Table 5.2.

quantities obtained from the self-similar model are reported in Table 5.5, for both the Gaussian and power law shape function profiles. The radial variation of the generalized Gaussian and power law flux function are shown in the Fig. 5.10 for different values of n_G and n_P, and the variation along the $r - z$ plane is shown in Fig. 5.11. The 3D configuration of the field lines for the generalized Gaussian and power law self-similar models are shown in the Figs. 5.12 and 5.13 for the parameter sets for runs $S1$ and $S2$ given in Table 5.3. The radial and

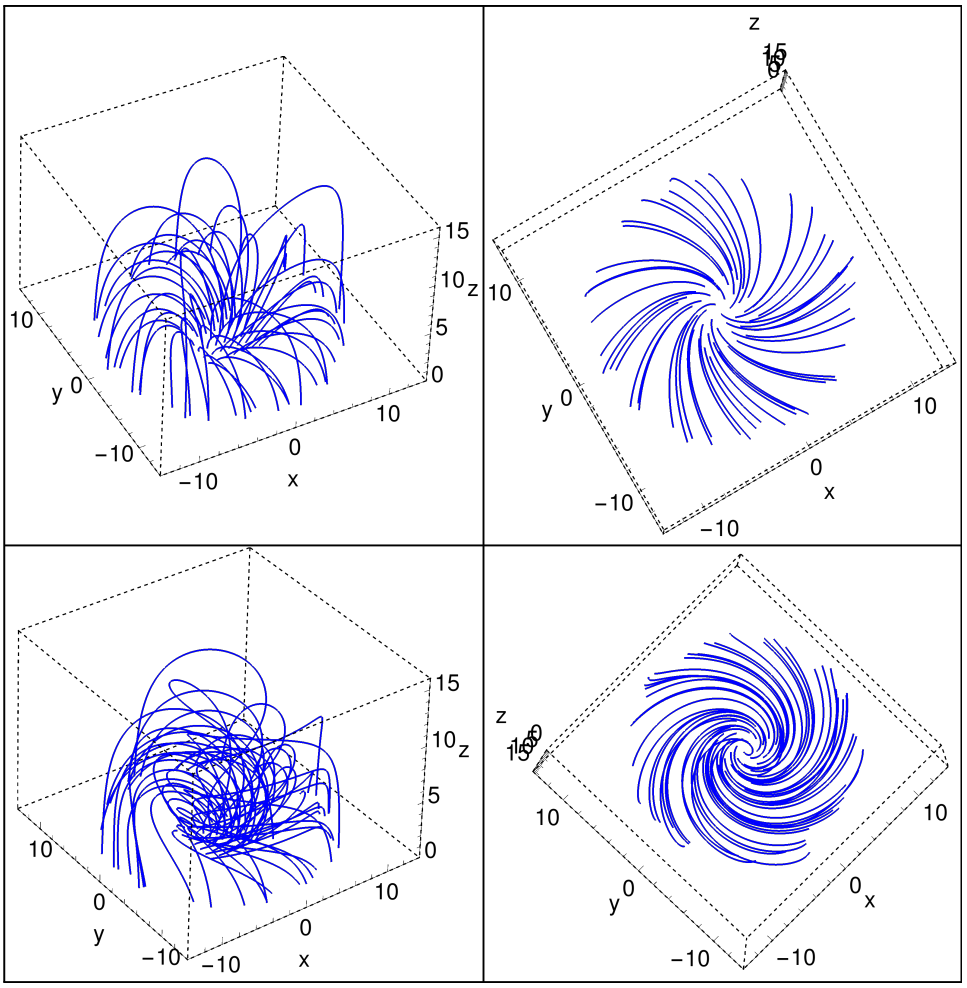

FIGURE 5.7: The 3D configuration of 50 different magnetic field lines for closed field fluxtube obtained from the Coulomb function helical fluxtube model. The left and right columns show the side and top view of the configuration. The domain of the simulation box is $-14 \leq x \leq 14$, $-14 \leq y \leq 14$ where the x and y axes are scaled in units of 10 km. The vertical domain is $0 \leq z \leq 15$ where the z axis is scaled in units of 150 km. The field line configurations for the bottom and the top rows are simulated for the parameter sets of runs $C4$ and $C10$ respectively in Table 5.2.

vertical distribution of the magnetic field components are shown in Figs. 5.14 and 5.15 respectively for both the Gaussian and power law models, whereas the density inside the fluxtube does not vary along $r-$direction but decreases along the $z-$direction which is shown in the Fig. 5.16. The variation of p and T in the $r-z$ plane obtained from the self-similar open field model are shown in Figs. 5.25 and 5.26 for Gaussian and power law shape function profiles. Conclusions drawn from Figures [5.6, 5.7, 5.9, 5.12, 5.13, 5.16, 5.24, 5.25, 5.26, 5.28] and Tables [5.2,

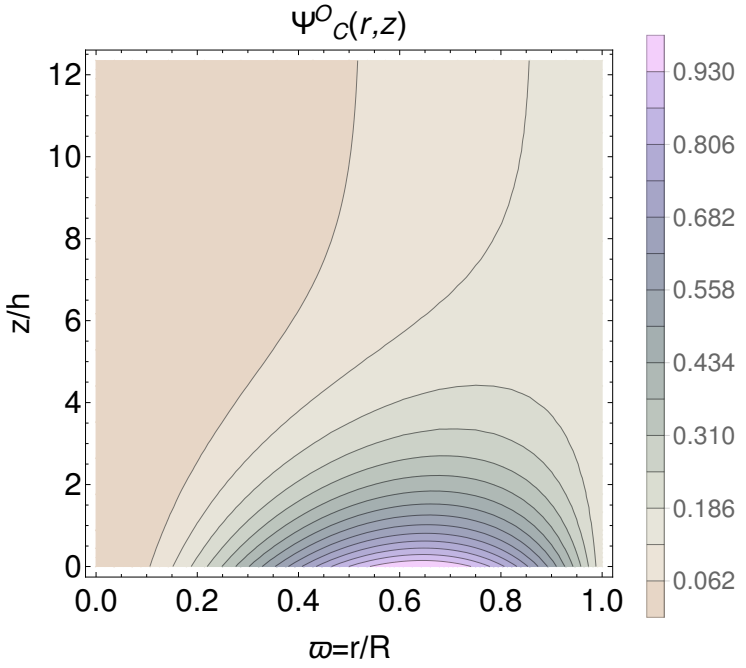

FIGURE 5.8: A contour plot of the flux function corresponding to run $C4$ in Table 5.2, obtained from the Coulomb function open fluxtube model. The horizontal axis is scaled to the radius R and the vertical axis is scaled to the pressure scale height $h = 162$ km. The contours have been normalized with respect to the maximum value of the flux function.

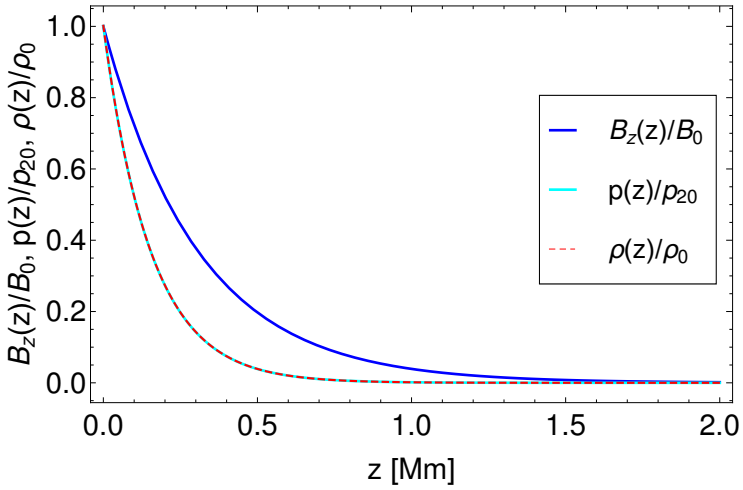

FIGURE 5.9: The vertical distribution of B_z, p and ρ, normalized with respect to the values at the fluxtube center, B_0, p_{20} and ρ_0 respectively, obtained from Coulomb function open field model for the parameter set of run $C4$ in Table 5.2. The horizontal axis is scaled in the units of Mm. The values of the scale factors are $B_0 = 1$ kG, $p_{20} = 1.03 \times 10^5$ dyne cm^{-2} and $\rho_0 = 2.44 \times 10^{-7}$ g cm^{-3}.

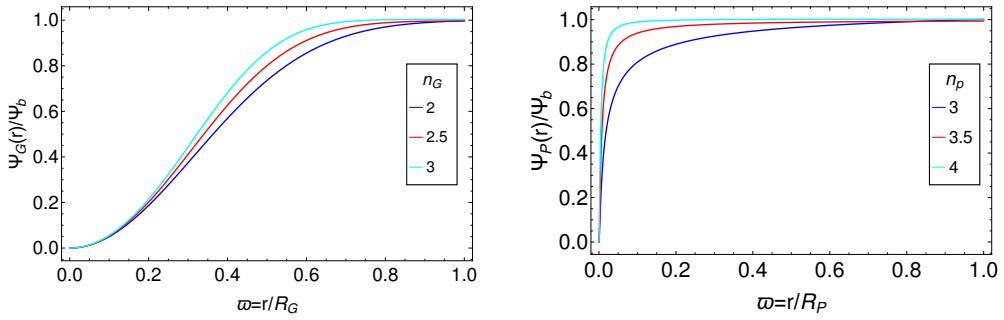

FIGURE 5.10: The radial variation of the flux function, normalized with respect to the maximum values for different values of n for generalized Gaussian (*left*) and power law (*right*) shape functions for the parameter set of run $S1$ in Table 5.3. The horizontal axes are scaled with the total radius R.

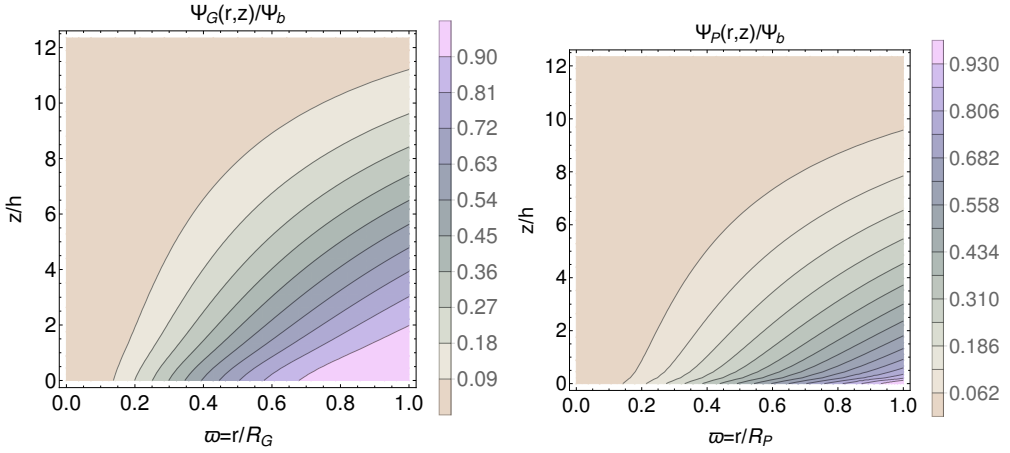

FIGURE 5.11: Contour plots of the flux functions for Gaussian (*left*) and power law (*right*) profiles for $n_P = 3$ for the parameter set of run $S1$ in Table 5.3. The horizontal axes are scaled with the total radii $R_G = 214$ and $R_P = 261$ km, and the vertical axes are scaled with the pressure scale height $h = 162$ km. The contours are normalized with respect to the maximum value of the flux function.

5.3, 5.5] are discussed in §5.7.

For the self-similar closed field model, we study the allowed parameter range with $\bar{\chi} = 0.01 - 10$ and $\bar{f} = 0.01 - 1$ for the different combinations of the parameter set $\{\Psi_m, B_0, B'_{z0}\}$, which are shown in the Table 5.4 for runs $S1 - S19$. For these runs, we find the following results:

Run #	Ψ_b	B_0	p_c	B'_{z0}	χ	f	n_G	n_P	ψ_b	$\bar{f}$	$\bar{B}'_{z0}$	$\bar{\chi}$	R_G	R_P
	[10^{17} Mx]	[kG]	[10^5 dyne cm^{-2}]	[G km^{-1}]	[cm^{-2}]	[10^{-30} cm^{-4}]							[km]	[km]
$S1$	1	1	1	1	10^{-16}	4.56	2	3	0.01	456	1	1	214	261
$S2$	1	1	1	1	10^{-14}	4.56	2	3	0.01	456	1	100	214	261
$S3$	1	1	0.8	1.5	10^{-18}	8.56	2.5	3.5	0.01	856	1.5	0.01	196	138
$S4$	1	1	0.5	2	10^{-16}	14.56	3	4	1	1456	2	1	186	100
$S5$	1	2	1	1	10^{-14}	4.56	2	3	0.005	456	0.5	100	151	184
$S6$	1	2	0.8	1.5	10^{-18}	8.56	2.5	3.5	0.005	856	0.75	0.01	139	98
$S7$	1	2	0.5	2	10^{-16}	14.56	3	4	0.005	1456	0.25	1	131	71
$S8$	5	1	1	1	10^{-14}	0.182	2	3	0.005	18.2	1	100	479	584
$S9$	5	1	0.8	1.5	10^{-18}	0.342	2.5	3.5	0.005	34.2	1.5	0.01	439	308
$S10$	5	1	0.5	2	10^{-16}	0.582	3	4	0.005	58.2	2	1	416	225
$S11$	5	2	1	1	10^{-14}	0.182	2	3	0.025	18.2	0.5	100	339	413
$S12$	5	2	0.8	1.5	10^{-18}	0.342	2.5	3.5	0.025	34.2	0.75	0.01	310	218
$S13$	5	2	0.5	2	10^{-16}	0.582	3	4	0.025	58.2	0.25	1	294	159
$S14$	10	1	1	1	10^{-14}	0.0456	2	3	0.1	4.56	1	100	678	826
$S15$	10	1	0.8	1.5	10^{-18}	0.0856	2.5	3.5	0.1	8.56	1.5	0.01	621	436
$S16$	10	1	0.5	2	10^{-16}	0.145	3	4	0.1	14.56	2	1	589	318
$S17$	10	2	1	1	10^{-14}	0.0456	2	3	0.05	4.56	0.5	100	479	584
$S18$	10	2	0.8	1.5	10^{-18}	0.0856	2.5	3.5	0.05	8.56	0.75	0.01	439	308
$S19$	10	2	2	0.5	10^{-16}	0.145	3	4	0.05	14.56	0.25	1	416	225

TABLE 5.3: Different combinations of the input parameters and the dimensionless parameters for the self-similar model where R_G and R_P represents the radii of the fluxtubes for generalized Gaussian and power law profiles respectively.

1. The radius of the fluxtube at the transition region (R_t) is more than the radius at the photosphere (R_0), which implies that the fluxtube is expanding with height, as expected.

2. For the same Ψ_m, with the increase of B_0, both R_0 and R_t increase, while for same B_0, with the increase of Ψ_m, both R_0 and R_t increase.

As an example, we show the solution of the fluxtube, including the magnetic and thermodynamic structures for the parameter set for run $S1$ in Table 5.4. The radial variation of the flux function is shown in Figure 5.17, and the variation along the $r-z$ plane is shown in Figure 5.18.

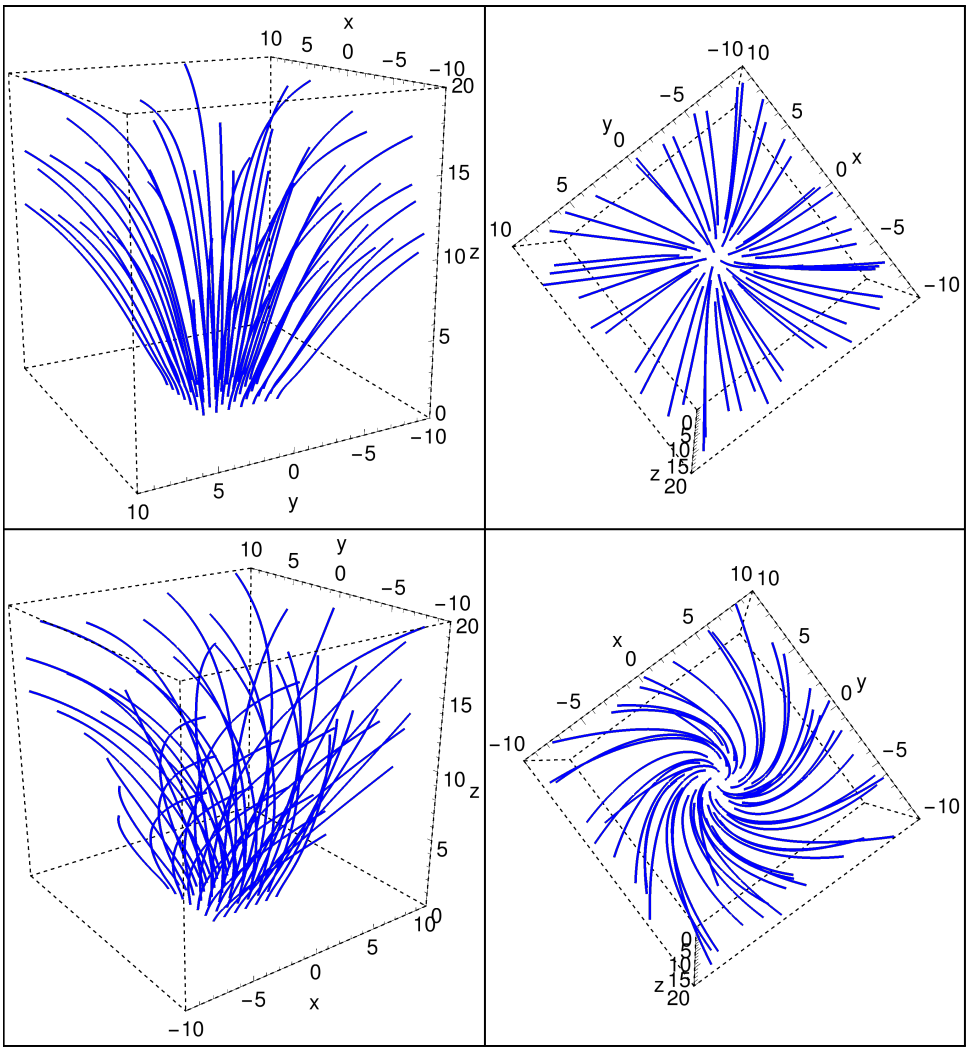

FIGURE 5.12: The 3D configuration of 50 different open field lines inside the fluxtube obtained from self-similar model for Gaussian profile. The left and the right columns show the side and the top view of the configurations. The domain of the simulation box is $-10 \leq x \leq 10$, $-10 \leq y \leq 10$ and $0 \leq z \leq 20$ where the x, y and z axes are scaled in units of 100 km. The field line configurations for the bottom and the top rows are simulated for the parameter values of Table 5.3 corresponding to runs $S1$ and $S2$ respectively.

The radial variation of the magnetic field components B_z, B_r, B_ϕ are shown in Figure 5.19, and the variation along $r - z$ plane is shown in Figure 5.20, where all the components B_z, B_r, B_ϕ go to zero at the boundary. The 3D geometry of the field lines inside the fluxtube is shown in Figure 5.21, which indicates a closed field configuration. The radius of the fluxtube increases with the vertical height, z, as seen in Figure 5.22.

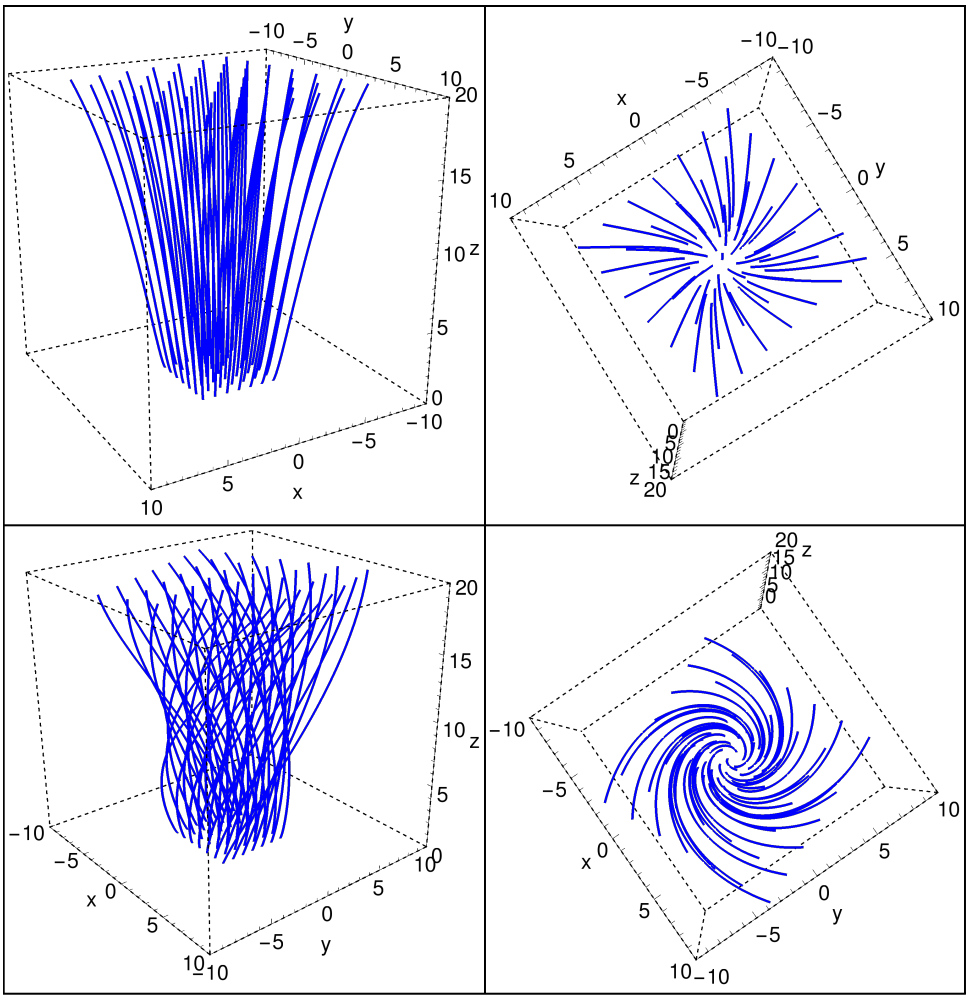

FIGURE 5.13: The 3D configuration of 50 different open field lines inside the fluxtube obtained from self-similar model for power law profile with $n_P = 3$. The left and the right columns show the side and the top view of the configurations. The domain of the simulation box is $-10 \leq x \leq 10$, $-10 \leq y \leq 10$ and $0 \leq z \leq 20$ where the x, y and z axes are scaled in units of 100 km. The field line configurations for the bottom and the top rows are simulated for the parameter sets of runs $S1$ and $S2$ respectively corresponding to Table 5.3.

The magnetic and thermodynamic quantities obtained from the model are given in Table 5.5, and we observe the following:

1. The vertical magnetic field strength decreases from the axis ($r = 0$) to the boundary R_c.

2. There is no radial variation of the gas pressure at the photosphere ($z = 0$), whereas at the transition region ($z = 2$ Mm), p increases with r from the axis

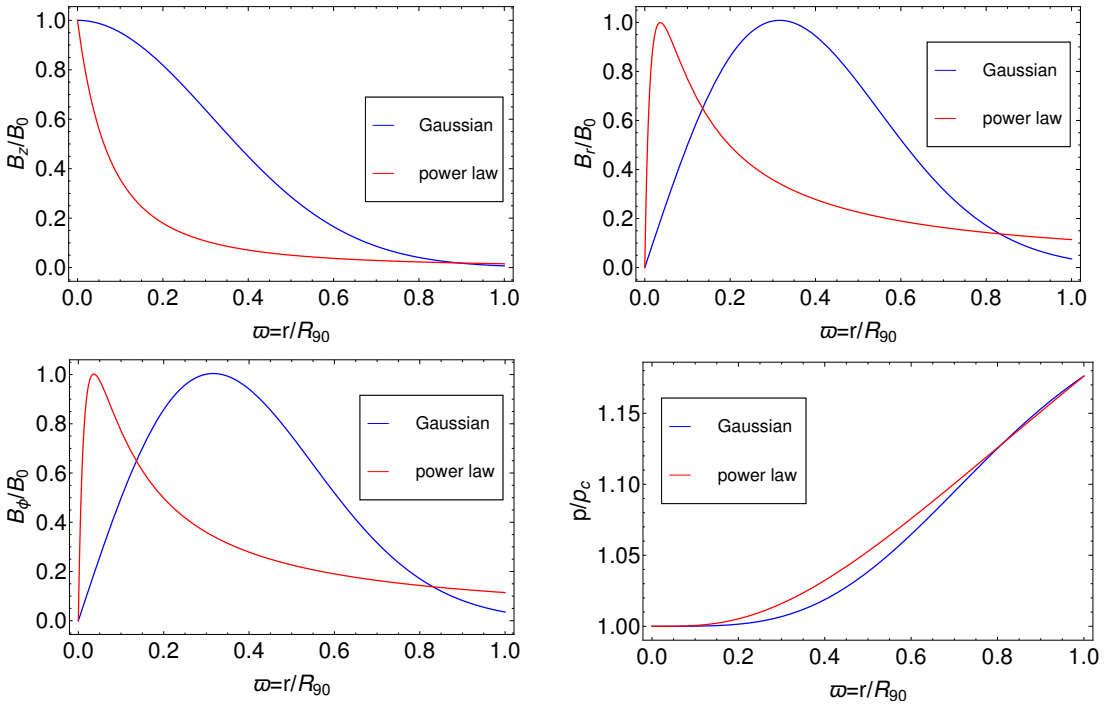

FIGURE 5.14: The radial distribution of the magnetic field components B_z, B_r, B_ϕ and gas pressure p normalized with respect to the values at the fluxtube center, B_0, p_c, for Gaussian and power law shape functions for the parameter set of run $S1$ in Table 5.3. The horizontal axes are scaled with the total radius of the fluxtube R and the values of the scale factors are $B_0 = 1$ kG and $p_c = 10^5$ dyne cm^{-2}.

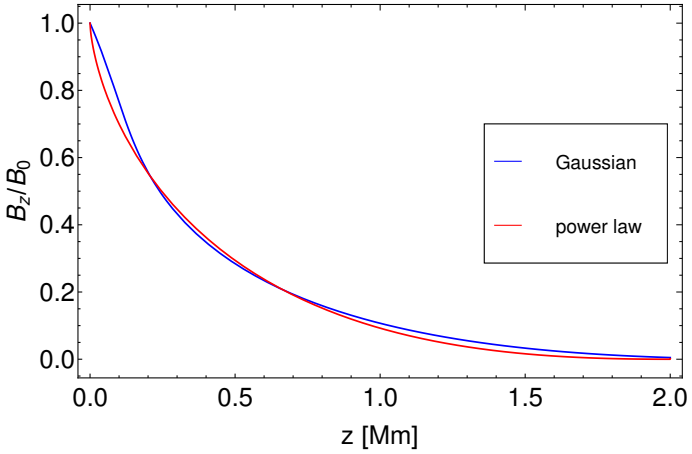

FIGURE 5.15: The vertical distribution of B_z at the axis of the fluxtube, obtained from the self-similar model for the Gaussian and power law profiles for the parameter set of run $S1$ in Table 5.3.

to the boundary and p decreases with vertical height, z, from the photosphere to the transition region.

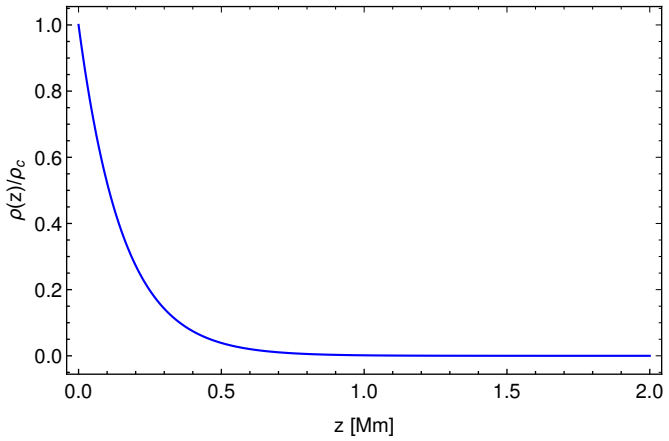

FIGURE 5.16: The vertical distribution of density, $\rho(z)$ obtained from the self-similar model for the parameter set of run $S1$ in Table 5.3, which is normalized with respect to $z = 0$ value, ρ_c, for both Gaussian and power law profiles. The horizontal axis is scaled in units of Mm. The value of scale factor $\rho_c = 2.37 \times 10^{-7}$ g cm^{-3}.

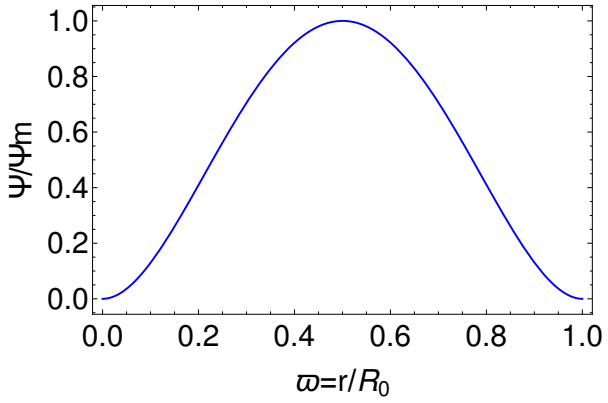

FIGURE 5.17: The radial variation of the normalized flux function, Ψ, for the parameter set of run $S1$ in Table 5.4 is shown. The horizontal axis is scaled with the fluxtube radius R_0.

3. The density, ρ has no variation with r, but it decreases with z, from the photosphere to the transition region.

4. The temperature, T has no radial variation at $z = 0$, but it increases with height at the boundary.

This implies that the fluxtube has a nearly plane-parallel atmosphere and is non-isothermal.

Run #	Ψ_m [10^{17} Mx]	B_0 [kG]	B'_{z0} [G km^{-1}]	$\bar{\chi}$	$\bar{f}$	ψ_m [10^{-2}]	R_0 [Mm]	R_t [Mm]
S1	1	1	1	0.01	0.01	1	0.565	22.70
S2	1	1	1	0.1	0.01	1	0.565	22.70
S3	1	1.5	1.2	0.1	0.1	0.67	0.461	18.53
S4	1	2	1.5	1	1	0.5	0.40	16.05
S5	1	1	1	10	0.01	1	0.565	22.70
S6	1	1.5	1.2	0.01	1	0.67	0.461	18.53
S7	1	2	1.5	0.1	1	0.5	0.40	16.05
S8	5	1	1	1	0.01	5	1.26	50.77
S9	5	1.5	1.2	10	0.1	3.33	1.03	41.45
S10	5	2	1.5	0.01	1	2.50	0.89	35.90
S11	5	1	1	0.1	0.01	5	1.26	50.77
S12	5	1.5	1.2	1	0.1	3.33	1.03	41.45
S13	5	2	1.5	10	1	2.5	0.89	35.90
S14	10	1	1	0.01	0.01	10	1.78	71.80
S15	10	1.5	1.2	0.1	0.1	6.67	1.46	58.67
S15	10	2	1.5	1	1	5	1.26	50.77
S17	10	1	1	10	0.01	10	1.78	71.80
S18	10	1.5	1.2	0.01	0.1	6.67	1.46	58.67
S19	10	2	1.5	0.1	1	5	1.26	50.77

TABLE 5.4: The different combinations of the input parameters for the self-similar closed field model are shown where R_0 and R_t represent the radii of the fluxtube at $z = 0$ and $z = z_t$ respectively.

5.6 Comparing our models with observations

We compare our models with the observations reported by the high resolution and high cadence instruments. The small scale magnetic structures in the solar

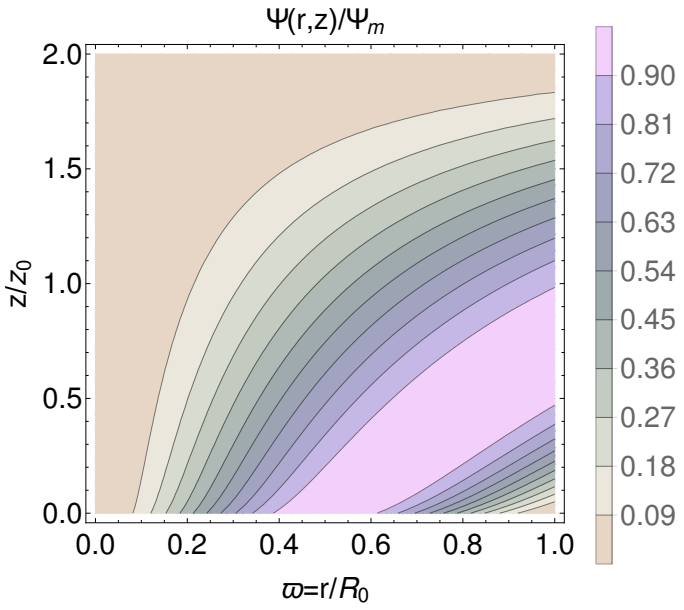

FIGURE 5.18: A contour plot of the normalized flux function is shown along the $r-z$ plane, corresponding to run $S1$ in Table 5.4. The horizontal axis is scaled with the radius of the fluxtube, R_0, and the vertical axis is scaled to a constant $z_0 = 1$ Mm. The contours are normalized with respect to the maximum value Ψ_m.

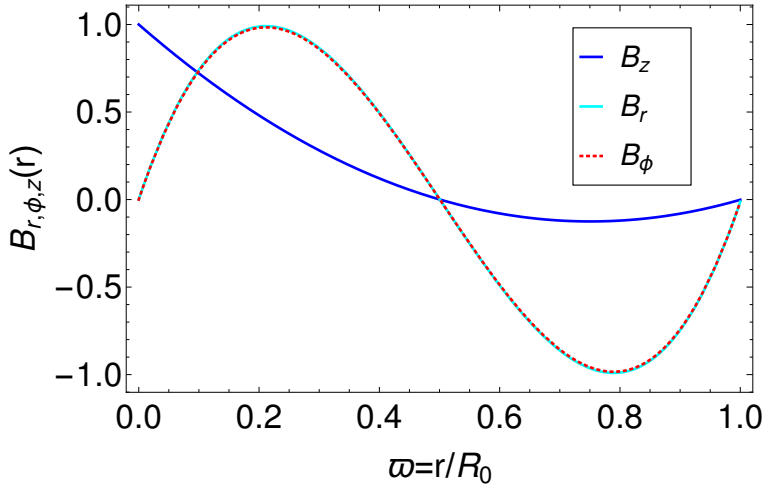

FIGURE 5.19: The radial variation of the magnetic field components B_z, B_r, B_ϕ for the parameter set of run $S1$ in Table 5.4 is shown. The horizontal axis is scaled with the fluxtube radius R_0.

photosphere are often found in the forms of the magnetic bright points (MBPs) which are small scale magnetic fluxtubes with open field lines (Berger *et al.* 1995;

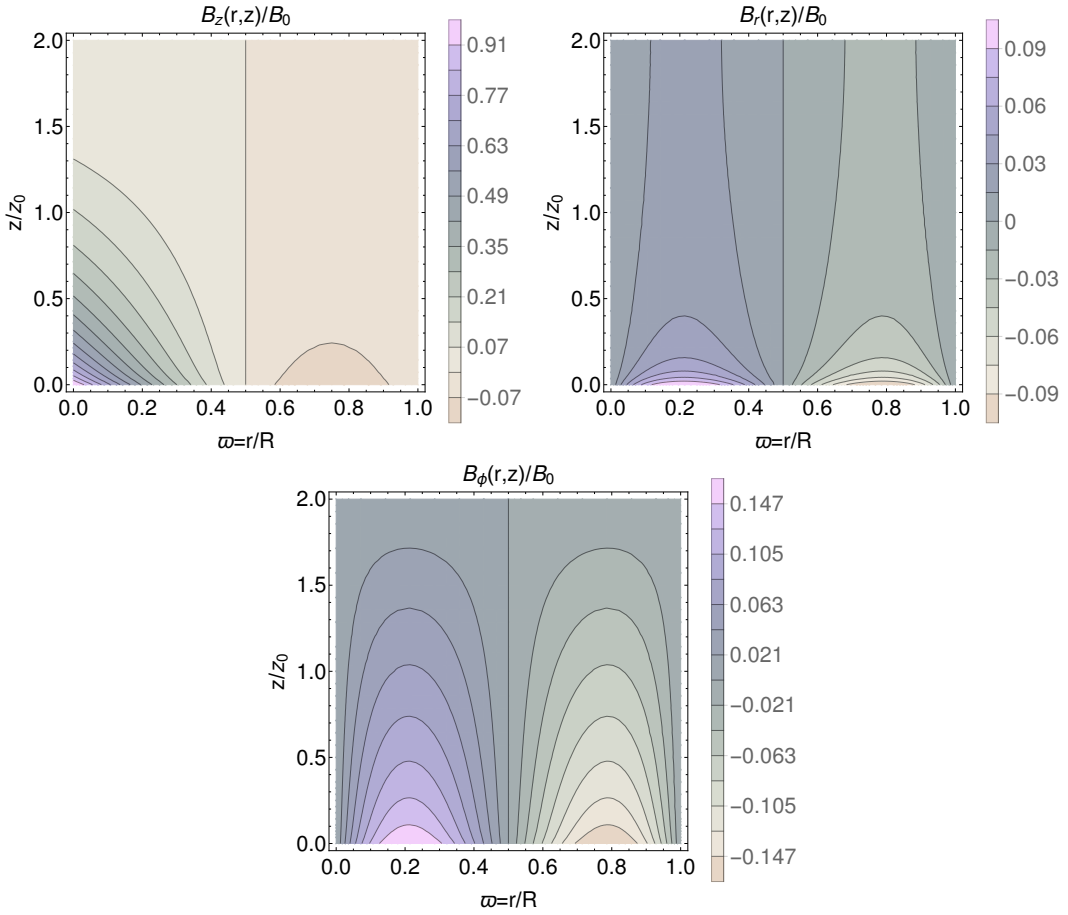

FIGURE 5.20: The 2D variation of B_z, B_r, B_ϕ along $r-z$ plane, corresponding to run $S1$ in Table 5.4 is shown above. The horizontal axes are scaled with the radius of the fluxtube, R, and the vertical axes are scaled to a constant $z_0 = 1$ Mm. The contours are normalized with respect to B_0.

Centeno *et al.* 2007; Lagg *et al.* 2010). Therefore the MBPs are the best candidates to compare our open field fluxtube models with the observations. MBPs can be identified by spectropolarimetric measurements or they can be seen by the G-band filtergrams (Utz *et al.* 2009, 2013; Yang *et al.* 2016). Next, we compare the observed magnetic field strength, size and the thermodynamic quantities of the MBPs with that obtained from our models. The MBPs are observed as a region of the unipolar flux concentration, therefore, in the Coulomb function model, we construct a cylindrical boundary of cut-off radius r_b inside the total simulation domain, where the line of sight magnetic field B_z vanishes. The magnetic field strength inside the cylinder of the cut-off radius is always positive. From the

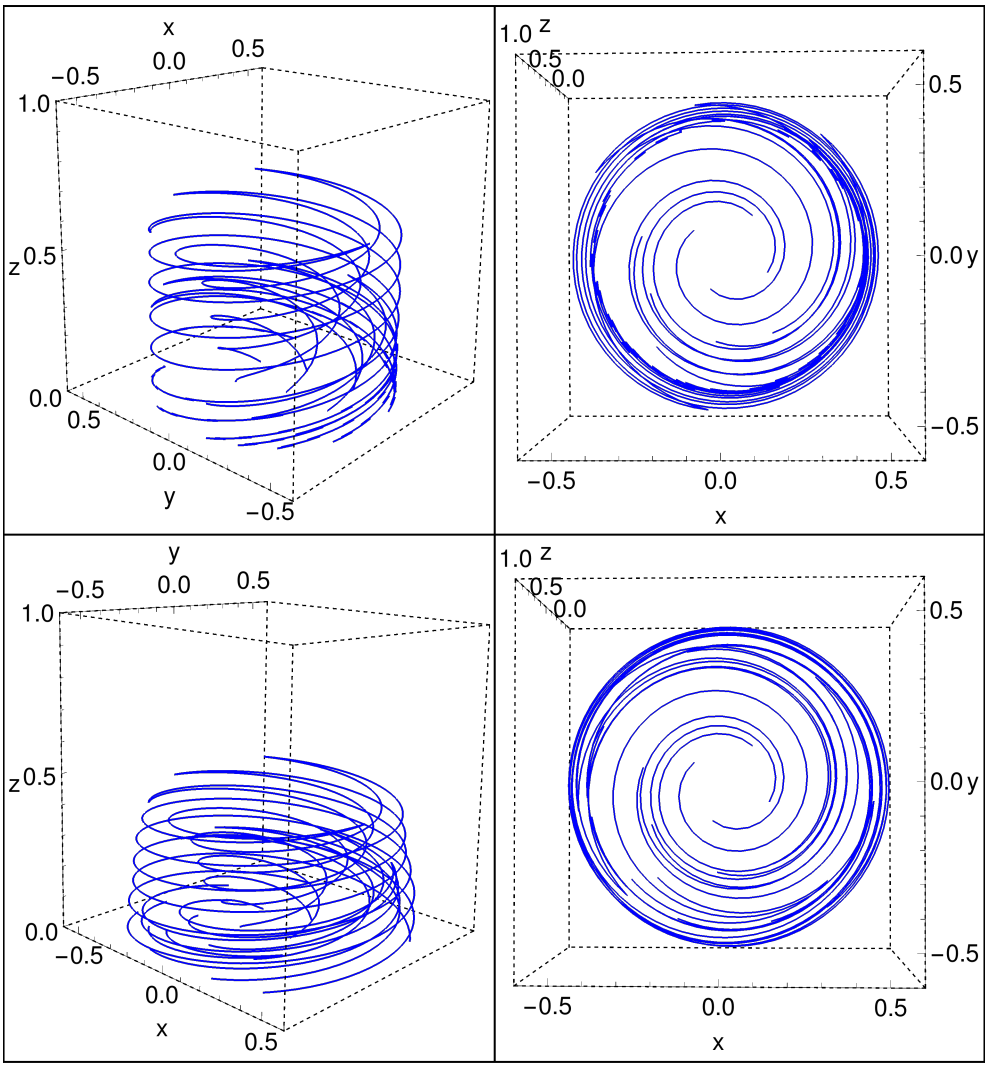

FIGURE 5.21: The 3D geometry of 10 different magnetic field lines for self-similar closed field fluxtube model. The left and right columns show the side and top view of the configuration. The domain of the simulation box is $-0.5 \leq x \leq 0.5$, $-0.5 \leq y \leq 0.5$, where the x and y axes are scaled in units of 500 km. The vertical domain is $0 \leq z \leq 1$ where the z axis is scaled in units of 2 Mm. The field line configurations for the bottom and the top rows are simulated for the parameter sets of runs S1 and S2 respectively in Table 5.4.

recent observations by Utz *et al.* (2009, 2013), it has been reported that the MBPs number distribution for the size, peaks in the range 160-200 km and the magnetic field strength is at $\sim$ 1.4 kG. From the Fig. 5.4 we see that the B_z vanishes at r_b = 84 km, where R = 120 km is the entire radial simulation domain. We choose the parameter range, 1 kG $\leq B_0 \leq$ 1.5 kG and 100 km $\leq R \leq$ 180 km, for

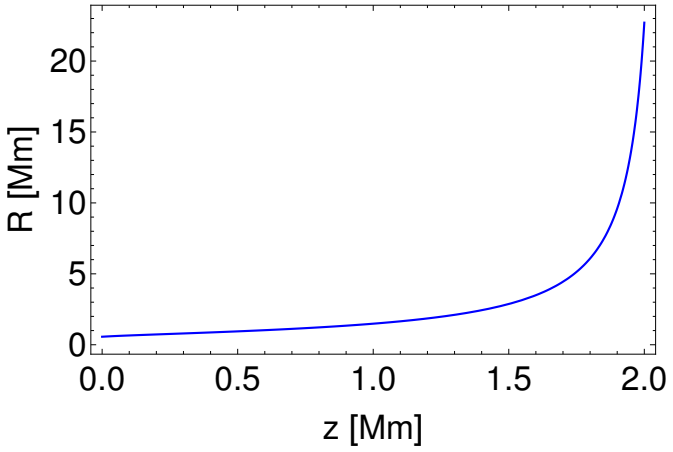

FIGURE 5.22: The vertical variation of the fluxtube radius corresponding to run S1 in Table 5.4 is shown.

which the magnetic and thermodynamic quantities obtained from our model is in reasonable agreement with the solar atmosphere (Vernazza *et al.* 1981), and the selection of the $\{R, B_0\}$ parameter space is also consistent with the observations of MBP size and field strength distributions (Utz *et al.* 2009, 2013). The values of the magnetic and thermodynamic quantities obtained from the Coulomb function open field model are reported in Table 5.5. For the self-similar model, the choice of the parameter space is consistent with the MBPs. We take the flux value in the range of 10^{17}–10^{18} Mx which is the typical flux value for MBPs (Zhang *et al.* 1998; Hagenaar *et al.* 1999; Guglielmino *et al.* 2011). According to the previous studies by Shelyag *et al.* (2010) and SM18, the gas pressure at the axis of MBP is lesser than its boundary gas pressure, so we have chosen the parameter $p_c < p_0$. The field strength of the magnetic footpoints observed in the photosphere for MBPs are $\sim$ 1 kG with a distribution peak at 1.3 kG (Utz *et al.* 2013). Thus, we use the value of B_0 in the typical range of 1–2 kG (Zhang *et al.* 1998) in our model. The vertical gradient of the magnetic field strength at the photosphere is $\sim$ 1 G-km^{-1} (Wittmann 1974; Pahlke and Wiehr 1990; Balthasar and Schmidt 1993). Hence we use the value of B'_{z0} in the range of 1–2 G-km^{-1} in our model. We have reported the combinations of the free parameters and the corresponding input parameters in Table 5.3. Within the parameter sets of runs $S1$–$S19$ in Table 5.3

Models	r	z	B_z	p	ρ	T
		[Mm]	[G]	[dyne cm^{-2}]	[g cm^{-3}]	[K]
Coulomb function closed field (SM18)	0	0	2370	1.358×10^4	3.22×10^{-8}	5656
	0	2	2.19	3.09×10^{-2}	7.33×10^{-14}	5656
	r_0	0	0	1.373×10^4	3.22×10^{-8}	5718
	r_0	2	0	3.12×10^{-2}	7.33×10^{-14}	5718
Coulomb function open field (SM19)	0	0	1000	1.03×10^5	2.44×10^{-7}	5656
	0	2	2.61	0.234	5.56×10^{-13}	5656
	r_0	0	0	1.04×10^5	2.44×10^{-7}	5690
	r_0	2	0	0.2445	5.56×10^{-13}	5890
Generalized Gaussian (SM19)	0	0	1000	1.0×10^5	2.37×10^{-7}	5630
	0	2	3.44	0.227	5.44×10^{-13}	5630
	R_G	0	6.73	1.17×10^5	2.37×10^{-7}	6620
	R_G	2	2.2	1.54	5.44×10^{-13}	38000
Power-law (SM19)	0	0	1000	1.0×10^5	2.37×10^{-7}	5630
	0	2	75	0.227	5.44×10^{-13}	5630
	R_P	0	50	1.17×10^5	2.37×10^{-7}	6620
	R_P	2	19	1.75	5.44×10^{-13}	43000
Self-similar closed field (in preparation)	0	0	1000	1.22×10^5	2.91×10^{-7}	5631
	0	2	0.62	0.277	6.63×10^{-13}	5631
	R_c	0	0	1.22×10^5	2.91×10^{-7}	5631
	R_c	2	0	0.778	6.63×10^{-13}	15760

TABLE 5.5: The values of magnetic field strength and thermodynamic quantities obtained from the various fluxtube models, where $r_0 = 84$ km, $R_G = 214$ km, $R_P = 261$ km, and $R_c = 282$ km.

and 5.4, we notice that the minimum and maximum radii of the fluxtubes are 151 and 678 km respectively for Gaussian model, 71 and 826 km respectively for the power-law model, and 400 and 1780 km for the closed field model, which are in the reasonable agreement with the observations of MBP size distributions (Utz *et al.* 2009). The values of the magnetic and thermodynamic quantities obtained from

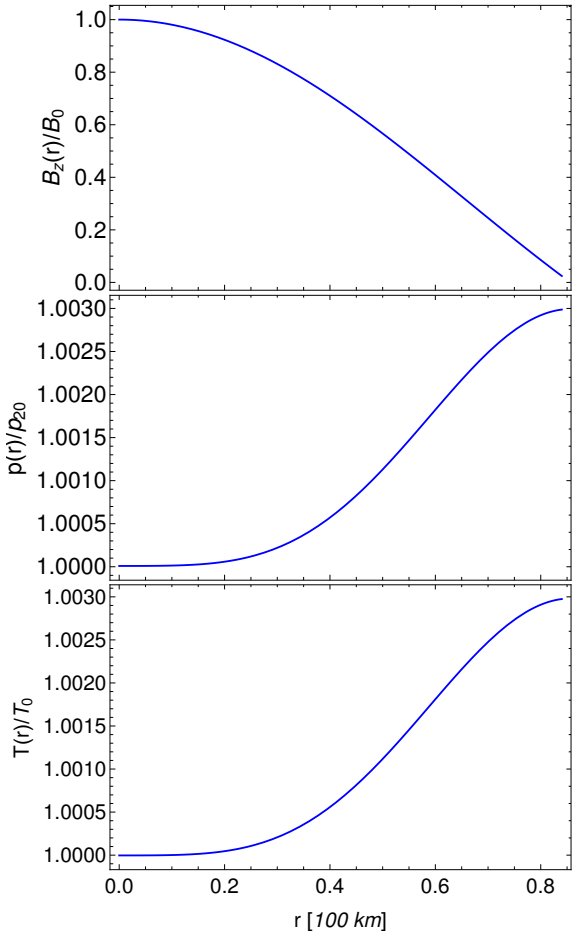

FIGURE 5.23: The vertical distribution of B_z, p and T, normalized with respect to the value at the center of the fluxtube, B_0, p_{20} and T_0 respectively from the axis of the fluxtube to the MBP boundary for $r_b = 84$ km at $z = 0$, obtained from the Coulomb function open fluxtube model for the parameter set of run $C4$ in Table 5.2. The horizontal axis is scaled in the units of 100 km and the values of the scale factors are $B_0 = 1$ kG, $p_{20} = 1.03 \times 10^5$ dyne cm^{-2} and $T_0 = 5656$ K.

the self-similar open and closed field models are reported in Table 5.5 respectively, which are also in reasonable agreement with the solar atmosphere reported by Vernazza *et al.* (1981).

Functions	Formulae for the Coulomb function model
$s(\varpi)$	$c(F_0\big(-\alpha-\kappa^2,\sqrt{a}\varpi^2\big)+F_0^*\big(-\alpha-\kappa^2,\sqrt{a}\varpi^2\big)$
$Z(\bar{z})$	$\exp\Big(-\dfrac{2\sqrt{2}\kappa a^{1/4}\bar{z}}{\tau}\Big)$
$\psi_p(\varpi)$	$\dfrac{i\sqrt{a}b\varpi^2}{4\psi_b}\Big[e^{i\sqrt{a}\varpi^2}\sum_{n=0}^{\infty}\dfrac{F_2^1\big(n+2,1;n+2-i\alpha;\frac{1}{2}\big)(-i\sqrt{a}\varpi^2)^n}{(n+1-i\alpha)n!}-e^{-i\sqrt{a}\varpi^2}\sum_{n=0}^{\infty}\dfrac{F_2^1\big(n+2,1;n+2+i\alpha;\frac{1}{2}\big)(i\sqrt{a}\varpi^2)^n}{(n+1+i\alpha)n!}\Big]$
$\psi_C(\varpi,\bar{z})$	$s(\varpi)Z(\bar{z})+\psi_p(\varpi)$
$B_r(\varpi,\bar{z})$	$\dfrac{B_0\sqrt{2}\psi_b\kappa}{a^{1/4}}s(\varpi)Z(\bar{z})$
$B_z(\varpi,\bar{z})$	$\dfrac{B_0\psi_b}{2\sqrt{a}\varpi}[s'(\varpi)Z(\bar{z})+\psi_p'(\varpi)]$
$B_\phi(\varpi,\bar{z})$	$\dfrac{B_0\sqrt{2}\alpha^{1/2}\psi_b}{a^{1/4}}[s(\varpi)Z(\bar{z})+\psi_p(\varpi)]$
$p(\varpi,\bar{z})$	$B_0^2\Big[\Big(\dfrac{\psi_b^2s^2(\varpi)}{8\pi}+\bar{p}_{20}\Big)Z^2(\bar{z})+\Big(\dfrac{\psi_b^2s(\varpi)\psi_p(\varpi)}{4\pi}+\dfrac{b\psi_bs(\varpi)}{2\sqrt{2a}}\Big)Z(\bar{z})+\Big(\dfrac{\psi_b^2\psi_p^2}{8\pi}+\dfrac{b\psi_b\psi_p}{2\sqrt{2a}}\Big)\Big]$
$\rho(\bar{z})$	$\dfrac{4\sqrt{2}\kappa a^{1/4}p_{20}}{gR}Z^2(\bar{z})$
$T(\varpi,\bar{z})$	$\dfrac{\bar{\mu}B_0^2gR}{4\sqrt{2}R_g\kappa a^{1/4}p_{20}}\Big[\Big(\dfrac{\psi_b^2s^2(\varpi)}{8\pi}+\bar{p}_{20}\Big)+\Big(\dfrac{\psi_b^2s(\varpi)\psi_p(\varpi)}{4\pi}+\dfrac{b\psi_bs(\varpi)}{2\sqrt{2a}}\Big)\dfrac{1}{Z(\bar{z})}+\Big(\dfrac{\psi_b^2\psi_p^2}{8\pi}+\dfrac{b\psi_b\psi_p}{2\sqrt{2a}}\Big)\dfrac{1}{Z^2(\bar{z})}\Big]$
Functions	Formulae for the self-similar model
$\xi(\varpi,\bar{z})$	$\sqrt{\dfrac{\tau}{\psi_bD_0}}\varpi y(\bar{z})$
$\psi_G(\varpi,\bar{z})$	$1-\dfrac{\Gamma(2/n_G,\xi^{n_G})}{\Gamma(2/n_G)};\quad(n_G>0)$
$\psi_P(\varpi,\bar{z})$	$1-(1+\xi)^{1-n_P}\big(1+\xi(n_P-1)\big);\quad(n_P>2)$
$\psi_Q(\varpi,\bar{z})$	$16(\xi^4-2\xi^3+\xi^2)$
$B_r(\varpi,\bar{z})$	$-\dfrac{B_0\varpi}{D_0}y(\bar{z})y'(\bar{z})D_X(\xi)$
$B_z(r,z)$	$\dfrac{B_0}{D_0}y^2(z)D_X(\xi)$
$B_\phi(\varpi,\bar{z})$	$\dfrac{\sqrt{\bar{\chi}}B_0}{D_0}\varpi y^2(\bar{z})D_X(\xi)$
$p(\varpi,\bar{z})$	$B_0^2\Big[\dfrac{\bar{f}}{2}\psi^2+\bar{p}_ce^{-2\bar{k}\bar{z}}\Big]$
$\rho(\bar{z})$	$\dfrac{2\bar{k}\bar{z}\bar{p}_cB_0^2}{gz_0}e^{-2\bar{k}\bar{z}}$
$T(\varpi,\bar{z})$	$\dfrac{\bar{\mu}gz_0}{2R_g\bar{k}\bar{z}\bar{p}_c}\Big(\dfrac{\bar{f}}{2}\psi^2e^{2\bar{k}\bar{z}}+\bar{p}_c\Big)$

TABLE 5.6: A formulary of different functions obtained for the Coulomb function helical fluxtube and self-similar model. Here, $s(\varpi)$, $Z(\bar{z})$ and $\psi_p(\varpi)$ are given by eqns (5.18, 5.19, 5.23), and $\bar{p}_{20}=p_{20}/B_0^2$. ξ is the self-similar parameter where $y(\bar{z})$ is obtained by solving eqn (5.71) and $\bar{p}_0=p_0/B_0^2$, $\bar{p}_c=p_c/B_0^2$, $\bar{k}=kz_0$. The value of the constants are $\bar{\mu}=1.12$, $g=2.74\times10^4$ cm s^{-2}, $k=3.4\times10^{-8}$ cm^{-1} and $z_0=10^8$ cm.

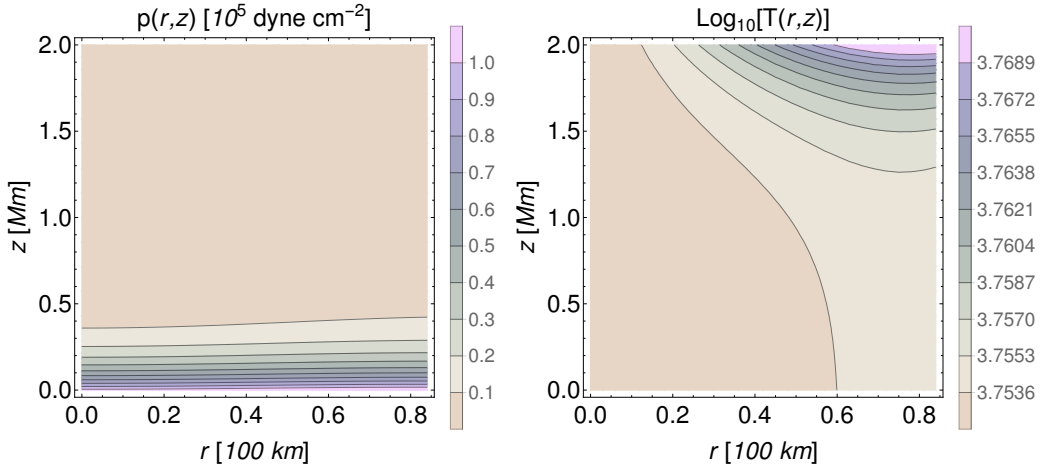

FIGURE 5.24: The 2D variation of p (*left*) and T (*right*) in the $r-z$ plane for $r_b = 84$ km obtained from the Coulomb function model for the parameter set of run $C4$ in Table 5.2. The horizontal axes are scaled in the units of 100 km and the vertical axes are scaled in the units of Mm.

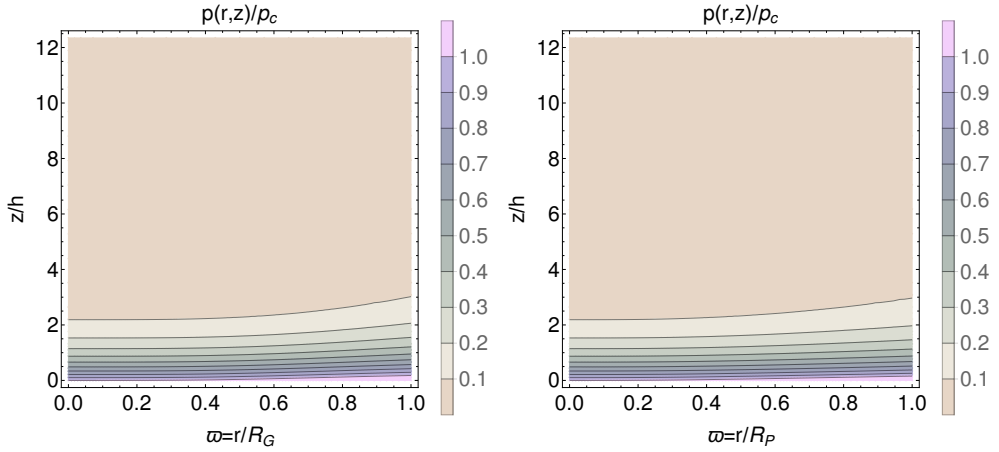

FIGURE 5.25: The 2D variation of p in the $r-z$ plane obtained from the self-similar model for Gaussian (*left*) and power law (*right*) profiles with $n_P = 3$, for the parameter set of run $S1$ in Table 5.3. The horizontal axes are scaled with the total radii $R_G = 150$ and $R_P = 130$ km, and the vertical axes are scaled with the pressure scale height, $h = 162$ km.

5.7 Discussion of the models

We discuss the findings of our simulations below:

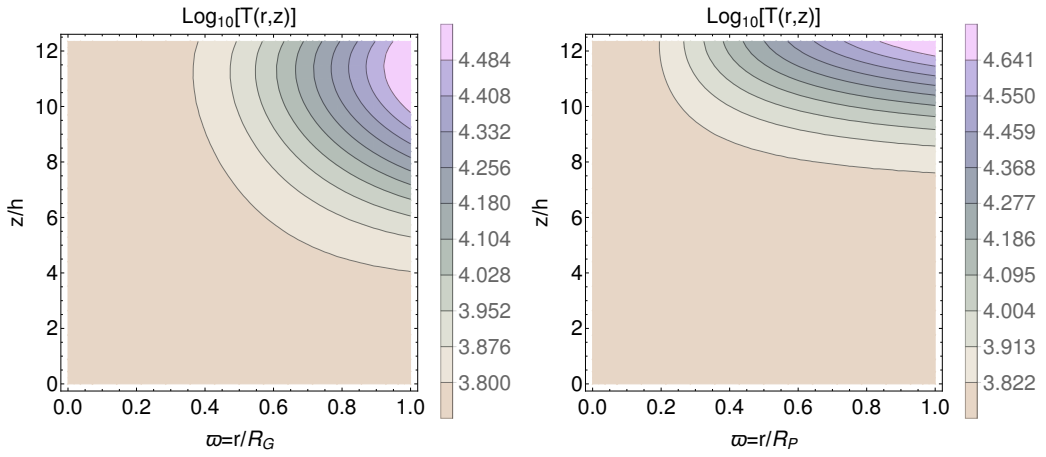

FIGURE 5.26: The 2D variation of T in the $r-z$ plane for Gaussian (*left*) and power law (*right*) profiles with $n_P = 3$ obtained from the self-similar model for the parameter set $S1$ in Table 5.3. The horizontal axes are scaled with the total radii $R_G = 150$ km and $R_P = 130$ km, and the vertical axes are scaled with the pressure scale height, $h = 162$ km.

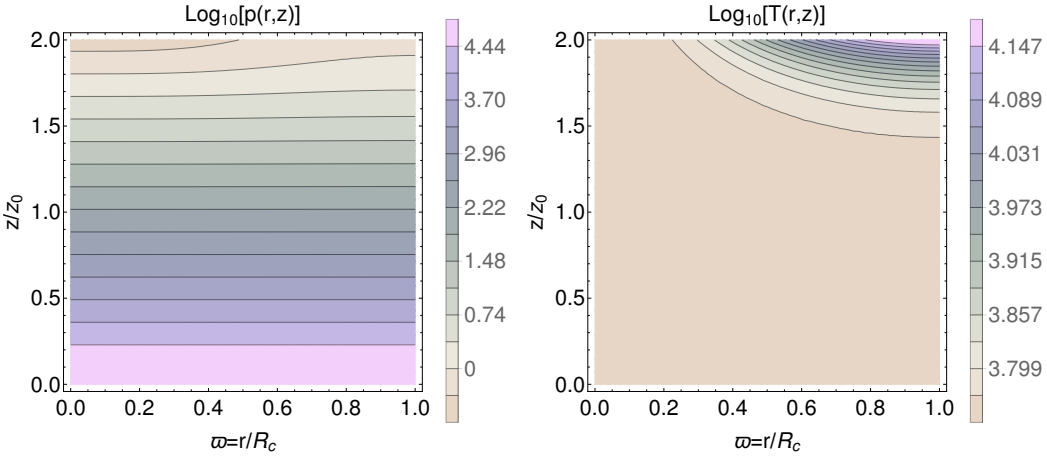

FIGURE 5.27: The 2D variation of p *(left)* and T *(right)* in the $r-z$ plane obtained from the self-similar closed field model for the parameter set of run S1 in Table 5.4. The horizontal axes are scaled with respect to $R_c = 282$ km, and the vertical axes are scaled with $z_0 = 1$ Mm.

1. The Coulomb function model is easier to implement for the numerical studies as it consists of two free parameters (R, B_0); on the other hand, the self-similar model consists of five free parameters (Ψ_b, B_0, p_c, B'_{z0} and χ). From Table 5.5, we see that the rise of the gas pressure along the radial direction from the axis to the boundary is higher for the self-similar model than the

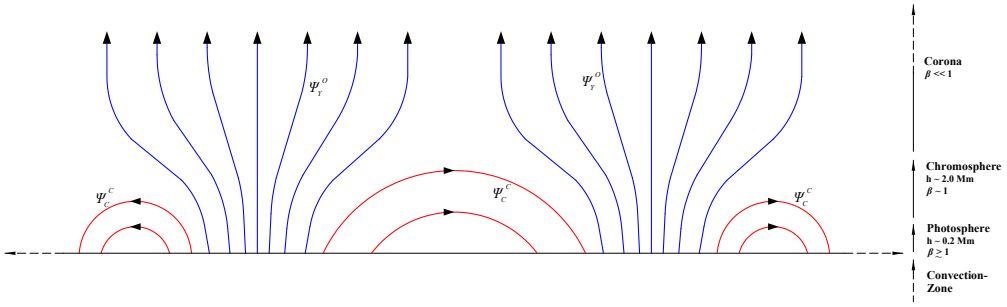

FIGURE 5.28: A cartoon diagram of magnetic canopy structure is shown, where the closed field lines (*red*), which is obtained by the Coulomb function closed field solution, Ψ_C^C, rise and fall back in the photosphere, present between two open field fluxtubes. The open field lines (*blue*), obtained by Coulomb function open field and self-similar solution, Ψ_Y^O ($Y = C$, for Coulomb function and $Y = S$ for self-similar models), of two neighboring fluxtubes merge together to form magnetic canopy structure [An improvised version of the illustration in Judge (2006)].

Coulomb function model at higher z. The density within the fluxtube does not vary with r; hence, the rise of the temperature from axis to the boundary at higher z is also higher for the self-similar model relative to the Coulomb function model. For the Coulomb function model, the radial boundary of the fluxtube is defined where B_z vanishes; on the other hand, for the self-similar model, $B_z(R) \neq 0$, whereas B_z reduces along the radial direction from axis to the boundary for the Gaussian model faster than the Power-law model.

2. The radial size and the magnetic field strength at the center of the fluxtube are the free parameters in the Coulomb function model. The magnetic and thermodynamic structure of the fluxtube remains similar for different values of the free parameters, whereas the magnitude of the magnetic and thermodynamic quantities vary. We have explored the parameter space and notice that in the domain of 100 km $\leq R \leq$ 180 km, and 1 kG $\leq B_0 \leq$ 1.5 kG, the magnetic and thermodynamic quantities are in reasonable agreement with the solar atmosphere (Vernazza *et al.* 1981), which also validate the MBP size and magnetic field strength distribution (Utz *et al.* 2009, 2013). For the self-similar model, the radial sizes of the fluxtubes depend on the choice of the dimensionless input parameters $\{\psi_b, \bar{f}, \bar{B'_{z0}}, \bar{\chi}\}$. In the domain

of the selected parameter space (see Table 5.3 and 5.3), the maximum and minimum radii of the fluxtubes are 678 and 151 km respectively obtained from the Gaussian model, 826 and 184 km respectively for power-law model and 1780 and 400 km respectively for the self-similar closed field model. All these quantities are in reasonable agreement with the observation of MBP size distribution by Utz *et al.* (2009).

3. For the Coulomb function model, we notice that the value of α decreases with R (see Table 5.2), which lowers the poloidal current I_p and the twist of the field lines. The 3D geometry of the field lines for different twists are shown in the Figs. 5.6 and 5.7 for open and closed field Coulomb function models respectively. In the self-similar model, the twist of the field lines increases with $\bar{\chi}$ and are shown in Figs. 5.12 and 5.13 for Gaussian and power-law profiles respectively, which follows from eqn (5.77).

4. The gas pressure for both Coulomb function and self-similar models increases along radial direction from axis to the boundary, whereas it decreases along the vertical height from photosphere to the transition region (see Figs. 5.24, 5.25, and 5.27) which is similar to the result obtained by Shelyag *et al.* (2010) for MBPs, where the gas pressure inside the MBPs increases radially though the change is not significant, and decreases vertically. Gent *et al.* (2013, 2014) have studied for the cases of single and multiple fluxtubes, where the internal gas pressure is nearly same along the radial distance but decreases with height. The density within the fluxtube does not change radially but it decreases along z, for both Coulomb function and self-similar models (see Figs. 5.9 and 5.16). Our model predicts that the atmosphere inside the fluxtube is nearly plane parallel which is comparable to the model obtained for MBPs by Shelyag *et al.* (2010).

5. In the solar atmosphere, the temperature in the transition region rises perhaps because the shock dissipation of waves plays a dominant role, which is not included in our model. We have also not implemented the temperature

profile by Vernazza *et al.* (1981) (VAL model); however, our model is self-consistent, obtained by solving the GSE without shock heating. Therefore, we do not see the drastic rise of the temperature with height. Our vertical simulation domain is restricted from the photosphere to the transition region where our input external atmosphere model is valid. Both the fluxtube models we built are non-isothermal where the temperature increases along the radial direction for both Coulomb function open field and self-similar models. The vertical variation of the temperature is constant at the axis but it increases with height away from the axis for the Coulomb function open field and self-similar models (see Figs. 5.24 and 5.26).

6. Hewitt *et al.* (2014), Uitenbroek and Criscuoli (2013), Riethmüller and Solanki (2016) have reported the simulation results of MBPs by using MuRAM and Copenhagen-Stagger code where the obtained values of magnetic field strength, pressure, density and temperature inside the fluxtube are in reasonable agreement with our predictions.

7. The 2D simulations of the propagation of linear and non-linear magneto acoustic waves through an open magnetic fluxtube, embedded in the solar atmosphere from the photosphere to corona were carried out by Fedun *et al.* (2011). We can incorporate our solutions as the background condition for such numerical studies of waves and their kinematic properties taking realistic inputs of field strength and pressure distribution observed in the solar atmosphere.

8. The Coulomb function model gives both open and closed field fluxtube solutions, which can be co-added to build the canopy structure. A cartoon diagram of the magnetic canopy is shown in Fig. 5.28, where the closed field lines (*red*), Ψ_C^C, are present between the open field fluxtubes and obtained from the Coulomb function, where the open field lines (*blue*), Ψ_C^O and Ψ_S^O, of the neighboring fluxtubes merge to each other to form a canopy structure. This is similar to structures assumed in the numerical simulations by Gent

et al. (2014), constructed by a different self-similar fluxtube solution. We can use our solutions for inputs to simulations to build such canopy structures. The self-similar fluxtube model gives an open field structure of the fluxtube which is embedded in a continuous magnetic medium and spans up to infinity in the radial direction. The magnetic and thermodynamic quantities we estimated from both Coulomb function and self-similar models are nearly similar, whereas there are some differences in the structures of the magnetic and thermodynamic profiles.

Future advancement of the observations of magnetic and thermodynamic structures of the MBPs will provide a better selection of the parameter inputs and discriminate between our models.

5.8 Summary and Conclusions

We have constructed two different models of fluxtubes with twisted magnetic fields which are the Coulomb function helical fluxtube model and self-similar model by solving GSE semi-analytically. We tabulate the expressions of magnetic and thermodynamic functions for Coulomb and self-similar models in Table 5.6 and highlight the novel features of this work below.

1. By incorporating the form of gas pressure and poloidal current we have solved GSE to obtain the flux function for the Coulomb function model. The solution of the Coulomb function model is the combination of a homogeneous part and a particular part. The homogeneous part with closed geometry is separable with a Coulomb function in r whereas the z part decreases exponentially with height, and the particular part with open geometry is a power series of r which is independent of z.

2. Using appropriate BCs and employing the presence of the sheet current at the boundary of the fluxtube, we have determined the parameters $a(R)$, $\alpha(R)$, $\kappa(R)$, $b(R, B_0)$, $\psi_b(R, B_0)$ and $\bar{p}(R, B_0)$ in terms of the input parameters $\{R, B_0\}$, which are the free parameters in the model, and k is calculated from the pressure values at photosphere and transition region obtained from Avrett and Loeser (2008) model. The values of the parameters for Coulomb function model are listed in Table 5.2.

3. In the Coulomb function model, the solution consisting of homogeneous and particular parts together represents an open field fluxtube solution, where the field lines rise from the photosphere. The homogeneous solution depicts a closed field fluxtube model which is discussed in SM18. The values of the magnetic field strength and thermodynamic quantities inside the fluxtube are calculated and are summarized in Table 5.5. The 3D visualization of both open and closed field lines are shown in the Figs. 5.6 and 5.7 for the parameter set of run no. $C4$ and $C10$ corresponding to Table 5.2.

4. In the self-similar model, we have employed an extra term $p_c \exp(-2kz)$ with p_1 in eqn (5.66), to maintain the hydrostatic pressure balance under the influence of stratified solar gravity, and taken two options for the shape functions, $D_X(\xi)$ from eqn (5.68), which is the extension of previous models by ST58; Yun (1971); Osherovitch (1979, 1982). We have incorporated the resulting two different shape functions, generalized Gaussian and power-law profiles, to obtain open field fluxtube solutions. We have taken a range of the parameters Ψ_b, B_0, p_c, B'_{z0} and χ (see Table 5.3 and 5.4), that are consistent with the solar atmosphere to study the structure and the properties of the fluxtubes. The size of the fluxtubes and the magnitude of the thermodynamic and magnetic field strengths depend on the choice of the input parameters, but the magnetic and thermodynamic structures remain similar. We have calculated the magnetic field strength and the thermodynamic

quantities inside the fluxtube which are given in Table 5.5, for the parameter set of run no. $S1$ corresponding to Table 5.3 and 5.4.

5. Preliminary calculations using the constraint of relative helicity based on the formulations given in (Prasad *et al.* 2014; Prasad and Mangalam 2016) and applying the constrained energy minimization principle (Mangalam and Krishan 2000; Finn and Antonsen 1983; Taylor 1974) indicate that stable configurations are possible for some regions in the parameter space of $\{B_0, R\}$. We plan a complete solution of this allowed region and test it with numerical simulations in a paper in preparation.

The fluxtube models presented here give useful estimates of the magnitude and the distribution of the magnetic field strength and thermodynamic quantities from the photosphere to the transition region which can be verified by future observations. Work on self-similar closed and twisted field structure is in progress. The solutions we obtained for different fluxtubes can be used for the dynamical simulation of wave propagation through the fluxtubes, which is important for studying the coronal heating by waves.

Chapter 6

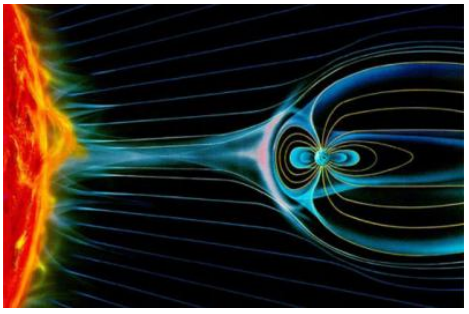

Image source: https://now.uiowa.edu

Magnetic reconnection and flares

6.1 Introduction

All plasmas, whether it is in the laboratory, solar atmosphere, or in the distant universe, can generate magnetic fields. Simultaneously the magnetic field can also be destroyed by a process called magnetic reconnections in nearly all plasma settings in the universe. This process occurs due to the topological reconstruction of the magnetic field caused by the change of the field line connectivity and allows the release of stored magnetic free energy in the form of thermal energy, which is a source of the free energy (and also radiation, kinetic energy, etc.).

The creation of a reconnection event in the terrestrial laboratory is a very challenging task as the Reynolds number of the terrestrial plasma is very low. In contrast, plenty of reconnection events have been seen in the solar atmosphere for

the presence of plasma with high Reynolds numbers. Several phenomena in the solar atmosphere such as the motion of the chromospheric ribbons, dynamics of the coronal loops, and the solar flares are the consequences of the magnetic reconnection. It has been proposed that reconnection is partly responsible for heating the solar corona up to a million Kelvin (Cargill 2014; Klimchuk 2015), which is addressed as the *coronal heating problem*. The study of magnetic reconnection is an important topic in solar physics.

6.2 Null points and current sheet

Before surveying several reconnection models, we will first focus on the two important aspects of the reconnection theory, which are called the null points, and the current sheet (Priest and Forbes 2000). Null points, neutral points, or X-points are locations where the magnetic field vanishes. Null points can be generated due to the presence of multiple sources containing magnetic fields, e.g. the field formed by the presence of two bar magnets. A current sheet is a thin current-carrying layer, where the magnitude and/or the direction of the magnetic field changes across the layer. It can be present only in a conducting medium such as a plasma. The presence of the null points typically gives rise to the current sheets in the plasma. In the next two sections, we have discussed a two-dimensional scenario of null points and current sheet respectively.

6.2.1 Two-dimensional null points

A two dimensional magnetic field (B_X, B_Y) near a neutral point can be expanded in a Taylor series form, and keeping only the first order, linear terms, the components

have the form

$$B_X = bX + 2cY \tag{6.1}$$

$$B_Y = -2aX + dY, \tag{6.2}$$

where a, b, c, d are the arbitrary constants. Using the condition $\nabla \cdot \mathbf{B} = 0$, we can write $b = -d$ from eqns (6.1, 6.2). The field components are related to the magnetic flux function, Ψ as follows

$$B_X = \frac{\partial \Psi}{\partial Y}, \qquad B_Y = -\frac{\partial \Psi}{\partial X}, \tag{6.3}$$

and by using eqns (6.1) and (6.2), we obtain the flux function as

$$\Psi = aX^2 + bXY + cY^2 + C, \tag{6.4}$$

where, C is a constant of integration, which vanishes due to the condition that Ψ is zero at the origin i.e. $\Psi(X = Y = 0) = 0$.

Rotating the XY-axes through an angle θ to obtain a new xy-axes, we use the relation

$$X = x\cos\theta - y\sin\theta, \qquad Y = x\sin\theta + y\cos\theta. \tag{6.5}$$

Substituting this into eqn (6.4) gives

$$\begin{aligned}\Psi = &\frac{1}{2}[(a+c) + b\sin 2\theta + (a-c)\cos 2\theta]x^2 \\ &+ [(c-a)\sin 2\theta + b\cos 2\theta]xy \\ &+ \frac{1}{2}[(a+c) - b\sin 2\theta - (a-c)\cos 2\theta]y^2.\end{aligned} \tag{6.6}$$

The angle of rotation θ is arbitrary, so we choose it in such a way that the second term in the RHS of eqn (6.6) vanishes, which implies

$$\tan 2\theta = \frac{b}{a-c}, \tag{6.7}$$

and the form of the flux function turns out to be

$$\Psi = \frac{B_0}{2L}(y^2 - \beta^2 x^2), \tag{6.8}$$

where,

$$\frac{B_0}{L} = (a+c) - \sqrt{b^2 + (a-c)^2}, \qquad \beta^2 = \frac{\sqrt{b^2 + (a-c)^2} + (a+c)}{b^2 + (a-c)^2 - (a+c)}, \tag{6.9}$$

and L is the length scale over which the magnetic field is varying. The field components in the new reference frame are

$$B_x = B_0 \frac{y}{L}, \qquad B_y = B_0 \beta^2 \frac{x}{L}, \tag{6.10}$$

so the B_x and B_y vanish at the x and y axes respectively. The field lines are given by the contours of Ψ = const. For $\beta^2 < 0$, the field lines of eqn (6.8) become elliptical and the origin is referred to as the O-type neutral points. On the other hand, for $\beta^2 > 0$, the field lines become hyperbolic and we call them as the X-type neutral points. Fig. 6.1 shows the structure of the null points for both O and X type.

6.2.2 Current sheets

The current sheets that are formed at the null points are due to the discontinuity of the field strengths and/or the direction. When the discontinuity across a current sheet is tangential, then the plasma flow along the sheet is zero. In an equilibrium

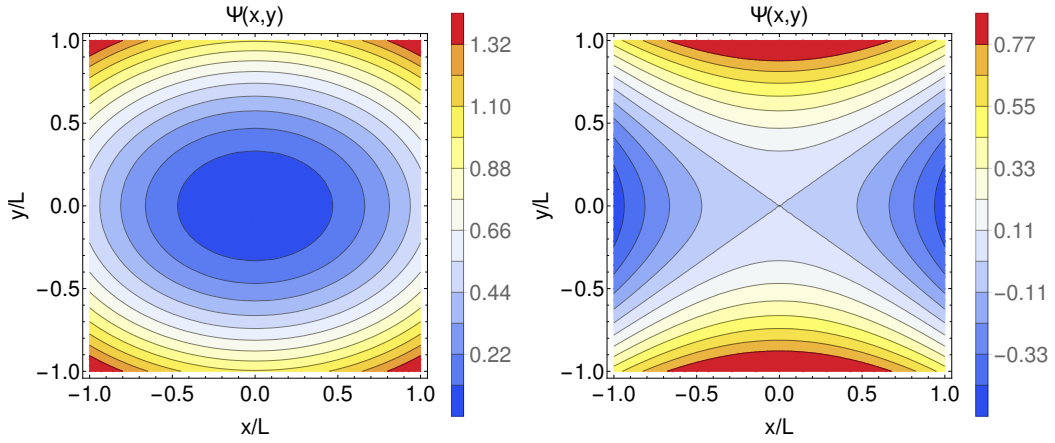

FIGURE 6.1: Two dimensional neutral points. The figure on the left shows the O-type neutral points for $\beta^2 = -0.5$, and the figure on the right shows the X-type neutral point for $\beta^2 = 0.5$.

condition, the total pressure balance across the current sheet is given by

$$p_2 + \frac{B_2^2}{8\pi} = p_0 + \frac{B_0^2}{8\pi} = p_1 + \frac{B_1^2}{8\pi}, \tag{6.11}$$

where the subscripts $\{2, 0, 1\}$ denote the values on one side, sheet centre, and the other side. In particular, if the central field, B_0 vanishes, then we get a neutral sheet. If the ambient pressures p_1 and p_2 also vanish, then eqn (6.11) reduces to

$$\frac{B_2^2}{8\pi} = p_0 = \frac{B_1^2}{8\pi}. \tag{6.12}$$

If a magnetic field in a current sheet varies along x and directed along the y direction, i.e. $\mathbf{B} = B_y(x)\hat{\mathbf{y}}$, then from Ampére's law we obtain

$$j_z = \frac{1}{4\pi}\frac{\partial B_y}{\partial x}, \tag{6.13}$$

which implies that a steep gradient of B_y along x produces a current along the sheet and normal to the field lines.

Instabilities can occur in a current sheet due to the tangential discontinuities. Consider a current sheet with uniform flows $\mathbf{v_1}$ and $\mathbf{v_2}$, and field strengths $\mathbf{B_1}$ and

$\mathbf{B_2}$, on either side of the sheet. For an ideal, incompressible plasma, an instability, which is called the Kelvin-Helmohltz instability (Priest 1982) may occur in such a current sheet if one of the following conditions are satisfied:

$$\rho|(\mathbf{v_2} - \mathbf{v_1})|^2 > |\mathbf{B_1}|^2 + |\mathbf{B_2}|^2 \tag{6.14}$$

$$\rho\big[|\mathbf{B_1} \times (\mathbf{v_2} - \mathbf{v_1})|^2 + |\mathbf{B_2} \times (\mathbf{v_2} - \mathbf{v_1})|^2\big] > |\mathbf{B_1} \times \mathbf{B_2}|^2. \tag{6.15}$$

Eqn (6.14) implies that the current sheet becomes unstable if the kinetic energy due to the tangential velocity difference $(\mathbf{v_2} - \mathbf{v_1})$ exceeds the magnetic energy density. The fluid has to work to distort the field lines, therefore the magnetic fields try to stabilize the current sheet. Eqn (6.15) is the instability condition due to the relative orientation of the plasma flows and the field lines. This condition arises because the plasma flows that are normal to the field are more susceptible towards the instability. As these conditions are valid for the ideal and incompressible fluids, in a non-ideal plasma, a current sheet may remain be unstable even if the conditions (6.14) and (6.15) are not satisfied.

6.3 Reconnection models

In astrophysical settings, the magnetic Reynolds number is very high, so the magnetic field lines are glued to the plasma medium. But, if there exists a very thin region, the magnetic field gradient inside that region becomes sufficiently high, and the field lines can slip through this and reconnect. For example, in Figure 6.2, a field line initially joining A to B in the plasma medium [see Figure 6.2 (a)] carries out and reconnects to an oppositely field line to form a new field line AC [see Figure 6.2 (c)]. In this process, a narrow region of a current sheet with high magnetic gradient is formed [see Figure 6.2 (b)] containing a null point of X-type.

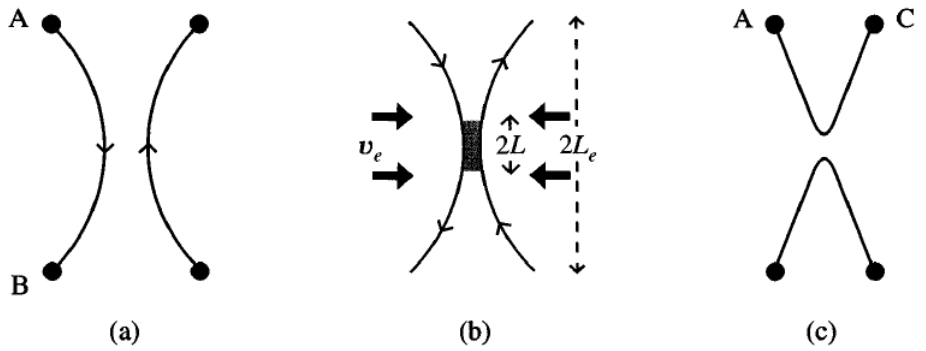

FIGURE 6.2: Reconnection of field lines: (a) Before reconnection, A is joined to B; (b) During reconnection, a thin current sheet is formed between the opposite field lines; (c) After reconnection, A is connected to C. Image courtesy: Priest and Forbes (2000).

The two important aspects of the reconnection are the nature of the reconnection and the field line breaking at the time of steady-state occurrence, and the speed of the line breaking event towards the reconnecting site. Sweet (1958a,b) and Parker (1957, 1963) developed a model where, a magnetic diffusive layer is present, and showed that the reconnection rate is related with the speed of the incoming field lines into the diffusion region. Later on, Petschek (1964) extended the model by proposing that the diffusion region is restricted to a small portion between the oppositely directed field lines, so that the effective size of the diffusion region is shorter, which makes the reconnection process faster. Magnetic energy is converted into the Ohmic heating at a slow rate during magnetic diffusion; this depends on the thickness of the current sheet and the diffusivity of the plasma. The diffusion can drive resistive instabilities which leads to fast reconnection.

6.3.1 Sweet-Parker model

In this model it is considered that the two flux system of oppositely directed magnetic field meet at a particular zone, say at $x = 0$, where the field $B = 0$ (Sweet 1958a; Parker 1957). The flux systems are pushed together by some external means

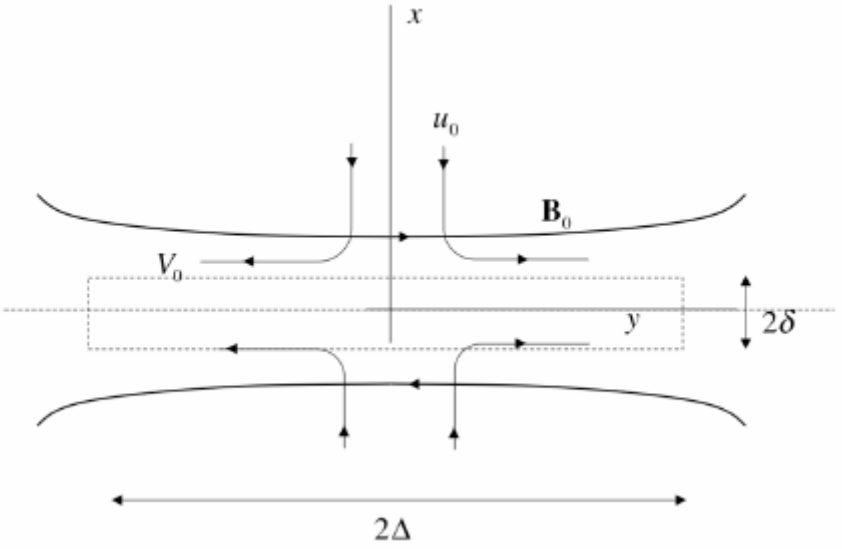

FIGURE 6.3: The geometry of the Sweet-Parker model of reconnection.

with velocity u_0, i.e. $v_x(|x| \to \infty) \to |u_0|$. As the flux system comes closer, the current density j_z will intensify around $x = 0$, and an extended current sheet is produced in $\pm y$-direction. Suppose the length of the current sheet is 2Δ. In order to conserve the mass of the plasma, the mass flux of the plasma is forced out along the $\pm y$-direction have to be same as the mass flux of the plasma that are coming from the $\pm x$-direction. The reconnection process occurs in some small region of length 2δ and the velocity of the outgoing plasma along the $\pm y$-direction is v_0. The situation is sketched in Figure 6.3. Uzdensky and Kulsrud (2000) have improved the Sweet-Parker model to calculate the reconnection rate. In the steady state, the plasma enters in the current sheet at velocity u_0 and the resistivity holds the magnetic field for some time in the fluid to reconnect, and flow out along the current sheet. No more plasma can enter in that layer until the previous bit of fluid leaves the sheet. The ratio of the inward to the outward velocity u_0/v_0 gives the rate at which the flux is destroyed by reconnection. This ratio is called the *reconnection rate*. If we assume incompressibility, $\nabla.\mathbf{v} = 0$, then from Figure 6.3 we see that

$$u_0\Delta = v_0\delta. \tag{6.16}$$

Away from the inner layer the field is governed by the ideal MHD, so

$$E_z = \frac{u_0}{c} B_0. \tag{6.17}$$

Within the inner layer the resistivity dominates, so

$$E_z = \frac{\eta}{c} j_z = \eta \frac{B_0}{4\pi c \delta}. \tag{6.18}$$

From eqns (6.17) and (6.18), we have

$$u_0 = \frac{\eta c}{4\pi \delta}. \tag{6.19}$$

The outer region in the x component is force balanced, hence,

$$\frac{\partial}{\partial x}\left(p + \frac{B^2}{8\pi}\right) = 0. \tag{6.20}$$

As $B(x = 0) = 0$, and we take $p(x = 0) = p_m$, so that

$$\frac{B_0^2}{8\pi} = p_m - p_0, \tag{6.21}$$

where p_0 and B_0 are the upstream pressure and magnetic field at infinity respectively. Using the force balance equation, $\rho(\mathbf{v}.\nabla)\mathbf{v} = -\nabla p$ along the y direction we obtain,

$$\frac{\partial}{\partial y}\left(\frac{\rho v_y^2}{2}\right) = -\frac{\partial p}{\partial y}, \tag{6.22}$$

and integrating eqn (6.22) from $y = 0$ to $y = \Delta$, we find

$$\frac{\rho v_0^2}{2} = p_m - p_0. \tag{6.23}$$

The eqns (6.21) and (6.23), yield

$$v_0 = \frac{B_0}{\sqrt{4\pi\rho}} \equiv v_A, \tag{6.24}$$

where v_A is called the Alfvén velocity. So the outflow velocity is equal to the upstream Alfvén velocity. Using eqns (6.16), (6.19), and (6.24) we obtain

$$\left(\frac{\Delta}{\delta}\right)^2 = \frac{4\pi v_A \Delta}{\eta c} \equiv S_0, \tag{6.25}$$

where S_0 is called the *Lundquist number*. Hence from eqns (6.16) and (6.25) the reconnection rate is calculated to be,

$$u_0/v_0 = \frac{\delta}{\Delta} = \frac{1}{\sqrt{S_0}}. \tag{6.26}$$

In astrophysical settings, $S_0 \gg 1$, so that reconnection rate according to this model is very slow. If the field lines are pushed harder from the outside, i.e. u_0 increases, then the outflow velocity will also be increased to keep the recnnection rate same and this is set by the resistivity. Therefore pushing harder at fixed S_0, just compresses the magnetic field but does not increase the rate of reconnection. For a typical value of $S_0 \sim 10^{10}$ in astronomical settings, the reconnection rate is $\sim 10^{-5}$ which is very slow that is not inferred for the cases of solar flares, CME and other astrophysical phenomena. It has been observed that the "fast reconnection" can occur if the effects outside resisitive MHD are accounted by the Ohm's law. From eqn (6.26), we can say that for a large S_0 value, the reconnection layer δ can become so small that the ideal MHD assumption breaks down, and other physics dominates the reconnection process. However mechanisms based on this theory are quite complicated and difficult to analyze for a general geometry.

For comparing the Sweet-Parker model with the solar observation, we take some typical observational values for solar flares given in Table 6.1. The obtained value for $S_0 = \dfrac{\Delta v_A}{\eta c/4\pi} = 2.7 \times 10^{12}$. This gives an Alfvén time scale, $\tau_A = \Delta/v_A = 37$ s, which is much shorter than the Sweet-Parker model time scale, $\tau_{sp} = \dfrac{\Delta\sqrt{S_0}}{v_A} = 6 \times 10^7$ s. Therefore we can see that the Sweet-Parker model cannot produce the expected reconnection rate for the flare event.

Reconnection models	Time scale, τ	B (G)	ρ (g cm^{-3})	v_A (cm s^{-1})	T_e (eV)	Δ (km)	S_0	τ_A (s)	τ (s)
Sweet-Parker	$\frac{\Delta\sqrt{S_0}}{v_A}$	300	10^{-15}	2.7×10^7	100	10^4	2.7×10^{12}	37	6×10^7
Petschek	$\frac{8\tau_A \ln S_0}{\pi}$	300	10^{-15}	2.7×10^7	100	10^4	2.7×10^{12}	37	30

TABLE 6.1: Time scales for various reconnection models for a typical solar flare event.

6.3.2 Petschek model

We have seen in the previous section, that the reconnection rate from the Sweet-Parker model is not in agreement with the observations. Petschek (1964) suggested that the Sweet-Parker diffusion region is limited to a small segment (of length $L << L_e$) of the boundary between opposing fields. The diffusion region is thinner and therefore the reconnection can take place faster. He suggested that slow-mode MHD shock waves propagate from the diffusion region, which acts as a kind of an obstacle in the flow, which is supersonic relative to the slow-mode wave speed across the magnetic field. To distinguish the outer region from the Sweet-Parker diffusion region, we denote the flow velocity and the magnetic field at large distance (L_e) by v_e and B_e respectively. The properties of the fast reconnection depends on two parameters namely, external reconnection rate $M_e(= v_e/v_{Ae})$ and the magnetic Reynolds number, $R_{me} = L_e v_{Ae}/\eta \equiv S_0$, where S_0 is called the *Lundquist number*. The steady state magnetic field, B_i is carried into the diffusion layer at the same speed v_i as it trying to diffuse outward. Hence,

$$v_i = \eta/l. \tag{6.27}$$

The conservation of mass of the plasma implies that

$$4\rho L v_i = 4\rho l v_0,$$

which gives

$$v_i = \frac{l v_0}{L} = \sqrt{\frac{\eta v_0}{L}}. \tag{6.28}$$

The internal reconnection ratio, $M_i = \dfrac{v_i}{v_{Ai}}$ is given by,

$$M_i = \frac{1}{\sqrt{R_{mi}}},$$

where $v_0 = v_{Ai} = \dfrac{B_i}{\sqrt{4\pi\rho}} = \dfrac{\eta R_{mi}}{L}$ is the Alfvén speed in the diffusion region. The magnetic Reynolds number inside the diffusion region is given by

$$R_{mi} \equiv \frac{L v_{Ai}}{\eta}, \tag{6.29}$$

and the flux conservation condition says that,

$$v_i B_i = v_e B_e, \tag{6.30}$$

which leads to,

$$\frac{M_i}{M_e} = \frac{v_i/v_{Ai}}{v_e/v_{Ae}} = \frac{B_e^2}{B_i^2}. \tag{6.31}$$

So from the definition of $R_{me}(= \dfrac{L_e v_{Ae}}{\eta})$ and eqn (6.29) we obtain,

$$\frac{L}{L_e} = \frac{1}{R_{me} M_e^{1/2} M_i^{3/2}}. \tag{6.32}$$

The magnetic field decreases substantially from a uniform value B_e at large distance to B_i, which is the value near the diffusion region. So according to eqn (6.30), the velocity near the diffusion region will be increased from v_e to v_i. The effect of the shock is to provide a normal field component B_N, which is associated with a small distortion in the inflow field of the uniform value B_e at large distance so that the field lines gets curved [see Figure 6.4]. The magnetic field in the upper inflow region is the uniform horizontal field $B_e\hat{\mathbf{x}}$ plus the normal component which vanishes at the diffusion region. Neglecting the inclination of the field lines, the y-component field on the x-axis is $-2B_N$ from $-L_e$ to $-L$ and $2B_N$ from L to L_e. Here the normal component on the x-axis can be treated as the series of poles. Each pole produces m/r field at r distance, and the flux produced in the upper

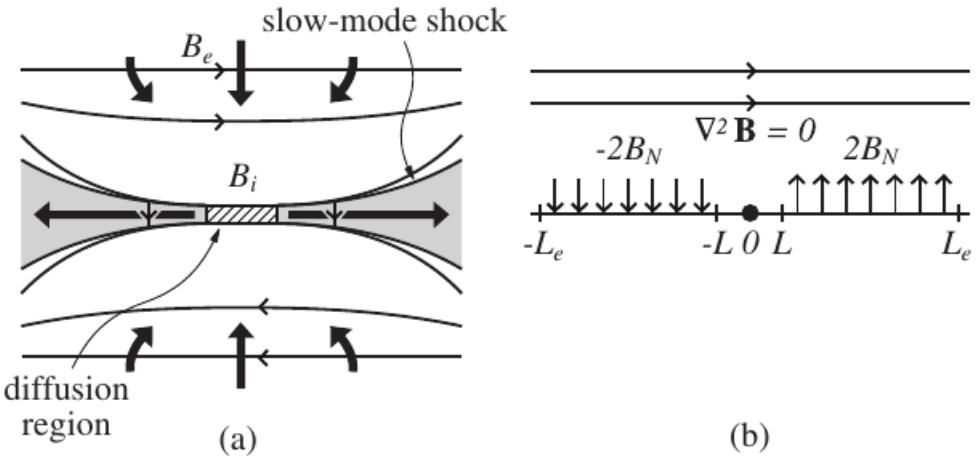

FIGURE 6.4: (a) Petschek model, in which the central shaded region is the diffusion region and the other two shaded regions represent plasma that is heated and accelerated by the shocks. (b) Notation for the analysis of the upper inflow region [picture courtesy: Priest (1982)].

half-plane by that pole is $\pi r \dfrac{m}{r} = \pi m$. If the pole occupies a distance $\mathrm{d}x$, then the value of the field is $2B_N\ \mathrm{d}x$.

Integrating along the x-axis from $x = -L_e$ to $x = L_e$, we find,

$$\begin{aligned} B_e - B_i &= \frac{1}{\pi}\int_{-L_e}^{-L} -2B_N \frac{\mathrm{d}x}{x} + \frac{1}{\pi}\int_{L}^{L_e} 2B_N \frac{\mathrm{d}x}{x} \\ \Rightarrow B_e - B_i &= \frac{2B_N}{\pi}\left[\int_{-L_e}^{-L} \frac{\mathrm{d}x}{x} + \int_{L}^{L_e} \frac{\mathrm{d}x}{x}\right] \\ &= \frac{4B_N}{\pi} \ln\left(\frac{L_e}{L}\right) \\ \Rightarrow B_i &= B_e\left(1 - \frac{4M_e}{\pi} \ln \frac{L_e}{L}\right). \end{aligned} \tag{6.33}$$

As, $M_e = \dfrac{v_e}{v_{Ae}} = \dfrac{B_N}{B_e}$, the magnetic fields are comparable in the diffusion region i.e. $B_i \approx B_e$. Hence, we can simplify (6.31) to find

$$\frac{L}{L_e} = \frac{1}{R_{me} M_e^2}. \tag{6.34}$$

Petschek proposed that this process will choke when B_i becomes very small. So, if we put $B_i \approx \frac{1}{2}B_e$ then we have from (6.33)

$$\begin{aligned} M_e &= \frac{\pi}{8 \ln \frac{L_e}{L}} \\ &= \frac{\pi}{8(\ln R_{me} + 2 \ln M_e)} \end{aligned} \tag{6.35}$$

As, $M_e << 1$, so, the maximum rate that can be obtained from eqn (6.35) is

$$M_{e,max} = \frac{\pi}{8 \ln R_{me}} = \frac{\pi}{8 \ln S_0}. \tag{6.36}$$

So, we see that the Petschek model reconnection rate is faster than the Sweet-Parker model rate. For the same set of solar flare parameters discussed earlier (see Table 6.1), the time scale for the Petschek model reconnection is $\tau_P = \dfrac{8\tau_A \ln S_0}{\pi} = 30$ s, which is in a good agreement with the Alfvén time scale, $\tau_A = 37$ s. Therefore, we see that the reconnection rate obtained from the Petschek model is in better agreement with the observations of the solar flare events.

6.4 Application of magnetic reconnection: Flares

A solar flare is a massive explosion that occurs when the stored magnetic energy is released in the form of kinetic and thermal energy, causing the emission of the electromagnetic radiation including radio, x-ray and gamma rays. Giovanelli (1946) first suggested that the chromospheric solar flare event is based on reconnection. Sweet (1958a) and Parker (1957) used the Giovanelli's X-point reconnection model to explain the snapping of the stored magnetic energy into the kinetic and thermal energy which is observed in the solar flares. Various ground and space-based telescopes have been used to observe the solar corona, where the magnetic structures reconfigure in a very dynamic manner by magnetic reconnection. In fact,

reconnection is one of the key phenomena for the existence of the hot solar corona. The flares can be classified as the small scale and large scale flares, according to the amount of mass and energy that they eject. We will now discuss these flares briefly, and the models associated with them.

6.4.1 Large scale flares: 2D flux rope model

Large scale flares are usually associated with the coronal mass ejections (CMEs), which are the large scale eruptions of mass and the magnetic flux from the lower part of the corona into the interplanetary medium. The magnetic field lines are opened due to the CMEs that lead to the formation of the flux ribbons and loops which are due to the release of the stored magnetic energy from reconnection of the open field lines that close.

A 2D flux rope model has been developed by Priest and Forbes (1990), Forbes and Priest (1995). A flux rope is a magnetic fluxtube with twisted magnetic fields. This model explains the basic phenomena of eruptive flares based on the reconnection theory. According to the model, when the flux ropes approach each other in the photosphere, they lose their equilibrium. The configuration is given by the Grad-Shafranov equation

$$\nabla^2\Psi + \frac{1}{2}\frac{\mathrm{d}B_z^2}{\mathrm{d}\Psi} = 0, \tag{6.37}$$

in the xy plane of $y \geq 0$, $|x| < \infty$, where $y = 0$ corresponds to the photosphere. The field component B_z is perpendicular to xy plane, and the flux function, Ψ is defined by $(B_x, B_y, B_z) = \left[\frac{\partial\Psi}{\partial y}, -\frac{\partial\Psi}{\partial x}, B_z(\Psi)\right]$. The boundary condition of the flux function at the photosphere is given by

$$\Psi(0, y) = \Psi_0\mathbb{H}(\lambda - |x|), \tag{6.38}$$

where, $\mathbb{H}$ is the heavyside step function, and $x = \pm\lambda$ are the locations of the two sources of opposite polarities. If these two sources move towards each other, a vertical current sheet forms, and then distribution of the flux function becomes,

$$\Psi(x,y) = \mathrm{Re}\left[\frac{\mu I}{2\pi}\ln\left(\frac{\sqrt{\zeta^2+b^2}+i\sqrt{h^2-b^2}}{\sqrt{\zeta^2+b^2}-i\sqrt{h^2-b^2}}\right) + i\frac{\Psi_0}{\pi}\ln\left(\frac{\sqrt{\zeta^2+b^2}+\sqrt{b^2+\lambda^2}}{\sqrt{\zeta^2+b^2}-\sqrt{b^2+\lambda^2}}\right)\right], \tag{6.39}$$

for $|\zeta - ih| > a$, where $\zeta = x + iy$, h is the rope height, a is the flux rope radius, b is the height of the current sheet, and I is the flux rope current. For $|\zeta - ih| \leq a$, the flux function, Ψ has the form

$$\Psi(x,y) = f(r,I), \tag{6.40}$$

where, $r = \sqrt{x^2+(y-h)^2}$, and the $f(r,I)$ is the solution for the isolated flux rope in the absence of the current sources given by Parker (1974c). The vertical field strength, B_z inside the flux rope ($r < a$) can be obtained by using the form (6.40) in eqn (6.37), whereas $B_z = 0$ at $r > a$ as $\Psi(x,y)$ becomes a potential field. The equilibrium value of $h = \lambda\xi$ is given by

$$\lambda = \begin{cases} \frac{1+\xi^2}{4\xi^2}a_0 \exp\left[\left(\frac{\pi}{4}+\ln\frac{2\lambda_0}{a_0}-\arctan\frac{1}{\xi}\right)\left(\frac{1+\xi^2}{2\xi}\right)\right]; & \text{for } \xi \leq \sqrt{3} \\ \frac{(3\xi^2-1)\sqrt{2(\xi^2-1)}}{4\xi^2(\xi^2+1)}a_0 \exp\left[\left(\frac{\pi}{4}+\ln\frac{2\lambda_0}{a_0}-\arctan\sqrt{\frac{\xi^2-1}{2\xi^2}}\right)\left(\frac{\sqrt{2(\xi^2-1)}}{\xi}\right)\right]; & \text{for } \xi \geq \sqrt{3} \end{cases} \tag{6.41}$$

where, ξ is a parametric variable, a_0 and λ_0 are the values of a and λ respectively at the point where the current has the maximum value of $I_0 = \dfrac{4\Psi_0}{\mu}$. The current at an arbitrary point is given by

$$I = \begin{cases} I_0 \frac{2\xi}{\xi^2+1}; & \text{for } \xi \leq \sqrt{3} \\ I_0 \frac{\xi}{\sqrt{2(\xi^2-1)}}; & \text{for } \xi \geq \sqrt{3} \end{cases} \tag{6.42}$$

while the radius is $a = a_0 \dfrac{I_0}{I}$, and the height of the current sheet is $b = \xi\lambda\sqrt{\dfrac{\xi^2-3}{3\xi^2-1}}$. In this model an assumption made is that the radius of the flux rope, a is sufficiently smaller than the flux rope height, h.

Figure 6.5(a) shows the height of the flux ropes which is in the equilibrium where the sources are separated by 2λ and $a_0 = 0.1\lambda_0$. If the source points start to move towards each other [see Figure 6.5(b)] then a catastrophe occurs at the time when λ reaches the point where the middle and the lower branch of the equilibrium curve meet. In Figure 6.5(c) the magnetic configuration loses equilibrium and the flux ropes are snapped out. After losing equilibrium state, and if there is no reconnection, then the flux ropes settle in a new equilibrium that contains a current sheet. On the other hand, if the reconnection occurs then the flux ropes continue to move in the upward direction indefinitely [see Figure 6.5(d)], though the velocity of the erupted flux ropes slow down as they cross the upper equilibrium height.

6.4.2 Small scale flares: emerging flux model

Small scale flares or the compact flares are more localized [Priest (1982); Zirin (1988)] which appear to form simple loops (Svestka 1976). This type of flare releases energy in an impulsive way, and show evidence of small scale rather than with the large scale flares. The small scale flares have a compositional signature which shows the existence of the He^3 and Fe elements.

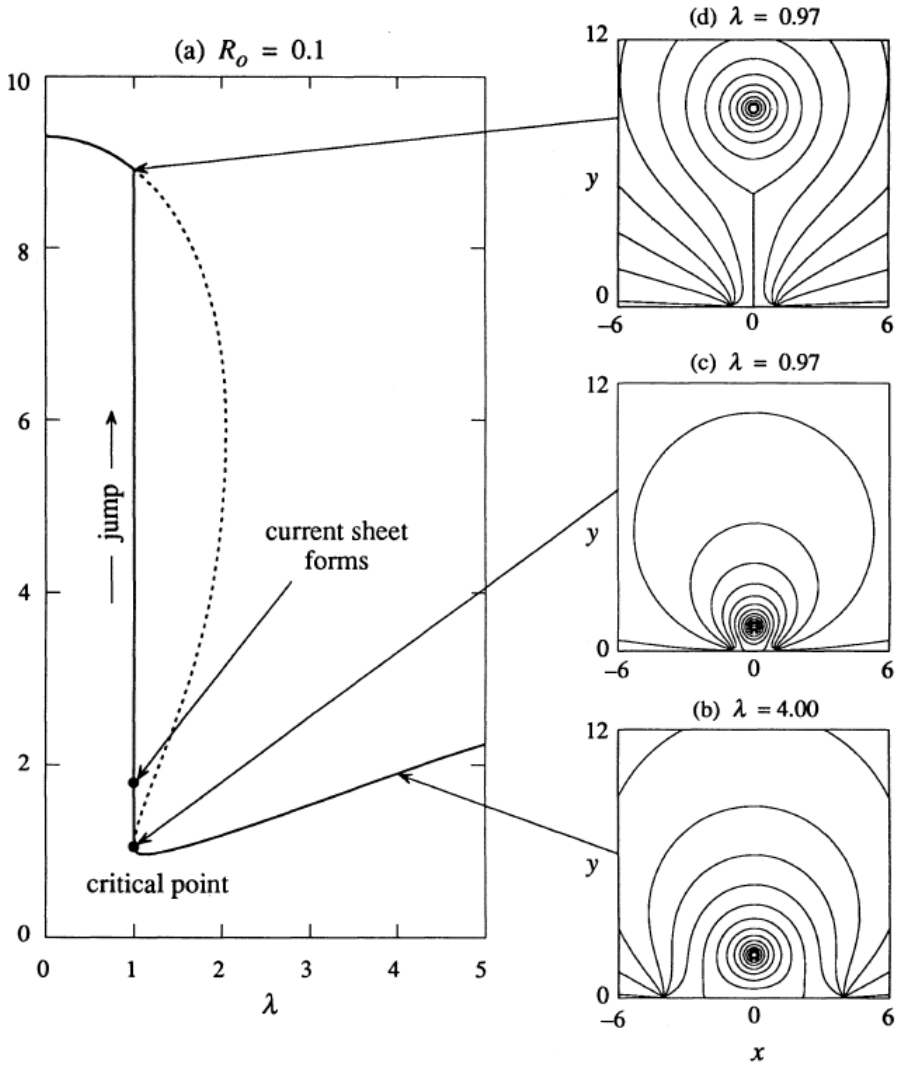

FIGURE 6.5: The flux rope model given by Forbes and Priest (1995). (a) Evolution of the 2D arcade containing flux ropes with the poles separated by 2λ. (b), (c) The poles moves towards each other in the photosphere, and the flux ropes move upward. (d) In the absence of the magnetic reconnection, the flux ropes settle in a new equilibrium that contain a current sheet, or the flux ropes are thrown out in the medium after the reconnection.

Heyvaerts *et al.* (1977) proposed the emerging flux model to explain the compact flares. According to the model, the magnetic loops emerge from the convection region and push up the pre-existing fields which lead to the formation of the coronal current sheet as shown in Figure 6.6. The resistivity of the plasma within the current sheet is very low, and when the ratio of the current to the mass density exceeds a threshold value of instability, the current sheet is thrown up which leads

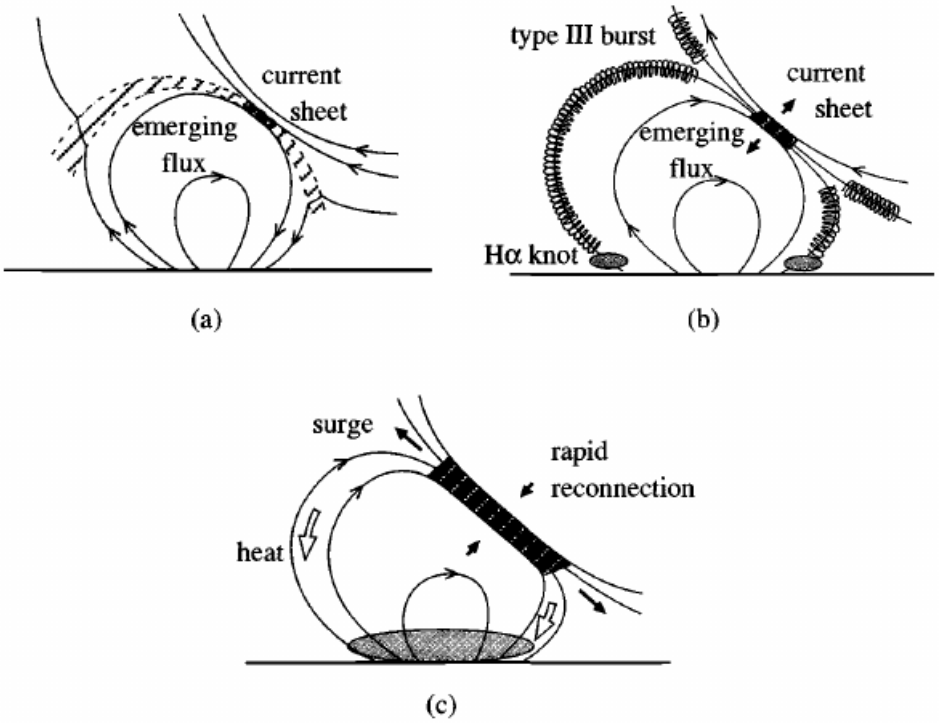

FIGURE 6.6: The emerging flux model by Heyvaerts *et al.* (1977) for small scale flares: (a) The pre-flare phase when the emerging flux and the pre-existing fields form a current sheet. (b) The impulsive phase, when the reconnection happens. (c) The quasi-static reconnection, which leads to the heating.

to a rapid energy release. If the emerging flux comes near the region of the closed magnetic loops, then all the footpoints of the separatrices stay in the photosphere [see Figure 6.6(b)]. This allows the reconnection to occur with four ribbons instead of two as shown in Figure 6.6(c). Such multiple ribbon reconnection events have been observed by Machado *et al.* (1988).

Observationally, there is a distinction between the large, two ribbon and compact flares, though the mechanism for all the events is magnetic reconnection. For both the large and small scale flares, the distribution of the events follow the power-law form:

$$\frac{\mathrm{d}N}{\mathrm{d}E} \sim E^{-\alpha}, \tag{6.43}$$

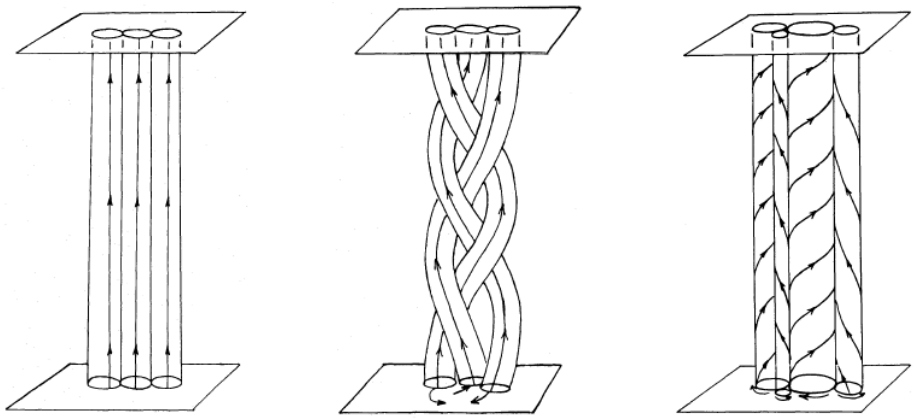

(a) (b) (c)

FIGURE 6.7: Topological states of the magnetic fluxtubes given by Parker (1983) model: (a) Magnetic fluxtubes in the uniform magnetic field. (b) Some fluxtubes after being braided to each other. (c) Twisted fluxtubes formed by the cellular rotaion of the plasma.

where, $\mathrm{d}N$ is the number of events within the energy range E and $E+\mathrm{d}E$, and α is the power-law index. Lu *et al.* (1993) proposed that this continuous distribution of the power law is due to the cascade of small and elementary reconnection events. Parker (1972) suggested that for a complicated topology of the field lines of two or more, the equilibrium of the system is violated, which causes the dissipation and merging of the field lines. Such a system in a turbulent medium gives rise to the small scale magnetic fields. Parker (1983) proposed that these small scale twisted field lines in a packed bundle give rise to the dynamical non-equilibrium (see Fig. 6.7) which is responsible for the nanoflare events observed in the solar corona. Parker (1988) proposed that the extremely small flares which are known as microflares and nanoflares are the contributing factors for the heating of the solar corona. On the other hand [Rosner and Vaiana (1978); Litvinenko (1994); Vlahos *et al.* (1995)] have suggested that the power-law distribution of the flare events is due to a stochastic trigger mechanism. Recent observations of Ramesh *et al.* (2013), Kishore *et al.* (2016), Kumari *et al.* (2017) (and references therein) have reported that the energy distribution of the radio flare events follows the power-law distribution.

6.5 Summary

This chapter is premier for understanding solar flares, and the energy distribution of the flare events which is presented in Chapter 7. The main references and texts for this chapter are [Priest and Forbes (2000); Parker (1983); Heyvaerts *et al.* (1977); Priest and Forbes (1990)]. We summarize the key points of this chapter in the following:

1. The importance of studying magnetic reconnection for understanding several magnetic phenomena in the solar atmosphere like flares. We also discussed the formation of the null points and the current sheets in a magnetic medium, which leads to the magnetic reconnection.

2. We presented several reconnection models, and compared the reconnection time scales for a typical flare event (see Table 6.1), and saw that the Petschek model gives a better agreement with the observational values for flare time scale.

3. We discussed several models for the large (Priest and Forbes 1990; Forbes and Priest 1995), and small scale flares (Heyvaerts *et al.* 1977; Parker 1983), and deducted that the energy distribution for both types of the flares is of the power-law form.

4. The small scale flares, which are called the micro, nano, or pico-flares occur due to the emerging flux mechanism and show the power-law energy distribution is seen for the radio bursts. This type of flares mainly occur due to the snapping out of the braided and wrapped fluxtubes. We will discuss this in Chapter 7 in more detail.

Chapter 7

Image source: https://en.wikipedia.org

Energy distribution of solar flare events

7.1 Introduction

In this chapter, we discuss the winding number distribution of a braided magnetic system using the "self-organized criticality" (SOC) model (Berger and Asgari-Targhi 2009). If two field lines are stretched between two planes $z = 0$ to $z = L$, then the winding number, w is defined as

$$w = \frac{1}{\pi} \int_0^L \left| \frac{\mathrm{d}\phi_{12}}{\mathrm{d}z} \right| \mathrm{d}z, \tag{7.1}$$

The work presented in this chapter is published in Sen *et al.* (2018).

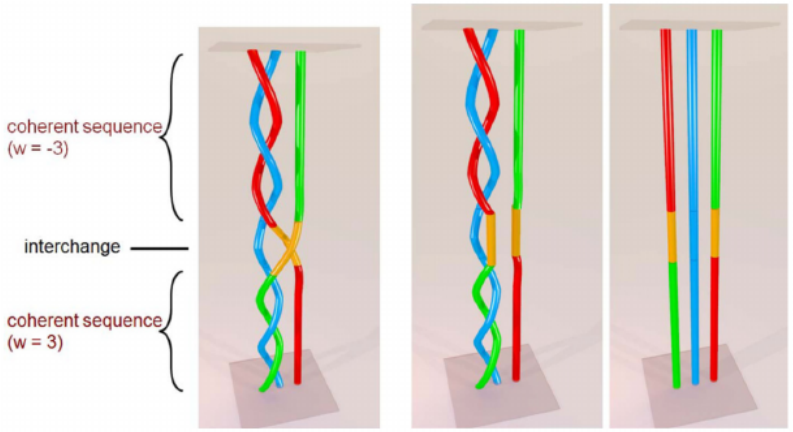

FIGURE 7.1: A cartoon diagram for explaining the self-organized criticality (SOC) model given by Berger and Asgari-Targhi (2009). *Left:* A three-braid configuration with two coherent sequences separated by an interchange. *Middle:* The interchange is removed by reconnection. *Right:* The final relax configuration with the crossings canceled out.

where ϕ_{12} is the twist angle between the field lines (Mangalam and Prasad 2018). This model of braided magnetic fields can release stored magnetic energy in the form of kinetic and thermal energy into the solar atmosphere. It has been observed that the energy distribution of such events follows the power-law distribution (Kishore *et al.* 2016; Ramesh *et al.* 2013; Sasikumar Raja *et al.* 2014) (and references therein). We have calculated the power-law index of the energy distribution theoretically for different cases, and compare these results with the flare observations taken by the Gauribidanur Radio telescope (Sen *et al.* 2018).

The sections where the two field lines braid with each other is called a coherent sequence. In Fig. 7.1 *(left image)* the blue and the green tubes in the left are braided by the winding number $w = +3$, whereas the red and the blue tubes are braided by the winding number $w = -3$. The +ve and -ve signs represent the anticlockwise and clockwise twist respectively. In Fig. 7.1 *(middle image)* a swapping occurs between the red and the green tubes which are called interchange, and the *right* image shows the relaxed condition of the tubes after the crossings are canceled out.

The braiding of the magnetic field lines or the fluxtubes in the solar atmosphere can occur through several mechanisms listed below.

- Due to the random motions of the photospheric magnetic footpoints, the field lines that are linked with the footpoints braid.
- Sometimes, large fluxtube fragments at its photospheric footpoints and the individual fragmented pieces of the flux elements disperse. These fragmented elements flow with the granular motion and coalesce with other elements forming a new flux element. This process increases the complexity of the braiding structure (Berger 1994).
- The fragmented magnetic footpoints of a coronal loop interact with the small scale loops, and these small loops reconnect with the larger loops which gives an effective motion of the magnetic footpoints of the field lines (Schrijver *et al.* 1998; Priest *et al.* 2002).

7.2 The SOC Model

In order to model the self-organized criticality, some arbitrary initial braid having m number of sequences and $m-1$ number of interchanges are considered. At each step one new coherence sequence is added with one interchange, and one of the existing interchanges get eliminated through a reconnection event simultaneously. If $n(w)$ is the sequence having crossing number w then,

$$m = \sum_{w=-\infty}^{\infty} n(w), \tag{7.2}$$

and the total number of crossings is given by,

$$\bar{c}_{tot} = \sum_{w=-\infty}^{\infty} \mid w \mid n(w). \tag{7.3}$$

The probability distribution function of sequence length w is defined as $f(w)$, i.e. it has the probability of having a sequence in the winding number range w to $w+\delta w$. At each time step the $f(w)$ is changed by δw by the following contribution:

1. The probability $p(w)$, that the new sequence adds to $f(w)$
2. A sequence will disappear if the left sequence of the reconnection region has winding number w. So there is a probability $f(w)$ that $n(w)$ of sequences having w winding number will decrease by one.
3. The sequence at the right of the reconnection has the probability of $f(w)$ of removing of a w sequence.
4. If the left has w_1 winding number, and in the right part having $w_2 = w - w_1$ winding number, then a new w sequence will be created.

Therefore the change in $n(w)$ is given by,

$$\begin{aligned}\delta n(w) &= p(w) - 2f(w) + \int_{-\infty}^{\infty} f(w_1)\mathrm{d}w_1 \int_{-\infty}^{\infty} f(w_2)\delta(w-(w_1+w_2))\mathrm{d}w_2 \\ &= p(w) - 2f(w) + \int_{-\infty}^{\infty} f(w_1)\mathrm{d}w_1 f(w-w_1).\end{aligned} \tag{7.4}$$

For steady state $\delta n(w) = 0$, hence from eqn (7.4) we obtain,

$$\begin{aligned}p(w) - 2f(w) + \int_{-\infty}^{\infty} f(w_1)f(w-w_1)\mathrm{d}w_1 = 0 \\ \Rightarrow p(w) - 2f(w) + (f * f)(w) = 0,\end{aligned} \tag{7.5}$$

where $(f * f)(w)$ denotes the convolution. Taking the Fourier transformation of eqn (7.5) we obtain,

$$\begin{aligned} \tilde{p}(k) - 2\tilde{f}(k) + \tilde{f}^2(k) = 0 \\ \Rightarrow \tilde{f}(k) = 1 - \sqrt{1 - \tilde{p}(k)} \end{aligned} \tag{7.6}$$

If we consider the sequence follows the Poisson distribution,

$$p_P(w) = \frac{\lambda}{2} \exp(-\lambda_c |w|), \tag{7.7}$$

where λ_c is the correlation length, then the Fourier transformation of $p_P(w)$ is given by,

$$\tilde{p_P}(k) = \frac{\lambda_c^2}{\lambda_c^2 + k^2}. \tag{7.8}$$

Therefore from eqn (7.8), we get

$$\tilde{f}(k) = 1 - \frac{|k|}{\sqrt{\lambda_c^2 + k^2}}. \tag{7.9}$$

The inverse Fourier transformation of eqn (7.9) gives

$$f(w) = \frac{\lambda_c}{2}[L_{-1}(\lambda_c w) - I_1(\lambda_c w)], \tag{7.10}$$

where $L_{-1}(\lambda_c w)$ is the Struve L-function and $I_1(\lambda_c w)$ is the Bessel function (Abramowitz and Stegun 1972). Expanding eqn (7.10), we obtain, $f(w) \propto w^{-2}$.

The photospheric footpoints undergoes random motions, so the probability distribution function of the winding number, $p(w)$ is assumed as the Poisson distribution by Berger and Asgari-Targhi (2009). We have extended the model by incorporating two different profile functions which follows the Gaussian distribution,

$$p_G(w) = \frac{1}{\lambda_c \sqrt{2\pi}} \exp\left(\frac{-w^2}{2\lambda_c^2}\right) \tag{7.11}$$

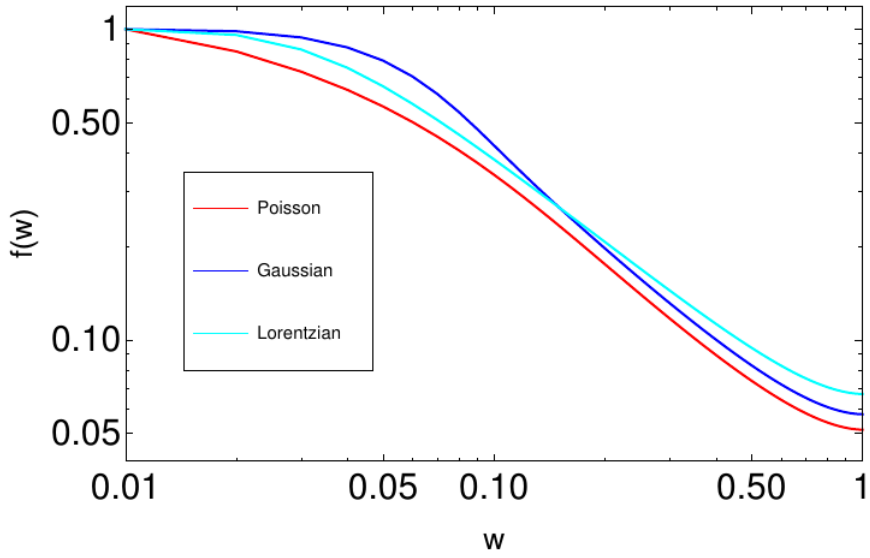

FIGURE 7.2: Distribution of winding number for Poisson, Gaussian and Lorentz profiles.

and the Lorentz distribution,

$$p_L(w) = \frac{\lambda_c}{\pi(\lambda_c^2 + w^2)}. \tag{7.12}$$

The $f(w)$ distribution for Gaussian and Lorentz profiles are obtained numerically, which are shown in Fig. 7.2. This represents that the distribution of $f(w)$ for all the three profiles are having likely the same nature, but with different slopes.

7.2.1 Energy calculation

The free energy due to the braided magnetic field lines is given by $E_f = a\bar{c}^2$ where, a depends on the length and the diameter of the magnetic fluxtubes. The flare energy omitting the a term is:

$$E = \Delta E_f/a = \bar{c}_i^2 - \bar{c}_f^2, \tag{7.13}$$

where, $\bar{c}_i$, and $\bar{c}_f$ are the initial and final crossing numbers of the braiding system respectively. The reconnection occurs when the number of crossing reaches up to a certain critical limit say, $\bar{c}_{crit}$. If two oppositely sequences of w_1 and w_2 ($w_2 > w_1$) merge together then the length becomes $|w_2| - |w_1|$ from the initial total length, $w_1 + w_2$. This gives the change in the length to be $2w_1$, hence,

$$\begin{aligned} E &= \bar{c}_{crit}^2 - (\bar{c}_{crit} - 2w_1)^2 \\ &= 4\bar{c}_{crit}|w_1| - 4w_1^2 \end{aligned} \tag{7.14}$$

but as $w_1 << w_{crit}$,

$$E \simeq 4\bar{c}_{crit}|w_1|$$

Therefore the probability distribution of E is given by

$$F(E) = 2\int_0^{\infty}\int_{-\infty}^{-w_1} f(w_1)f(w_2)\delta(E - 4\bar{c}_{crit}w_1)\mathrm{d}w_2. \tag{7.15}$$

Assuming the distribution of the coherence length follows the power-law, we consider

$$f(w_1) = b|w_1|^{\beta}, \qquad (\beta > 1). \tag{7.16}$$

Hence,

$$\begin{aligned}
F(E) &= 2\int_0^{\infty} f(w_1)\delta(E - 4\bar{c}_{crit}w_1)\mathrm{d}w_1 \int_{-\infty}^{-w_1} b|w_2|^{-\beta}\mathrm{d}w_2 \\
&= 2b\int_0^{\infty} f(w_1)\frac{\delta\left(w_1 - \frac{E}{4\bar{c}_{crit}}\right)}{4\bar{c}_{crit}}\frac{w_1^{1-\beta}}{1-\beta}\mathrm{d}w_1 \\
&= \frac{2b^2}{\beta-1}\int_0^{\infty}\frac{w_1^{1-2\beta}}{4\bar{c}_{crit}}\delta\left(w_1 - \frac{E}{4\bar{c}_{crit}}\right)\mathrm{d}w_1 \\
&= \frac{2b^2}{\beta-1}\left(\frac{1}{4\bar{c}_{crit}}\right)^{2-2\beta}E^{1-2\beta} \\
\Rightarrow F(E) &= \frac{2b^2}{\beta-1}\left(\frac{1}{4\bar{c}_{crit}}\right)^{2-2\beta}E^{1-2\beta}. \qquad (7.17)
\end{aligned}$$

Therefore, if we define $\alpha = 2\beta - 1$ then the energy E follows the power law from eqn (7.17) as,

$$F(E) \propto E^{-\alpha}. \qquad (7.18)$$

We have seen earlier that for Poisson distribution, $\beta = 2$, hence the value of α is 3. The values of β for Gaussian, and Lorentz profiles are obtained numerically by taking the average values of $\frac{\mathrm{d}\ln f(w)}{\mathrm{d}\ln(w)}$ over w; the values of α are found to be 2.5, and 0.94 for the Gaussian and Lorentz profiles respectively. The model thus demonstrates that, braid patterns can organize themselves so that coherence lengths and flare energies obey power-law energy distributions.

Mangalam and Prasad (2018) have formulated the energy for the two twisted field lines and calculated the lower bound of the twist energy, E_t in terms of global winding numbers,

$$W = \frac{1}{2\pi}\int_0^L \int\int B_{1z}B_{2z}\mathrm{d}^2x_1\mathrm{d}^2x_2\mathrm{d}z, \qquad (7.19)$$

where B_{1z}, and B_{2z} are the longitudinal components, and L is the vertical span of the field lines. The lower bound of the twist energy, E_t for the system is given by

$$E_t \geq \frac{W^2}{8R^4 B_0^2 g^2}, \tag{7.20}$$

where R is the radius of the cylindrical cross section of the flux, B_0 is the field strength at $z = 0$, and $g \approx 4$.

7.3 Radio observations of solar flare events

Radio observation is a very useful and complementary tool for weak energy signatures in the solar atmosphere. Ramesh *et al.* (2010) presented evidence from low-frequency radio observations for the existence of weak, transient events whose energies were compatible with that of nanoflares (energy $\sim 10^{24}$ erg) postulated by Parker (1988). The estimated mean energy bursts ($\sim 10^{21}$ergs) is about $\sim 10^{12}$ times lesser than the observed largest flare ($\sim 10^{33}$ erg) and are called picoflares (Ramesh *et al.* 2013). Our interest is to investigate these flare events using observations of type-I radio bursts which is known as radio noise storms. The noise storms are very short-lived ($\sim 0.1 - 1s$) and narrowband radio enhancement which is superimposed with the background broad-band, long-lasting ($\sim$ few hours-days) signals which are of type-I or noise storm continuum. The bursts are the cause of the successive emission of the electrons which are unlike the transient acceleration associated with the flares.

It is now accepted that this radiation is the plasma emission due to the coupling of Langmuir and low-frequency waves and the circular polarization is the cause of the propagation of the wave in the vicinity of the magnetic field. The type-I radio bursts are considered to be the signatures of many small steps in coronal evolution, whose cumulative effect is the gradual evolution of the corona.

7.3.1 Observations

The observations of the radio data, are taken by the "Gauribidanur Radio Heliograph" or GBRH on March 12, 2011, at 65 MHz frequency, which is maintained by Indian Institute Astrophysics (IIA), Bangalore, India. The co-ordinates of the GBRH array are longitude $77^0 27' 7''$ E, and latitude $13^0 36' 12''$ N. GBRH is a T-shaped radio interferometer array which produces the 2D radio image of the corona of the sun with the angular resolution 10'×15' (RA×Dec). The tilting of the antenna and the arrays are operated electronically. The polarimeter array is extended along East-West direction. The temporal data recorded by the polarimeter is essentially the E-W beam of the array whose amplitude is proportional to the strength of the emission from the whole Sun at the observing frequency weighted by the antenna gain in that direction.

7.3.2 Data and Analysis

The radio data that we obtain from the GBRH is essentially the temporal variation of the sine and cosine visibilities of the solar corona, which was taken on 12/09/2011 at 65 MHz frequency. These visibilities are the cause due to the superposition of radio burst of type-I and the background noises. Hence, we have to eliminate the noise from the raw data for further analysis. To remove it, we subtract the offset counts of 1.437×10^4, which is the value where the sine and cosine visibility almost overlaps. The visibility amplitude is obtained by taking the square root of the squares of the sine, and cosine visibilities, i.e. if V_c and V_s are the cosine and sine visibilities, then the visibility amplitude, V is given by,

$$V = \sqrt{V_c^2 + V_s^2}. \tag{7.21}$$

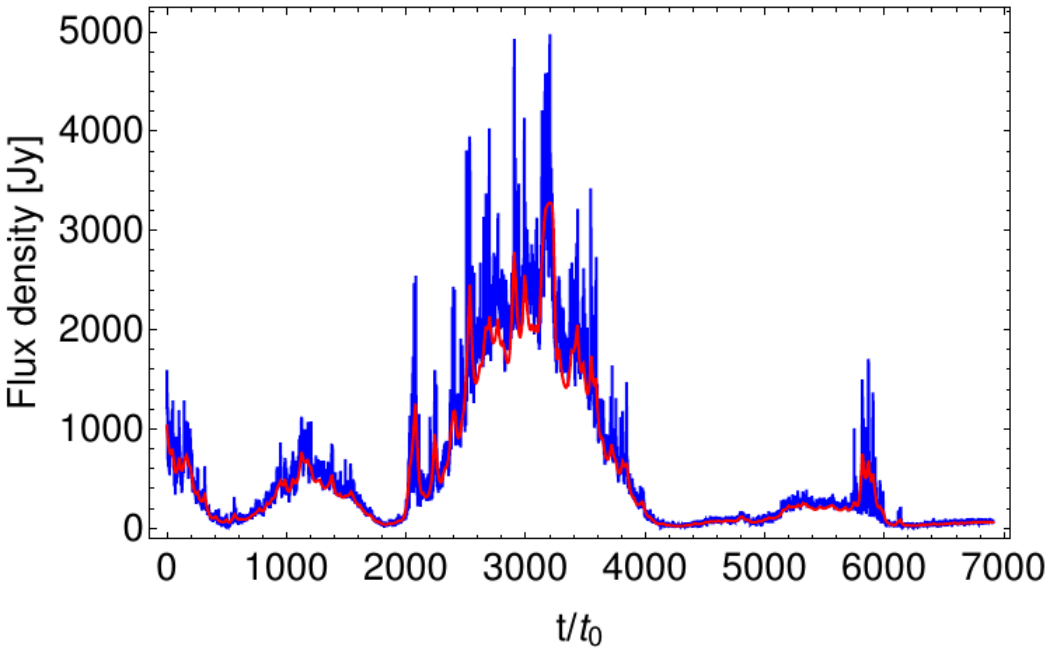

FIGURE 7.3: The blue curve is the energy flux density value which is the superposition of the radio burst-I with the background broadband continuum, where $t_0 = 500$ ms. The red curve is the fit of the lower background envelope which is the background broadband continuum.

The temporal variation of the energy distribution is due to the superposition of the type-I radio or noise storm burst with the background broadband continuum of type-I, which is shown by the blue curve in Fig. 7.3. So, for analyzing the flare energy distribution, we have to eliminate the background broadband continuum from visibility amplitude. To do this, we fit the lower envelope of the visibility curve by the estimated background method using the "Statistic-sensitive Nonlinear Iterative Peak clipping" (SNIP) algorithm (Tomoyori *et al.* 2015), which is shown by the red curve in Fig. 7.3. The temporal distribution of the flux response without the noise is obtained by subtracting the background envelope value from the noise storm visibility, which is shown in Fig. 7.4 where the spikes represent the radio bursts.

To find the flux density distribution function $F(S)$, which is the number of radio bursts in the flux density range S to $S + \mathrm{d}S$, we construct a histogram of the

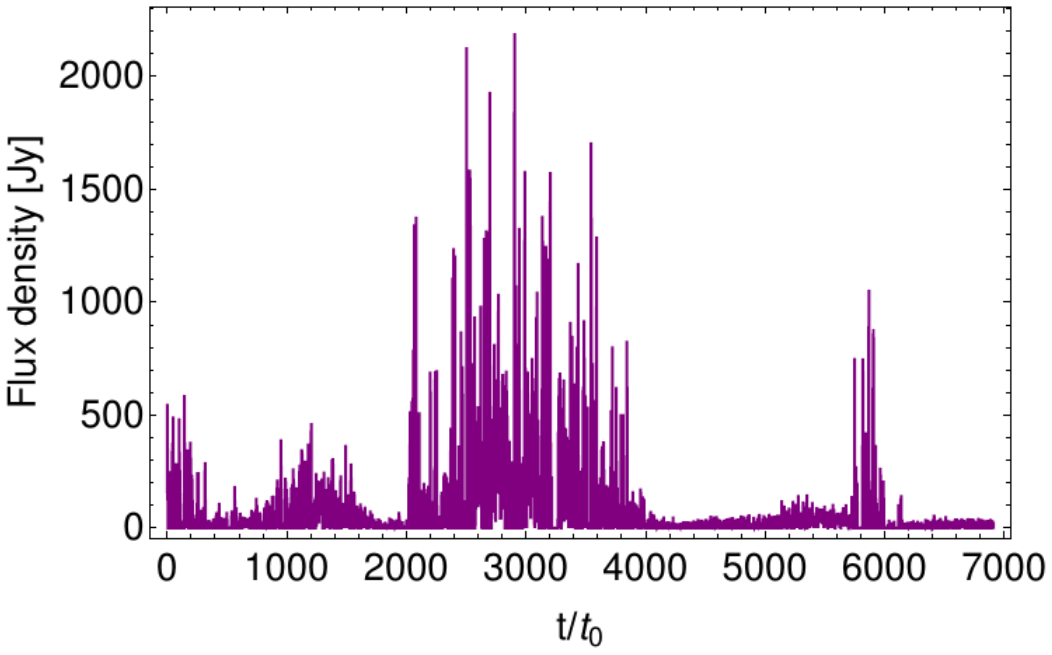

FIGURE 7.4: Temporal variation of flux density eliminating background noise, where $t_0 = 500$ ms.

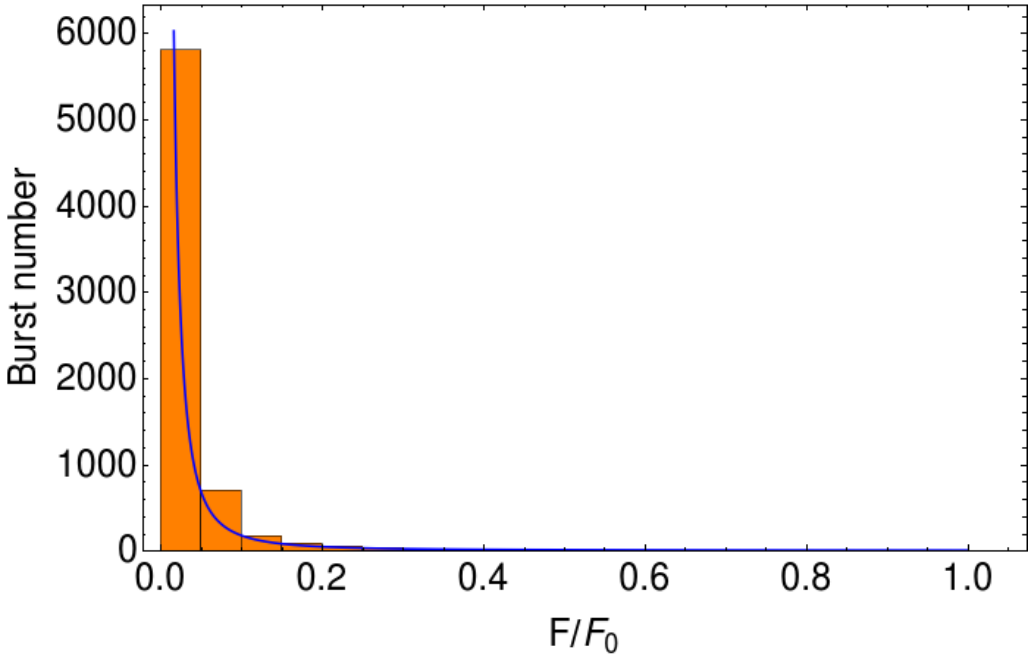

FIGURE 7.5: Histogram plot of the number of radio bursts with respect to flux density, where $F_0 = 2000$ Jy. The blue curve shows the energy power-law distribution curve.

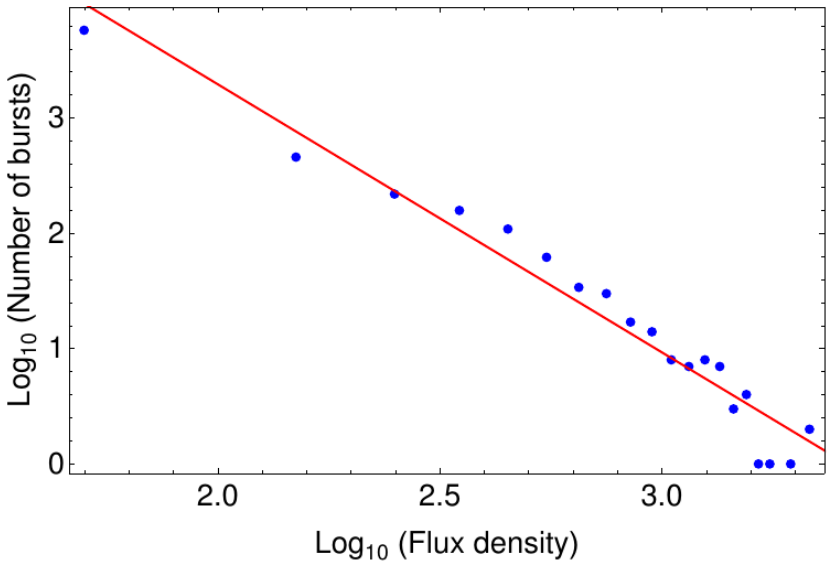

FIGURE 7.6: Logarithimic scale plot of S vs $F(S)$. The value of the slope ≈ 2.5.

number of radio bursts with the flux density shown in Fig. 7.5. To estimate the index of the power-law of flux density distribution we fit a curve which goes through the peaks of every bar of the histogram and plot the number distribution of bursts in a particular flux density bin with its corresponding flux density in the Log-Log scale, shown in Fig. 7.6. The blue points in Fig. 7.6 represent the peaks of the histogram bars. We fit a straight line (red) that follows the blue points, to estimate the index of the power-law. The slope is found to be ≈ 2.5. The results for other flare events on different dates and frequencies are listed in Table 7.1.

Date	Frequency (MHz)	Power-law index
12/03/2011	65	-2.51
14/02/2011	65	-2.05
12/03/2011	80	-2.41
14/02/2011	80	-2.15

TABLE 7.1: Radio observations of type-I bursts and estimated power-law index for energy distribution for different flare events and frequencies obtained from GBRH.

7.3.3 Results

The values of the power-law indices for the energy distribution are 3, 2.5, and 0.94 for Poisson, Gaussian, and Lorentz profiles respectively, obtained from the SOC model. We have also reported the observation for the weak ($\sim 10^{21}$erg) circularly polarized, type-I radio burst. The distribution of the number of bursts in the flux density range S to $S + \mathrm{d}S$ follows the power-law distribution i.e. $F(S)\mathrm{d}S \propto S^{\alpha}\mathrm{d}S$ with $\alpha \approx$ -2.2 to -2.7 has been reported by Ramesh *et al.* (2013), which is in a reasonable agreement with our observations, where the α varies from 2.05 to 2.51. This implies that the energy distribution power-law index obtained from the SOC model are in good agreement for the Poisson and Gaussian profiles for the winding number distribution, whereas the assumption is not suitable for the Lorentz distribution. Fig. 7.5 represents that the number of bursts occurs more towards the lower flux density. It is to be noted that the spikes that appeared in Fig. 7.4 are due to the radio flares. These weak-energy releases belong to the picoflare category and can contribute to the coronal heating. Evidence has been presented to the effect that the emerging magnetic flux may provide enough energy to heat the corona by the release of magnetic energy (Schrijver *et al.* 1997). These results suggest a possible connection with the type-I noise storms since newly emerging flux has been reported to be one of the causes for the onset of the former. Present observation says the power emitted in the type-I burst ($\sim 10^{21}$ erg s^{-1}) is smaller than the energy required ($\sim 10^{27} - 10^{28}$ erg s^{-1}) for the heating of the corona. So type-I radio burst is one of the weak energy releases and coronal heating is contributed by all these bursts in total.

7.4 Summary and Discussions

This chapter is devoted to calculating the winding number, and energy distribution of a two-braided system of the magnetic field lines, obtained from the SOC model Berger and Asgari-Targhi (2009), and the energy bounds for such a system has been calculated in terms of the global winding numbers by Mangalam and Prasad (2018). We have estimated the power-law index of the energy distribution for the solar flare events by radio data obtained from the GBRT. A part of this chapter is published in Sen *et al.* (2018). The SOC model gives an well understanding of how the new random inputs of the braided structure is in balance by the loss of the braiding due to reconnections. Berger *et al.* (2015) have used a *forest-fire* model to explain the braiding to be self-organized due to the reconnections. The magnetic fields in the photosphere are in discrete flux elements. This discreteness can enhance the braiding complexities or the amount of the braided structure that can be hold by the corona. The braiding of the field lines is more efficient for a smoothly distributed field lines across the boundary. In this model, the braiding is associated along the loop axis. This model can be improved by including the braiding along the transverse direction by implementing the internal twists, and for a multi-braid system.

Chapter 8

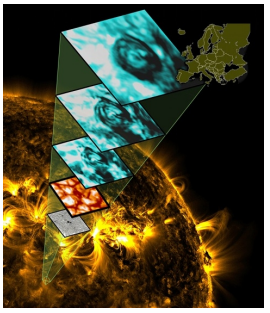

Image source: www.arstechnica.com

Summary and Conclusions

8.1 Summary

In Chapter 1, a brief overview of the solar interior, its atmosphere, and the magnetic structure are discussed. A brief historical overview of the magnetic fluxtube models and its importance of the study is also discussed in this Chapter. Chapter 2 is focused on the basics of MHD. The derivation of GSE was presented which is a key ingredient for building the fluxtube models that we use in our work. In Chapter 3, we discuss the magnetic configurations of fluxtubes. Here we discussed observational implications of fluxtubes in the solar atmosphere, the magnetic properties of the fluxtubes, the governing equations to solve fluxtube models, and a historical overview of various fluxtube models. This chapter formed the background material for studying solar fluxtubes.

In Chapter 4, we constructed a fluxtube model in the axisymmetry with a twisted magnetic field. Incorporating realistic boundary conditions (BCs) for solar atmosphere, we found a magnetohydrostatic equilibrium solution for fluxtubes by solving GSE analytically, which is a combination of the Coulomb function in r, and an exponential function along z. The magnetic configuration of the fluxtube obtained from this model is closed. We calculate the magnetic and thermodynamic structure of the fluxtube and see that the findings are in reasonable agreement with the observations of MBPs. This has been published in Sen and Mangalam (2018a).

In Chapter 5, we have extended the closed field model discussed in Chapter 4 by incorporating an inhomogeneous part with the homogeneous Coulomb function solution. The inhomogeneous part is a power series solution of the hypergeometric function and independent of z. Using this new solution, and incorporating BCs appropriate for the solar atmosphere, we obtained the magnetic and thermodynamic structure of the fluxtube. We also constructed another class of fluxtube models based on the self-similar formulation. We have extended the model by implementing two different magnetic shape functions which are the generalized Gaussian, and power-law functions, and obtain the magnetohydrostatic equilibrium solution by taking the stratified solar gravity. The magnetic configuration of the fluxtube obtained from both these models is open, which means the field lines do not come back within the comparable domain. We compared the estimated value of the magnetic and thermodynamic structure with the observations and other simulations of MBPs and saw that the estimations are in reasonable agreement. This has been published in Sen and Mangalam (2019). We have also discussed the self-similar closed field twisted magnetic fluxtube model, where we have incorporated a quadratic magnetic shape function and found an analytical fluxtube solution. This work is in preparation.

Chapter 6 is devoted to the discussions about magnetic reconnections, and various

solar flare models. This chapter is the background material for understanding the next chapter. In Chapter 7, we discuss the winding number distribution for the braided magnetic field lines using the SOC model and estimate the power-law indices for the energy distribution of the braided system. We also calculate the power-law indices from the observational study of the radio flare events on 12 March 2011, and 14 February 2011, from the data obtained by GBRT. We see that the theoretical estimations are in reasonable agreement with the observations. This is partly published in Sen *et al.* (2018)

Finally, here, we discuss the summary and conclusions of the Thesis, highlight the novel aspects and their impact, and the future directions.

8.2 Novel aspects and their impact

The Thesis aimed to construct magnetohydrostatic equilibrium models of magnetic fluxtubes with twisted magnetic fields. The fluxtube solutions obtained from these models are useful to estimate the magnetic and thermodynamic structures of the fluxtubes in the stratified solar atmosphere. The models are also the verifiable means to calculate the magnetic structure of the MBPs observed in the solar atmosphere. In the case of topological aspects of magnetic braiding of the field lines, the theoretical prediction of the energy distribution gives a useful estimate of the power-law index for the solar flares. This estimation is compared with the observations of the radio flare events. The novel points of the work are listed below.

1. We provide a new and distinct magnetohydrostatic equilibrium fluxtube solution with the twisted magnetic field in the stratified solar atmosphere,

called as the Coulomb function helical fluxtube model. The fluxtube solution of the Coulomb function model has two parts, which are homogeneous, and the particular. The homogeneous part is a combination of the Coulomb function in r and an exponential function in z, and the particular part is a power series solution of the hypergeometric function in r with no z dependence. The homogeneous solution gives a closed field magnetic structure of the fluxtube, whereas the particular part gives the open field magnetic configuration.

2. We constructed another class of fluxtube solution based on the self-similar formulation. We have implemented a twist in it, and obtain the magneto-hydrostatic equilibrium model in the solar atmosphere taking into account gravity. Using two different magnetic shape functions, which are the generalized Gaussian, and power-law functions, we built the open field magnetic configuration of the fluxtubes. While specifying the shape function in the quadratic form, the magnetic field line configuration of the fluxtube becomes closed.

3. Incorporating appropriate BCs for a realistic solar atmosphere in both models, we found fluxtube solutions for the open and closed field models that are used to calculate the magnetic and thermodynamic structures inside the fluxtubes. This is in a reasonable agreement with the MBPs.

4. The open field fluxtube solutions are the useful inputs for the numerical simulation models for studying the propagation of the MHD waves through the solar atmosphere.

5. The closed field fluxtube models can be used as the building blocks for making realistic structures like magnetic canopies, or coronal loops.

6. We calculated the winding number distribution for a braided system of magnetic field lines using the SOC model and used this model to calculate the energy distribution of a two braid system.

7. This theoretical prediction of the power-law index for the energy distribution of the braided system gives a useful comparison with the observational studies for the solar flare events. The data was obtained from GBRT for the radio flare events on March 12, 2011, and February 14, 2011.

8.3 Caveats

We list some of the caveats below:

1. With the further advancement of the spatial and temporal resolution of the telescopes, the observations for the small scale fluxtubes in the solar atmosphere can be compared with the theoretical predictions of the models.

2. The fluxtube models we have developed span from the photosphere to the transition region. With the more realistic inputs of the solar parameters, e.g. magnetic field strengths and thermodynamic quantities, we can extend the models up to the corona.

3. The radial span of the fluxtube models (Sen and Mangalam 2019, 2018a,b) are of the order of a few hundred km. These small scale structures are comparable with MBPs. On the other hand, the large scale fluxtubes, sunspots have the radial size of a few tens of Mm, and the radial variation of the pressure profiles is not similar to our models. So the fluxtube models that we have developed can not explain the sunspots structure fully.

4. With the radio data set obtained from the GBRT, a large statistical study for the solar flare events can be made to confirm the winding number and (Sen *et al.* 2018; Mangalam and Prasad 2018) power-law indices of the energy distribution.

8.4 Future directions

There are several promising future aspects of all the problems discussed in the Thesis. With further improvements in the observations of small scale fluxtubes in the solar atmosphere, we can improve the fluxtube models accordingly. For the reconstruction of the magnetic field line topology for a multi-braid system, we can extend the Mangalam and Prasad (2018) model to incorporate comprehensive Monte-Carlo simulations (Berger and Asgari-Targhi 2009). The other plans are in the following.

1. Preliminary calculations using the constraint of relative helicity based on the formulations given in (Prasad *et al.* 2014; Prasad and Mangalam 2016) and applying the constrained energy minimization principle (Mangalam and Krishan 2000; Finn and Antonsen 1983; Taylor 1974) indicate that stable configurations of the fluxtubes are possible for some regions in the parameter space of the models. We plan a complete solution of this allowed regions and test it with numerical simulations in a paper in preparation.

2. The semi-analytical fluxtube solutions discussed above of the variation of magnetic field strength with the depth is used to derive the run of plasma density and pressure. The aim is to apply the models as the background condition for numerical studies of waves and their kinematic properties taking realistic inputs of field strength and pressure distribution observed in the lower solar atmosphere. We plan to calculate the energy transport from the photosphere to corona which plays a key role in the heating of solar corona, through wave heating in the context of the twisted self-similar field models. (Solov'ev 1997) extended the self-similar sunspot models by introducing a current sheet at the sunspot boundary. In addition, we plan to include under typical coronal conditions, the Ohmic heating, due to phase mixing, that

can provide magnetic energy on a time scale comparable with the coronal radiative time.

3. We plan to further explore the energy released through the small scale reconnection events arising from braiding and correlate them to the energy content in the force-free fields. The fraction of energy budget available can be dissipated by reconnections; so we need to complement braiding theory with the reconnection models. We also plan to compare our model with the radio data from the GBRT and analyze using the Statistic Sensitive non-linear iterative peak clipping (SNIP) algorithm (Tomoyori *et al.* 2015).

4. We plan to extend the study of topological and statistical properties of the braiding of the magnetic field lines (Mangalam and Prasad 2018). We plan on building detailed braiding topologies and evaluating energy distribution through estimates of crossing numbers of multiple braids. As we explore more analytic solutions, we can use this method to verify them and apply them to more active regions. As an example, we have calculated the power-law distribution for the braiding and resulting energy distributions. We find that our estimates using the nonlinear force-free fields are in good agreement with the SOC model. We have studied the effect of different input distributions like Gaussian and Lorentzian for the SOC model and found that the Poisson distribution fits best with our NLFFF solutions. The energy released from these braided structures can be significant.

"I am busy just now again on electro-magnetism, and I think I have got hold of a good thing, but can't say. It may be a weed instead of a fish that, after all my labor, I may at last pull up."

– Michael Faraday

Figure source: `www.independent.co.uk`

The End!

Bibliography

Abramowitz, Milton and Stegun, Irene A., 1972, *Handbook of Mathematical Functions with Formulas, Graphs, and Mathematical Tables*, Dover, New York City, ninth dover printing, tenth gpo printing edn.

Aschwanden, M. J., Nightingale, R. W. and Alexander, D., 2000, "Evidence for Nonuniform Heating of Coronal Loops Inferred from Multithread Modeling of TRACE Data", *Astrophys. J.*, **541**, 1059–1077. [DOI], [ADS]

Atanasiu, C. V., Gnter, S., Lackner, K. and Miron, I. G., 2004, "Analytical solutions to the GradShafranov equation", *Physics of Plasmas*, **11**(7), 3510–3518. [DOI], [http://aip.scitation.org/doi/pdf/10.1063/1.1756167]URL: `http://aip.scitation.org/doi/abs/10.1063/1.1756167`

Avrett, E. H. and Loeser, R., 2008, "Models of the Solar Chromosphere and Transition Region from SUMER and HRTS Observations: Formation of the Extreme-Ultraviolet Spectrum of Hydrogen, Carbon, and Oxygen", *Astrophys. J. Suppl.*, **175**, 229-276. [DOI], [ADS]

Babcock, Horace W. and Babcock, Harold D., 1955, "The Sun's Magnetic Field, 1952-1954.", *Astrophys. J.*, **121**, 349. [DOI], [ADS]

Balthasar, H. and Schmidt, W., 1993, "Polarimetry and spectroscopy of a simple sunspot. 2: On the height and temperature dependence of the magnetic field", *Astron. Astrophys.*, **279**, 243–250. [ADS]

Beckers, J. M. and Schröter, E. H., 1968, "The Intensity, Velocity and Magnetic Structure of a Sunspot Region. I: Observational Technique; Properties of Magnetic Knots", *Solar Physics*, **4**(2), 142–164. [DOI], [ADS]

Beckers, J. M. and Schröter, E. H., 1969, "The Intensity, Velocity and Magnetic Structure of a Sunspot Region. IV: Properties of a Unipolar Sunspot", *Solar Phys.*, **10**(2), 384–403. [DOI], [ADS]

Berger, M. A., Asgari-Targhi, M. and Deluca, E. E., 2015, "Self-organized braiding in solar coronal loops", *Journal of Plasma Physics*, **81**(4), 395810404. [DOI], [ADS]

Berger, Mitchell A., 1994, "Coronal heating by dissipation of magnetic structure", *Space Sci. Rev.*, **68**(1-4), 3–14. [DOI], [ADS]

Berger, Mitchell A. and Asgari-Targhi, Mahboubeh, 2009, "Self-organized Braiding and the Structure of Coronal Loops", *Astrophys. J.*, **705**(1), 347–355. [DOI], [ADS]

Berger, T. E., Schrijver, C. J., Shine, R. A., Tarbell, T. D., Title, A. M. and Scharmer, G., 1995, "New Observations of Subarcsecond Photospheric Bright Points", *Astrophys. J.*, **454**, 531–544. [DOI], [ADS]

Boersma, J., 1968, "Expansions of Coulomb Wave Functions", *American Mathematical Society*, **23**, 51–59

Bogdan, T. J., Carlsson, M., Hansteen, V. H., McMurry, A., Rosenthal, C. S., Johnson, M., Petty-Powell, S., Zita, E. J., Stein, R. F., McIntosh, S. W. and Nordlund, Å., 2003, "Waves in the Magnetized Solar Atmosphere. II. Waves from Localized Sources in Magnetic Flux Concentrations", *Astrophys. J.*, **599**, 626–660. [DOI], [ADS]

Byrd, P. and Friedman, D., 1971, *Handbook of Elliptic Integrals for Engineers and Scientists*, Springer-Verlag Berlin Heidelberg GmbH, 1971

Cargill, P. J., 2014, "Active Region Emission Measure Distributions and Implications for Nanoflare Heating", *Astrophys. J.*, **784**(1), 49. [DOI], [ADS]

Centeno, R., Socas-Navarro, H., Lites, B., Kubo, M., Frank, Z., Shine, R., Tarbell, T., Title, A., Ichimoto, K., Tsuneta, S., Katsukawa, Y., Suematsu, Y., Shimizu, T. and Nagata, S., 2007, "Emergence of Small-Scale Magnetic Loops in the Quiet-Sun Internetwork", *Astrophys. J. Lett.*, **666**, L137–L140. [DOI], [ADS], [arXiv:0708.0844]

Chandrasekhar, S., 1956, "On Force-Free Magnetic Fields", *Proceedings of the National Academy of Science*, **42**(1), 1–5. [DOI], [ADS]

Cowling, T. G., 1972, *Magnetohydrodynamics, Monographs in Astronomical subjects 2*, Adam Hilger, Bristol, UK.

Cram, L. E. and Wilson, P. R., 1975, "Hydromagnetic Waves in Structured Magnetic Fields", *Solar Phys.*, **41**(2), 313–327. [DOI], [ADS]

Defouw, R. J., 1976, "Wave propagation along a magnetic tube.", *Astrophys. J.*, **209**, 266–269. [DOI], [ADS]

Deinzer, W., Hensler, G., Schuessler, M. and Weisshaar, E., 1984a, "Model calculations of magnetic flux tubes. I - Equations and method. II - Stationary results for solar magnetic elements", *Astron. Astrophys.*, **139**(2), 426–449. [ADS]

Deinzer, W., Hensler, G., Schussler, M. and Weisshaar, E., 1984b, "Model Calculations of Magnetic Flux Tubes - Part Two - Stationary Results for Solar Magnetic Elements", *Astron. Astrophys.*, **139**, 435. [ADS]

Dixit, A. and Moll, V., 2015, "The confluent hypergeometric function and Whittaker functions", *Scientia Series A*, **26**, 49–61

Erdélyi, R. and Fedun, V., 2010, "Magneto-Acoustic Waves in Compressible Magnetically Twisted Flux Tubes", *Solar Phys.*, **263**, 63–85. [DOI], [ADS]

Evershed, J., 1909, "Radial movement in sun-spots", *The Observatory*, **32**, 291–292. [ADS]

Fedun, V., Erdélyi, R. and Shelyag, S., 2009, "Oscillatory Response of the 3D Solar Atmosphere to the Leakage of Photospheric Motion", *Solar Phys.*, **258**, 219–241. [DOI], [ADS]

Fedun, V., Verth, G., Jess, D. B. and Erdélyi, R., 2011, "Frequency Filtering of Torsional Alfvén Waves by Chromospheric Magnetic Field", *Astrophys. J. Lett.*, **740**, L46. [DOI], [ADS]

Finn, J. M. and Antonsen, Jr., T. M., 1983, "Turbulent relaxation of compressible plasmas with flow", *Physics of Fluids*, **26**, 3540–3552. [DOI], [ADS]

Forbes, T. G. and Priest, E. R., 1995, "Photospheric Magnetic Field Evolution and Eruptive Flares", *Astrophys. J.*, **446**, 377. [DOI], [ADS]

Frazier, E. N. and Stenflo, J. O., 1972, "On the Small-Scale Structure of Solar Magnetic Fields", *Solar Physics*, **27**(2), 330–346. [DOI], [ADS]

Gent, F. A., Fedun, V., Mumford, S. J. and Erdélyi, R., 2013, "Magnetohydrostatic equilibrium - I. Three-dimensional open magnetic flux tube in the stratified solar atmosphere", *Mon. Not. Roy. Astron. Soc.*, **435**, 689–697. [DOI], [ADS], [arXiv:1305.4788 [astro-ph.SR]]

Gent, F. A., Fedun, V. and Erdélyi, R., 2014, "Magnetohydrostatic Equilibrium. II. Three-dimensional Multiple Open Magnetic Flux Tubes in the Stratified Solar Atmosphere", *Astrophys. J.*, **789**, 42. [DOI], [ADS], [arXiv:1405.0613 [astro-ph.SR]]

Giovanelli, R. G., 1946, "A Theory of Chromospheric Flares", *Nature*, **158**(4003), 81–82. [DOI], [ADS]

Goosens, M., 2003, *An Introduction to Plasma Astrophysics and Magnetohydrodynamics*, Centrum voor Plasma Astrofysica, Heverlee

Grad, H. and Rubin, H., 1958, *Hydromagnetic Equlibria and Force-Free Fields*, U.S. Government Printing Office, International Conference on the Peaceful Uses of Atomic Energy, Geneva, 31, 190-197

Guglielmino, S. L., Pillet, V. M., del Toro Iniesta, J. C., Rubio, L. R. B., Zuccarello, F., Solanki, S. K. and Solanki, 2011, "Small-scale flux emergence events observed by Sunrise/IMaX", in *Advances in Plasma Astrophysics*, (Eds.) Bonanno, A., de Gouveia Dal Pino, E., Kosovichev, A. G., IAU Symposium, 274, [DOI], [ADS]

Hagenaar, H. J., Schrijver, C. J., Title, A. M. and Shine, R. A., 1999, "Dispersal of Magnetic Flux in the Quiet Solar Photosphere", *Astrophys. J.*, **511**, 932–944. [DOI], [ADS]

Hewitt, R. L., Shelyag, S., Mathioudakis, M. and Keenan, F. P., 2014, "Plasma properties and Stokes profiles during the lifetime of a photospheric magnetic bright point", *Astron. Astrophys.*, **565**, A84. [DOI], [ADS], [arXiv:1404.0132 [astro-ph.SR]]

Heyvaerts, J., Priest, E. R. and Rust, D. M., 1977, "An emerging flux model for the solar phenomenon.", *Astrophys. J.*, **216**, 123–137. [DOI], [ADS]

Hindman, B. W. and Jain, R., 2008, "The Generation of Coronal Loop Waves below the Photosphere by p-Mode Forcing", *Astrophys. J.*, **677**, 769-780. [DOI], [ADS], [arXiv:0805.1942]

Howard, Robert, 1959, "Observations of Solar Magnitic Fields.", *Astrophys. J.*, **130**, 193. [DOI], [ADS]

Howard, Robert and Stenflo, J. O., 1972, "On the Filamentary Nature of Solar Magnetic Fields", *Solar Physics*, **22**(2), 402–417. [DOI], [ADS]

Judge, P., 2006, "Observations of the Solar Chromosphere", in *Solar MHD Theory and Observations: A High Spatial Resolution Perspective*, (Eds.) Leibacher, J.,

Stein, R. F., Uitenbroek, H., Astronomical Society of the Pacific Conference Series, 354, [ADS]

Kadomtsev, B. B., 1966, "Hydromagnetic Stability of a Plasma", *Reviews of Plasma Physics*, **2**, 153. [ADS]

Kishore, P., Ramesh, R., Hariharan, K., Kathiravan, C. and Gopalswamy, N., 2016, "Constraining the Solar Coronal Magnetic Field Strength using Split-band Type II Radio Burst Observations", *Astrophys. J.*, **832**(1), 59. [DOI], [ADS]

Klimchuk, James A., 2015, "Key Aspects of Coronal Heating", in *AAS/AGU Triennial Earth-Sun Summit*, [ADS]

Kruskal, M. D. and Kulsrud, R. M., 1958, "Equilibrium of a Magnetically Confined Plasma in a Toroid", *Physics of Fluids*, **1**(4), 265–274. [DOI], [ADS]

Kulsrud, R., 2010, *Plasma Physics for Astrophysics*, Princeton University Press, USA

Kumari, Anshu, Ramesh, R., Kathiravan, C. and Gopalswamy, N., 2017, "New Evidence for a Coronal Mass Ejection-driven High Frequency Type II Burst near the Sun", *Astrophys. J.*, **843**(1), 10. [DOI], [ADS]

Lagg, A., Solanki, S. K., Riethmüller, T. L., Martínez Pillet, V., Schüssler, M., Hirzberger, J., Feller, A., Borrero, J. M., Schmidt, W., del Toro Iniesta, J. C., Bonet, J. A., Barthol, P., Berkefeld, T., Domingo, V., Gandorfer, A., Knölker, M. and Title, A. M., 2010, "Fully Resolved Quiet-Sun Magnetic flux Tube Observed with the SUNRISE/IMAX Instrument", *Astrophys. J. Lett.*, **723**, L164–L168. [DOI], [ADS], [arXiv:1009.0996 [astro-ph.SR]]

Leighton, Robert B., 1959, "Observations of Solar Magnetic Fields in Plage Regions.", *Astrophys. J.*, **130**, 366. [DOI], [ADS]

Litvinenko, Yu. E., 1994, "An Explanation for the Flare Frequency - Energy Dependence", *Solar Phys.*, **151**(1), 195–198. [DOI], [ADS]

Livingston, W., 1991, "Radial filamentary structure in a sunspot umbra", *Nature*, **350**(6313), 45–46. [DOI], [ADS]

Low, B. C. and Lou, Y. Q., 1990, "Modeling Solar Force-free Magnetic Fields", *Astrophys. J.*, **352**, 343. [DOI], [ADS]

Lu, Edward T., Hamilton, Russell J., McTiernan, J. M. and Bromund, Kenneth R., 1993, "Solar Flares and Avalanches in Driven Dissipative Systems", *Astrophys. J.*, **412**, 841. [DOI], [ADS]

Lundquist, S., 1951, "On the Stability of Magneto-Hydrostatic Fields", *Physical Review*, **83**(2), 307–311. [DOI], [ADS]

Machado, Marcos E., Moore, Ronald L., Hernandez, Ana M., Rovira, Marta G., Hagyard, Mona J. and Smith, Jesse B., Jr., 1988, "The Observed Characteristics of Flare Energy Release. I. Magnetic Structure at the Energy Release Site", *Astrophys. J.*, **326**, 425. [DOI], [ADS]

Mangalam, A. and Krishan, V., 2000, "Models of Flux Tubes from Constrained Relaxation", *Journal of Astrophysics and Astronomy*, **21**, 299. [DOI], [ADS]

Mangalam, A. and Prasad, A., 2018, "Topological and statistical properties of nonlinear force-free fields", *Advances in Space Research*, **61**(2), 738–748. [DOI], [ADS], [arXiv:1711.02881 [astro-ph.SR]]

Meyer, F., Schmidt, H. U. and Weiss, N. O., 1977, "The stability of sunspots.", *Mon. Not. Roy. Astron. Soc.*, **179**, 741–761. [DOI], [ADS]

Muller, R. and Mena, B., 1987, "Motions around a decaying sunspot", *Solar Phys.*, **112**, 295–303. [DOI], [ADS]

Muller, R., Roudier, T., Vigneau, J. and Auffret, H., 1994, "The proper motion of network bright points and the heating of the solar corona", *Astron. Astrophys.*, **283**, 232–240. [ADS]

Murawski, K., Solov'ev, A. and Kraśkiewicz, J., 2015a, "A Numerical Model of MHD Waves in a 3D Twisted Solar Flux Tube", *Solar Phys.*, **290**, 1909–1922. [DOI], [ADS]

Murawski, K., Solov'ev, A., Musielak, Z. E., Srivastava, A. K. and Kraśkiewicz, J., 2015b, "Torsional Alfvén waves in solar magnetic flux tubes of axial symmetry", *Astron. Astrophys.*, **577**, A126. [DOI], [ADS], [arXiv:1501.00252 [astro-ph.SR]]

Osherovich, V. A., 1984, "Magnetic flux tube in a stratified atmosphere under the influence of the vertical magnetic field", *Solar Phys.*, **94**, 207–217. [DOI], [ADS]

Osherovitch, V. A., 1979, "A DESCRIPTION OF THE SUNSPOT-TWISTED MAGNETIC FIELD UNDER 'SIMILARITY' ASSUMPTION", *Solar Phys.*, **64**, 261–265. [ADS]

Osherovitch, V. A., 1982, "A new Magneto-hydrostatic theoty of Sunspots", *Solar Phys.*, **77**, 63–68. [ADS]

Pahlke, K.-D. and Wiehr, E., 1990, "Magnetic field, relative Doppler shift and temperature for an inhomogeneous model of sunspot umbrae", *Astron. Astrophys.*, **228**, 246–252. [ADS]

Papathanasoglou, D., 1971, "Observation of Filamentary Structure in Sunspot Umbrae", *Solar Phys.*, **21**(1), 113–115. [DOI], [ADS]

Parker, E. N., 1957, "Sweet's Mechanism for Merging Magnetic Fields in Conducting Fluids", *J. Geophys. Res.*, **62**(4), 509–520. [DOI], [ADS]

Parker, E. N., 1963, "The Solar-Flare Phenomenon and the Theory of Reconnection and Annihiliation of Magnetic Fields.", *Astrophys. J. Suppl.*, **8**, 177. [DOI], [ADS]

Parker, E. N., 1972, "Topological Dissipation and the Small-Scale Fields in Turbulent Gases", *Astrophys. J.*, **174**, 499. [DOI], [ADS]

Parker, E. N., 1974a, "Hydraulic Concentration of Magnetic Fields in the Solar Photosphere. I. Turbulent Pumping", *Astrophys. J.*, **189**, 563–568. [DOI], [ADS]

Parker, E. N., 1974b, "Hydraulic Concentration of Magnetic Fields in the Solar Photosphere. II. Bernoulli Effect", *Astrophys. J.*, **190**, 429–436. [DOI], [ADS]

Parker, E. N., 1974c, "The Dynamical Properties of Twisted Ropes of Magnetic Field and the Vigor of New Active Regions on the Sun", *Astrophys. J.*, **191**, 245–254. [DOI], [ADS]

Parker, E. N., 1983, "Magnetic neutral sheets in evolving fields. I - General theory.", *Astrophys. J.*, **264**, 635–647. [DOI], [ADS]

Parker, E. N., 1988, "Nanoflares and the solar X-ray corona", *Astrophys. J.*, **330**, 474–479. [DOI], [ADS]

Peter, H., Gudiksen, B. V. and Nordlund, A., 2005, "Coronal Heating Through Braiding of Magnetic Field Lines Synthesized Coronal EUV Emission and Magnetic Structure", in *Chromospheric and Coronal Magnetic Fields*, (Eds.) Innes, D. E., Lagg, A., Solanki, S. A., ESA Special Publication, 596, [ADS]

Petschek, H. E., 1964, "Magnetic Field Annihilation", in *The Physics of Solar Flares, Proceedings of the AAS-NASA Symposium held 28-30 October, 1963 at the Goddard Space Flight Center, Greenbelt, MD. Edited by Wilmot N. Hess. Washington, DC: National Aeronautics and Space Administration, Science and Technical Information Division, 1964., p.425*, 50, [ADS]

Piddington, J. H., 1978, "The Flux-Rope-Fibre Theory of Solar Magnetic Fields", *Astrophys. Space Sci.*, **55**(2), 401–425. [DOI], [ADS]

Pikel'Ner, S. B., 1963, "Formation of the Chromospheric Network and the Structure of the Magnetic Field", *Soviet Astron.*, **6**, 757. [ADS]

Prasad, A. and Mangalam, A., 2016, "A Global Galactic Dynamo with a Corona Constrained by Relative Helicity", *Astrophys. J.*, **817**, 12. [DOI], [ADS], [arXiv:1511.03392]

Prasad, A., Mangalam, A. and Ravindra, B., 2014, "Separable Solutions of Force-Free Spheres and Applications to Solar Active Regions", *Astrophys. J.*, **786**, 81. [DOI], [ADS], [arXiv:1404.0910 [astro-ph.SR]]

Priest, E. R. and Forbes, T. G., 1990, "Magnetic Field Evolution during Prominence Eruptions and Two-Ribbon Flares", *Solar Phys.*, **126**(2), 319–350. [DOI], [ADS]

Priest, Eric, 2014, *Magnetohydrodynamics of the Sun*. [DOI], [ADS]

Priest, Eric and Forbes, Terry, 2000, *Magnetic Reconnection*. [ADS]

Priest, Eric R., Heyvaerts, Jean F. and Title, Alan M., 2002, "A Flux-Tube Tectonics Model for Solar Coronal Heating Driven by the Magnetic Carpet", *Astrophys. J.*, **576**(1), 533–551. [DOI], [ADS]

Priest, Eric Ronald, 1982, *Solar magneto-hydrodynamics*. [ADS]

Ramesh, R., Kathiravan, C., Barve, Indrajit V., Beeharry, G. K. and Rajasekara, G. N., 2010, "Radio Observations of Weak Energy Releases in the Solar Corona", *Astrophys. J. Lett.*, **719**(1), L41–L44. [DOI], [ADS]

Ramesh, R., Sasikumar Raja, K., Kathiravan, C. and Narayanan, A. Satya, 2013, "Low-frequency Radio Observations of Picoflare Category Energy Releases in the Solar Atmosphere", *Astrophys. J.*, **762**(2), 89. [DOI], [ADS]

Riethmüller, T. L. and Solanki, S. K., 2016, "The dark side of solar photospheric G-band bright points", *ArXiv e-prints*. [ADS], [arXiv:1612.07887 [astro-ph.SR]]

Roberts, B. and Webb, A. R., 1978, "Vertical motions in an intense magnetic flux tube.", *Solar Phys.*, **56**(1), 5–35. [DOI], [ADS]

Roberts, P. H., 1967, *An Introduction to Magnetohydrodynamics*. [ADS]

Rosner, R. and Vaiana, G. S., 1978, "Cosmic flare transients: constraints upon models for energy storage and release derived from the event frequency distribution.", *Astrophys. J.*, **222**, 1104–1108. [DOI], [ADS]

Ruzmaikin, A. and Berger, M. A., 1998, "On a source of Alfven waves heating the solar corona", *Astron. Astrophys.*, **337**, L9–L12. [ADS]

Ryutova, M., 2015, *Physics of Magnetic Flux Tubes*, Springer, Newyork

Ryutova, M., Berger, T. and Title, A., 2008, "On the Fine Structure and Formation of Sunspot Penumbrae", *Astrophys. J.*, **676**(2), 1356–1366. [DOI], [ADS]

Sasikumar Raja, K., Ramesh, R., Hariharan, K., Kathiravan, C. and Wang, T. J., 2014, "An Estimate of the Magnetic Field Strength Associated with a Solar Coronal Mass Ejection from Low Frequency Radio Observations", *Astrophys. J.*, **796**(1), 56. [DOI], [ADS], [arXiv:1611.05249 [astro-ph.SR]]

Schlüter, A. and Temesváry, S., 1958, "The internal constitution of sunspots", *Symposium - International Astronomical Union, Cambridge: Cambridge University Press*, **6**, 263–274. [DOI]

Schrijver, C. J., Title, A. M., Harvey, K. L., Sheeley, N. R., Wang, Y. M., van den Oord, G. H. J., Shine, R. A., Tarbell, T. D. and Hurlburt, N. E., 1998, "Large-scale coronal heating by the small-scale magnetic field of the Sun", *Nature*, **394**(6689), 152–154. [DOI], [ADS]

Schrijver, Carolus J., Title, Alan M., Hagenaar, Hermance J. and Shine, Richard A., 1997, "Modeling the distribution of magnetic fluxes in field concentrations in a solar active region", *Solar Phys.*, **175**(2), 329–340. [DOI], [ADS]

Sen, S. and Mangalam, A., 2018a, "Model of a fluxtube with a twisted magnetic field in the stratified solar atmosphere", *Advances in Space Research*, **61**, 617–627. [DOI], [ADS], [arXiv:1705.08100 [astro-ph.SR]]

Sen, S. and Mangalam, A., 2018b, "Flux tube model in the solar atmosphere", in *IAU Symposium*, (Eds.) Banerjee, D., Jiang, J., Kusano, K., Solanki, S., IAU Symposium, 340, [DOI], [ADS]

Sen, S., Mangalam, A. and Ramesh, R., 2018, "Energy distribution of solar flare events", in *IAU Symposium*, (Eds.) Banerjee, D., Jiang, J., Kusano, K., Solanki, S., IAU Symposium, 340, [DOI], [ADS], [arXiv:1805.08431 [astro-ph.SR]]

Sen, Samrat and Mangalam, A., 2019, "Open and Closed Magnetic Configurations of Twisted Flux Tubes", *Astrophys. J.*, **877**(2), 127. [DOI], [ADS], [arXiv:1904.03149 [astro-ph.SR]]

Severnyi, A. B., 1959, "Fine Structure of the Magnetic Field and Depolarization of Radiation in Sunspots.", *Soviet Astron.*, **3**, 214. [ADS]

Shafranov, V., 1958, "*Zh. Eksp. Teor. Fiz*", *Journal of Theoretical and experimental physics*, **33**, 710–722

Sheeley, N. R., Jr., 1966, "Measurements of Solar Magnetic Fields", *The Astrophysical Journal*, **144**, 723. [DOI], [ADS]

Sheeley, N. R., Jr., 1967, "Observations of Small-Scale Solar Magnetic Fields", *Solar Physics*, **1**(2), 171–179. [DOI], [ADS]

Shelyag, S., Mathioudakis, M., Keenan, F. P. and Jess, D. B., 2010, "A photospheric bright point model", *Astron. Astrophys.*, **515**, A107. [DOI], [ADS], [arXiv:1003.1653 [astro-ph.SR]]

Solov'ev, A. A., 1997, "Modeling of the magnetic structure of sunspots", *Astronomy Reports*, **41**, 121–127. [ADS]

Solov'ev, A. A. and Kirichek, E. A., 2015, "Magnetohydrostatics of a vertical flux tube in the solar atmosphere: Coronal loops, a model of a ring flare filament", *Astronomy Letters*, **41**, 211–224. [DOI], [ADS]

Solov'ev, A. A. and Kirichek, E. A., 2016, "Analytical Model of an Asymmetric Sunspot with a Steady Plasma Flow in its Penumbra", *Solar Phys.*, **291**(6), 1647–1663. [DOI], [ADS]

Solov'ev, L., 1968, "THE THEORY OF HYDROMAGNETIC STABILITY OF TOROIDAL PLASMA CONFIGURATIONS", *Journal of Experimental and Theoretical Physics*, **26**, 626–643

Srivastava, A. K., Shetye, J., Murawski, K., Doyle, J. G., Stangalini, M., Scullion, E., Ray, T., Wójcik, D. P. and Dwivedi, B. N., 2017, "High-frequency torsional Alfvén waves as an energy source for coronal heating", *Scientific Reports*, **7**, 43147. [DOI], [ADS]

Steiner, O., Pneuman, G. W. and Stenflo, J. O., 1986, "Numerical models for solar magnetic fluxtubes", *Astron. Astrophys.*, **170**, 126–137. [ADS]

Stenflo, J. O., 2013, "Solar magnetic fields as revealed by Stokes polarimetry", *Astron. Astrophys. Rev.*, **21**, 66. [DOI], [ADS], [arXiv:1309.5454 [astro-ph.SR]]

Stepanov, V. E., 1965, "The structure and the motion of magnetic fields in sunspots", in *Stellar and Solar Magnetic Fields*, (Ed.) Lust, R., IAU Symposium, 22, [ADS]

Steshenko, N. V., 1967, *Publ. Crime. Astrophys. Obs.*, **37**, 21

Su, Jiangtao, Liu, Yu, Zhang, Hongqi, Mao, Xinjie, Zhang, Yin and He, Han, 2010, "Observational Evidence of Unwinding and Chirality Changing in Penumbral Filaments by Hinode", *Astrophys. J.*, **710**(1), 170–179. [DOI], [ADS]

Svestka, Z., 1976, *Solar Flares*. [ADS]

Sweet, P. A., 1958a, "The Neutral Point Theory of Solar Flares", in *Electromagnetic Phenomena in Cosmical Physics*, (Ed.) Lehnert, B., IAU Symposium, 6, [ADS]

Sweet, P. A., 1958b, "The production of high energy particles in solar flares", *Il Nuovo Cimento*, **8**(S2), 188–196. [DOI], [ADS]

Taylor, J. B., 1974, "Relaxation of Toroidal Plasma and Generation of Reverse Magnetic Fields", *Physical Review Letters*, **33**, 1139–1141. [DOI], [ADS]

Thalmann, J. K., Tiwari, S. K. and Wiegelmann, T., 2013, "Comparison of Force-free Coronal Magnetic Field Modeling Using Vector Fields from Hinode and Solar Dynamics Observatory", *Astrophys. J.*, **769**, 59. [DOI], [ADS], [arXiv:1304.3619 [astro-ph.SR]]

Title, Alan M., Frank, Zoe A., Shine, Richard A., Tarbell, Theodore D., Topka, Kenneth P., Scharmer, Goran and Schmidt, Wolfgang, 1993, "On the Magnetic and Velocity Field Geometry of Simple Sunspots", *Astrophys. J.*, **403**, 780. [DOI], [ADS]

Tomoyori, K., Hirano, Y., Kurihara, K. and Tamada, T., 2015, "Background elimination using the SNIP algorithm for Bragg reflections from a protein crystal measured by a TOF single-crystal neutron diffractometer", in *Journal of Physics Conference Series*, 664, [DOI], [ADS]

Tsinganos, K. C., 1979, "Sunspots and the physics of magnetic flux tubes. IV - Aerodynamic lift on a thin cylinder in convective flows", *Astrophys. J.*, **231**, 260–269. [DOI], [ADS]

Uitenbroek, H. and Criscuoli, S., 2013, "A novel method to estimate temperature gradients in stellar photospheres.", *Mem. Soc. Astron. Ital.*, **84**, 369–374. [ADS]

Utz, D., Hanslmeier, A., Möstl, C., Muller, R., Veronig, A. and Muthsam, H., 2009, "The size distribution of magnetic bright points derived from Hinode/SOT observations", *Astron. Astrophys.*, **498**, 289–293. [DOI], [ADS], [arXiv:0912.2637 [astro-ph.SR]]

Utz, D., Jurčák, J., Hanslmeier, A., Muller, R., Veronig, A. and Kühner, O., 2013, "Magnetic field strength distribution of magnetic bright points inferred from filtergrams and spectro-polarimetric data", *Astron. Astrophys.*, **554**, A65. [DOI], [ADS], [arXiv:1304.5508 [astro-ph.SR]]

Uzdensky, D. A. and Kulsrud, R. M., 2000, "Two-dimensional numerical simulation of the resistive reconnection layer", *Physics of Plasmas*, **7**(10), 4018–4030. [DOI], [ADS], [arXiv:astro-ph/0003305 [astro-ph]]

van Ballegooijen, A. A., 1986, "Cascade of magnetic energy as a mechanism of coronal heating", *Astrophys. J.*, **311**, 1001–1014. [DOI], [ADS]

Vernazza, J. E., Avrett, E. H. and Loeser, R., 1981, "Structure of the solar chromosphere. III - Models of the EUV brightness components of the quiet-sun", *Astrophys. J. Suppl.*, **45**, 635–725. [DOI], [ADS]

Vigeesh, G., Hasan, S. S. and Steiner, O., 2009, "Wave propagation and energy transport in the magnetic network of the Sun", *Astron. Astrophys.*, **508**, 951–962. [DOI], [ADS], [arXiv:0909.2325 [astro-ph.SR]]

Vigeesh, G., Steiner, O. and Hasan, S. S., 2011, "Stokes Diagnostics of Magneto-Acoustic Wave Propagation in the Magnetic Network on the Sun", *Solar Phys.*, **273**, 15–38. [DOI], [ADS], [arXiv:1104.4069 [astro-ph.SR]]

Vlahos, L., Georgoulis, M., Kluiving, R. and Paschos, P., 1995, "The statistical flare.", *Astron. Astrophys.*, **299**, 897. [ADS]

Wittmann, A., 1974, "Computation and Observation of Zeeman Multiplet Polarization in Fraunhofer Lines. III: Magnetic Field Structure of Spot Mt. Wilson 18488", *Solar Phys.*, **36**, 29–44. [DOI], [ADS]

Yang, Y., Li, Q., Ji, K., Feng, S., Deng, H., Wang, F. and Lin, J., 2016, "On the Relationship Between G-Band Bright Point Dynamics and Their Magnetic Field Strengths", *Solar Phys.*, **291**, 1089–1105. [DOI], [ADS], [arXiv:1604.00152 [astro-ph.SR]]

Yun, H. S., 1971, "A Magnetostatic Sunspot Model with 'Twisted' Field", *Solar Phys.*, **16**, 398–403. [DOI], [ADS]

Yun, Hong Sik, 1970, "Theoretical Models of Sunspots", *Astrophys. J.*, **162**, 975. [DOI], [ADS]

Zhang, H., Scharmer, G., Lofdahl, M. and Yi, Z., 1998, "Fine Structures of Magnetic Field in Solar Quiet Region", *Solar Phys.*, **183**, 283–290. [DOI], [ADS]

Zirin, Harold, 1988, *Astrophysics of the sun*. [ADS]